

Title	Formation and characterisation of ordered porous vanadium oxide inverse opal materials for Li-ion batteries
Authors	Armstrong, Eileen
Publication date	2015
Original Citation	Armstrong, E. 2015. Formation and characterisation of ordered porous vanadium oxide inverse opal materials for Li-ion batteries. PhD Thesis, University College Cork.
Type of publication	Doctoral thesis
Rights	© 2015, Eileen Armstrong. - http://creativecommons.org/licenses/by-nc-nd/3.0/
Download date	2024-04-17 21:26:07
Item downloaded from	https://hdl.handle.net/10468/2051



UCC

University College Cork, Ireland
Coláiste na hOllscoile Corcaigh

Formation and Characterisation of Ordered Porous Vanadium Oxide Inverse Opal Materials for Li-ion Batteries



UCC

Coláiste na hOllscoile Corcaigh, Éire
University College Cork, Ireland

A thesis presented for the degree of Doctor of Philosophy to the National
University of Ireland, Cork.

by

Eileen Armstrong, B.Sc (Hons)

Department of Chemistry and the Tyndall National Institute,
University College Cork, Ireland

February 2015

Supervisor

Dr. Colm O'Dwyer

Declaration

I, Eileen Armstrong, hereby confirm that the work presented in this thesis is my own research, carried out under the direction of Dr. Colm O'Dwyer and due reference has been made, where necessary, to work of other authors. No part of this thesis has been previously submitted to this or any other university.

Signed

Eileen Armstrong

Eileen Armstrong

*Dedicated to
my mum and dad
Bríd and Luke Armstrong.*

Acknowledgements

I would firstly like to thank my supervisor Dr. Colm O'Dwyer, for all his help and encouragement throughout my PhD, his enthusiasm and dedication was always very inspiring. Thank you to the Irish Research Council for funding this work.

I would like to thank Prof. Dr. Clivia Sotomayor Torres and the entire Phononic and Photonic nanostructures (P2N) group at ICN2 in Barcelona, for their warm welcome and help while I was there. I'd particularly like to thank Dr. Worawut Khunsin from whom I learned so much, the continued help throughout my project made all the difference and is much appreciated.

Thank you to all the administration and technical staff in the Chemistry Department at UCC.

Thank you to everyone in the Physics Dept. and in the MSSSI at the University of Limerick where my PhD began.

I would like to thank the Applied Nanoscience Group, past and present, especially Elaine, Colm, Michal and Will. I particularly wish to thank our postdocs, Dr. David McNulty and Dr. Hugh Geaney for all their help and encouragement, particularly over my last year of work.

I want to particularly thank Cian, Roisín, John, Atul T. and everyone in Labs 115 and 343, for the warm welcome when we moved to UCC from UL, for their support and the many laughs. I'd especially like to say thank you to Elsa in Lab 343, 'mon petit lapin' for always keeping my spirits up especially throughout my thesis write-up. I'd also like to thank Timothy Collins for help with the statistical analysis of my opal structures (Cocorico!).

Thank you to my close friends Deirdre, Marie Clare, Sinéad, Sweta, Katie, Brónadh and Jennifer, for always being there for me, and for understanding my continuous neglect of them while doing this PhD. I'm very lucky to have such lovely friends.

Most especially I wish to thank my entire family in particular my sisters, Trudy and Jennifer, my brother Norbert, my aunt Eileen (particularly for all the help with my forgotten maths and physics over the years), my uncle Pdraig, my aunt Mary, and Delia for all the care and good wishes, to everyone, for their support, encouragement and love (including Shelley, Belle, Spock and Sasha!). Lastly and most importantly, I want to thank my mum, Bríd, and my dad, Luke, for their support in everything I do, for all their care, encouragement, worry, for their belief in me, and their love, your continuous hard work and intelligence is something to aspire to and you've always inspired me to do my very best.

Abstract

This thesis presents several routes towards achieving artificial opal templates by colloidal self-assembly of polystyrene (PS) or poly(methyl methacrylate) (PMMA) spheres and the use of these template for the fabrication of V_2O_5 inverse opals as cathode materials for lithium ion battery applications. First, through the manipulation of different experimental factors, several methods of affecting or directing opal growth towards realizing different structures, improving order and/or achieving faster formation on a variety of substrates are presented. The addition of the surfactant sodium dodecyl sulphate (SDS) at a concentration above the critical micelle concentration for SDS to a 5 wt% solution of PMMA spheres before dip-coating is presented as a method of achieving ordered 2D PhC monolayers on hydrophobic Au-coated silicon substrates at fast and slow rates of withdrawal. The effect that the degree of hydrophilicity of glass substrates has on the ordering of PMMA spheres is next investigated for a slow rate of withdrawal under noise agitation. Heating of the colloidal solution is also presented as a means of affecting order and thickness of opal deposits formed using fast rate dip coating. E-beam patterned substrates are shown as a means of altering the thermodynamically favoured FCC ordering of polystyrene spheres (PS) when dip coated at slow rate. Facile routes toward the synthesis of ordered V_2O_5 inverse opals are presented with direct infiltration of polymer sphere templates using liquid precursor. The use of different opal templates, both 2D and 3D partially ordered templates, is compared and the composition and arrangement of the subsequent IO structures post infiltration and calcination for various procedures is characterised. V_2O_5 IOs are also synthesised by electrodeposition from an aqueous $VOSO_4$ solution at constant voltage. Electrochemical characterisation of these structures as cathode material for Li-ion batteries is assessed in a half cell arrangement for samples deposited on stainless steel foil substrates. Improved rate capabilities are demonstrated for these materials over bulk V_2O_5 , with the improvement attributed to the shorter Li ion diffusion distances and increased electrolyte infiltration provided by the IO structure.

Publications

- Ordered 2D Colloidal Photonic Crystals on Gold Substrates by Surfactant-Assisted Fast-Rate Dip Coating, **E. Armstrong**, W. Khunsin, M. Osiak, M. Blömker, C. M. Sotomayor Torres, and C. O'Dwyer, *Small* (2014), 10, 1895-1901.
- 2D and 3D Vanadium Oxide Inverse Opals and Hollow Sphere Arrays, **E. Armstrong**, M. Osiak, H. Geaney, C. Glynn, and C. O'Dwyer, *CrystEngComm* (2014), 16, 10804-10815.
- Synthetic Routes for the Preparation of Ordered Vanadium Oxide Inverted Opal Electrodes for Li-Ion Batteries, **E. Armstrong**, W. Khunsin, C. M. Sotomayor Torres, M. Osiak, and C. O'Dwyer, *ECS Transactions* (2014), 58(25), 7-14.
- Investigations into Structure and Chemistry of 1D, 2D and 3D Structured Vanadium Oxide Nanomaterials for Li-ion Batteries, **E. Armstrong**, M. Osiak, C. Glynn, and C. O'Dwyer, *ECS Transactions*, (2014), 58 (14), 3-12.
- Light Scattering Investigation of 2D and 3D Opal Template Formation on Hydrophilized Surfaces, **E. Armstrong**, W. Khunsin, M. Osiak, C. M. Sotomayor Torres, and C. O'Dwyer, *ECS Transactions* (2014), 58, 9-18.
- Structuring Materials for Lithium-ion Batteries: Advancements in Nanomaterial Structure, Composition, and Defined Assembly on Cell Performance, M. Osiak, H. Geaney, **E. Armstrong**, and C. O'Dwyer, *J. Mater. Chem. A* (2014), 2 9433-9460.
- Artificial Opal Template Growth and Inverse Opal Applications, **E. Armstrong**, C. O'Dwyer, In preparation
- Electrodeposited Vanadium Oxide Inverse Opal as Lithium Ion Battery Cathodes, **E. Armstrong**, D. McNulty, and C. O'Dwyer, In preparation
- Epitaxial growth of visible to infra-red transparent conducting In_2O_3 nanodot dispersions and reversible charge storage as a Li-ion battery anode, M. Osiak, W. Khunsin, **E. Armstrong**, T. Kennedy, C. M. Sotomayor Torres, K. Ryan, and C. O'Dwyer, *Nanotechnology* (2013), 24, 065401.
- Core-Shell Tin Oxide, Indium Oxide, and Indium Tin Oxide Nanoparticles on Silicon with Tunable Dispersion: Electrochemical and Structural Characteristics as a Hybrid Li-Ion Battery Anode, M.J. Osiak, **E. Armstrong**, T. Kennedy, C. M. Sotomayor Torres, K. M. Ryan, C. O'Dwyer, *ACS Appl. Mater. Interfaces* (2013), 5, 8195-8202.
- Linking Precursor Composition to Nanoscale Structure and Optical Transparency in Polymer Assisted Fast-Rate Dip-Coating of Vanadium Oxide Thin Films, C. Glynn, D.

Creedon, H. Geaney, **E. Armstrong**, T. Collins, M. A. Morris and C. O'Dwyer, In preparation

Oral Presentations

- Light Scattering Investigation of 2D and 3D Opal Template Formation On Hydrophilized Surfaces for Ordered Porous Nanostructured Materials
224th ECS Meeting in San Francisco, California (October 27-November 1, 2013)
- Investigations Into Structure and Chemistry of 1D, 2D and 3D Structured Vanadium Oxide Nanomaterials for Li-Ion Batteries
224th ECS Meeting in San Francisco, California (October 27-November 1, 2013)

Poster Presentations

- Inverse Opal Vanadium Oxide Nanostructures for Li-ion Batteries: Formation and Optical Characterisation
NANOSMAT-2013, Granada, SPAIN
22-25 September 2013
Winner Best Poster
- Ordered Vanadium Oxide Inverted Opals for Li-ion Battery Electrodes and Optical Probing of Phase Changes
Tyndall Student Poster Competition, Tyndall National Institute, Cork
24-25 July 2014
Finalist
- Ordered Vanadium Oxide Inverted Opals for Li-ion Battery Electrodes and Optical Probing of Phase Changes
Institute of Physics in Ireland Spring Meeting, Royal Marine Hotel, Dun Laoghaire, Co. Dublin, Rosse Medal Competition
8th March 2014
Finalist
- Ordered Vanadium Oxide Inverted Opal Li-Ion Battery Electrodes and Optical Probing of Phase Changes
224th ECS Meeting in San Francisco, California
October 27-November 1, 2013

- Three-dimensional Ordered Macroporous LiFePO₄ Inverted Opal Thin Film Cathodes for High Performance Lithium Batteries
Globe Forum Dublin 2010, The Conference Centre, Dublin, Ireland,
17-18 November 2010
- Three-dimensional Ordered Macroporous LiFePO₄ Inverted Opal Thin Film Cathodes for High Performance, Ultrafast Charging Lithium-ion Batteries.
The Institute of Physics in Ireland 40th Spring Meeting, Carlingford, Co. Louth, Ireland,
15-17 April 2011

Table of Contents

Declaration	i
Acknowledgements	iii
Abstract	iv
Chapter 1 Introduction	1
1.1 Motivation	2
1.2 Overview of Thesis	5
1.3 References	7
Chapter 2 Literature Review: Artificial Opal Template Growth and Inverse Opal Applications	8
2.1 Introduction	9
2.2 Optical Characteristics of Photonic Crystals	10
2.3 Colloidal Self-Assembly	21
2.3.1 Binary Colloidal Crystals	31
2.3.2 Patterned Substrates and Constrained PhC Assembly	36
2.4 Inverse Opals: Formation and Emerging Technological Applications	39
2.4.1 Inverted Opals for Optoelectronics and Telecommunications	40
2.4.2 Inverted Opals for TPV Systems, and DSSCs	46
2.4.3 Inverted Opals for Lithium Ion Batteries	51
2.4.4 IO Cathodes	53
2.4.5 IO Anodes	55
2.4.6 IO Current Collector and Separator	58
2.5 Conclusions and Outlook	66
2.6 References	69
Chapter 3 Experimental	78
3.1 Introduction	79
3.2 Colloidal Sphere Assembly	79
3.2.1 Dip Coating	79

3.2.2	Surfactant-assisted Dip Coating	81
3.2.3	Patterned Substrates	83
3.2.4	Electrophoretic Deposition	85
3.3	Vanadium Pentoxide Precursor Infilling	86
3.3.1	Drop Casting/Dip Coating	87
3.3.2	Electrodeposition	88
3.4	Structure and Elemental Characterisation Techniques	89
3.4.1	Reflectance/Transmission Spectroscopy	89
3.4.2	Electron Microscopy	92
3.4.3	Raman Scattering Spectroscopy	93
3.4.4	X-ray Diffraction	93
3.5	Electrochemical Characterisation	94
3.6	References	96
Chapter 4	Ordered 2D Colloidal Photonic Crystals on Gold Substrates	
	by Surfactant-assisted Fast-rate Dip Coating	98
4.1	Introduction	99
4.2	Results and Discussion	101
4.2.1	Morphological Effects of Sodium Dodecyl Sulphate Addition	101
4.2.2	Optical Characterisation	106
4.3	Conclusion	114
4.4	References	116
Chapter 5	Methods of Affecting and Directing Opal Growth by Dip Coating	119
5.1	Introduction	120
5.1.1	Substrate Hydrophilicity and Temperature Effects on Order	121
5.1.2	Patterning as a Route to Deterministic Assembly	122
5.2	Results and Discussion	124
5.2.1	Colloidal Photonic Crystal Dip Coating on Hydrophilized Glass	124
5.2.2	Dip-coating with Applied Heat	134

5.2.3	Dip-coating of Artificial Opals on e-Beam Patterned Substrates	141
5.2.4	Binary-like Colloidal PhC using Patterned Substrates	147
5.3	Conclusions	150
5.3.1	Substrate Hydrophilicity and Increased Temperature	150
5.3.2	Patterning	151
5.4	References	153
Chapter 6	2D and 3D Vanadium Oxide Inverse Opals and Hollow Sphere Arrays	157
6.1	Introduction	158
6.2	Results and Discussion	161
6.2.1	Methods for 2D and 3D Opal Template Formation	161
6.2.2	Methods for 2D and 3D Inverse Opal Formation	164
6.2.3	2D Monolayer Vanadium Oxide IOs and Hollow Sphere Arrays	177
6.3	Conclusions	181
6.4	References	182
Chapter 7	Electrodeposited Vanadium Oxide Inverse Opal Lithium-ion Battery Cathodes	186
7.1	Introduction	187
7.2	Results and Discussion	189
7.2.1	Electrodeposition of V ₂ O ₅	189
7.2.2	Structure of Electrodeposited V ₂ O ₅ Inverse Opals	192
7.2.3	Electrochemical Characterisation – IOs as Lithium-ion Battery Cathodes	197
7.2.4	Structural Characterisation of Li Intercalated IOs	210
7.2.5	Flooded Cell Measurements	215
7.3	Conclusions	216
7.4	References	218
Chapter 8	Conclusions	221
8.1	Introduction	222
8.2	Ordered 2D Colloidal Photonic Crystals on Gold Substrates by Surfactant-assisted	

	Fast Rate Dip-Coating	222
8.3	Methods of Affecting and Directing Opal Growth during Dip Coating	223
8.4	2D and 3D Vanadium Oxide Inverse Opals and Hollow Sphere Arrays	224
8.5	Electrodeposited Vanadium Oxide Inverse Opal Lithium-ion Battery Cathodes	225
8.6	Summary of Conclusions	227
8.7	Future Work	228
	8.7.1 Sphere Deposition on Patterned Substrates	228
	8.7.2 Binary Colloidal Crystals by One-Step EPD	229
	8.7.3 V ₂ O ₅ IO Formation and Optical/Electrochemical Characterisation	231
8.8	References	235

*“And time yet for a hundred indecisions,
And for a hundred visions and revisions,
Before the taking of a toast and tea.”*

The Love Song of J. Alfred Prufrock (32-34)

T.S Eliot

Chapter 1

Introduction

1.1 Motivation

So named for their resemblance in structure and iridescence to the natural opal,¹ artificial opals, assembled from ordered, periodic arrangements of colloidal spheres exhibit a host of unique and highly useful optical properties,^{2, 3} a consequence of a periodic variation in refractive index on the sub-micron wavelength scale. The ability to influence the propagation of electromagnetic waves in a similar way a semiconductor does for electrons and the formation of a photonic band gap (PBG) that disallows the propagation of certain frequencies of light is a particularly attractive quality.⁴ The promise offered by these photonic crystals (PhCs) or artificial opals is seemingly ever-expanding. Not only in the field of photonics, where it is becoming increasingly recognized that light and not electrons holds the answer to our information-transfer needs, but throughout applied sciences. Light can travel faster in dielectric materials than an electron does in metallic wire, it can carry a larger amount of information per second, and photons being less strongly interacting than electrons offer reduced energy losses.⁵ Progress towards achieving all-optical integrated circuits may lie with the photonic crystal⁶ but the unique optical and structural properties of these materials are progressively reaching beyond optical and information-transfer applications alone.

The use of these structures as templates for the formation of three dimensionally ordered porous architectures or inverse opals (IOs) has led to a multitude of new potential.⁷ The accessible surfaces and scalable skeletal dimensions provided by the three-dimensional (3DOM) materials created by infilling of the opal-like templates with material precursors have proven useful for numerous applications within the fields of energy storage,⁸ biological sensing,⁹ communications,⁶ optics¹⁰ and optoelectronics.¹¹ Colloidal crystal assembly offers certain advantages over other techniques for photonic crystal fabrication, particularly its low cost and large area preparation potential. Currently a large variety of methods exist for colloidal self-assembly¹² but optical and photonic applications are highly reliant on the

structural order and lattice orientation of the artificial opal and/or inverse opal (IO) and colloidal crystallization still suffers implementation limitations and high degrees of local disorder. The position and wavelength range of the PBG are affected by lattice structure and symmetry, as well as by filling fraction. The ability therefore, to design and direct lattice orientation is of great interest for artificial opal assembly and application progression. The majority of current self-assembly routes are also restricted to the thermodynamically favoured FCC crystal arrangement for monodisperse colloidal spheres, limiting the design characteristics of the subsequent IO material. Certain applications rely less on high degrees of order and can tolerate some degree of imperfection or polycrystallinity giving IO materials a versatility of application. For example, within the field of energy storage and generation the attraction and/or benefit of the IO structure lies not with its optical characteristics but with its networked, three dimensional porosity. In these cases, assembly is limited only by practical material restraints, synthesis constraints and the compatibility of the opal template units with material precursors and support materials.

There is currently a substantial need for a battery technology that can keep pace with the rapid growth in portable electronics and the need for clean energies and electric vehicles. Since their introduction to the market by Sony in the early 1990s,¹³ lithium ion batteries (LIBs), which offer specific energies higher than other electrochemical power sources, have received a considerable amount of attention and are the leading battery choice for most portable electronics. However, the active material electrodes for current thin film LIBs often suffer performance limitations due to the brittle and disordered electrode architectures. With the added pressures of miniaturization and increasing high-power demands, the question of what materials, designs and techniques are available to create and optimize electrodes that will allow high charge/discharge rates while limiting electrical disconnections is extremely significant. 3D ordered macroporous (3DOM) electrodes,

formed using sacrificial opal templates, have shown considerable improvements in power and energy density for lithium-ion batteries.¹⁴ These inverted opal (IO) architectures provide a continuous network of electrode material, a large interfacial area and open access for lithium insertion, which has reportedly led to significant improvements in rate capabilities. V_2O_5 aerogel was the first material tested in IO form for potential battery application.¹⁵ First proposed as a potential cathode material by Whittingham,¹⁶ V_2O_5 with its low cost and layered geometry is ideally suited as an insertion host for LIBs. Vanadium has multiple valence states allowing the formation of a number of oxides and V_2O_5 is particularly attractive, due to its mixed valence of V^{4+} and V^{5+} making it ideally suited for redox-dependent applications.¹⁷ However, initially as micron sized particles, V_2O_5 suffered electrochemical performance limitations due to severe capacity fading issues and poor conductivity. The IO structure is a promising solution, providing increased open-space to accommodate the volumetric expansion of the V_2O_5 material on Li insertion and an increased surface area for better electrolyte contact. The 3D porous structure and nanoscale walls of an IO have the potential therefore to greatly improve battery performance, as was shown in the early work by Sakamoto.¹⁵ However, since this first foray into IO battery testing little investigation has been given to the synthesis and cycling ability of V_2O_5 IO materials as LIB cathodes, with much of the efforts into V_2O_5 IO application concentrating on electrochromics. V_2O_5 with its high theoretical specific capacity and ternary phase formation¹⁶ has shown significant potential in a number of porous and nanostructured forms and so crystalline V_2O_5 in its IO form merits further investigation as a potential replacement cathode material.¹⁸⁻²⁰

1.2 Overview of this Thesis

In the following chapter, **Chapter 2**, the fundamental photonic crystal concepts are introduced and the attractive optical characteristics of these complex structures are discussed. An overview of several growth techniques for the formation of artificial opals by colloidal self-assembly is provided. Recent strides in directing and manipulating the natural growth towards improved order and unique structures are considered. The application of artificial opal PhCs as templates for the formation of IO PhCs is then outlined with an emphasis on the application of IOs to a number of functional devices and fields, particularly within energy storage technologies.

Chapter 3 provides a comprehensive outline of the various experimental procedures used regarding sample preparation through colloidal assembly and precursor infilling, structural characterization through microscopy and spectroscopy and the electrochemical processing procedure used.

In **Chapter 4** surfactant addition is investigated to direct order when dip coating opal photonic crystal sphere templates at a relatively (orders of magnitude) faster rate compared with the state of the art. At faster rates of withdrawal colloidal order often degenerates, insufficient time is provided for spheres to reach their preferred energy and spheres lacking in strong net repulsive forces particularly suffer disorder. Deposition on gold surfaces that quickly turn hydrophobic in air is also problematic. The addition of the surfactant sodium dodecyl sulphate (SDS) at a concentration above the critical micelle concentration for SDS to a 5 wt% solution of poly(methyl methacrylate) (PMMA) spheres before dip-coating is investigated as a route towards improving order on hydrophobic metallic surfaces at fast and slow rates of withdrawal. The ability to form 2D opals was examined using angle resolved light reflectance spectroscopy with the 2D diffraction from the monolayer opals compared to the theoretical dispersion from a planar diffraction grating.

Chapter 5 investigates the effect of several other factors on the assembly of polymer spheres by dip-coating. Firstly the effect of surface hydrophilicity on the order of the colloidal deposit is investigated for a slow rate of withdrawal under noise agitation. A structural comparison is made using angle resolved transmission measurements for deposits on two different degrees of hydrophilic glass substrates. The use of increased temperature as a method of affecting order and thickness at the faster withdrawal rate is next discussed. Lastly, in this chapter the use of e-beam patterned substrates is demonstrated as a means of altering the favoured FCC ordering of polystyrene spheres (PS) when dip coated.

In **Chapter 6**, facile routes toward the synthesis of ordered IO V_2O_5 , using polymer sphere templates and direct infiltration using liquid precursor are investigated. The use of different opal templates, both 2D and 3D partially ordered templates, is compared and the composition and arrangement of the subsequent IO structures post infiltration and calcination for various procedures is characterised.

Chapter 7 discusses the synthesis of V_2O_5 IOs by electrodeposition from an aqueous $VOSO_4$ solution at constant voltage. Electrochemical characterisation of these structures, deposited on stainless steel foil substrates, is then performed. The electrochemical performance of the electrodeposited IO materials is compared through galvanostatic cycling and rate capability tests with the electrochemical performance of drop cast IO structures from chapter 6 and as-deposited samples formed by direct electrodeposition on to a substrate with no template present. Investigations into the changes that occur to the electrodeposited IO material during reversible lithium insertion and removal were made using Raman scattering and X-ray diffraction. The extent of changes to the phase and structure of the V_2O_5 for different levels of lithium insertion is discussed and related to cyclic voltammetry results.

Chapter 8 summarises the results presented in Chapters 4, 5, 6 and 7 and outlines the significant conclusions. Recommendations for future work are also presented.

1.3 References

1. Sanders, J. V., Colour of Precious Opal. *Nature* 1964, **204**, 1151-1153.
2. John, S., Strong localization of photons in certain disordered dielectric superlattices. *Phys. Rev. Lett.* 1987, **58**, 2486-2489.
3. Yablonovitch, E., Inhibited Spontaneous Emission in Solid-State Physics and Electronics. *Phys. Rev. Lett.* 1987, **58**, 2059-2062.
4. Joannopoulos, J. D.; Johnson, S. G.; Winn, J. N.; Meade, R. D., *Photonic Crystals Molding the Flow of Light*. Princeton University Press: 41 William Street, Princeton, New Jersey 08540, 2008.
5. Joannopoulos, J. D.; Villeneuve, P. R.; Fan, S., Photonic crystals: putting a new twist on light. *Nature* 1997, **386**, 143-149.
6. Blanco, A.; Chomski, E.; Grabtchak, S.; Ibsate, M.; John, S.; Leonard, S. W.; Lopez, C.; Meseguer, F.; Miguez, H.; Mondia, J. P.; Ozin, G. A.; Toader, O.; van Driel, H. M., Large-scale synthesis of a silicon photonic crystal with a complete three-dimensional bandgap near 1.5 micrometres. *Nature* 2000, **405**, 437-440.
7. Braun, P. V., Materials chemistry in 3D templates for functional photonics. *Chem. Mater.* 2013, 277-286.
8. Pikul, J. H.; Zhang, H. G.; Cho, J.; Braun, P. V.; King, W. P., High-power lithium ion microbatteries from interdigitated three-dimensional bicontinuous nanoporous electrodes. *Nat. Commun.* 2013, **4**, 1732-1736.
9. Fenzl, C.; Hirsch, T.; Wolfbeis, O. S., Photonic crystals for chemical sensing and biosensing. *Angewandte Chemie International Edition* 2014, **53**, 3318-3335.
10. Arsenault, A. C.; Puzzo, D. P.; Manners, I.; Ozin, G. A., Photonic-crystal full-colour displays. *Nat. Photonics* 2007, **1**, 468-472.
11. Nelson, E. C.; Dias, N. L.; Bassett, K. P.; Dunham, S. N.; Verma, V.; Miyake, M.; Wiltzius, P.; Rogers, J. A.; Coleman, J. J.; Li, X.; Braun, P. V., Epitaxial growth of three-dimensionally architected optoelectronic devices. *Nat. Mater.* 2011, **10**, 676-681.
12. von Freymann, G.; Kitaev, V.; Lotsch, B. V.; Ozin, G. A., Bottom-up assembly of photonic crystals. *Chem. Soc. Rev.* 2013, **42**, 2528-2554.
13. Nagura, T.; Tozawa, K., *Prog. Batteries Sol. Cells* 1990, **9**, 209-216.
14. Stein, A., Energy storage: Batteries take charge. *Nat. Nanotechnol.* 2011, **6**, 262-263.
15. Sakamoto, J. S.; Dunn, B., Hierarchical battery electrodes based on inverted opal structures. *J. Mater. Chem.* 2002, **12**, 2859-2861.
16. Whittingham, M. S., The Role of Ternary Phases in Cathode Reactions. *J. Electrochem. Soc.* 1976, **123**, 315-320.
17. McNulty, D.; Buckley, D. N.; O'Dwyer, C., Synthesis and electrochemical properties of vanadium oxide materials and structures as Li-ion battery positive electrodes. *J. Power Sources* 2014, **267**, 831-873.
18. Li, L.; Steiner, U.; Mahajan, S., Improved electrochromic performance in inverse opal vanadium oxide films. *J. Mater. Chem.* 2010, **20**, 7131-7134.
19. Tong, Z.; Hao, J.; Zhang, K.; Zhao, J.; Su, B.-L.; Li, Y., Improved electrochromic performance and lithium diffusion coefficient in three-dimensionally ordered macroporous V₂O₅ films. *J. Mater. Chem. C* 2014, **2**, 3651-3658.
20. Wang, S. Q.; Li, S. R.; Sun, Y.; Feng, X. Y.; Chen, C. H., Three-dimensional porous V₂O₅ cathode with ultra high rate capability. *Energy Environ. Sci.* 2011, **4**, 2854-2857.

Chapter 2

Literature Review: Artificial Opal Template Growth and Inverse Opal Applications

Abstract

Photonic crystals (PhCs) influence the propagation of light by their periodic variation in dielectric contrast or refractive index. This review outlines the attractive optical qualities inherent to most PhCs namely the presence of full or partial photonic band gaps and the possibilities they present towards the inhibition of spontaneous emission and the localization of light. Colloidal self-assembly of polymer or silica spheres is one of the most favoured and low cost methods for the formation of PhCs as artificial opals. Current growth methods for colloidal self-assembly are discussed and the use of these structures for the formation of inverse opal architectures is then presented. Inverse opal structures with their porous and interconnected architecture maintain a growing potential for application spanning several technological arenas - optics and optoelectronics, energy storage, communications, sensor and biological applications. This review presents several of these applications, with a particular emphasis on the use of these three dimensional porous structures in energy storage technology. Progress towards achieving all-optical integrated circuits may lie with the photonic crystal but the unique optical and structural properties of these materials allow the promise of these materials to continually expand reaching beyond optics alone.

2.1 Introduction

The continuous and ever increasing drive for miniaturization and higher speed information systems has led to the now widespread idea of using photons instead of electrons as the information carrier. While photons hold many advantages over electrons the manipulation and control of light presents some difficulties. Efforts to achieve all-optical integrated circuits have led to a growing interest in the fabrication and use of photonic crystals (PhCs); PhCs have a periodic variation in dielectric function that affects the propagation of photons much like the periodic potential in semiconductors affects the flow of electrons. The use of PhCs for the manipulation of light stems from the early ideas of Yablonovitch and John that a three-dimensional (3D) periodic array could, by the presence of an electromagnetic band gap, control the radiative properties of materials, and so limit spontaneous emission.^{1, 2} This concept was initially presented by E. Yablonovitch in the late 1980s.¹ S. John followed with the idea that periodic structures could affect photon localization by a random refractive index variation.² These two discoveries and the subsequent growth in PhC research for information management systems has led to an increasing awareness of the potential applications of PhCs within other technologies. For example, most recently PhC's have gained a lot of consideration as Li-ion battery electrodes. However, the electrochemical, electrochromic and other changes to ordered porous electrodes have received limited optical analysis.³ The substantial number of structural and optical advantages possessed by PhC's, make them ideally suited to many functional regimes that benefit from a porous, continuously interconnected, and in most cases, an optically significant material.

In this review, the attractive optical characteristics of PhCs are discussed and the fabrication techniques available for the formation of PhCs through colloidal self-assembly routes are reviewed. The application of these artificial opal PhCs as templates for the formation of inverse opal (IO) PhCs is then outlined with an emphasis on the application of

inverse opals (IOs) to a number of functional devices and fields.

2.2 Optical Characteristics of Photonic Crystals

PhCs exist throughout the natural world,⁴ from opal gemstones⁵ and beetles,⁶ to bird feathers,⁷⁻⁹ and butterfly wings,¹⁰⁻¹² and the common characteristic between all is their iridescent colour. This directional-dependent colour (colour that changes depending on angle of observation), does not arise from any absorption or pigmentation alone but is instead caused by the interaction of light with the periodic or random architecture of these materials' natural design, as shown in Fig. 2.1. PhCs are often most easily explained as an analogue to semiconductor materials. In a semiconductor, an electron passing through an ordered atomic lattice experiences a periodic potential, this interaction produces a band of energies over which electrons are forbidden to propagate in any direction. Much like a semiconductor affects the flow of electrons, a photonic crystal (PhC) affects the flow of photons. As a consequence of the differing dielectric media and the subsequent refractive index contrast within the crystal, light is scattered and/or diffracted from the different surfaces, producing a band of forbidden frequencies where interference of the scattered waves is destructive in all directions. Light cannot propagate within this region and the greater the refractive index contrast, the wider this photonic band gap (PBG) becomes. A full PBG is a characteristic only observed in PhCs where the propagation of light is prohibited in all directions. An incomplete PBG or pseudogap, sometimes referred to as a stop-band, is one that prohibits light from propagating in only some directions. The refractive index contrast and the lattice topology affects the existence of a full PBG but the wavelength range affected is determined by the length scale or lattice parameter of the crystal. The presence of the PBG and the potential ability to tune its position to suit specific frequencies is perhaps the most attractive quality of PhCs.

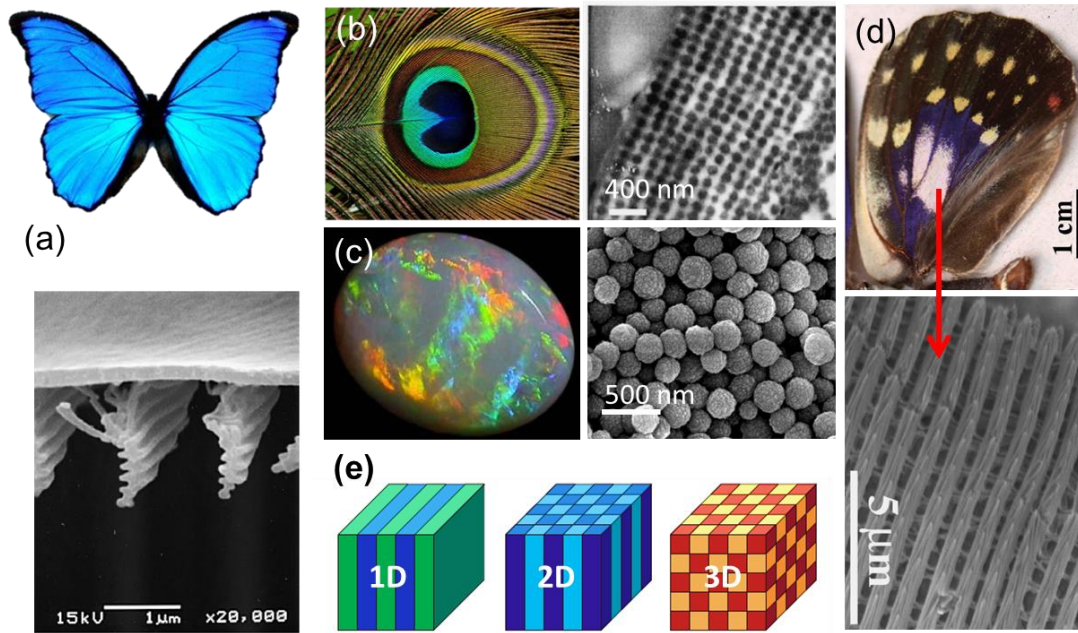


Fig. 2.1 Natural photonic crystals: (a) The blue iridescence and SEM image of the 1D structure of the Morpho butterfly¹². (b) Multi-coloured peacock feather and TEM image of transverse cross section of the 2D structure of blue wing⁹. (c) Natural opal gemstone and SEM image of the silica sphere structure within.¹³ (d) Wing of the male Sasakia Charonda butterfly and SEM image of the 3D structure of the white iridescent area.¹⁰ (e) Schematic representation of 1D, 2D and 3D PhC structures, with different colours representative of different dielectric constants, indicating periodicity in one, two or three directions.

The origin of this PBG can first be explored in order to better understand the full extent of the optical possibilities inherent in a PhC through its design. While PhCs can be classified as one-dimensional (1D), two-dimensional (2D) or three-dimensional (3D), with periodicity in one, two or three directions respectively (as outlined in the schematic in Fig. 2.1 (e)), for ease of description the properties of 1D PhC can first be examined. The optical phenomenon of greatest interest, that is, the PBG or stop-band, the subsequent inhibition of spontaneous emission, and the possibility of localized modes are transferable to all dimensional systems.

A number of comprehensive reviews,^{14, 15} and text books^{16, 17} are available for a more in depth approach to the underlying optics of PhC behaviour but all discussions on the propagation of light in a PhC and determination of the PBG, must invariably begin with

Maxwells Equations, the four equations governing all macroscopic electromagnetism.

$$\nabla \times E + \frac{\delta B}{\delta t} = 0 \quad (\text{Eq. 2.1})$$

$$\nabla \times H - \frac{\partial D}{\partial t} = J \quad (\text{Eq. 2.2})$$

$$\nabla \cdot B = 0 \quad (\text{Eq. 2.3})$$

$$\nabla \cdot D = \rho \quad (\text{Eq. 2.4})$$

where, E and H are the magnetic and electric fields, D and B the electric displacement and magnetic induction fields and ρ and J the free charge density and free current density respectively. In order to relate E to D and B to H , it is necessary to use the constitutive material equations, which can be greatly simplified in the absence of free charges and currents, if, together with the assumption that the dielectric constant ϵ is not frequency dependent, it is assumed that the materials are isotropic and only linear optics need be considered. These considerations reduce the constitutive material equations to:

$$D = \epsilon_0 \epsilon E \quad (\text{Eq. 2.5})$$

$$B = \mu_0 \mu H \quad (\text{Eq. 2.6})$$

Here, ϵ_0 is the vacuum permittivity, ϵ is a scalar dielectric function known as relative permittivity, μ is the relative magnetic permeability of the dielectric medium which for most dielectric materials is close to 1 and is assumed to be 1, and μ_0 is vacuum permeability. The assumptions and mathematical conventions used in reducing the constitutive equations to Eq. 2.5 and 2.6 are explained in more detail in Joannopoulos *et al.*¹⁶ However, by using these relations and the assumptions mentioned above including the absence of free current, Maxwell's equations become:

$$\nabla \times E(r, t) + \mu_0 \frac{\partial H(r, t)}{\partial t} = 0 \quad (\text{Eq. 2.7})$$

$$\nabla \times H(r, t) - \varepsilon_0 \varepsilon \frac{\partial E(r, t)}{\partial t} = 0 \quad (\text{Eq. 2.8})$$

$$\nabla \cdot H(r, t) = 0 \quad (\text{Eq. 2.9})$$

$$\nabla \cdot \varepsilon E(r, t) = 0 \quad (\text{Eq. 2.10})$$

Magnetic and electric fields are a function of both time and space and can be separated into a real spatial field and a complex exponential for a harmonically varying temporal part, to give:

$$E(r, t) = E(r)e^{-i\omega t} \quad (\text{Eq. 2.11})$$

$$H(r, t) = H(r)e^{-i\omega t} \quad (\text{Eq. 2.12})$$

These are inserted into Eq.2.6 and Eq. 2.7 above to formulate the curl equations that relate $H(r)$ and $E(r)$:

$$\nabla \times E(r) - i\omega\mu_0 H(r) = 0 \quad (\text{Eq. 2.13})$$

$$\nabla \times H(r) + i\omega\varepsilon_0\varepsilon_r E(r) = 0 \quad (\text{Eq. 2.14})$$

Looking solely at the magnetic field for mathematical convenience¹⁶ (the electric field can be derived similarly), these two equations can be decoupled to formulate an equation entirely in $H(r)$. Dividing Eq 2.14 by ε_r , obtaining the curl of the equation, and then substituting for $\nabla \times E(r)$ using Eq 2.9, gives a master wave equation describing the propagation of the magnetic field ($H(r)$) of a photon:

$$\nabla \times \left(\frac{1}{\varepsilon(r)} \nabla \times H(r) \right) = \frac{\omega^2}{c^2} H(r) \quad (\text{Eq. 2.15})$$

Where the speed of light $c = 1/\sqrt{\varepsilon_0\mu_0}$, ω is the frequency and ε_r is the macroscopic dielectric function of the material. This equation is in the form of an eigenvalue problem with eigenvector $H(r)$, eigenvalue ω^2/c^2 and eigen-operator $\nabla \times \frac{1}{\varepsilon_r} \nabla$. This operator, is known as the Hermitan operator and has real and positive eigenvalues, much like the Hamiltonian

operator of quantum mechanics and this allows us to view photonic crystals in solid-state physics terms and to assume some of the same properties, such as orthogonality and that all eigenfrequencies are real. However, it is important here to apply the transversality constraint; the two divergence equations $\nabla \cdot H(r) = 0$ and $\nabla \cdot \epsilon E(r) = 0$ must be taken into consideration, and with this constraint, the master equation for a material $\epsilon(r)$ can be solved to produce the mode $H(r)$ and the corresponding frequencies.

As mentioned above, a photonic crystal is a material whose dielectric function varies periodically, therefore:

$$\epsilon(r) = \epsilon(r + R) \quad (\text{Eq. 2.16})$$

where R is a lattice-translation vector, equal to $l_1 a_1 + l_2 a_2 + l_3 a_3$ where $l_1, l_2,$ and l_3 are integers. This periodicity requires the solution of Eq. 2.14 to satisfy what is known as the Floquet-Bloch theorem, which states that the solutions to the equations for periodic media are plane waves modulated by a periodic function with lattice periodicity, which gives:

$$H(r) = h_k(r) e^{ikr} \quad (\text{Eq. 2.17})$$

where k is a wave vector contained in the first Brillouin zone, a region of reciprocal space closer to the origin than to any other reciprocal lattice point and h_k is the periodic function of position sometimes referred to as the Bloch function:

$$h_k(r) = h_k(r + R) \quad (\text{Eq. 2.18})$$

Solving the master equation can be done by a number of computational methods, but the most commonly used approach is known as the plane-wave expansion method which involves the expansion of the magnetic and dielectric constant on the bases of a plane wave. The master equation Eq. 2.15, after some vector operations, can be reduced to a matrix, whose eigenvalues, a series of functions in the form $\omega_n(k)$ with $n = 1, 2, \dots$ form the photonic

bands. This band structure shows all the frequencies in which the optical modes are allowed for a given wave vector k . A photonic band gap (PBG) is a range of ω for which there are no propagating eignensolutions for any k , though there are above and below.

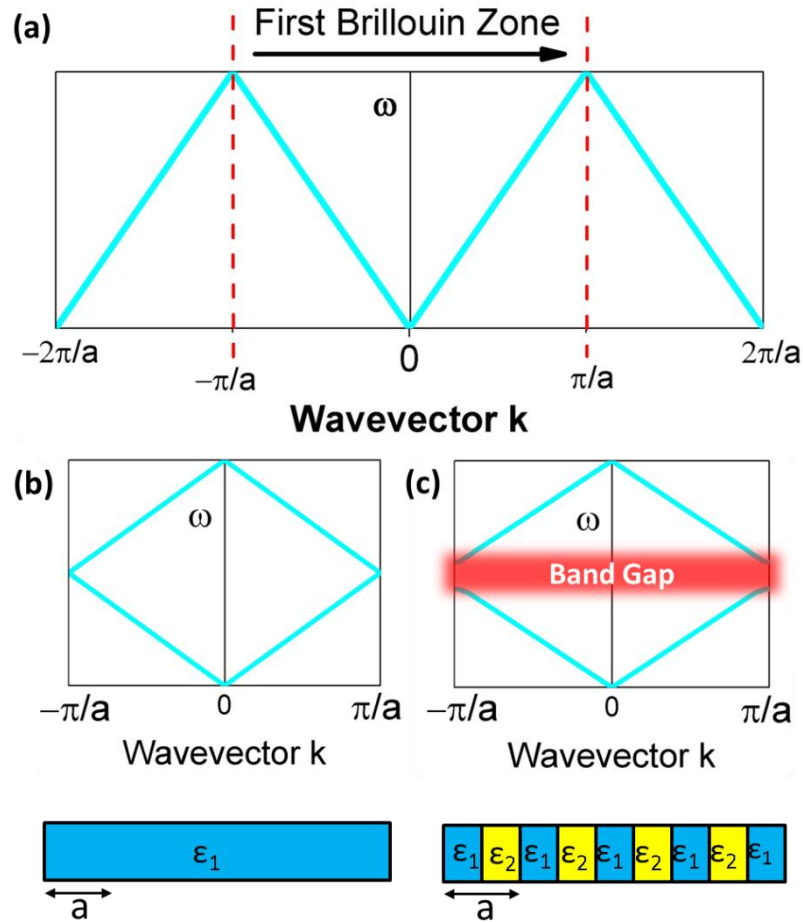


Fig. 2.2 Schematic illustrating: (a) The first Brillouin zone (b) The dispersion relation for a homogeneous material with a uniform dielectric function and artificial periodicity demonstrating the ‘folding effect’ of Blochs theorem and (c) A periodic material with a varying dielectric function and real lattice periodicity a , illustrating the presence of a gap where there no propagating solutions for k .

For every lattice vector (R) in real space, there is a lattice vector (G) in reciprocal space for which the dispersion relation is determined and periodicity in real space results in periodicity in the dispersion relation. Two states with wavevectors differing by $2\pi/a$ represent the same state exactly which means eignensolutions for the wavevector k need only be computed within the primitive cell of the reciprocal lattice, more conventionally realized as

the first Brillouin zone (BZ). This constitutes a ‘folding back’ of the dispersion relation into the first BZ, which is schematically represented in Fig. 2.2. The dispersion relation defines the relationship between angular frequency ω of the photon and its wavevector $k = \frac{2\pi}{\lambda}$ and in free space amounts to a linear dependence with the slope equal to the speed of light c , or in some cases, the group velocity of the wavepacket.

$$\omega = ck \quad (\text{Eq. 2.19})$$

This dispersion relation describes the optical properties of a material, and a plot of ω against k will indicate the allowed energies (bands) or states at given k -vectors.

For a one dimensional, homogeneous material with a uniform dielectric function, the band structure or dispersion relation is simply:

$$\omega = \frac{ck}{\eta} \quad (\text{Eq. 2.20})$$

where η is the refractive index of the material and is related to the permittivity by $\eta = \sqrt{\epsilon}$. Forward propagation results in a straight line as does backward propagation. This is shown in Fig. 2.2 (a) and (b). A periodic dielectric function causes forward moving waves to be partially reflected at every interface, interference of the forward and reflected waves creates a standing wave at the edge of the BZ where frequencies fulfil what is known as the Bragg condition, similar to X-ray diffraction theory but for optical wavelengths. Maxwell’s equations are scale invariant meaning there is no fundamental length scale for PhCs, such as the Bohr radius in atomic physics. Therefore, similar structures of different sizes behave similarly, if the lattice constant of a PhC is scaled by a factor s its mode profile and frequency are re-scaled versions of the old mode profile i.e. the solution to the master equation at one length scale provides the information for all length scales. For this reason the eigenfrequencies are usually given in a unit normalized to the lattice constant, $\omega = a/\lambda$ and

since $a/\lambda = \omega/(2\pi c/a)$ the energy is often expressed in these units, as per the dispersion relations shown in Fig. 2.3, which highlights the PBG variation due to refractive index contrast.

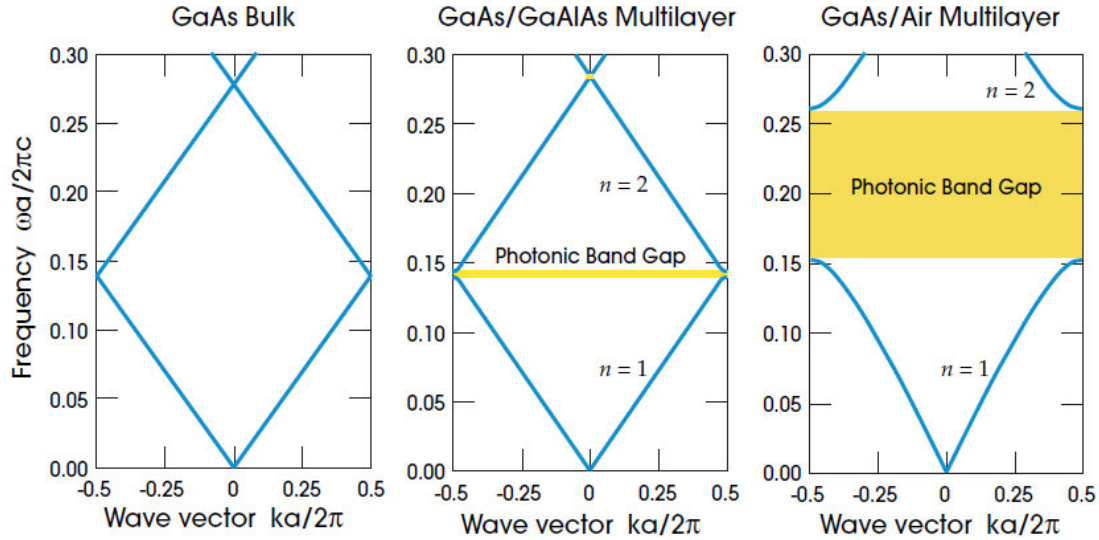


Fig. 2.3 The photonic band dependence on refractive index contrast computed for three different multilayer films with layers of width $0.5a$, in (a) the dielectric constant is the same for every layer $\epsilon=13$ in (b) layers alternate between a material of dielectric constant 13 and 12 and (d) shows the wider PBG for the larger contrast with alternating layers of dielectric constant 13 and 1.¹⁶

This PBG and the ability to manipulate it through material choice is the central driving force for the fabrication of PhCs because with it comes a litany of extremely useful optical phenomena. The initial theories from Yablonavich and John mentioned above still represent two of the most interesting and attractive qualities of PhCs. Spontaneous emission of excited atoms is a fundamental problem faced by many optoelectronic devices, causing energy loss, speed limitations and noise.^{18, 19} Spontaneous emission and the rate at which an atom decays is related to the number of allowed electromagnetic states available for an emitted photon, the PBG represents a region of forbidden modes, therefore the density of states (DOS) is zero inside the gap. This suppression of the density of states is what gives PBGs the potential to inhibit spontaneous emission.²⁰ At the edge of the PBG the DOS suddenly increases and this enhanced DOS subsequently enhances emission, which if

controlled could also be useful for certain devices. The ability to tune the position and width of the PBG or stopband and in turn manage spontaneous emission is extremely promising for a number of applications, including LEDs and low threshold lasers. The localization and the guiding of light through the introduction of defects is highly beneficial for the formation of waveguides and optical cavities. Point or line defects can be introduced to a PhC and introduce a state within the gap with a localized wavefunction, light that propagates with a frequency within the bandgap of the crystal will be confined within this mode since it is forbidden to propagate outside the defect. This is very beneficial for the manipulation of light around bends (see Fig. 2.4), obstacles, and for exotic optical effects such as cloaking when meta-material PhCs are used,²¹⁻²³ minimising losses compared with dielectric waveguides.²⁴

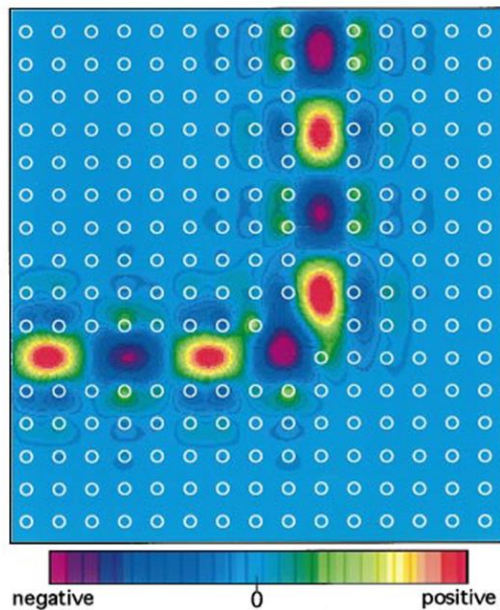


Fig. 2.4 A mode completely confined and guided smoothly around the sharp bend with 2D photonic crystal of dielectric rods in air, the white circles indicate the position of the rods.²⁴

A modification to Snell's Law for refraction of light between media of dissimilar refractive index, and Bragg's Law for optical diffraction can be derived to describe the wavelength-dependent 'structural colour' observable in colloidal opals or photonic crystals. As outlined in Fig. 2.5 below, the opal film is modelled as a multilayer of two media with

different refractive indices (in this case two, but it may vary depending on the complexity of the structure, porosity, phase homogeneity etc.). In the present case, one of these indices (η_1) is typically vacuum, air or a liquid, the other (η_2) that of the material. In the case of constructive interference of diffracted photons, Bragg's law is

$$m\lambda_m = 2\eta_{eff}d \cos \phi_2 \quad (\text{Eq. 2.21})$$

where d is the interplanar spacing defining the centroids of the spheres. It has a value of $d = D$, the sphere diameter, for (110) cross-section of fcc-packed opals, and $d = \sqrt{3}/2D$ for (111) - ordered PhCs, and so on.

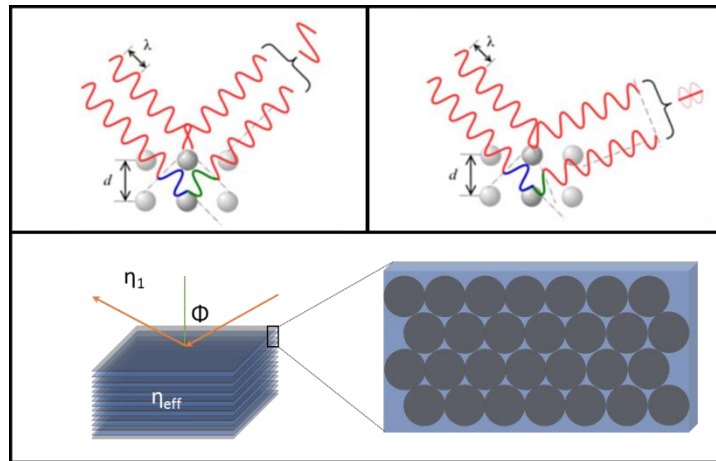


Fig. 2.5 Schematic outlining the interaction of light with the periodic material with an effective refractive index, and the light scattered by the sphere planes

The corresponding Snell's law criterion for the light incident at an angle ϕ_1 can be written as

$$\eta_1 \sin \phi_1 = \eta_2 \sin \phi_2 \quad (\text{Eq. 2.22})$$

Thus, the angle dependent diffraction or colour can be expressed in term of the incident angle generally as the Bragg-Snell law

$$m\lambda_m = 2d\sqrt{\eta_{eff} - \sin^2 \phi_1} \quad (\text{Eq. 2.23})$$

where η_{eff} is the effective refractive index of the media and depends on the relative refractive indices of the spheres and surrounding medium, and their the packing density.

Since the layer or slab in a well-defined opal is periodic, Fabry-Pérot resonances are observable at energies lower than the PBG provided the effective refractive index is well-defined and constitutes a homogeneous thin layer with effective refractive index η_{eff} . For ordered, simple thin film opals (but typically not for single monolayer opals as they are typically weaker and broader than diffraction contributions), η_{eff} and the number of layers can be estimated from the periodicity of the Fabry-Pérot resonances in optical reflection or transmission spectra. The number of layers, or the opal film thickness, is distinct from the *optical* thickness obtained from the spectral separation of the Fabry-Pérot fringes, which also includes the effective index. To estimate film thickness (at least for a simple 3D ordered opal of identical spheres), the fringes will appear in reflectance or transmission spectra at

$$\lambda_m = \frac{2L\eta_{eff}}{m} \quad (\text{Eq. 2.24})$$

where L is the sample thickness and m is the resonance order. In a fcc-packed opal crystal made from spheres of radius R with the (111) planes parallel to the substrate, simple geometrical analysis shows that L is related to the number of (111)-oriented layers N comprising the film according to $L = 2R + N\sqrt{3}R$.

The position of the bandgap is determined by the lattice constant and the spectra PBG width by the effective refractive index contrast and filling factor. If materials of high enough refractive index contrast are used in conjunction with materials with low absorption in the desired spectral range, then light with energies located inside the PBG will be reflected from the PhC without absorption, which makes PBG materials highly suited to optical filter

applications. The light that is reflected or diffracted by a PhC follows Bragg's Law and so can be used in determining the reciprocal lattice of a given structure. This facilitates probing of the optical characteristics of a given PhC by angle-resolved light reflection and transmission experiments, which is a useful characteristic when designing and synthesising PhCs for a particular application.

PhCs can be designed and formed by several methods, including sophisticated and expensive lithography techniques, both holographic²⁵ and mask²⁶ methods. However, one of the more popular approaches is the formation of artificial opals through the self-assembly of colloidal spheres of either silica or different polymers.^{14, 27} This route has the benefit of low cost and aside from limitations from natural imperfections that in some cases can lead to a certain degree of disorder, these approaches still offer amenable and useful properties for a host of real and theoretical applications in a number of technologies. However, perhaps the most significant application of artificial opals is in fact as templates for the formation of 3D PhCs in the form of inverse opals (IOs). Inverse opals are three dimensionally ordered macroporous materials formed through the infiltration of an artificial opal with a material precursor and then removal of the spheres. Provided a material of sufficiently high refractive index is used, IOs offer the possibility of achieving a complete PBG. The ability to control the structure and symmetry of 3D PhCs through template design has ensured a substantial and continuously growing interest in methods of artificial opal growth by colloidal self-assembly.

2.3 Colloidal Self-Assembly

As discussed above, the working range of a photonic crystal is dependent on the spatial periodicity of the refractive index. For this reason, periodicity needs to be on the order of a few hundred nanometers to 1 μm in order to operate in the visible or near-infrared region of the electromagnetic spectrum. The lattice constant of the photonic crystal must be

comparable to the wavelength of light. It is important to note that for self-assembly to occur, a balance must be made between the colloidal forces, the forces induced by colloidal phenomena and any external forces acting on the system, all of which can be either attractive driving forces or repulsive forces that can oppose coagulation of the spheres.

Various methods have been developed for the assembly of monodisperse spheres into ordered or semi-ordered lattices. The type of methods available are often discussed in terms of the various phenomena or forces used or manipulated in order to influence their assembly; gravitational or inertial forces, surface tension or capillary forces, or electric or magnetic fields. Certain methods can also involve some form of spatial confinement to further direct the self-assembly process. The predominant assembly routes are discussed in summary here with several reviews^{14, 15, 17, 27-30} available discussing the various methods and their effectiveness in further detail.

Among the oldest and simplest method of assembly is sedimentation^{31, 32}. Colloidal particles in solution will settle under gravity to produce thick, ordered structures, the thickness of which can be controlled by controlling the concentration of the sphere mixture. For this to occur naturally, with no external force applied, the density of the particles must be sufficiently higher than that of the dispersion medium. The movement of the spheres under gravity creates a diffusive force in the opposite direction due to the concentration gradient caused by the particle descent under gravity. For large particles, the effect of gravity will overtake the effect of diffusion, and the opposite is true of very small particles. Depending on the size of the spheres, this process of allowing the colloids to settle under gravitational forces can take from between several days to several months. For this reason, it is unsuited for large scale production and so other, more controllable and faster routes are more commonly used.

Sphere assembly/deposition has since been adapted by the application of external

forces, for example, the sedimentation of spheres under centrifugal or inertial force. The use of centrifugation, produces thick deposits of unsupported spheres, applicable to almost all sizes of spheres provided the density difference between them and the dispersant is sufficient and the centrifuge speed is strong enough³³⁻³⁶. This method, however, becomes more difficult for samples or applications requiring the use of a substrate.

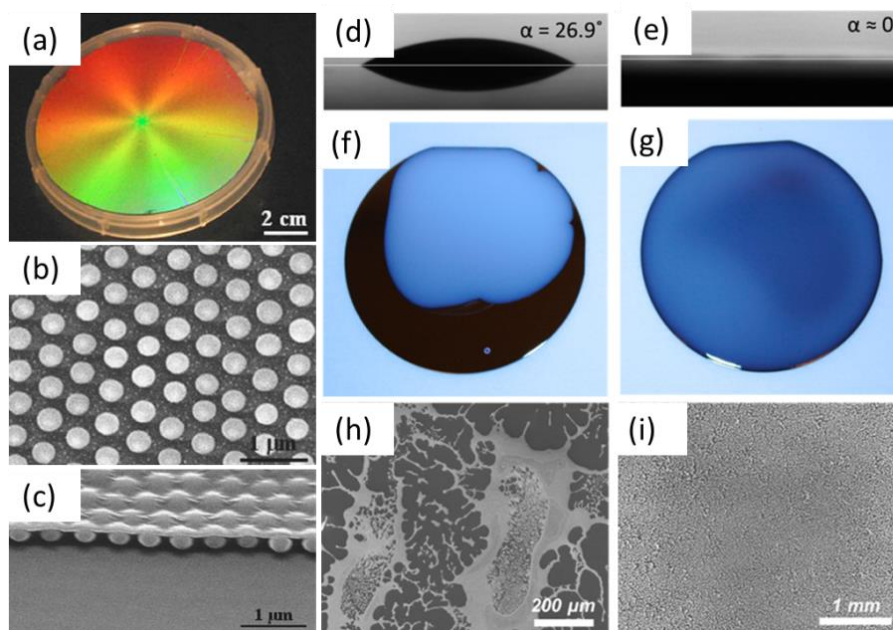


Fig. 2.6 (a) Wafer-scale non close packed monolayer colloidal crystal made by spin-coating on a 4-in. sample illuminated with white light. (b) High magnification SEM image of the typical top surface of the sample in (a) & (c) cross section SEM imaging showing a monolayer colloidal crystal polymer nanocomposite made by spin-coating. Contact angle measurement of (d) water ($\alpha = 26.9^\circ$) and (e) DMF ($\alpha \approx 0$ or immeasurable) and the comparison of wettability with 300 μL (50 mg/mL) of (f) silica spheres in water and (g) silica spheres in DMF solution droplets on piranha cleaned 2 inch Si substrates. SEM images after spin-coating at the same speed of silica spheres (h) in water and (i) in DMF.^{37, 38}

Manipulation of inertial forces through spin-coating^{37, 39-41} can produce polycrystalline deposits over large areas. However, with this technique the best results seem to occur for those involving some kind of localized restraint to ensure close packing of the spheres, such as what Jiang *et al.* demonstrated, whereby large, wafer scale 3D colloidal crystals were formed using silica spheres inside a polymer matrix, and then selective removal

of the spheres or polymer produced either colloidal crystals or macroporous polymers, respectively.³⁹ This is shown in Fig. 2.6 (a-c). They further developed the technique by producing non-close packed, two dimensional monolayer colloidal crystal-polymer nanocomposites through spin coating with a gradual increase in spin speed. Spin coating requires a lot of optimization and balance in terms of material concentrations, particle size and spin speed, it does have a tendency to produce patchy deposits which is why Jiang *et al.* advises priming the silicon substrate with 3-acryloxypropyl trichlorosilane to reduce patch formation.³⁷ Arcos *et al.* investigated the local and large scale order for spin coated colloids, showing thickness and symmetry to be controllable by solvent choice and spin speed⁴⁰.

More recently as shown by Fig. 2.6 (d-i), the addition of the organic solvent N,N-dimethylformamide (DMF) (Fig. 2.6 (e),(g),(i)) has been suggested as a means of producing enhanced uniformity and coverage for spin-coating silica sphere monolayers compared with spheres suspended in water (Fig. 2.6 (e),(g),(h)).³⁸ This further highlights the importance of the dispersal solvents properties, such as surface tension, evaporation rate and subsequent wettability, in achieving large scale coverage of uniform sphere structures by spin coating. However, the polycrystalline nature of most spin coated structures produced to date could make them more suited as templates for the production of monolayer porous materials with very low crack densities, as opposed to photonic applications directly.⁴⁰

The application of a magnetic or an electric field, in directing sedimentation has proved useful for the formation of highly ordered structures, at much faster rates than those methods relying on gravity alone. The surface charge of the colloidal particles and the pH of the entire solution can be controlled towards enhancing or slowing sedimentation of the spheres under the external force. A magnetic field can be modulated spatially in time and in magnitude and so can provide a versatile driving force for colloidal self-assembly.

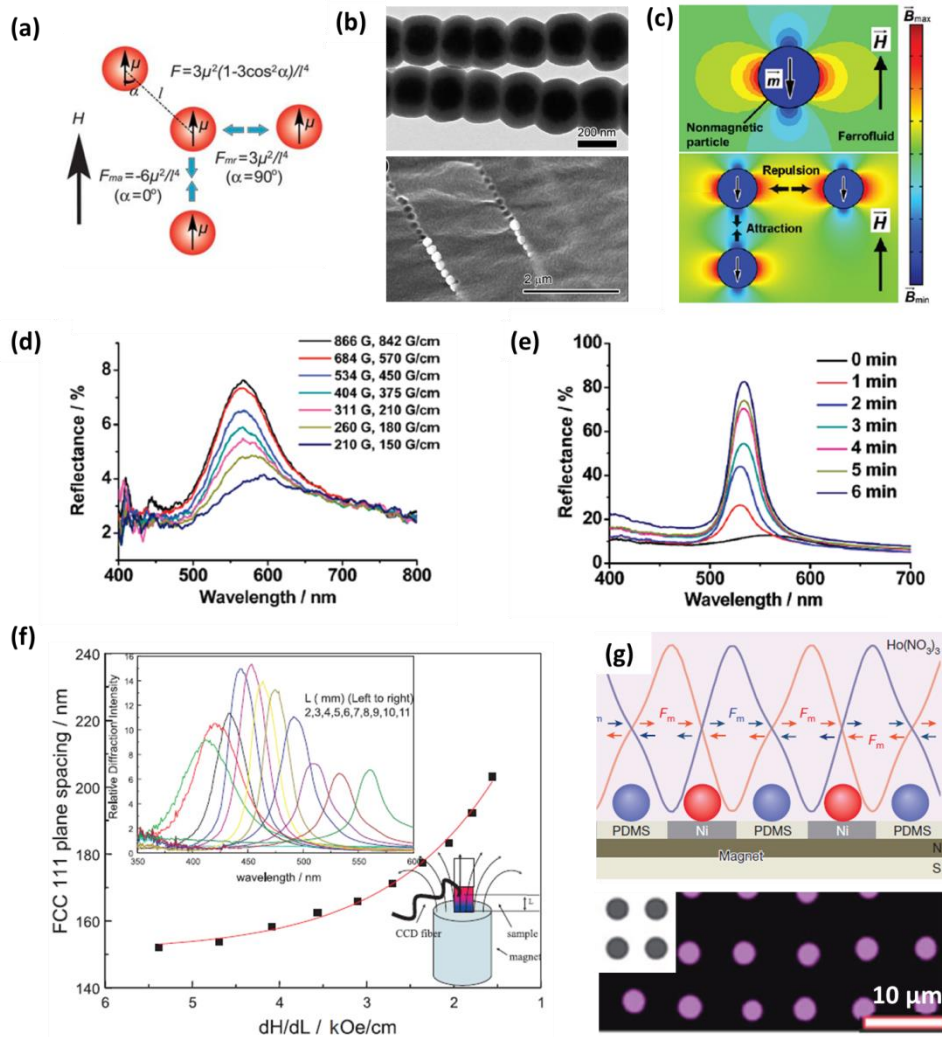


Fig. 2.7 Schematic illustration of the dipole–dipole interactions between two identical magnetic particles in an external magnetic field⁴² (b) TEM and SEM images of $\text{Fe}_3\text{O}_4@SiO_2$ particle chains fixed in a polymer matrix⁴³ (c) Magnetic field distribution around a non-magnetic particle with a dipole moment in the direction opposite to the applied magnetic field (top) and the dependence of interparticle dipole-dipole force on particle configuration (bottom), the colour bar indicates magnetic field strength.⁴³ The reflectance spectra for a 1 mm thick polystyrene (PS) film in ferrofluid solution for external magnetic fields with varying strength (d) and for a fixed magnetic field (2530 G) over time (e).⁴⁴ (f) Influence of the average magnetic field gradient, dH/dL on the lattice constant of a thick CCA composed of 134 nm superparamagnetic particles⁴⁵ (g) In-plane forces attracting paramagnetic particles (red) onto the nickel grids embedded in a layer of poly(dimethyl siloxane) (PDMS) placed on a permanent magnet of typical strength 0.442 (top) and (bottom) magnetic particles (purple) assembled on the nickel grids (grey).⁴⁶

Li *et al.* has investigated several methods of magnetic self-assembly, taking advantage of the dipole-dipole interactions between magnetic particles for the assembly of 1 – dimensional chain-like sphere assemblies (Fig. 2.7 (a-b)),⁴³ and using a ferrofluid for the

magnetic assembly of non-magnetic particles (polystyrene (PS) spheres) into 1D chains under a weak external magnetic field and into 3D structures with the application of a strong magnetic field (Fig. 2.7(c-e)).⁴⁴ Li also highlighted an improvement in the effect an externally applied magnetic field can have on the packing and order of the non-magnetic sphere assembly when sustained over for a period of time, see reflectance spectra in Fig. 2.7(e). Asher et al. assembled superparamagnetic non-close packed photonic crystals using highly charged superparamagnetic polystyrene-iron oxide composite colloidal particles, fabricated by the emulsion polymerization of styrene in the presence of ~10 nm iron oxide particles. The application of an inhomogeneous magnetic field to an aqueous assembly of these particles produced particle attraction towards the maximum of the local magnetic field gradient, compressing the already partially assembly colloidal arrays along the magnetic field gradient.

The lattice constant, as a balance between the magnetic packing forces and the interparticle electrostatic repulsive forces, was a minimum at the locus of the magnetic field gradient maximum. An increase in the magnetic field and magnetic field gradient saw a decrease in the lattice constant of the packing structure, shifting the diffraction wavelength of the assembled structure to lower wavelengths (Fig. 2.7(f)). Magnetic assembly has also been used for the assembly of colloidal particles into patterned structures as shown in Fig 2.7(g). Patterning of colloidal spheres by different methods will be discussed in more detail later. The necessity of using ferro- or paramagnetic materials, or the doping of latex particles with superparamagnetic nanoparticles⁴²⁻⁴⁵ can make magnetic-field-induced self-assembly seem less applicable than the use of, for example, an electric field⁴⁷⁻⁵² to direct sphere aggregation.

Electrophoretic deposition is a process where conductive electrodes are suspended in parallel in a solution of charged colloidal particles and the manipulation of the electric field induces sedimentation on the oppositely charged electrode by the process of electrophoresis. Control parameters include substrate choice and conditioning, sphere functionalization and

solution pH. This has been demonstrated for silica spheres, whereby Holgado *et al.* established electrophoretic deposition of silica particles as a method for controlling sedimentation velocity, thereby overcoming the sedimentation complications that arise for sphere sizes that are too small or too large.⁴⁸ Rogach *et al.* further developed the method showing its suitability for the formation of 3D ordered polystyrene sphere deposits, underlining the high level of quality and increased assembly time achievable through electrophoretic deposition.⁴⁹ Despite the fact that this method allows for the production of thick opals deposits, little investigation has been made into the influence of different experimental parameters on the nature of the deposits formed. For example, the influence of substrate used, time and voltage dependences and the degree of control which can be achieved over opal ordering remain open issues.

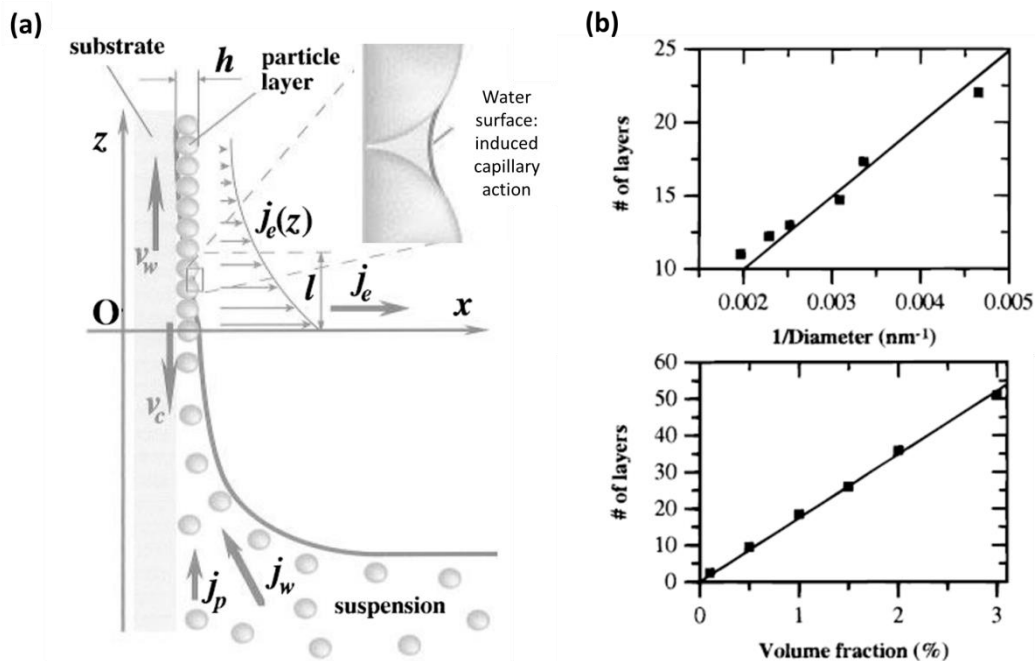


Fig. 2.8 (a) Schematic of the particle and water fluxes at the liquid-air contact line, in the vicinity of monolayer particle arrays growing on a substrate plate that is being withdrawn from a suspension with an inset highlighting the liquid bridge between two neighbouring particles. Here, v_w is the substrate withdrawal rate, v_c is the array growth rate, j_w is the water influx, j_p is the respective particle influx, j_e is the water evaporation flux, and h is the thickness of the array.⁵³ (b) Number of layers vs the inverse of the particle diameter, for samples grown from a 1% volume fraction solution (top) and the number of layers vs the particle volume fraction (bottom) for 298.6 nm spheres grown by the Colvin method.⁵⁴

The development of vertical deposition via evaporation induced self-assembly compelled by capillary interactions is one of the most frequently used methods for sphere assembly and has been shown to produce better quality films than those achieved through simple sedimentation. The development of this technique began with the early work of Dimitrov and Nagayama which outlined a process of convective assembly for the growth of homogeneous monolayers of PS spheres on planar substrates by controlling the position of the leading edge of a meniscus on a substrate vertically removed from a solution of colloidal spheres.⁵³ This process and the forces involved are outlined in the schematic in Fig. 2.8 (a). The factors governing the order, thickness and rate of formation of the film are quantified, from humidity and temperature to volume fraction.

The vertical deposition technique more directly refers to the method outlined by the Colvin group where a substrate is settled vertically in a solution of spheres forming a meniscus which is then swept vertically along the substrate as the solution evaporates, requiring no substrate removal. This action forces the colloidal particles to self-assemble on the substrate as the meniscus advances with evaporation, resulting in the formation of high-quality multi-layer films of close-packed silica spheres, with thicknesses up to 50 μm .⁵⁴ Jiang and colleagues applied the quantitative model developed by Dimitrov and Nagayama for the relationships between volume fraction and sphere diameter with the number of colloidal layers assembled by their stationary method. This vertical deposition technique, often referred to as the Colvin method, has since become a favoured technique for sphere assembly, due in most part to its simplicity and thickness control (see Fig. 2.8(b)), it is however somewhat limited by the time needed for solution evaporation and is highly sensitive to substrate and environmental conditions, such as evaporation rate.

Both of these methods are conceptually similar to the layer-by-layer scooping technique,⁵⁵ or the Langmuir-Blodgett technique^{56, 57}, however with vertical dip-coating the

film forms out of solution directly onto the substrate and by Langmuir Blodgett the spheres, latex or silica, are first arranged at the air-water interface or the surface of a non-miscible solvent. The arranged spheres are then transferred to the substrate by a moving barrier exerting a compaction force on the particles. Repeated cycles of Langmuir Blodgett can produce 3D structures but the transfer of the ordered layers from the liquid interface to the substrate can cause disruptions that limit the structural order. Langmuir Blodgett is therefore best suited to large-area monolayer formation but can provide a high degree of control for synthesising layered structures.

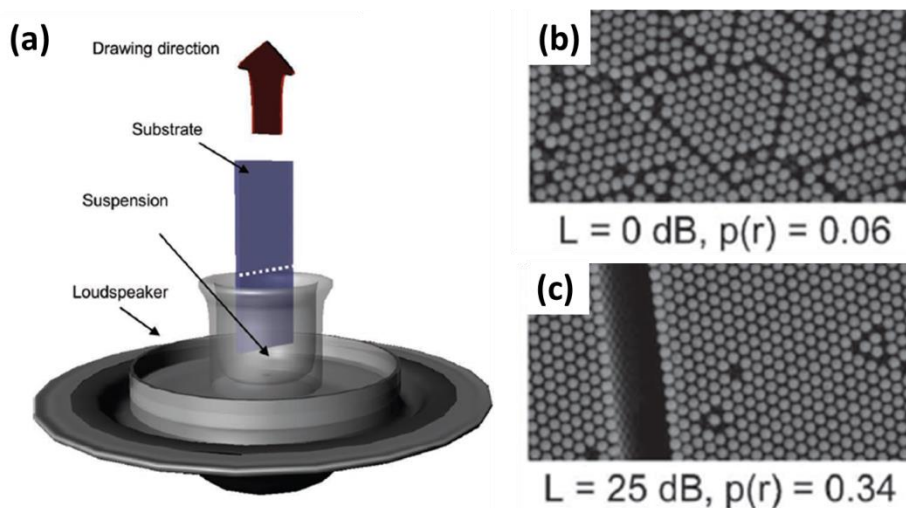


Fig. 2.9 (a) Schematic representation of the deposition process for a colloidal crystal from an aqueous suspension of poly(methyl methacrylate) (PMMA) spheres with acoustic vibrations with the white noise spectrum applied from below while the substrate was vertically drawn out of the suspension by a stepper motor and (b and c) SEM images of samples crystallized at noise levels L with calculated regularity measures $p(r)$ illustrating the higher degree of order for noise assisted crystallization.⁵⁸

Since Nagayama's early investigations into the use of dip-coating for the formation of well-ordered sphere assemblies, dip-coating has been substantially investigated and varied in order to optimize the process.⁵⁸⁻⁶⁸ Several methods have been investigated towards improving the order of dip-coated colloidal crystals, for example, Khunsin *et al.* investigated the effect of perturbative noise-like acoustic waves on colloidal crystal growth during dip-coating (Fig.

2.9(a)). The authors studied the overall changes in colloidal ordering as a function of the mean vibration magnitude^{58, 69} and observed an improvement in overall opal order when continuously displacing the meniscus, as shown in Fig. 2.9 (b and c).^{47, 57} They determined an optimum level of acoustic vibrations for increasing the effective crystallization time in the solution meniscus, leading to a less stressed lattice with no change in generic symmetry.

One of the limiting factors of both vertical deposition and dip coating is the settling of the colloidal solution over time. In particular, for larger sized particles, the long periods of time often required for achieving well-ordered opals through controlled withdrawal or evaporation of the dispersant liquid is problematic. Therefore, one of the major benefits of the noise agitation not initially highlighted by these works is quite simply the interruption it provides in the settling of the suspended spheres. Dip-coating as a whole provides a lot of potential for industry application with, for example, its suitability to a process-line-type production scenario. It also provides the desired controllability over sample assembly needed for industry application through the variety of controllable and adaptable parameters available, for example, the withdrawal rate, the concentration of spheres and the evaporation rate, providing several routes towards perfecting and idealizing sample formation standards.

Several of the techniques or effective forces already discussed have been further adapted or exploited by the addition of some type of spatial confinement. For example, Kim *et al.* demonstrated a method whereby regular convective assembly was modified by the addition of another glass substrate in front of the glass substrate attached to the dipping apparatus, with a gap of approximately 100 μm in between.⁷⁰ A small amount of colloidal suspension was then inserted into this gap with a capillary force strong enough to keep the suspension inside the gap. The raising of the back glass substrate at a specific rate while applying hot air to the meniscus edge caused the water in the colloidal suspension to evaporate, assembling the spheres into ordered structures and fixing them to the back

substrate. The meniscus thinning rate could be modulated by controlling the lift up rate of the substrate and the method was shown to be successful for the formation of both mono- and multi-layered structures as well as binary colloidal crystals (discussed in detail later).⁷⁰ A similar method produced two dimensional monolayers of poly(methyl methacrylate) (PMMA) spheres self-assembled from a colloidal solution dragged between two plates; the top plate was dragged at a constant velocity in the direction opposite to monolayer growth. The spheres were directed towards the contact line of the solution meniscus by evaporation induced convective assembly, much like the vertical deposition and dip-coating techniques discussed previously. However, this method allowed for smaller amounts of colloidal solution, producing monolayer particle arrays covering large areas provided that the particle concentration, sliding speed of the top substrate and wettability of the bottom substrate were optimized.⁷¹

2.3.1 Binary Colloidal Crystals

First observed in nature in the Brazillian opal,⁷² binary colloidal crystals (bCCs) consisting of spheres of two sizes, large (L) and small (S) particles, can offer a rich variety of crystal structures compared with the colloidal crystals discussed so far. The type of patterns and symmetries formed are generally characterized by the stoichiometry LS_N , where L represents the large spheres, S the small spheres, and N represents the number ratio of small to large spheres. These complicated structures however, have seen limited use to date due to the difficulties in formation and characterisation they present compared with their single sphere-size counterpart. The first laboratory example was created using charge-stabilized latex particles dispersed in water by Yoshimura and Hachisu, who connected the type of structures formed with the size ratio of the particles, the number ratio, and particle concentration.⁷³ Yoshimura and Hachisu also pointed out the similarity of these structures to the structure of

several metal alloys. The potential therefore, of bCCs, formed with polymer and/or silica spheres, lies not only in their photonic characteristics but in their exploitation as ideal models for the atomic arrangements^{74, 75} of certain metal compounds,^{62, 63} as well as lithographic templates for complex micro- and nano-structures and surface patterning.^{76, 77} Synthesis routes initially relied on sedimentation under gravity which (as with ordinary colloidal crystals) is extremely time consuming making it a less viable route for large scale production.

Over the last decade however several layer-by-layer⁷⁸⁻⁸¹ and co-deposition techniques^{76, 82-86} have been designed for the formation of both ordered and disordered bCCs. Van Blaaderen and co-workers reported the fabrication of bCCs through vertical deposition, where a 2D hexagonal close packed crystal of large silica spheres was grown first at the slow rate of ~ 1 to 2 mm a day on a glass substrate. The small particles, of either silica or polystyrene, were then deposited onto the large-particle template by the same method. These steps were successively repeated to create 3D structures of alternating layers of large and small spheres, and structures with stoichiometries of LS, LS₂, or LS₃ were grown by this method by varying the size ratios and volume fractions (see Fig. 2.10(a-b)). Kitaev and Ozin presented an accelerated vertical deposition technique where low pressure was applied to accelerate the rate of ethanol evaporation from a solution of both large and small negatively charged spheres at low concentrations, producing monolayer bCCs. In this case the smaller spheres were organized within the interstitial sites between the hexagonally ordered larger spheres. The number of small spheres between the larger was shown to vary with small sphere sizes and concentration⁸⁷ as seen in the SEM images in Fig. 2.10 (c).

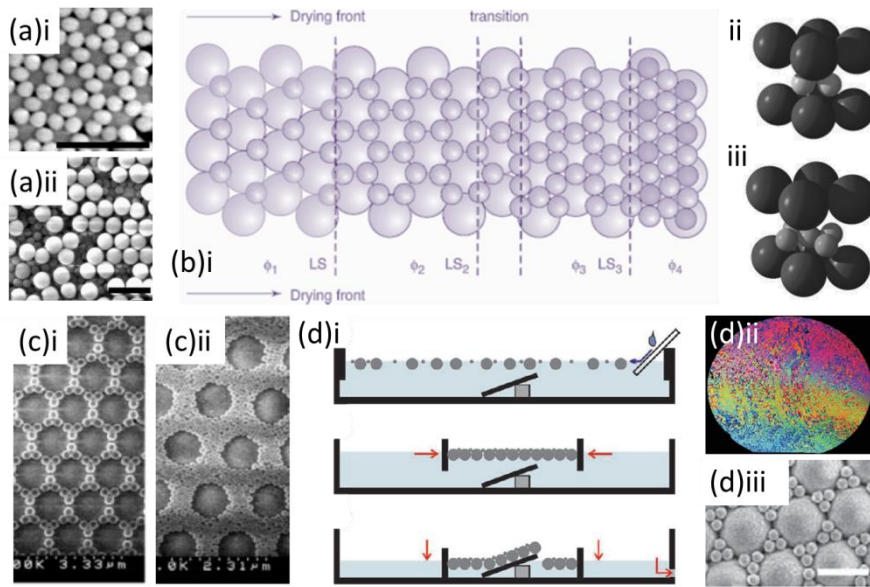


Fig. 2.10 SEM image of binary structure grown by a layer-by-layer technique showing (a) i a layer of smaller spheres on a 2D layer of larger 203 nm silica spheres in a LS_3 stoichiometry and (a) ii an incomplete third layer of larger spheres to illustrate over-layer formation and a schematic representation (b) i of the process of assembly for the smaller spheres onto the larger 2D structure as a function of volume fraction ϕ and diagrams for the unit cells of the (b) ii LS_2 and (b) iii LS_3 arrangements.⁷⁸ (c) SEM images of the variation in binary stoichiometry for different volume fractions ϕ and sizes d_s of small spheres (i) $\phi = 3.1 \times 10^{-4}$ $d_s = 290$ nm (ii) $\phi = 5.6 \times 10^{-4}$ $d_s = 145$ nm deposited by the accelerated vertical deposition.⁸⁷ (d) i Schematic representation outlining the formation of binary structures using the water air interface and compression forces (d) ii wafer surface after liquid lowering and the monolayer formed from 1063 nm and 225 nm sphere solution with size ratio 1:6 transferred from the water air interface and dried (d) iii SEM image of the top surface.⁷⁶

Both step wise spin coating⁷⁹ forming LS_2 and LS_3 stoichiometries, and confined-convective assembly⁸⁰ forming structures of LS_2 , LS_3 as well as the more complicated LS_4 and LS_5 stoichiometries have been presented as faster routes for the assembly of bCCs. Kim *et al.* suggested that confined convective assembly can be used to produce ordered binary structures for a size ratio ≤ 0.58 with anything above leading to the formation of only random configurations. If the diameter of the smaller spheres is too large, filling the interstices between the larger particles in the already assembled monolayer with the required periodicity will not be possible, therefore ordering will be disrupted.⁸⁰ Smaller spheres have also been

assembled on an already formed monolayer of larger spheres by electrophoretic deposition, producing several stoichiometries (e.g. LS, LS₂, LS₄ and LS₈) controlled by the size and the volume fraction of the small spheres used.⁸¹ It is important to note in this case that the monolayer of larger spheres is deposited through ordinary capillary interactions caused by solution evaporation, and therefore already in place to provide a template for the electric field induced assembly, designating this method as a layer-by-layer technique for 2D crystal formation and limiting the speed of the technique. Wang *et al.* described a vertical lifting co-assembly technique^{83, 88} for the formation of 3D bCCs. More recently, monolayer assembly using interactions at the water-air interface has become one of the more widely studied techniques for bCC assembly due in part to its adaptability to nearly any substrate. Shen *et al.*, first assembled the binary structure at the water-air interface in the presence of a surfactant (SDS) and then transferred it to the desired substrate, thus preparing monolayer bCCs over large areas in a short time.⁸² A colloidal mixture in ethanol was drop cast onto hydrophilic glass surrounded by DI water, spreading out rapidly across the slide and on to the surface of the water where the floating spheres then assembled into ordered 2D arrays on the surface with the help of added SDS which reduced overall surface tension. The glass slide reduces the spreading speed of the suspension enough so as to allow time for an ordered monolayer to self-assemble.

This approach prompted several other studies into the formation of bCCs using the water-air interface; Vogel *et al.* explored the assembling of bCCs using a Langmuir trough attempting to establish more control over the composition for a large range of size and number ratios. As shown in Fig. 2.10(d), a floating 2D binary crystal monolayer was compressed by the Langmuir trough and, as the water sub-phase was pumped out, transferred to the substrate which was submerged at an angle just below the water-air surface.⁷⁶ Dai *et al.* described another method where the binary colloidal solution with added ethanol was

dispersed into a liquid film on the chosen substrate. Solvent evaporation caused convective flow of the spheres towards the water-air interface and assembly into ordered binary arrays under de-wetting and capillary effects, provided that the size difference between the large and small spheres was sufficient. On the basis of this type of assembly Dai *et al.* established a phase diagram, in Fig. 2.11 as a function of volume ratio for the formation of monolayer bCCs offering an effective way for predicting the resulting pattern stoichiometries provided that the size and volume ratios for the spheres well dispersed on a water-air interface is known.⁸⁵

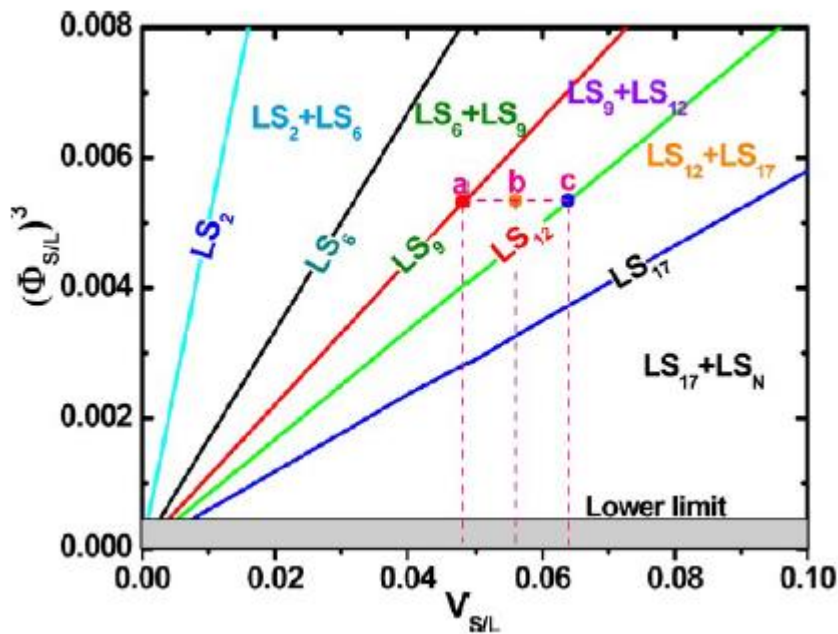


Fig.2.11 Phase diagram of monolayer bCCs, or $(\Phi_{S/L})^3$, as a function of $V_{S/L}$ for different monolayer LS_N bCCs. Each plot corresponds to the denoted single-phase line. The areas between two adjacent straight lines correspond to the denoted two-phase regions. Shadow area corresponds to a $\Phi_{S/L}$ smaller than the lower limit (or 0.077). The points a, b, and c indicate the LS_9 , LS_9 LS_{12} hybrid, and LS_{12} bCCs, respectively.⁸⁵

Very recently, a technique for the growth of bCCs within microfluidic devices has been presented by Harrison and co-workers.⁸⁶ A mixed colloidal dispersion was injected into a dispersion reservoir and pulled along a microfluidic channel fabricated *via* soft lithography in PDMS. Evaporation occurred through the evaporation reservoir at the other end and triggered self-assembly. For silica particles the suspension was repeatedly mixed via a

periodic chip rotator thereby counteracting the hydrodynamically amplified sedimentation and producing well-ordered bCCs.⁸⁶

As discussed above, binary colloidal crystal structure is primarily determined by the size ratio of large (L) to small (S) colloidal spheres, as well as the relative content of both spheres. The number and variety of assembly routes for bCCs developed so far are relatively few compared with ordinary colloidal crystals and the bulk of these generally refer to the formation of monolayer or 2D structures only, though some layer-by-layer techniques can deliver 3D structures. Several routes continue to suffer under lengthy time requirements, premature sedimentation of the larger particles and poor control over larger dimensions. Further development into a cost effective and fast single step method for controllable fabrication of bCCs is therefore needed, because 3D binary structures still hold great possibilities and are ideally suited as a complex template architecture for inverse opal fabrication, their untapped potential, both optically and structurally, could be of specific use to future optoelectronic development.^{88,89}

2.3.2 Patterned Substrates and Constrained PhC Assembly

As already discussed, most of these assembly routes utilize the naturally occurring gravitational or capillary forces incurred by colloidal particles, which can have different effects on colloidal assembly, being in most cases advantageous for thickness control, ordering, and domain size definition of the colloidal arrays. However, capillary interactions usually lead to the formation of close-packed colloidal crystals with the hexagonal or FCC (111) lattice plane almost always parallel to the substrate surface, thereby limiting the crystal orientation and type of packing. As the optical characteristics of the PhC, specifically the position and wavelength range of the PBG are affected by lattice structure and symmetry as well as filling fraction, therefore the ability to design and direct lattice orientation is of

interest for PhC investigations and application. For example, non-close packed spheres allow higher filling fractions⁹⁰ useful in creating wider PBG materials and have shown a lot of potential in the fabrication of nano-hole arrays⁹¹ and microwells.^{91, 92} As already mentioned earlier, control over defect positioning and density is also paramount when designing PhC structures for use in optoelectronic devices that require both long-range order and precise pattern registrations. Solid surface patterning through the use of colloidal sphere masks has also received a lot of attention for the formation of structures at sub-micrometer and nanoscale. This nanosphere lithography (NSL) could be improved if the assembly of the spheres could be controlled more precisely. With these rewards in mind, several routes towards directing colloidal growth have been investigated through the use of topographically⁹³⁻⁹⁷ or chemically^{98, 99} patterned substrate, the use of electrical or magnetic field manipulation or a combination of both.^{46, 100, 101}

Complex aggregates (polygonal and polyhedral clusters) of polymer spheres were assembled by Younan Xia *et al.*, by using a 2D array of holes patterned into photoresist and then removing the resist.⁹⁷ Van Blaaderen and colleagues demonstrated the templated assembly of silica particles by vertical deposition on silicon substrates patterned using a combination of electron-beam lithography and reactive ion etching. They determined that for many cases, symmetry tends to alter for a single layer but revert to its favoured hexagonal ordering for subsequent layers.⁹⁵ Silica spheres have been patterned into particle wires by coupling solvent chemistry and regions of hydrophilic silanol groups formed using self-assembled monolayers (SAMs) of octadecyltrichlorosilane (OTS) modified by UV irradiation, as shown in Fig. 2.12 (a)-(c).⁹⁹ Recently, Yuko Olsen *et al.* investigated the relationship between voltage and particle-to-hole size ratio when electrophoretically depositing on hole patterned substrates. They determined that for smaller hole sizes, a larger electric field was required for sphere deposition to occur. For example, no deposition

occurred for an applied voltage of 5 V/cm but particle deposition began in the larger 5 μm hole at 10 V/cm, however, an electric field of 15 V/cm was needed for spheres to assemble in the smaller 2 μm hole (see Fig. 2.12 (d)). The discovery of a voltage threshold for each size hole creates avenues for precise control in sphere deposition by the adjustments in pattern hole size and voltage. With the inclusion of a positively charged surface by application of poly-L-lysine, further anchoring of the negatively charged PS spheres within the pattern was encouraged. Olsen and co-workers created a variety of assembly patterns, including dimers, trimers and higher order assemblies with different separations, see Fig. 2.12(e).¹⁰¹

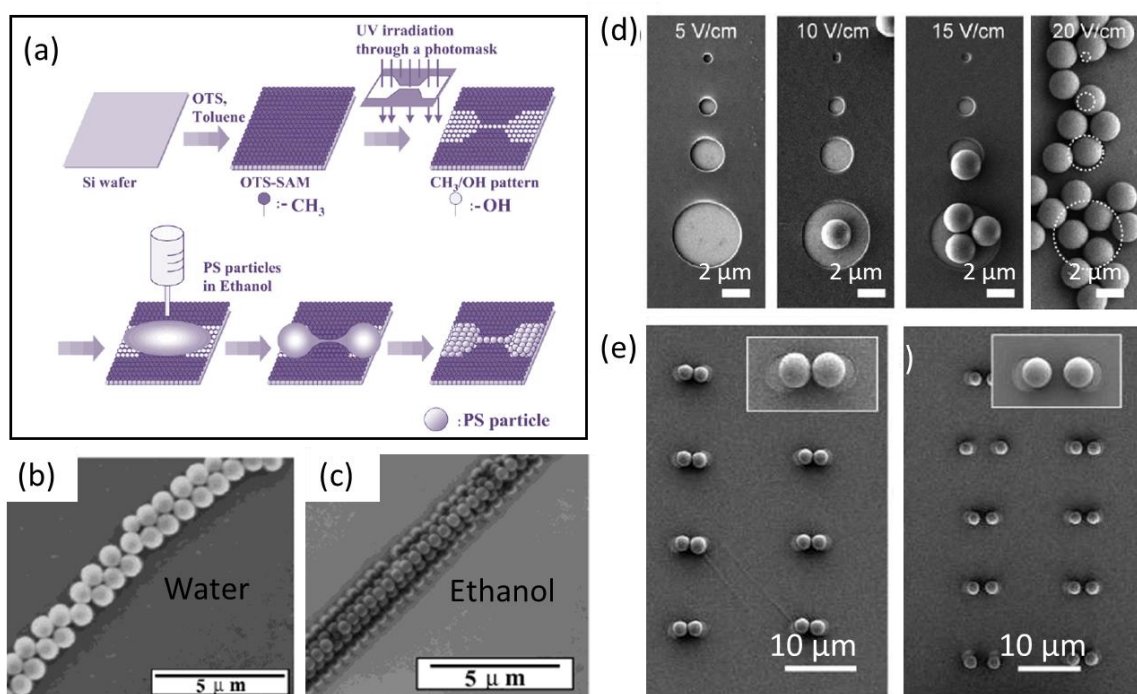


Fig. 2.12 (a) Schematic of the process for the fabrication of a particle wire using a patterned SAM and liquid bridge and SEM images of the wire structures formed for spheres in (b) an aqueous solution and (c) ethanol solution⁹⁹ (d) SEM images showing the effect of pattern hole size with respect to voltage applied. Four different hole sizes of 5 μm , 2 μm , 1 μm , and 500 nm were patterned onto an electrode. At 5 V/cm, no deposition was seen in any of the holes. With increasing voltage, depositions into subsequently smaller sized holes were observed. (e) SEM image of PS dimer structures constructed by EPD onto a two hole array pattern, with increased separation, showing the controlled spacing of the PS beads.

As has been shown, methods for artificial opal assembly abound, and while photonic crystals themselves offer immense opportunities, their popularity is perhaps derived more as

a result of the simplicity and diversity they provide as templates for the formation of three-dimensional porous structures, more specifically inverse opals (IO). Inverse opals are created by the infiltration of synthetic opals with a material of high refractive index and subsequent removal of the spheres to produce a structure of periodic voids (air) surrounded by continuously interconnected material, and this creates a large refractive index contrast that has the potential to produce a full PBG. Not only however, are these structures used for the formation of optically significant inverse opal materials, but they present a simple and ideal route for the formation of both ordered and disordered three-dimensionally porous structures highly beneficial to several areas of research.

2.4 Inverse Opals: Formation and Emerging Technological Applications

IO's are a close packed array of spherical voids, formed by infiltration of the PhC or artificial opal with a material of high refractive index and the removal of the spheres by chemical etching or calcination. In general, IO formation can be discussed in three steps: (1) opal template formation by one of the techniques outlined previously, (2) material infiltration and conversion, for example, by hydrolysis or other means, and (3) inversion by the removal of the spheres. As discussed above, most opal templates are formed using silica, PS or PMMA spheres. Silica spheres offer high temperature stability but require removal by wet chemical etching in non-aqueous HF or NH₄F, polymer spheres are removed more easily by either solvent removal, plasma treatment, or calcination at temperatures above the glass transition temperature of the sphere material. The type of spheres used should reflect the choice of infilled material and the method of synthesis, given that these can vary between three general approaches: a) impregnation with liquid precursor or sol-gel,^{102, 103} b) gas-phase depositions such as chemical vapour deposition (CVD)^{104, 105} and atomic layer deposition (ALD)^{106, 107} that take place at extremely high temperatures unsuitable for polymer templates, and c)

electrochemical deposition whereby the chosen material is precipitated out of an electrolyte and gradually nucleates and grows within the template interstitials.

Both the choice of network material and the method of synthesis are highly dependent on the desired application. A material with a sufficiently high refractive index, ideally higher than 2.8 and an optimal filling fraction can produce a full PBG in the near infrared and visible range, provided the material exhibits minimal absorption along the desired wavelength range. There are however, abundant applications that do not require a complete PBG but still benefit from the porosity, topology and symmetry of the IO structure and the optical characteristics maintained therein. Therefore, the technologies presently under investigation for functional enhancement by IO inclusion are wide-ranging and include for example, photochemistry and catalysis,^{107, 108} high pressure liquid chromatography,¹⁰⁹ solid-state dye and polymer lasers, as well as sensors, waveguides, optical switches¹¹⁰ and light emitting devices.¹¹¹ One of the more promising arenas of application, increasingly gaining attention is in energy storage and generation, such as thermophotovoltaic (TPV) systems, dye sensitized solar cells (DSSCs) and Li-ion batteries (LIBs).

2.4.1 Inverted Opals for Optoelectronics and Telecommunications

As discussed above, the optical characteristics of photonic crystals make them ideally suited to several light relevant applications. Through the introduction of defects that locally disrupt the periodicity, allowed states can be created within the band-gap, thereby producing light localization close to the defect, ideal for trapping and guiding light. The use of light as opposed to electrons for the transfer of information has become increasingly more prevalent with the collective aim of developing all-optical integrated circuits. The existence of the PBG or stop bands and the resultant reflection of certain wavelengths, as well as the localization properties and possibilities for suppressed or heightened spontaneous emission coupled with

the ability to control these characteristics through material choice and design bestow inverse opals with immeasurable application potential. They have thus far been investigated for a number of optical devices, including waveguides,^{24, 112} LEDs,^{111, 113} filters,¹¹⁴ optical switches¹¹⁰ as well as sensors both chemical and biological.¹¹⁵

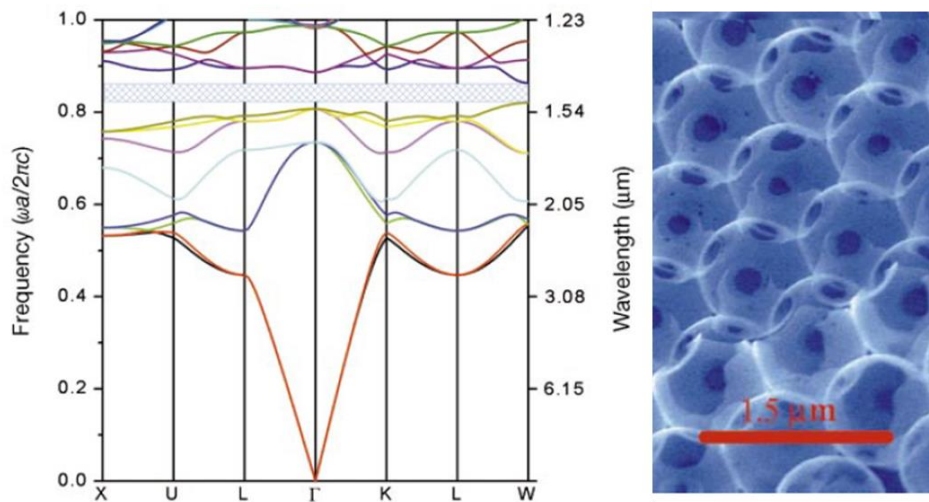


Fig. 2.13 Band structure of silicon inverse opal with an 88% infiltration of Si, the full PBG is shown by the crosshatched region, with a gap to mid gap ratio of 5.1% and SEM image of the (111) face of the silicon IO.

The first important step in photonic crystal applications within communications was the synthesis of a Si IO with a full PBG (see Fig. 2.13) within the frequency range relevant for telecommunications $\sim 1.5 \mu\text{m}$ and above the absorption edge of Si, therefore limiting absorptive losses. Si was grown by CVD within a template of silica spheres, using disilane (Si_2H_6) gas as the precursor.¹¹⁶ In a 2013 work, Feng Jin *et al.* demonstrated the lasing and amplified spontaneous emission of a resonant cavity fabricated by sandwiching a tert-butyl rhodamine B doped PMMA film between two polymeric IOs that acted as feedback mirrors. The polymeric IOs were formed as shown in Fig. 2.14 (a) by the infiltration of a PS sphere template with a photopolymerizable resin and polymerized by exposure to UV light. When the gain medium was sandwiched between two IO structures as in Fig. 2.14 (b), the overlap of the photonic stop band of the polymeric IOs with the photoluminescence band of the dye

molecules in the sandwiched layer produced single mode lasing emission.¹¹⁷ (see Fig. 2.14 (c) and (d))

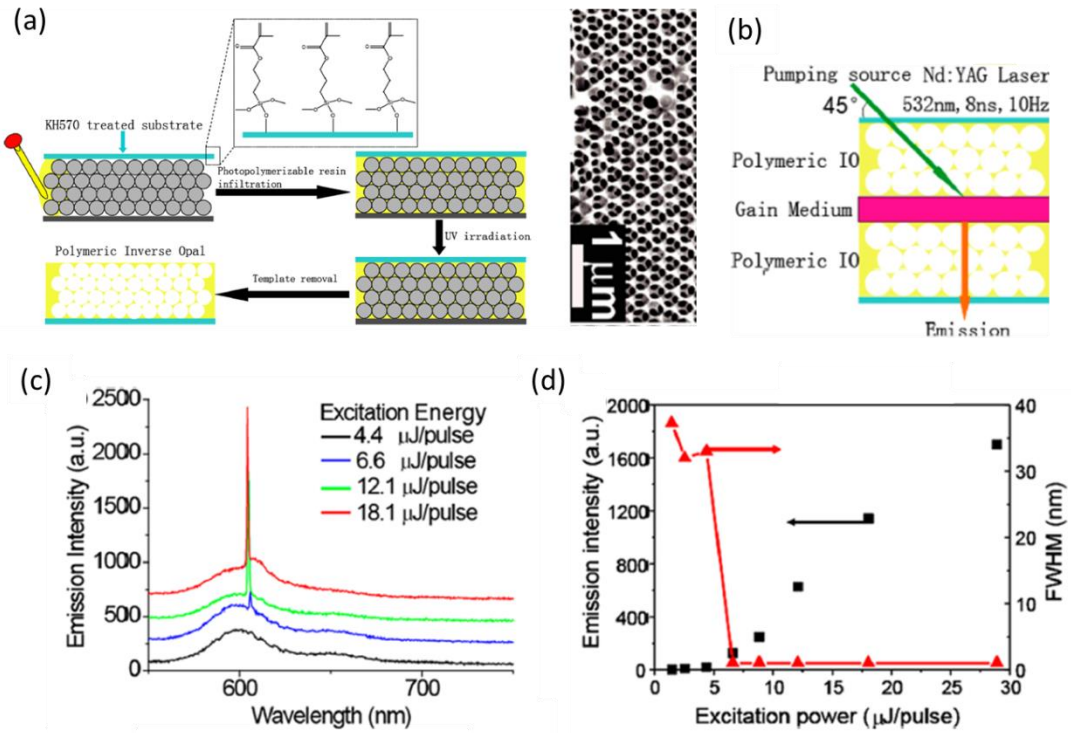


Fig. 2.14 (a) Schematic illustration of the construction process of the polymeric IOs and an SEM image of the resulting IO formed with 256 nm PS spheres. (b) Schematic outline of the fabricated lasing structure. (c) Emission spectra of the resonating cavity with photonic stop band at the wavelength of 610 nm under different excitation energy with spectra offset for clarity. (d) Dependence of the FWHM and integrated emission intensity on the excitation energy in the resonating cavity with 610 nm photonic stop band.

The epitaxial growth of group III-V semiconductor materials in 3D IO nanostructures using selective area epitaxy through a 3D artificial opal template has been demonstrated by Braun *et al.*, specifically, the formation of GaAs IOs (shown in Fig 2.15.(a) and (b)) for optical applications.¹¹³ A 3D PhC LED was then fabricated by incorporating a passivation layer of InGaAs between Si doped and C doped GaAs IO cladding layers during growth through the PhC template, thereby creating a LED heterostructure within the 3D PhC structure, shown schematically in Fig. 2.15 (c). This PhC LED displayed electrically driven emission at increasing drive currents (see Fig. 2.15 (d)).

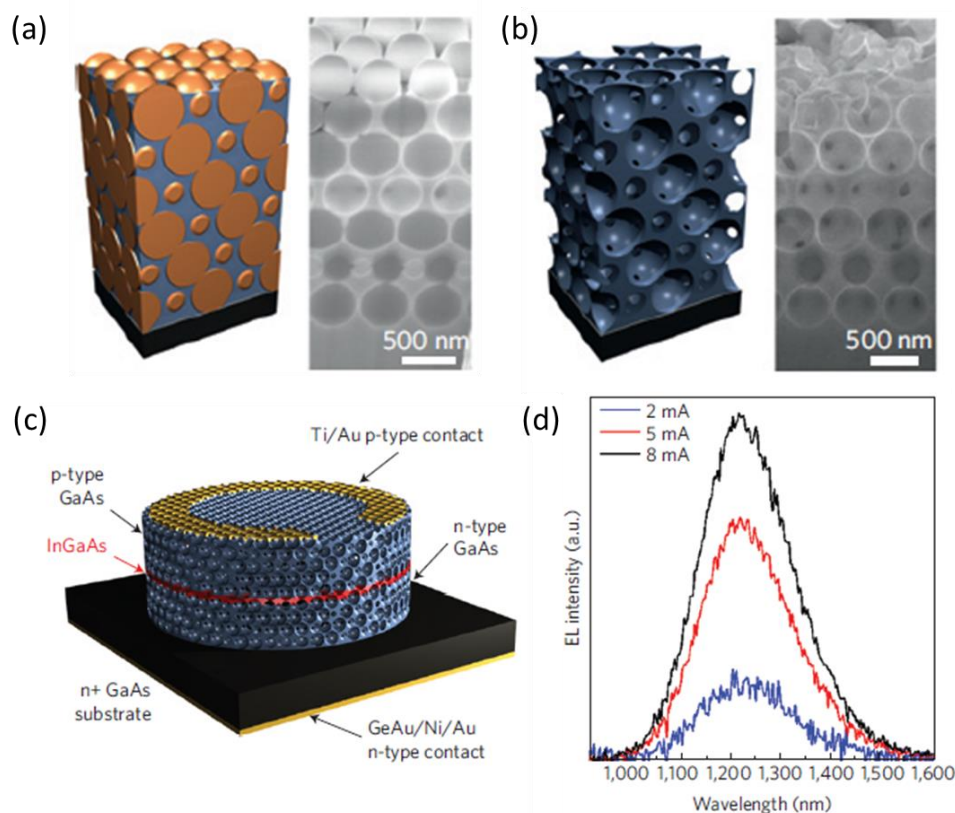


Fig. 2.15 Schematic and SEM image of (a) a GaAs filled PhC template and (b) an inverted GaAs structure after template removal (c) Schematic of a GaAs 3D photonic crystal LED fabricated by containing an InGaAs light-emitting layer (red) with a GaAs 3D PhC (blue). The complete structure was then lithographically patterned into a cylindrical mesa with a Au ring electrode on the surface and (d) the electroluminescence spectra from the 3D PhC LED with emission not modified by the 3D photonic structure and showing the intensity to be linearly dependent on drive current.¹¹³

The reflection of light at particular wavelengths and the dependence of these wavelengths on the refractive index contrast of the PhC make IOs extremely useful in sensor applications. Simply altering the refractive index contrast by replacing or altering one of the materials (usually air) with a material of different refractive index will produce a shift in the PBG or stopband of the IO structure. Hydrogel IOs in particular have been presented as pH,^{118, 119} humidity,¹²⁰ glucose¹²¹ and gas sensors.¹²² For example, amine-functionalized hydrogel IOs have been described for use in CO₂ gas sensing, formed through infiltration of a silica opal with dimethyl aminopropyl methacrylamide (DMAPMA) precursor which was then photopolymerized.

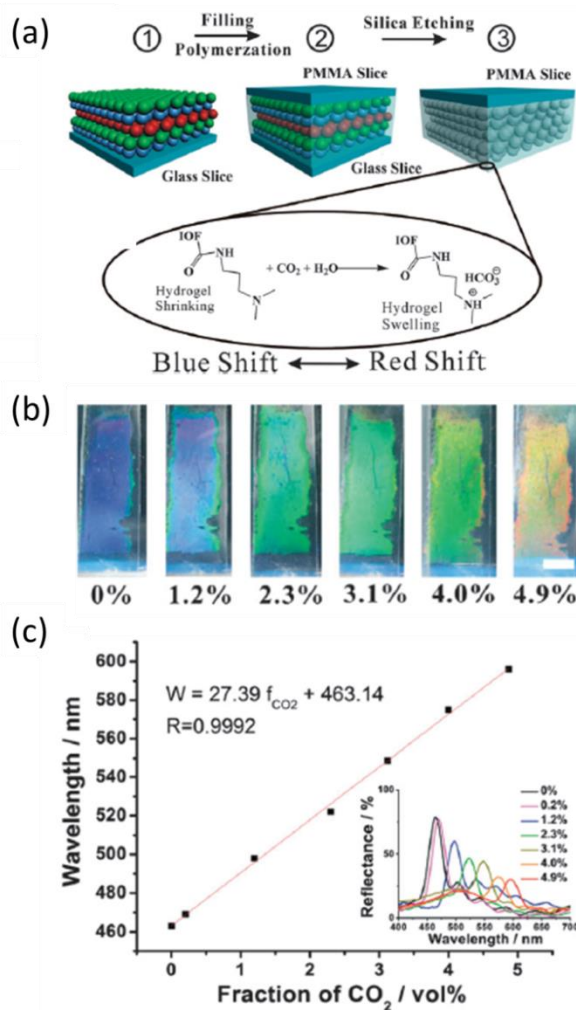


Fig. 2.16 (a) Schematic illustration for the fabrication of the CO₂ sensitive inverse opal film and the sensing mechanism of the inverse opal film (IOF) for CO₂ gas sensing (b) The induced color change of the CO₂ sensitive inverse opal film in pure water after being bubbled with 1 mL CO₂-N₂ mixtures from 0 to 4.9 vol%. Scale bar: 0.5 cm. (c) Plot of the diffraction maxima of the photonic film versus fractions of CO₂ in 1 mL CO₂-N₂ mixtures. Inset in panel (c): the reflectance spectra of the photonic film corresponding to the fractions in (b).¹²³

The resultant IO structure once the spheres are removed when immersed in pure water, exhibited a significant redshift in diffraction peak when CO₂ gas was injected into the water. A quantifiable relationship was observed between the colour diffraction from the PhC and CO₂ concentration over the whole concentration range. Bubbling CO₂ gas through the hydrogel functionalized with amino groups produced ion pairs more hydrophilic than the non-ionic amino groups and a Donnan potential that forces the hydrogel to swell, sensitivity

to CO₂ is developed by the increase of the fixed charge in the polymer network and a corresponding shift in the diffraction of light from the IO. These hydrogel IO structures were shown by Yijian Lai and colleagues as capable of detecting CO₂ from environmental gas samples.¹²³

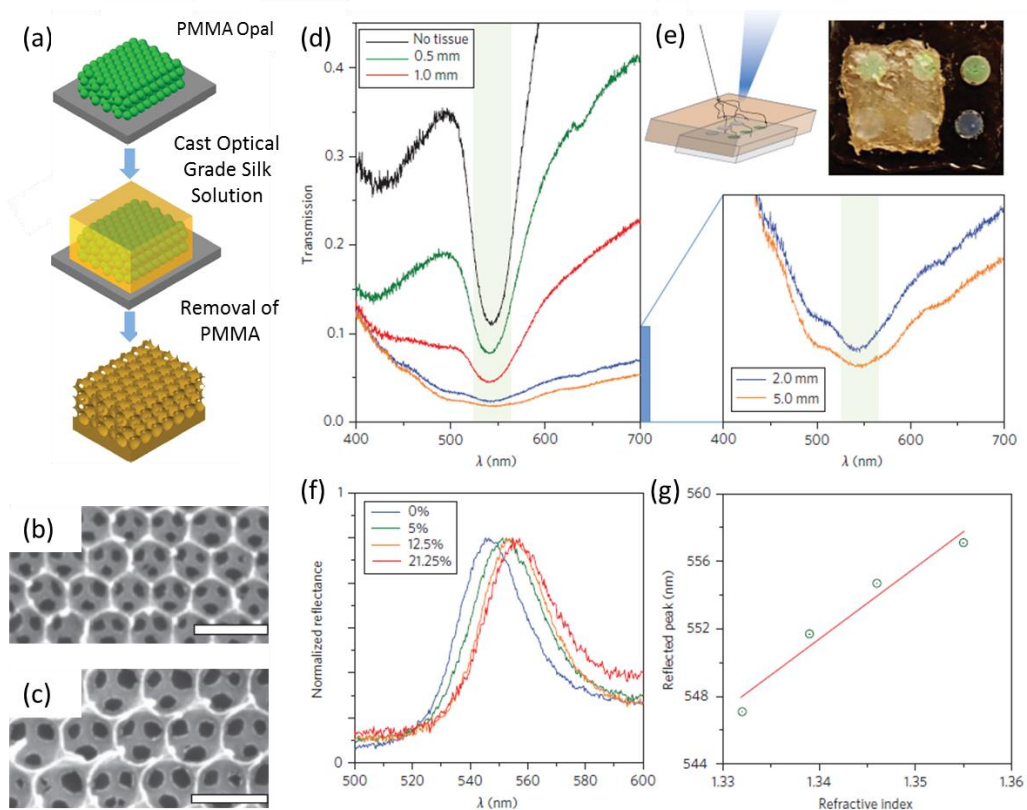


Fig. 2.17 (a) Schematic diagram of the process of formation for the silk fibroin IO structure and SEM images of IO structures formed with pore sizes (b) 240 nm and (c) 300 nm. (d) Transmission spectra for the silk IO lattice 300 nm when placed under tissue (chicken) slices of different thicknesses highlight pseudogap behaviour (e) An image of the silk IO under one layer of tissue (0.5 mm thick) with a cover glass inserted between the tissue and the IO to avoid swelling and magnified transmission spectra to emphasize the transmission dip in thick tissue (f) Glucose refractive index sensing for a silk IO with lattice constant 240 nm, showing reflectance spectra for different concentrations of glucose (0%, 5%, 12.5% and 21.25%). (g) Plot of wavelength of reflectance peaks as a function of refractive index.¹²⁴

IO sensors also hold a lot of possibilities for use in biological applications.^{124 125}

Biocompatible silk inverse opals formed as schematically outlined in Fig. 2.17(a) from a purified natural protein, silk fibroin, were fabricated by Omenetto *et al.* By examining the optical response from their silk IOs (Fig. 2.17 (b) and (c)) under tissue (chicken breast) of

between 2 and 5 nm, Omenetto and colleagues confirm the ability to still detect the photonic stop-band even under a high scattering environment (see Fig. 2.17 (d) and (e)). The biocompatibility and the degradable, implantable nature of silk IOs present a number of possible applications within biological environments, in particular once the photonic response can still be detected, under living tissue. They also highlight the potential these structures have with regard to colorimetric sensing, by applying different glucose concentrations to affect refractive index changes within the structure causing a shift in the stop band position, as shown in Fig. 2.17 (f) and (g).¹²⁴ The tunability of the stop band coupled with their low cost and ease of synthesis make IOs and PhCs in general^{115, 126} extremely applicable to both sensing and switching applications, They present a number of possibilities for functional sensing devices for both gas^{122, 123, 127} and solvent^{124, 128} detection, provided that material characteristics and design parameters can be tuned for fabrication within specific devices. However, one of their greatest application possibilities could be in bridging the medicinal and technical worlds, especially as research into the combination of biomaterials and PhC architectures continues. Not only do they show immense potential within sensing applications but throughout biological applications, including drug delivery¹²⁹ and as scaffolds for tissue regeneration.^{130, 131}

2.4.2 Inverted Opals for TPV Systems, and DSSCs

Metallic IOs are not normally favoured for optical applications due to their high absorbance in the visible range, but are showing increasing potential for modifying thermal emission as a result of the periodic modulation in the IO structure.¹³² One of the most limiting components in TPV systems for example, is the narrow band thermal emitter, which emits radiation in a narrowed range of energies towards the photovoltaic (PV) cell which then converts it to electricity. Therefore, the range of energies emitted must be comparable to the electronic

band gap energy of the PV cell in order to minimize losses and enhance efficiencies. Thermal emission is directly related to absorption and so at the energies within the photonic band gap, where the density of states is zero and absorption is low, thermal emission is limited. There is a difficulty however in finding a material that can withstand the high operating temperatures required for these devices. While the 3D PhC has the ability to provide enhanced optical responses over 1 and 2D structures, there is still considerable attention given to 2D PhCs for application in TPV structures. The use of TPV systems as a method of recycling the heat produced in many industrial or combustion processes could be a viable route for achieving portable energy, accessible in remote locations.¹³³

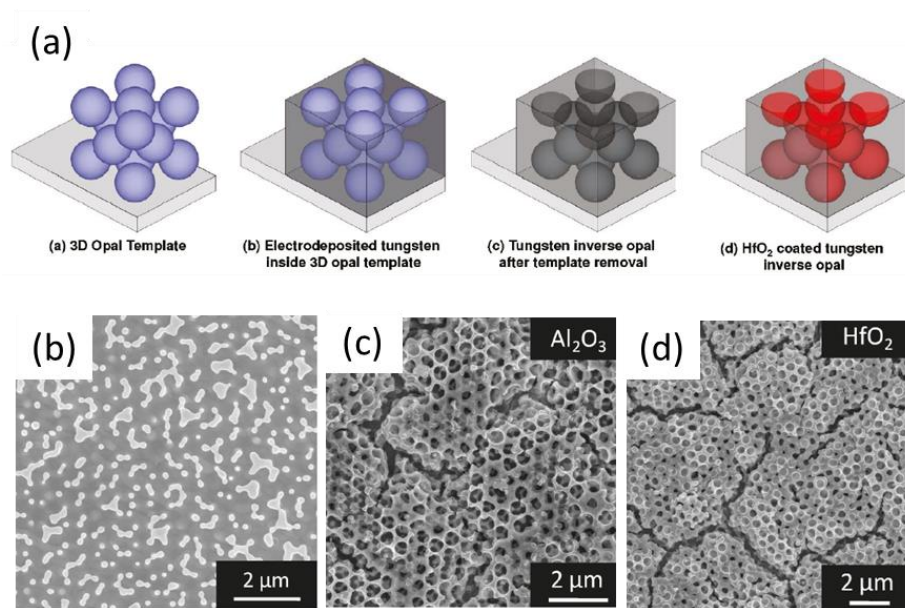


Fig. 2.18 (a) Schematic outline of formation of tungsten IOs on tungsten foil by electrodeposition into a 3D silica sphere template and coating of the tungsten IOs with HfO₂ or Al₂O₃ by ALD to impart thermal stability and SEM images (b) showing complete structural degradation after heating a tungsten inverse opal (not protected) to 1000 °C for 30 min in forming gas and of (c) Al₂O₃ coated and (d) HfO₂ coated tungsten IOs after heating to 1000 °C for 12 h.¹³⁴

In particular, tungsten IOs have the potential to become the leading candidate for selective emitters due to the high melting temperature of tungsten allowing thermal emission

over a broad range, however, the thermal stability of tungsten IOs is low.^{135, 136} One route towards improving this is the implementation of oxide passivation layers as a method of preventing surface diffusion and thereby maintaining structural integrity. This was presented by Arpin *et al.*, in 2011, by the application of protective coatings of alumina or hafnia to the surface of tungsten IOs using atomic layer deposition, shown in Fig. 2.18. This method allowed the production of IOs with thermal stability (for at least 12 hours) of up to 1000 °C with the alumina coating and up to 1400 °C for the hafnia coated IOs.¹³⁴

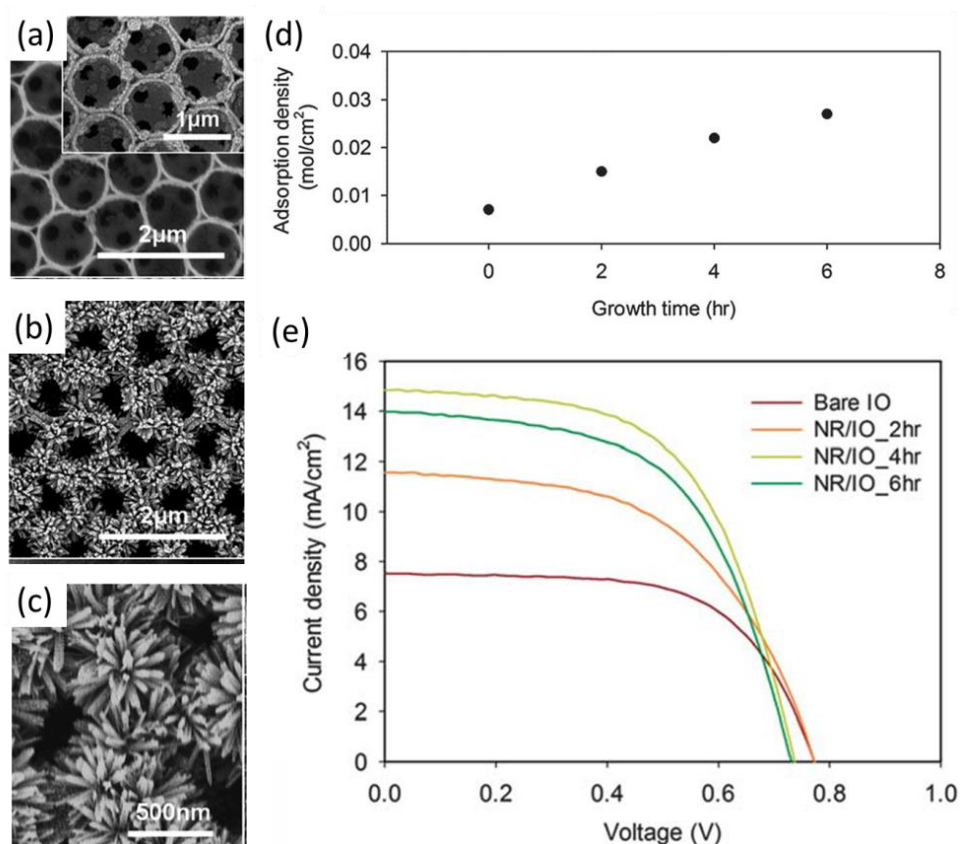


Fig. 2.19 SEM images of (a) the TiO₂ IO structure with an inset showing the TiO₂ IO coated with the TiO₂ nanoparticle seeds for nanorod growth (b) the nanorod-coated TiO₂ IO structure (c) Magnified SEM image of the nanorods on the surface of the IO structure (d) Dye-adsorption density versus growth time of the nanorods illustrating the increase in absorption with increase in surface area (e) J–V curves of DSSCs comprising bare IO and nanorod IO electrodes.¹³⁷

There is presently a growing interest in the use of PhCs for solar energy harvesting in DSSCs whereby the porosity of the IO structure allows for better electrolyte infiltration and improvements in the photo-collection efficiency through enhanced electron transport. Traditionally, DSSCs consist of a number of stacked layers, including, a glass slide, a transparent conducting oxide, a photoanode of semiconductor oxide particulates (frequently disordered TiO₂ nanoparticles) along with dyes, electrolyte and the counter electrode. During operation, electrons from the dye are injected due to photoexcitation into the TiO₂ nanoparticles. It is the magnitude of the electron flux in the injection/transport process as well as the recombination processes that occur between the photoexcited electrons and the redox ions in the electrolyte that determines the efficiency of the DSSC. Replacing the nanoparticle materials with 3D IOs has shown a lot of promise in improving electron transport characteristics, due to better electrolyte infiltration and shorter electron diffusion distances.¹³⁸ However, some issues have arisen due to a relatively lower specific area compared with conventional nanoparticle method leading to lower levels of dye absorption.¹³⁹

Some progress on improving this has been shown by the formation of mesoporous TiO₂ IO structures¹³⁹ and by Moon *et. al.* by combining the nanoparticles approach and the 3D IO layout.¹³⁷ Through the hydrothermal growth of TiO₂, 1D nanorods on the surface of the TiO₂ IO structure, outlined in the SEM images of Fig.2.19 (a-c), the effective surface area was increased up to a maximum of 4 times the surface area of a bare IO. This along with a slight improvement in scattering abilities in visible light and improved dye absorption (Fig. 2.19(d)), led to improvements in several of the DSSC properties over the bare IO structure, including the short circuit current and the photocurrent (see Fig.2.19 (e)).¹³⁷ The growth of nanorods on the surface of the IO structure could be of benefit to other IO applications as well, increasing the surface area while maintaining the connection to the overall IO base.

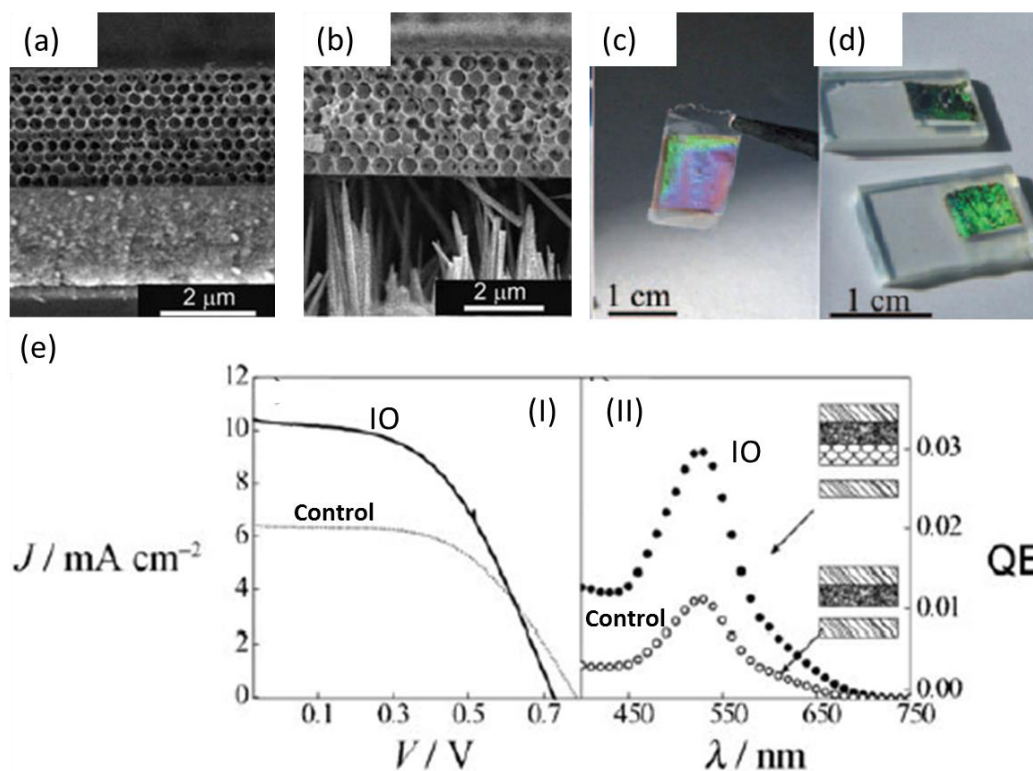


Fig. 2.20 SEM images of (a) 500 nm diameter IO silicon PhC on a 5 mm thick nanocrystalline TiO_2 layer and (b) 500 nm diameter silicon IO PhC on a substrate covered with 10 mm long ZnO nanowires (150–200 nm diameter) and photographs of (c) a preformed film peeled from the original substrate and ready to be deposited on to another (d) silicon IOs on dye sensitized ZnO nanowire electrodes after calcination at 500 °C for 2 h and (e) I Current–voltage curve (AM 1.5 illumination 112 mWcm^{-2} ; active area 0.25 cm^2) and (e)II quantum efficiency (monochromator slit opening 1.5 mm) for control and IO coupled DSSCs. The values for the reference cell are $J_{\text{sc}}=6.3 \text{ mAcm}^{-2}$, $V_{\text{oc}}=0.78 \text{ V}$, $h=2.33\%$, $\text{FF}=0.52$. The values for the PhC coupled cell are $J_{\text{sc}}=10.26 \text{ mAcm}^{-2}$, $V_{\text{oc}}=0.73 \text{ V}$, $h=3.2\%$, $\text{FF}=0.48$. QE = quantum efficiency.

However, the IO structure has also been applied to other aspects of the solar cell make-up both for DSSCs and for Si solar cells, with promising results. For example, carbon IOs have been investigated as a possible counter electrode material for DSSCs.¹⁴⁰ Si IOs have shown promise as back reflectors for Si solar cells.¹⁴¹ Their inclusion was shown to improve absorption of near-IR wavelengths and give a 10% enhancement to short circuit current with no degradation in the open-circuit voltage. Mihi *et al.* has also presented a technique for transferring preformed 3D Si PhCs onto different substrates including independently processed porous DSSCs of nanocrystalline TiO_2 and ZnO nanowire electrodes, see Fig. 2.20

(a) – (d).¹⁴² The performance of a device with and without the IO back-reflector were compared (Fig. 2.20 (e)) and the power efficiency for both devices with the IO structure i.e. either on TiO₂ or ZnO nanowires, was much better than that of the structure without, as shown by the external quantum efficiency plot in Fig. 2.20 (e)II, indicating the higher photocurrent for the IO-containing device. The ability to transfer Si IOs to DSSCs without disruption to structural integrity, could be adopted for other device types, that would benefit from the full or partial PBG provided by these Si IOs.¹⁴² As mentioned above, the initial attraction for IO incorporation in DSSCs stemmed from a need to improve electron transport, which IOs with their porous interconnected architecture allowed through better electrolyte infiltration and a three dimensional connected network. This advantage can also be considered for the adaption of IO structures for Li-ion battery electrodes.

2.4.3 Inverted Opals for Lithium Ion Batteries

Li-ion batteries power most of our portable electronics by virtue of their high energy and power density. It is well known however, that due to the brittle and disordered nature of the active electrode material presently used in most commercial Li-ion batteries and the subsequent need for conductive additives and/or binders to ensure good electrical contact, current batteries often suffer performance limitations, with electrical disconnections and poor ion and electron diffusion. There remains therefore, an ever-increasing need for a charge storage technology capable of providing the high performance and fast charging, needed to sustain our rapidly advancing, high-powered portable electronics industry as well as placate our need for cleaner energies, from electric vehicles to solar and wind storage, all, while maintaining stable and safe capacity retentions during operation. For this reason, a lot of consideration is currently given to the development of materials and architectures for the formation and optimization of electrodes in high-performance, rechargeable Li-ion

batteries.^{143, 144} In particular, the open but continuously interconnected material design of IO electrode architectures has been shown to promote stable, and more efficient electronic and ionic conduction during Li insertion and removal, substantially improving both power and rate capabilities.

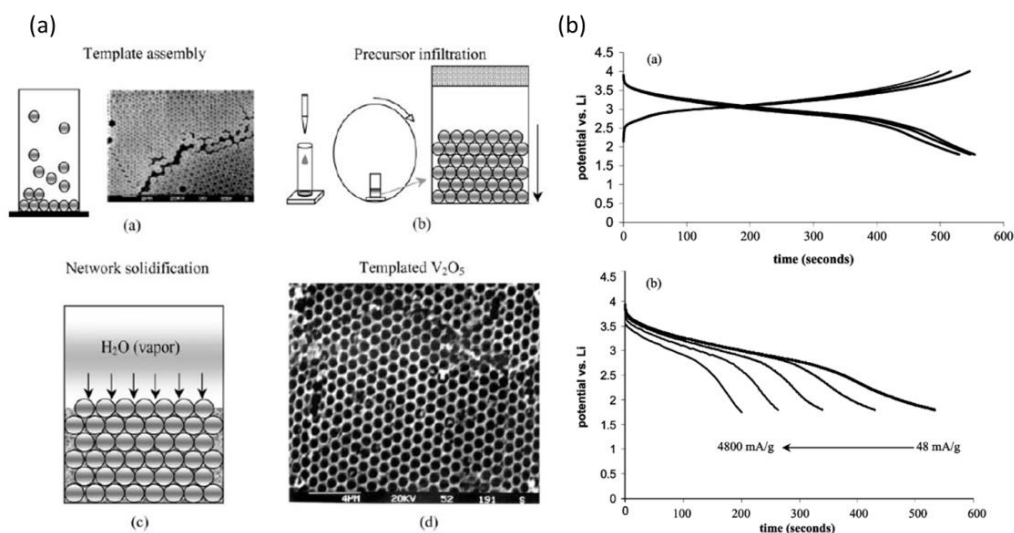


Fig. 2.21 (a) Process for fabricating the hierarchical V₂O₅ IO electrode, vanadium alkoxide precursor was infiltrated into a PS template, the precursor was exposed to water vapor for hydrolysis and condensation and sphere removal produced a V₂O₅ ambigel IO (b) galvanostatic characteristics for the hierarchical V₂O₅ electrode: (a) discharge–charge behavior at 48 mA g⁻¹ for three cycles; (b) discharge curves for a series of currents varying from 48 to 4800 mA g⁻¹.

The first investigation of inverted opal electrode design was completed on sol-gel vanadium pentoxide (V₂O₅) in its ambigel form (Fig. 2.21), a cathode material with high surface area and high porosity.¹⁴⁵ Xerogels, aerogels and ambigel are nanostructured materials formed from the drying of wet gel precursors, a different level of drying creates a different level of porosity and surface area. Ambigels are low density materials with a level of porosity and surface area between that of a xerogel (moderately low surface area and porosity) and aerogel (high porosity and high surface area obtained under supercritical drying conditions). This was formed by centrifuging 5 μl of IPA diluted vanadyl alkoxide into the sphere template, aging for 24 hours and removal of the spheres in toluene. Solvent exchange

was performed in cyclohexane to produce the aerogel-like material. Sakamoto and Dunn discovered in this 2002 study that the inverted structure with pores of ~800 nm, combined with the mesoporosity of the ambigel on the scale of 10 to 30 nm, led to higher capacities at higher discharge rates which they attributed to improved mass transport and better electrolyte infiltration. The inverted opal architecture should potentially reduce the tortuosity and resulting polarization caused by mass transport through the active material compared with other conventional electrode designs. Vanadium pentoxide IOs have been studied several times following this but have generally concentrated more heavily on electrochromic behaviour rather than Li-ion battery cycling. However, since the initial investigation using V₂O₅ ambigel, several studies have since investigated the potential benefits of the inverse opal design on battery performance, for a host of other materials and material composites both for anode and cathode materials as well as the current collector and separator.

2.4.4 IO Cathodes

The effects of the IO macroporosity have also been investigated for LiCoO₂, the cathode material currently used in most commercial LIBs. A PMMA sphere template was infiltrated with a mixture of lithium acetate and cobalt acetate and heated to form the desired phase of LiCoO₂. In order to improve the porosity, grain control agents poly (ethylene glycol) or platinum modifiers were added to the salt precursors. These IO structures however, showed poor cycling ability and at high temperature the phase transformation of the LiCoO₂ resulted in significant grain growth that led to disruptive shrinkage in the material pores.¹⁴⁶ Due to the scarcity of cobalt, its high cost and poor cycle life, LiCoO₂ is not considered as the most ideal cathode material for our growing energy needs moving forward. One example being considered as a potential replacement is LiFePO₄, a low cost material with a low toxicity and high thermal stability with a high theoretical specific capacity, it suffers however from poor

conductivity. The IO architecture has been investigated as route to overcoming this issue by increasing the interface between the electrode and electrolyte.¹⁴⁷⁻¹⁴⁹

The investigations into LiFePO_4 materials for battery applications have usually involved brittle, disordered particles, therefore an interconnected porous material could greatly decrease the diffusion distances the ions must travel, increase the surface area in contact with electrolyte and thus improve conductivity and overall performance. Doherty *et al.* investigated the performance of LiFePO_4 IOs of different pore sizes and calcination temperatures and found templates made with spheres of 240 nm, the largest used in the study, were found to have consistently higher discharge capacities than samples made with smaller diameter templates. Templates of PMMA spheres were infilled by drop-casting with precursor solution formed using iron nitrate nonahydrate ($\text{Fe}(\text{NO}_3)_3 \cdot 9\text{H}_2\text{O}$), lithium acetate (CH_3COOLi , Aldrich), and phosphoric acid. Some decomposition was observed in the IO structure during the necessary crystallization process by calcination at high temperatures, and it was suggested that templates of too small a sphere size are unlikely to produce uniform, undamaged IO structures. Discharge capacities close to the theoretical capacity of 170 mAh g^{-1} were observed at low discharge rates for samples calcined at temperatures between $500\text{--}800 \text{ }^\circ\text{C}$. At higher discharge rates it was the higher temperature calcined samples that performed best, i.e. the crystalline materials. Significantly less polarization was seen for samples prepared at $800 \text{ }^\circ\text{C}$ than those at $500 \text{ }^\circ\text{C}$, indicating an improved conductivity due to the increased sintering of grain boundaries. The benefit of the IO structure was outlined as the most ideal method for controlling pore size and while increased surface area did not produce the best results here the increased performance for the larger template diameters was attributed to better electrolyte soakage.¹⁴⁷

In a similar IO based approach, improved conductivity and shorter diffusion distances were achieved by combining the IO architecture with a conductive coating, FeF_3 IO

electrodes coated with the conducting polymer PEDOT. A PS template was first infiltrated with a solution of $\text{FeF}_3 \cdot 3\text{H}_2\text{O}$ in water and methanol with vacuum filtration to remove any residual solution. After the spheres were removed in toluene the conducting polymer PEDOT was then coated onto the surface of the FeF_3 IO electrodes by the *in-situ* polymerization of EDOT. The complete electrode had the benefit of increased conductivity from the PEDOT and the short diffusion distances of the porous FeF_3 structure. This combination produced a reported capacity of 210 mAh g^{-1} at a current density of 20 mA g^{-1} and high power capability of 120 mAh g^{-1} at a current density of 1 A g^{-1} at room temperature, with good cycling stability, all attributed to the enhanced ionic and electronic transport in the porous, conducting-polymer coated cathode.¹⁵⁰

2.4.5 IO Anodes

Due to its low cost, chemical stability and high electrical conductivity, carbon is presently the leading candidate as the anode material of LIBs and graphitic carbon is currently used in commercial LIB anodes. While carbon benefits from a high electrical conductivity, its performance at high discharge is limited by poor ionic conductivity. The IO structure has proven attractive as a possible architecture to improve overall carbon performance due in most part to its attractive mass transport capabilities and easier electrolyte infiltration. The first forays into the synthesis of carbon IOs concentrated mainly on optical capabilities,¹⁵¹ however since then, C IOs have shown a lot of potential as a solution to rate limitations in LIBs.¹⁵² The rate capability of a LIB is affected by a number of factors including charge-transfer reactions at the surface of the electrodes and the solid state diffusion of Li ions within the electrodes. The IO structure can potentially improve both of these through their increased surface areas, and macroporosity, shortening diffusion lengths. Significant improvement over non-templated carbon was reported by Stein *et al.* for hard C IOs synthesised using a PMMA

sphere template and resorcinol-formaldehyde (RF) polymer precursor.¹⁵² Their potential as anode materials has been further emphasised by recent investigations into further improving their battery performance through surface modification.¹⁵³

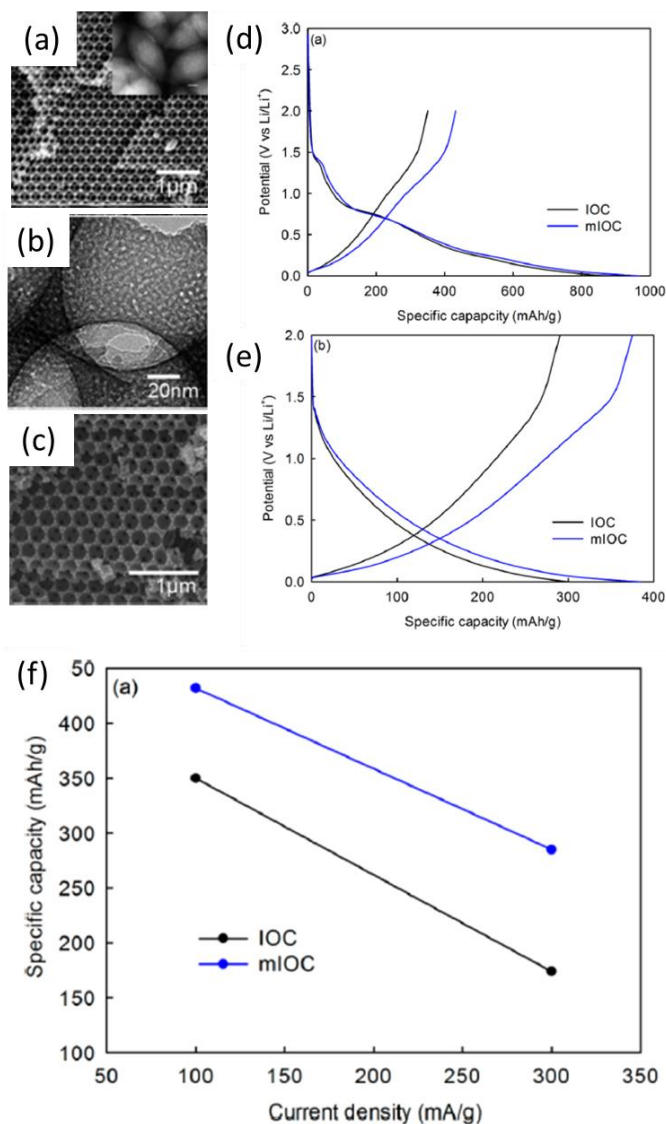


Fig. 2.22 SEM images of the (a) IO C (b) amino-group coated IO C (c) mesoporous IO C and the discharge/charge profiles for the IO C and mesoporous coated IO C for the (d) first and (e) the tenth cycle and (f) the variation in specific capacity with an increase in specific current illustrating a greater decrease for the IO C compared with the mesoporous structure.

Kang *et al.* investigated the battery performance of C IOs (Fig. 2.22 (a)) formed by the infiltration of a PS template with a phloroglucinol/formaldehyde (PF) resol precursor and compared this with the performance of both mesoporous C IO (Fig. 2.22(b)) and C IO coated

with amino-groups (Fig. 2.22 (c)).¹⁵³ The amino-groups were grafted on to the C IOs by dispersion of C IO material in deionized water, and the addition of 8.3 mmol of p-phenylenediamine and 8.3 mmol of sodium nitrate, 10 ml hydrochloric acid was subsequently added dropwise and the complete mixture was stirred for 4 h at room temperature. Mesoporous IOs were fabricated by adding a block copolymer Pluronic F127 to the PF-resol for infiltration of the PS template. Large irreversible specific capacities were presented for all the C IOs and attributed to the formation of a solid electrolyte interphase (SEI) layer on the IO material. The amino coated C, with an initial capacity of 359 mAh/g, showed very little improvement over the ordinary C IO material, however the first specific capacity for the mesoporous material is reported for a specific current of 100 mA/g as 432 mAh/g compared to the 350 mAh/g of the ordinary IO (see Fig. 2.22(d)) and to the ~372 mAh/g of commercial graphite. After 10 cycles the reversible specific capacity of the mesoporous C IO material was 375 mAh/g compared with the 290 mAh/g of the ordinary IO structure (Fig. 2.22 (e)) and the decrease in this capacity with increasing cycle number was less for the mesoporous IO structures. This was attributed to an easier ion transport channel and shorter solid-state diffusion lengths in the mesoporous IO material. The decrease in specific capacity of the C IO as the specific current increased from 100 to 300 mA/g was larger than that of the mesoporous structure (see Fig. 2.22 (f)). This was attributed to the faster Li-ion intake of the material and/or faster diffusion within the material due to the access afforded by the mesopores.¹⁵³

Both dense walled and porous walled germanium IOs have also been investigated for the anode of lithium ion batteries.¹⁵⁴ Formed by chemical vapour deposition onto silica sphere templates, the resultant structures more closely resembled their template counterpart more so than the more familiar IO open-network structures. However, coulombic efficiencies of over 90% after the first cycle were reported for these germanium IOs, both for the dense

and porous walled IO material, which is presented as much higher than those of other germanium anodes, such as nanowires or thin film electrodes. An enhanced rate performance was also shown at high current rates for the porous walled IO and the higher capacity of ~10% attributed to the increase in surface area and the increase in Li-ion flux at the electrode electrolyte interface. The walls of the porous IO structure were shown through SEM and TEM to swell significantly during lithiation but no pulverization was seen which was accredited to the facile strain relaxation allowed by the free space available in the IO pores.

Several other materials have been investigated for IO anodes, including TiO_2 ¹⁵⁵ and NiO ¹⁵⁶ and in general, both cathode and anode IO materials have shown promising potential in enhancing the transport kinetics in the batteries, but have displayed only moderate improvements in rate performance and cycling stability. The macroporosity of the active material improves ion transport but does little to improve electron transport, the IO structure does not extend to the current collecting substrate or material. This has been suggested as the main reason for poor rate performance. For this reason in recent years, concentration has moved towards applying the IO structure to the current collector in order to improve electron transport. The active material is then applied to the IO structure as nanoparticles or thin films thereby allowing the dimensionality and connectivity of the IO network to extend to the active electrode as well. Essentially the use of a 3D IO structure as a support material allows the formation of nanocomposite active materials with improved conductivity or stability. These investigations have produced some of the most promising results towards achieving high power and high energy density batteries.¹⁴³

2.4.6 IO Current Collector and Separator

Zhang *et al.* reported superior rate performance in bicontinuous electrodes formed using a Ni IO support for the active material, synthesised by electrodeposition into a PS sphere template

(of either 1.8 μm or 466 nm diameter), with a current of $\sim 2 \text{ mA cm}^{-2}$ using a commercial electroplating solution (Techni Nickel S, Technic Corp), as outlined in Fig. 2.23(a). The Ni IO was electropolished before infilling with the active material in order to increase the overall porosity to $\sim 94\%$, see Fig. 2.23(b). The active cathode material MnO_2 was then electrodeposited on to the Ni framework and lithiated in a molten salt solution of LiNO_3 and LiOH . This three-dimensional bicontinuous lithiated MnO_2 cathode (Fig. 2.23(c)) with a thickness of $\sim 30 \text{ nm}$ was shown to retain 76% of its capacity when discharged at 185C, and 38% when discharged at 1,114C, as shown in Fig. 2.23(d). The authors reported that the use of smaller sized spheres at the templating stage resulted in a greater energy density for a given thickness of active material, due to the increase in surface area of the smaller pored system.¹⁵⁷

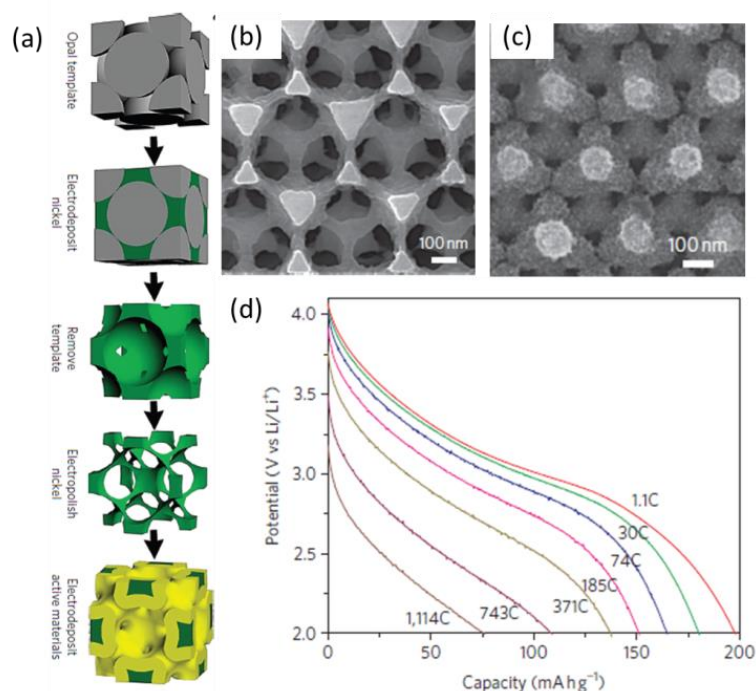


Fig. 2.23 (a) Schematic for the formation of the bicontinuous electrode fabrication process, the yellow indicates the electrolytically active MnO_2 and the green is the Ni current collector and SEM images for (b) the polished Ni IO and (c) the lithiated MnO_2/Ni composite electrode (d) Ultrafast discharge of the lithiated MnO_2 material, at C-rates ranging from 1.1 to 1,114C.¹⁵⁷

Large volume changes (up to 400%) can occur with silicon anodes during lithium insertion and extraction which leads to electrode pulverization and a loss of electric contact between the active material and the current collector (see schematic Fig. 2.24(a)). In order to alleviate this, Zhang and colleagues also investigated the use of a Ni IO current collector (Fig. 2.24 (b)) with a thin film of silicon material. A PS sphere template was formed on a tungsten foil by vertical deposition, infiltrated with Ni by electrodeposition and the spheres then removed in tetrahydrofuran. The resultant Ni IO (Fig. 2.24 (d)) was then electro-polished to increase pore size as before and a thin film of silicon deposited by CVD from dislane. This produced a bi-continuous anode of thin layer silicon on a porous 3D Ni metal scaffold (Fig. 2.24(c and e)) that showed improved cycling behaviour compared to a thick layer of silicon deposited on a planar Ni foil.

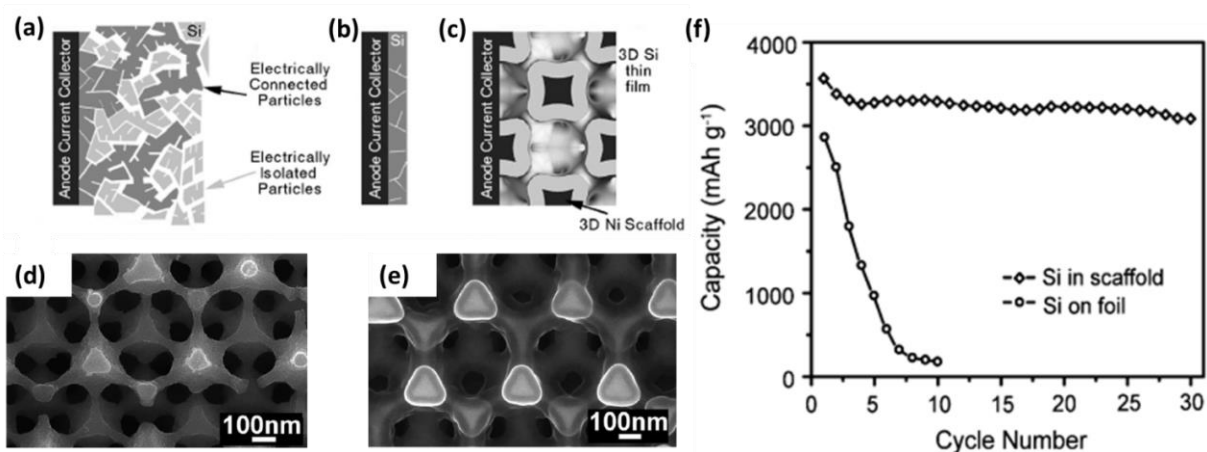


Fig. 2.24 (a) Illustration of the loss of electric contact in a thick silicon film on a current collector foil during cycling (b) Silicon thin film showing good contact to Ni substrate. (c) Bicontinuous bulk anode consisting of a silicon thin film on a 3D porous Ni scaffold. SEM image of (d) the Ni scaffold and (e) silicon coated Ni after CVD. (f) Capacity retention comparison of a 3D silicon anode and a foil supported silicon anode at a 0.05C rate.¹⁵⁸

After 10 cycles only 10 % capacity remained for the flat film on the Ni foil, which was attributed to pulverization of the silicon material and loss of electrical contact. The spherical pores of the 3D Ni provided a nanoscale reaction space for the silicon to lithium

alloying/dealloying and limited the electrical disconnections due to volume changes responsible for the capacity fading in the flat film sample. Therefore the 3D structured electrode presented much higher specific capacity overall and much higher capacity retention, as shown by Fig. 2.24(f).

Recently, Ni/Si composite electrodes have been fabricated by the electrodeposition of a silicon layer on to a Ni IO scaffold.^{159, 160} In one such study, the battery performance of the Si-on-Ni IO structure was compared to a Si-on-Ni nanocable array of equal active material mass. The Si on Ni IO material did exhibit higher volumetric capacities and better rate capabilities than the nanocable array, however, both suffered capacity fading common with Si anodes, which they attributed in this case to the formation of an SEI layer on the silicon surface. Silicon film thickness was varied for a number of samples and a decrease in capacity retention was seen for silicon thickness of ~50 nm. Li insertion increases the thickness of the silicon material, causing the porosity of the IO to decrease which is believed to lower electrolyte infiltration and contact thereby lower capacity values. Therefore IO performance can be optimized through Silicon film thickness and IO pore size.¹⁶⁰

One of the disadvantages of thin film active materials atop conductive IOs is that volume expansion on lithium insertion can still be problematic, causing the material to delaminate from the IO current collector. Some success in alleviating this problem was seen by integrating IO C with geometrically entrapped active nanoparticles, in this case SnO₂ as is schematically shown in Fig 2.25.¹⁶¹ The macroporous nature of the C IO allows easy access for the Li ions and the geometrical constrains of the elastic C IO can better accommodate the volume changes in the active nanoparticles on lithium insertion and removal, reducing tendencies to self-aggregate and/or delaminate from the conductive IO.

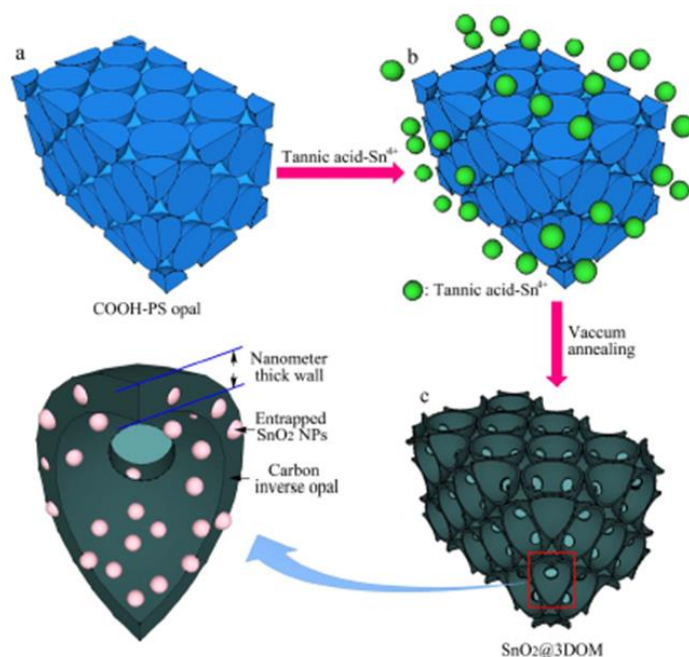


Fig. 2.25 Schematic illustration showing the preparation of the C IO electrode with entrapped SnO_2 nanoparticles.¹⁶¹

Most research into the utilization of the IO architecture within LIBs has concentrated on the active components. Recently however, Hwan Kim *et al.* presented a study looking at the formation and potential benefits of an IO separator.¹⁶² The separator membrane takes its place between anode and cathode, and in most current LIBs is made of porous (randomly distributed) polyolefin materials. It is incumbent for high battery performance that fast and uniform ionic flow can occur through the electrolyte soaked separator. In this work by Kim and colleagues, an IO separator was formed by combining the template assembly and infiltration into a single step. In a polyethylene terephthalate (PET) nonwoven substrate, vertical deposition was used to assemble silica spheres in the presence of a UV cross-linked ethoxylated trimethylolpropane triacrylate (ETPTA) polymer matrix. The ETPTA monomer formed between the assembled spheres and was cured under UV irradiation for 15 s with the help of a photoinitiator. The silica spheres were then removed in hydrofluoric acid which resulted in a thin and flexible IO separator with a thickness of $\sim 20 \mu\text{m}$, see Fig. 2.26(a). The

ideal $\text{SiO}_2/\text{ETPTA}$ composition for the formation of a well ordered well packed IO structure by this method was reported as 74/26 (v/v), composition ratios above and below this produced non close packed randomly dispersed spheres and poorly ordered aggregated assemblies, respectively. In a LiCoO_2 cathode/graphite anode cell, the OCV profile for the ordered IO separator is comparable to that of a polypropylene/polyethylene/polypropylene (PP/PE/PP) commercial separator. The behaviour of the disordered structures is less comparable, with sharp decreases in OCV profiles attributed to leakage currents.

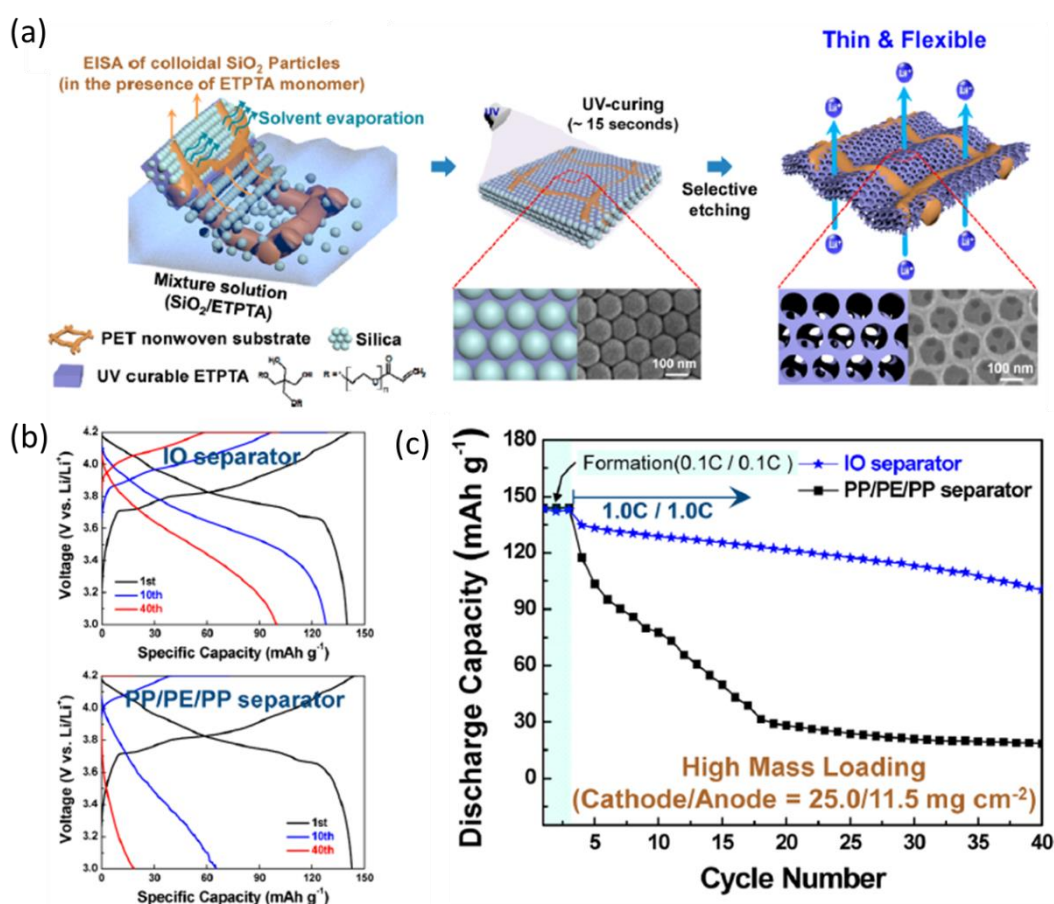


Fig. 2.26 (a) Schematic representation of IO separator manufactured via the simple one-pot EISA of SiO_2 nanoparticles in the presence of a UV-curable ETPTA monomer inside a PET nonwoven substrate, followed by UV-cross-linking and selective removal of the SiO_2 nanoparticle superlattices and the cycling performance of cells, where the cells were assembled with high-mass-loading electrodes (cathode/anode = $25.0/11.5 \text{ mg cm}^{-2}$) and IO separator ($\text{SiO}_2/\text{ETPTA} = 74:26$ (v/v)) or PP/PE/PP separator. The cells were cycled between 3.0 and 4.2 V at a charge/discharge current density of 1.0 C/1.0 C. (b) Variation in the charge/discharge profiles with cycling. (c) Capacity retention as a function of the cycle number.¹⁶²

The flexibility of this IO material while little different from current separator materials could be of interest within other applications, the seamless nanoscaffold structure is not disrupted when wound around a stainless steel rod with a diameter of 1.5 mm. The mechanical stability of the IO structure is maintained even after frequent bending deformation. This is however dependent on the non-woven substrate material. This IO separator has been shown to greatly improve ion transport under harsh conditions such as high mass loading, fast charging/discharging and highly polar liquid electrolyte compared with an example of a commercial separator, as shown in Fig. 2.26(b) and (c). The Ragone plot, describes the relationship between energy and power density, and the use of IO separator saw an increase in energy density compared with commercial PP/PE/PP separator for high power densities, i.e. a change in the Ragone plot was seen for a change in separator. While only the first step, the high wettability and 3D ordered macroporous interconnected nature of the IO separator presented by Hwan Kim *et al.* could lead to expanded thinking within battery performance optimization and material investigations. The higher ion conductivity of this IO separator appears very promising.¹⁶²

Today's energy needs require a storage technology with the energy density of a battery and a power density of a supercapacitor. Supercapacitors store charge differently to batteries. In supercapacitors the charge is stored at the interface between electrode and electrolyte whereas in a battery it is stored in the electrode bulk. In 2013 Pikul *et al.*,¹⁶³ presented a microbattery design, schematically depicted in Fig. 2.27(a), consisting of 3D bicontinuous interdigitated microelectrodes formed from thin layers of nickel-tin, for the anode, and lithiated manganese oxide, for the cathode, electrodeposited onto interdigitated highly porous Ni scaffolds, shown in Fig. 2.27 (b). The Ni scaffolds were fabricated through electro-deposition on PS opal templates assembled on glass with gold sputter coated into interdigitated rectangular templates on the glass. The top down view of the interdigitated

electrodes are shown in Fig. 2.27 (c). The rate capabilities for this type of microbattery were examined to determine what possibilities the IO structure provided in terms of the energy and power densities (see Fig. 2.27 (d)).

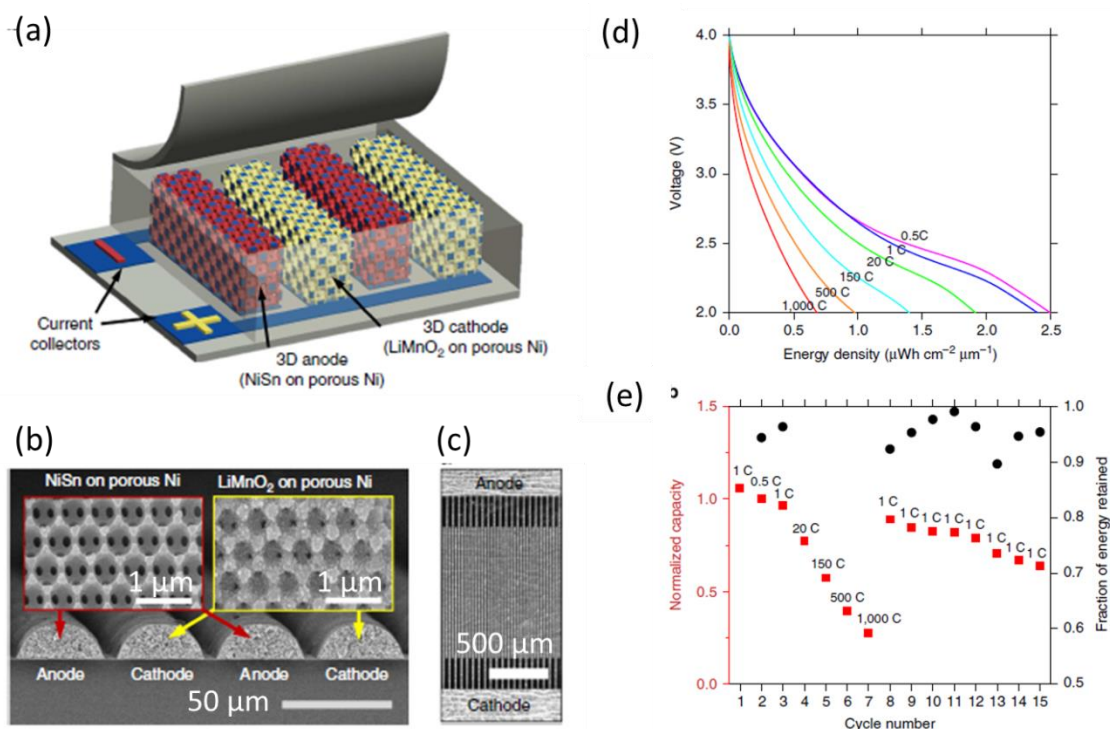


Fig. 2.27 (a) Schematic illustrating the microbattery design (b) Cross-section SEM image of the interdigitated electrodes spanning two periods with insets of the magnified Ni scaffold coated with nickel–tin on the left and lithiated manganese oxide electrode on the right (c) A top-down SEM image of the interdigitated electrodes (d) Discharge profiles for different rates (e) Capacity of the microbattery for the first 15 cycles at the noted C rate, normalized to the energy at 0.5 C. The secondary y axis indicates the percentage of capacity retained in the given cycle when compared with the previous cycle (calculated for low C rate cycles only).¹⁶³

Higher power densities up to $7.4 \text{ mW cm}^{-2} \mu\text{m}^{-1}$, without sacrificing energy density, were reported. After four high rate cycles the microbattery cell retains 92% of its energy and 64% after 15 high rate cycles, see Fig. 2.27(d). This is attributed to a reduction in ion diffusion lengths through the active electrode material, the time for ion diffusion in electrolyte, and electrical resistances across the entire microbattery. This meets or exceeds the high power densities of the best supercapacitors with comparable energy density, 2000 times greater and $2\times$ greater than the power density and energy density, respectively, of other 3D

microbatteries. This first example of a full battery system of IO electrodes highlights the full extent of the possibilities IOs bring to battery and energy research and design. The shorter diffusion distances, the increase in surface area and electrolyte infiltration and the lessened requirements for conductive additives ensure IO electrodes a place in future energy storage developments.

2.5 Conclusions and Outlook

In summary, the growth of PhCs by colloidal assembly routes has been presented with particular emphasis on directing and improving lattice arrangements through adaptations of long established methods, for example, using acoustic vibrations,⁵⁸ confinement⁷¹ or patterned substrates.⁹⁶ Assembly is essentially a balance of colloidal and external forces. Polymer spheres in particular are well suited to surface functionalization, offering further scope to manipulate their assembly behaviour. Through particle growth or resizing, and other factors such as untried sphere/solvent, sphere/solvent/substrate couplings there remains room for further improvement and development. Assembly is still limited somewhat by the time requirements necessary for much of the growth methods discussed and uncontrolled defect registrations remain continuously problematic for ordered self-assembly particularly on functional substrates. Lithographic methods can provide more specific defect placement but these routes are expensive and prove more difficult in the fabrication of layered or 3D structures. It is therefore likely that colloidal assembly will maintain its favour and encourage continuous examination and adaptation given its low cost and versatility.

The intent of this review was to highlight the wide ranging uses of PhC structures, specifically IOs. These structures have already been shown as highly advantageous within a number of fields, and they will no doubt play an important role in bridging optical and electrical functions, and further the development and progress towards achieving all-optical

information management and/or optoelectronic device design. The flexibility of IOs to span various applications is remarkable, whether within sensing, lasing, or energy storage to name a few. The complete scope of possible applications for these structurally advantageous and optically useful materials has no doubt still to be discovered. Given the availability of different material precursors and various synthesis routes, the scientific and technological potential of IO's are very attractive (particularly within the biological and energy sciences where defects are not major issues for function such as for photonics, but contribute to surface area, as one example).

There is also an untapped potential for applications that do not specifically exploit the unique optical properties of these materials but instead rely solely on the structural advantages they provide as nanostructured networks of active material. The development of non-destructive device and material diagnostic methods through the exploitation of the optical characteristics of these IO materials could lead to increased understanding of the chemical and interfacial processes happening during device function. In particular the unique diffractive optics of these materials and the ability to gain information from diffraction signatures on the lattice structure and integrity of a given IO could provide information on the nature of the network material and its ability to withstand certain stresses such as the intercalation of Li or other ions. Therefore, if the photonic abilities of these materials were coupled with their other operational capabilities and advantages, a new route towards material testing and design could be forged.

Going forward, future applications will no doubt concentrate on the optical and energy related potential of these materials. Their scalability is particularly attractive, allowing designs and behaviour modelling on large scales to be directly translated to the nanoscale (synthesis routes allowing). However, before any real-world application of the self-assembly approach to the fabrication and design of these materials can prosper certain issues still need

to be addressed, for example, that of overall stability, both thermal and mechanical stability in particular. This is perhaps where the coupling of patterning techniques and chemical functionalization with self-assembly methods could prove successful. Defect density remains a limiting factor in many self-assembly approaches, particularly on broader device scales and for those applications requiring very precise defect positioning. While the full scale optical and optical-dependent application of these materials requires some further optimization, the structural advantages they supply towards templating three-dimensional macroporous functional devices is extremely relevant and applicable even now. The central limiting factor with regard to this is simply what precursors are available and compatible. Artificial opal structures can however present vulnerability with respect to irreversible structural changes related to environment and certain application processes. This is particularly limiting for structural dependent applications, making their reusability low and potentially increasing costs. Therefore, investigations into material design coupled with the addition of optical diagnostic methods particularly for those areas presently neglecting the optical significance IOs present could lead to a deeper understanding, allowing these materials to reach their full and exciting potential throughout the scientific arenas.

2.6 References

1. Yablonovitch, E., Inhibited Spontaneous Emission in Solid-State Physics and Electronics. *Phys. Rev. Lett.* (1987), **58**, 2059-2062.
2. John, S., Strong Localization of Photons in Certain Disordered Dielectric Superlattices. *Phys. Rev. Lett.* (1987), **58**, 2486-2489.
3. Stein, A., Energy storage: Batteries take charge. *Nat. Nanotechnol.* (2011), **6**, 262-263.
4. Kinoshita, S.; Yoshioka, S., Structural Colors in Nature: The Role of Regularity and Irregularity in the Structure. *Chem. Phys. Chem.* (2005), **6**, 1442-1459.
5. Sanders, J. V., Colour of Precious Opal. *Nature* (1964), **204**, 1151-1153.
6. Liu, F.; Yin, H.; Dong, B.; Qing, Y.; Zhao, L.; Meyer, S.; Liu, X.; Zi, J.; Chen, B., Inconspicuous structural coloration in the elytra of beetles *Chlorophila obscuripennis* (Coleoptera). *Phys Rev E* (2008), **77**, 012901.
7. Zi, J.; Yu, X.; Li, Y.; Hu, X.; Xu, C.; Wang, X.; Liu, X.; Fu, R., Coloration strategies in peacock feathers. *Proc. Natl. Acad. Sci. U. S. A.* (2003), **100**, 12576-12578.
8. Yin, H.; Shi, L.; Sha, J.; Li, Y.; Qin, Y.; Dong, B.; Meyer, S.; Liu, X.; Zhao, L.; Zi, J., Iridescence in the neck feathers of domestic pigeons. *Phys. Rev. E* (2006), **74**, 051916.
9. Yoshioka, S.; Kinoshita, S., Effect of Macroscopic Structure in Iridescent Color of the Peacock Feathers. *Forma* (2002), **17**, 169-181.
10. Matějková-Plskova, J.; Jancik, D.; Maslan, M.; Shiojiri, S.; Shiojiri, M., Photonic Crystal Structure of Wing Scales in *Sasakia Charonda* Butterflies. *Materials Transactions* (2010), **51**, 202-208.
11. Matějková-Plskova, J.; Shiojiri, S.; Shiojiri, M., Fine structures of wing scales in *Sasakia charonda* butterflies as photonic crystals. *Journal of Microscopy* (2009), **236**, 88-93.
12. Yoshioka, S.; Kinoshita, S., Wavelength-selective and anisotropic light-diffusing scale on the wing of the Morpho butterfly. *Proc. R. Soc. London, Ser. B* (2004), **271**, 581-587.
13. Gaillou, E.; Fritsch, E.; Aguilar-Reyes, B.; Rondeau, B.; Post, J.; Barreau, A.; Ostroumov, M., Common Gem Opal: An Investigation of Micro- to Nano-Structure. *American Mineralogist* (2008), **93**, 1865-1873.
14. von Freymann, G.; Kitaev, V.; Lotsch, B. V.; Ozin, G. A., Bottom-up Assembly of Photonic Crystals. *Chem. Soc. Rev.* (2013), **42**, 2528-2554.
15. Joannopoulos, J. D.; Villeneuve, P. R.; Fan, S., Photonic crystals: putting a new twist on light. *Nature* (1997), **386**, 143-149.
16. Joannopoulos, J. D.; Johnson, S. G.; Winn, J. N.; Meade, R. D., *Photonic Crystals Molding the Flow of Light*. Princeton University Press: 41 William Street, Princeton, New Jersey 08540, (2008).
17. Ozin, G. A.; Arsenault, A. C.; Cademartiri, L., *Nanochemistry: A Chemical Approach to Nanomaterials*. Royal Society of Chemistry: (2009).
18. Mesfin, W.; Sajeev, J., Coherent control of spontaneous emission near a photonic band edge. *J. Opt. B: Quantum Semiclassical Opt.* (2003), **5**, R43.
19. Liu, J.-f.; Wang, X.-h., Spontaneous emission in micro- and nano-structures. *Front. Phys. China* (2010), **5**, 245-259.
20. Koenderink, A.; Bechger, L.; Schriemer, H.; Lagendijk, A.; Vos, W., Broadband Fivefold Reduction of Vacuum Fluctuations Probed by Dyes in Photonic Crystals. *Physical Review Letters* (2002), **88**, 143903.

21. O'Brien, S.; McPeake, D.; Ramakrishna, S. A.; Pendry, J. B., Near-infrared Photonic Band Gaps and Nonlinear Effects in Negative Magnetic Metamaterials. *Phys. Rev. B* (2004), **69**, 241101.
22. Povinelli, M. L.; Johnson, S. G.; Joannopoulos, J. D.; Pendry, J. B., Toward Photonic-Crystal Metamaterials: Creating Magnetic Emitters in Photonic Crystals. *Appl. Phys. Lett.* (2003), **82**, 1069-1071.
23. Smith, D. R.; Pendry, J. B.; Wiltshire, M. C. K., Metamaterials and Negative Refractive Index. *Science* (2004), **305**, 788-792.
24. Mekis, A.; Chen, J.; Kurland, I.; Fan, S.; Villeneuve, P.; Joannopoulos, J., High Transmission through Sharp Bends in Photonic Crystal Waveguides. *Phys. Rev. Lett.* (1996), **77**, 3787-3790.
25. Campbell, M.; Sharp, D. N.; Harrison, M. T.; Denning, R. G.; Turberfield, A. J., Fabrication of photonic crystals for the visible spectrum by holographic lithography. *Nature* (2000), **404**, 53-56.
26. Shir, D.; Nelson, E. C.; Chen, Y. C.; Brzezinski, A.; Liao, H.; Braun, P. V.; Wiltzius, P.; Bogart, K. H. A.; Rogers, J. A., Three dimensional silicon photonic crystals fabricated by two photon phase mask lithography. *Appl. Phys. Lett.* (2009), **94**, -.
27. Galisteo-López, J. F.; Ibisate, M.; Sapienza, R.; Froufe-Pérez, L. S.; Blanco, Á.; López, C., Self-Assembled Photonic Structures. *Adv. Mater.* (2011), **23**, 30-69.
28. Li, F.; Josephson, D. P.; Stein, A., Colloidal Assembly: The Road from Particles to Colloidal Molecules and Crystals. *Angewandte Chemie International Edition* (2011), **50**, 360-388.
29. Zhang, J.; Li, Y.; Zhang, X.; Yang, B., Colloidal Self-Assembly Meets Nanofabrication: From Two-Dimensional Colloidal Crystals to Nanostructure Arrays. *Adv. Mater.* (2010), **22**, 4249-4269.
30. Li, Z.; Wang, J.; Song, Y., Self-assembly of latex particles for colloidal crystals. *Particuology* (2011), **9**, 559-565.
31. Vlasov, Y. A.; Astratov, V. N.; Baryshev, A. V.; Kaplyanskii, A. A.; Karimov, O. Z.; Limonov, M. F., Manifestation of intrinsic defects in optical properties of self-organized opal photonic crystals. *Phys. Rev. E* (2000), **61**, 5784-5793.
32. Davis, K. E.; Russel, W. B.; Glantschnig, W. J., Settling suspensions of colloidal silica: observations and X-ray measurements. *J. Chem. Soc., Faraday Trans.* (1991), **87**, 411-424.
33. Holland, B. T.; Blanford, C. F.; Stein, A., Synthesis of Macroporous Minerals with Highly Ordered Three-Dimensional Arrays of Spheroidal Voids. *Science* (1998), **281**, 538-540.
34. Waterhouse, G. I. N.; Waterland, M. R., Opal and inverse opal photonic crystals: Fabrication and characterization. *Polyhedron* (2007), **26**, 356-368.
35. Velev, O. D.; Lenhoff, A. M., Colloidal crystals as templates for porous materials. *Curr. Opin. Colloid Interface Sci.* (2000), **5**, 56-63.
36. Suzuki, Y.; Sawada, T.; Tamura, K., Colloidal crystallization by a centrifugation method. *J. Cryst. Growth* (2011), **318**, 780-783.
37. Jiang, P.; Prasad, T.; McFarland, M. J.; Colvin, V. L., Two-dimensional nonclose-packed colloidal crystals formed by spincoating. *App. Phys. Lett.* (2006), **89**, -.
38. Choi, J.-Y.; Alford, T. L.; Honsberg, C. B., Solvent-Controlled Spin-Coating Method for Large-Scale Area Deposition of Two-Dimensional Silica Nanosphere Assembled Layers. *Langmuir* (2014), **30**, 5732-5738.
39. Jiang, P.; McFarland, M. J., Large-Scale Fabrication of Wafer-Size Colloidal Crystals, Macroporous Polymers and Nanocomposites by Spin-Coating. *J. Am. Chem. Soc.* (2004), **126**, 13778-13786.

40. Arcos, C.; Kumar, K.; González-Viñas, W.; Sirera, R.; Poduska, K. M.; Yethiraj, A., Orientationally correlated colloidal polycrystals without long-range positional order. *Phys. Rev. E* (2008), **77**, 050402.
41. Pichumani, M.; Bagheri, P.; Poduska, K. M.; Gonzalez-Vinas, W.; Yethiraj, A., Dynamics, Crystallization and Structures in Colloid Spin Coating. *Soft Matter* (2013), **9**, 3220-3229.
42. Ge, J.; He, L.; Hu, Y.; Yin, Y., Magnetically induced colloidal assembly into field-responsive photonic structures. *Nanoscale* (2011), **3**, 177-183.
43. He, L.; Wang, M.; Ge, J.; Yin, Y., Magnetic Assembly Route to Colloidal Responsive Photonic Nanostructures. *Acc. Chem. Res.* (2012), **45**, 1431-1440.
44. He, L.; Hu, Y.; Kim, H.; Ge, J.; Kwon, S.; Yin, Y., Magnetic Assembly of Nonmagnetic Particles into Photonic Crystal Structures. *Nano Lett.* (2010), **10**, 4708-4714.
45. Xu, X.; Friedman, G.; Humfeld, K. D.; Majetich, S. A.; Asher, S. A., Superparamagnetic Photonic Crystals. *Adv. Mater.* (2001), **13**, 1681-1684.
46. Demirors, A. F.; Pillai, P. P.; Kowalczyk, B.; Grzybowski, B. A., Colloidal assembly directed by virtual magnetic moulds. *Nature* (2013), **503**, 99-103.
47. Böhmer, In Situ Observation of 2-Dimensional Clustering during Electrophoretic Deposition. *Langmuir* (1996), **12**, 5747-5750.
48. Holgado, M.; García-Santamaría, F.; Blanco, A.; Ibisate, M.; Cintas, A.; Míguez, H.; Serna, C. J.; Molpeceres, C.; Requena, J.; Mifsud, A.; Meseguer, F.; López, C., Electrophoretic Deposition To Control Artificial Opal Growth. *Langmuir* (1999), **15**, 4701-4704.
49. Rogach, A. L.; Kotov, N. A.; Koktysh, D. S.; Ostrander, J. W.; Ragoisha, G. A., Electrophoretic Deposition of Latex-based 3D Colloidal Photonic Crystals: A Technique for Rapid Production of High-Quality Opals. *Chem. Mater.* (2000), **12**, 2721-2726.
50. Yeh, S.-R.; Seul, M.; Shraiman, B. I., Assembly of ordered colloidal aggregates by electric-field-induced fluid flow. *Nature* (1997), **386**, 57-59.
51. Trau, M.; Saville, D. A.; Aksay, I. A., Assembly of Colloidal Crystals at Electrode Interfaces. *Langmuir* (1997), **13**, 6375-6381.
52. Prieve, D. C.; Sides, P. J.; Wirth, C. L., 2-D assembly of colloidal particles on a planar electrode. *Curr. Opin. Colloid Interface Sci.* (2010), **15**, 160-174.
53. Dimitrov, A. S.; Nagayama, K., Continuous Convective Assembling of Fine Particles into Two-dimensional Arrays on Solid Surfaces. *Langmuir* (1996), **12**, 1303-1311.
54. Jiang, P.; Bertone, J. F.; Hwang, K. S.; Colvin, V. L., Single-Crystal Colloidal Multilayers of Controlled Thickness. *Chem. Mater.* (1999), **11**, 2132-2140.
55. Oh, J. R.; Moon, J. H.; Yoon, S.; Park, C. R.; Do, Y. R., Fabrication of Wafer-scale Polystyrene Photonic Crystal Multilayers via the Layer-by-layer Scooping Transfer Technique. *J. Mater. Chem.* (2011), **21**, 14167-14172.
56. Bardosova, M.; Hodge, P.; Pach, L.; Pemble, M. E.; Smatko, V.; Tredgold, R. H.; Whitehead, D., Synthetic Opals made by the Langmuir–Blodgett Method. *Thin Solid Films* (2003), **437**, 276-279.
57. van Duffel, B.; Ras, R. H. A.; De Schryver, F. C.; Schoonheydt, R. A., Langmuir-Blodgett Deposition and Optical Diffraction of Two-dimensional Opal. *J. Mater. Chem.* (2001), **11**, 3333-3336.
58. Khunsin, W.; Amann, A.; Kocher-Oberlehner, G.; Romanov, S. G.; Pullteap, S.; Seat, H. C.; O'Reilly, E. P.; Zentel, R.; Torres, C. M. S., Noise-Assisted Crystallization of Opal Films. *Adv. Funct. Mater.* (2012), **22**, 1812-1821.

59. Ghosh, M.; Fan, F. Q.; Stebe, K. J., Spontaneous pattern formation by dip coating of colloidal suspensions on homogeneous surfaces. *Langmuir* (2007), **23**, 2180-2183.
60. Fu, Y. N.; Jin, Z. G.; Liu, Z. F.; Liu, Y.; Li, W., Self-assembly of colloidal crystals from polystyrene emulsion at elevated temperature by dip-drawing method. *Mater. Lett.* (2008), **62**, 4286-4289.
61. Hsueh, C.; Moraila Martínez, C. L.; Doumenc, F.; Rodríguez-Valverde, M. A.; Guerrier, B., Self-assembly in Drying Complex Fluid at Low Capillary Number. *Chem. Eng. Process.: Process Intensif.*
62. Wang, Y.; Chen, L.; Yang, H.; Guo, Q.; Zhou, W.; Tao, M., Large-area self assembled monolayers of silica microspheres formed by dip coating. *Mater. Sci.-Pol.* (2010), **28**, 467-478.
63. Gu, Z. Z.; Fujishima, A.; Sato, O., Fabrication of high-quality opal films with controllable thickness. *Chem. Mater.* (2002), **14**, 760-765.
64. Berteloot, G.; Daerr, A.; Lequeux, F.; Limat, L., Dip coating with colloids and evaporation. *Chem. Eng. Process.: Process Intensif.* (2013), **68**, 69-73.
65. Liu, Z.; Ya, J.; Xin, Y.; Ma, J.; Zhou, C., Assembly of polystyrene colloidal crystal templates by a dip-drawing method. *Journal of Crystal Growth* (2006), **297**, 223-227.
66. Takeda, S.; Wiltzius, P., Growth of Highly Ordered Colloidal Crystals Using Self-Assembly at Liquid-Liquid Interfaces. *Chem. Mater.* (2006), **18**, 5643-5645.
67. Deleuze, C.; Sarrat, B.; Ehrenfeld, F.; Perquis, S.; Derail, C.; Billon, L., Photonic Properties of Hybrid Colloidal Crystals Fabricated by a Rapid Dip-coating Process. *Phys. Chem. Chem. Phys.* (2011), **13**, 10681-10689.
68. Armstrong, E.; Khunsin, W.; Osiak, M.; Blömker, M.; Torres, C. M. S.; O'Dwyer, C., Ordered 2D Colloidal Photonic Crystals on Gold Substrates by Surfactant-Assisted Fast-Rate Dip Coating. *Small* (2014), **10**, 1895-1901.
69. Khunsin, W.; Kocher, G.; Romanov, S. G.; Torres, C. M. S., Quantitative Analysis of Lattice Ordering in Thin Film Opal-based Photonic Crystals. *Adv. Funct. Mater.* (2008), **18**, 2471-2479.
70. Kim, M. H.; Im, S. H.; Park, O. O., Rapid Fabrication of Two- and Three-Dimensional Colloidal Crystal Films via Confined Convective Assembly. *Adv. Funct. Mater.* (2005), **15**, 1329-1335.
71. Kim, S.; Choi, H. D.; Kim, I. D.; Lee, J. C.; Rhee, B. K.; Lim, J. A.; Hong, J. M., Formation of a polymer particle monolayer by continuous self-assembly from a colloidal solution. *J. Colloid Interface Sci.* (2012), **368**, 9-13.
72. Sanders, J. V.; Murray, M. J., Ordered arrangements of spheres of two different sizes in opal. *Nature* (1978), **275**, 201-203.
73. Hachisu, S.; Yoshimura, S., Optical demonstration of crystalline superstructures in binary mixtures of latex globules. *Nature* (1980), **283**, 188-189.
74. Leunissen, M. E.; Christova, C. G.; Hynninen, A.-P.; Royall, C. P.; Campbell, A. I.; Imhof, A.; Dijkstra, M.; van Roij, R.; van Blaaderen, A., Ionic colloidal crystals of oppositely charged particles. *Nature* (2005), **437**, 235-240.
75. Vermolen, E. C. M.; Kuijk, A.; Fillion, L. C.; Hermes, M.; Thijssen, J. H. J.; Dijkstra, M.; van Blaaderen, A., Fabrication of large binary colloidal crystals with a NaCl structure. *Proc. Natl. Acad. Sci. U. S. A.* (2009), **106**, 16063-16067.
76. Vogel, N.; de Viguierie, L.; Jonas, U.; Weiss, C. K.; Landfester, K., Wafer-Scale Fabrication of Ordered Binary Colloidal Monolayers with Adjustable Stoichiometries. *Adv. Funct. Mater.* (2011), **21**, 3064-3073.
77. Singh, G.; Griesser, H. J.; Bremmell, K.; Kingshott, P., Highly Ordered Nanometer-Scale Chemical and Protein Patterns by Binary Colloidal Crystal Lithography Combined with Plasma Polymerization. *Adv. Funct. Mater.* (2011), **21**, 540-546.

78. Velikov, K. P.; Christova, C. G.; Dullens, R. P. A.; van Blaaderen, A., Layer-by-Layer Growth of Binary Colloidal Crystals. *Science* (2002), **296**, 106-109.
79. Wang, D.; Möhwald, H., Rapid Fabrication of Binary Colloidal Crystals by Stepwise Spin-Coating. *Adv. Mater.* (2004), **16**, 244-247.
80. Kim, M. H.; Im, S. H.; Park, O. O., Fabrication and Structural Analysis of Binary Colloidal Crystals with Two-Dimensional Superlattices. *Adv. Mater.* (2005), **17**, 2501-2505.
81. Huang, X.; Zhou, J.; Fu, M.; Li, B.; Wang, Y.; Zhao, Q.; Yang, Z.; Xie, Q.; Li, L., Binary Colloidal Crystals with a Wide Range of Size Ratios via Template-Assisted Electric-Field-Induced Assembly. *Langmuir* (2007), **23**, 8695-8698.
82. Yu, J.; Yan, Q.; Shen, D., Co-Self-Assembly of Binary Colloidal Crystals at the Air–Water Interface. *ACS Appl. Mater. Interfaces* (2010), **2**, 1922-1926.
83. Wang, J.; Ahl, S.; Li, Q.; Kreiter, M.; Neumann, T.; Burkert, K.; Knoll, W.; Jonas, U., Structural and optical characterization of 3D binary colloidal crystal and inverse opal films prepared by direct co-deposition. *J. Mater. Chem.* (2008), **18**, 981-988.
84. Mukhopadhyay, R.; Al-Hanbali, O.; Pillai, S.; Hemmersam, A. G.; Meyer, R. L.; Hunter, A. C.; Rutt, K. J.; Besenbacher, F.; Moghimi, S. M.; Kingshott, P., Ordering of Binary Polymeric Nanoparticles on Hydrophobic Surfaces Assembled from Low Volume Fraction Dispersions. *J. Am. Chem. Soc.* (2007), **129**, 13390-13391.
85. Dai, Z.; Li, Y.; Duan, G.; Jia, L.; Cai, W., Phase Diagram, Design of Monolayer Binary Colloidal Crystals, and Their Fabrication Based on Ethanol-Assisted Self-Assembly at the Air/Water Interface. *ACS Nano* (2012), **6**, 6706-6716.
86. Malekpourkoupaei, A.; Kostiuk, L. W.; Harrison, D. J., Fabrication of Binary Opal Lattices in Microfluidic Devices. *Chem. Mater.* (2013), **25**, 3808-3815.
87. Kitaev, V.; Ozin, G. A., Self-Assembled Surface Patterns of Binary Colloidal Crystals. *Adv. Mater.* (2003), **15**, 75-78.
88. Wang, J.; Li, Q.; Knoll, W.; Jonas, U., Preparation of Multilayered Trimodal Colloid Crystals and Binary Inverse Opals. *J. Am. Chem. Soc.* (2006), **128**, 15606-15607.
89. Wan, Y.; Cai, Z.; Xia, L.; Wang, L.; Li, Y.; Li, Q.; Zhao, X. S., Simulation and fabrication of binary colloidal photonic crystals and their inverse structures. *Mater. Lett.* (2009), **63**, 2078-2081.
90. Fenollosa, R.; Meseguer, F., Non-Close-Packed Artificial Opals. *Adv. Mater.* (2003), **15**, 1282-1285.
91. Jiang, P., Surface-Templated Nanostructured Films with Two-Dimensional Ordered Arrays of Voids. *Angew. Chem., Int. Ed.* (2004), **43**, 5625-5628.
92. Ren, Z.; Li, X.; Zhang, J.; Li, W.; Zhang, X.; Yang, B., Tunable Two-Dimensional Non-Close-Packed Microwell Arrays Using Colloidal Crystals as Templates. *Langmuir* (2007), **23**, 8272-8276.
93. Jin, C.; McLachlan, M. A.; McComb, D. W.; De La Rue, R. M.; Johnson, N. P., Template-Assisted Growth of Nominally Cubic (100)-Oriented Three-Dimensional Crack-Free Photonic Crystals. *Nano Lett.* (2005), **5**, 2646-2650.
94. Zhang, J.; Alsayed, A.; Lin, K. H.; Sanyal, S.; Zhang, F.; Pao, W.-J.; Balagurusamy, V. S. K.; Heiney, P. A.; Yodh, A. G., Template-directed convective assembly of three-dimensional face-centered-cubic colloidal crystals. *Appl. Phys. Lett.* (2002), **81**, 3176-3178.
95. Hoogenboom, J. P.; Rétif, C.; de Bres, E.; van de Boer, M.; van Langen-Suurling, A. K.; Romijn, J.; van Blaaderen, A., Template-Induced Growth of Close-Packed and Non-Close-Packed Colloidal Crystals during Solvent Evaporation. *Nano Lett.* (2004), **4**, 205-208.

96. Dziomkina, N. V.; Vancso, G. J., Colloidal Crystal Assembly on Topologically Patterned Templates. *Soft Matter* (2005), **1**, 265-279.
97. Yin, Y.; Lu, Y.; Gates, B.; Xia, Y., Template-Assisted Self-Assembly: A Practical Route to Complex Aggregates of Monodispersed Colloids with Well-Defined Sizes, Shapes, and Structures. *J. Am. Chem. Soc.* (2001), **123**, 8718-8729.
98. Masuda, Y.; Itoh, T.; Koumoto, K., Self-Assembly Patterning of Silica Colloidal Crystals. *Langmuir* (2005), **21**, 4478-4481.
99. Masuda, Y.; Tomimoto, K.; Koumoto, K., Two-Dimensional Self-Assembly of Spherical Particles Using a Liquid Mold and Its Drying Process. *Langmuir* (2003), **19**, 5179-5183.
100. Hayward, R. C.; Saville, D. A.; Aksay, I. A., Electrophoretic assembly of colloidal crystals with optically tunable micropatterns. *Nature* (2000), **404**, 56-59.
101. Qian, F.; Pascall, A.; Bora, M.; Han, T. Y.-J.; Guo, S.; Ly, S.; Worsley, M. A.; Kuntz, J. D.; Olson, T. Y., On-Demand and Location Selective Particle Assembly via Electrophoretic Deposition for Fabricating Structures with Particle-to-Particle Precision. *Langmuir* (2014).
102. Armstrong, E.; Osiak, M.; Geaney, H.; Glynn, C.; O'Dwyer, C., 2D and 3D vanadium oxide inverse opals and hollow sphere arrays. *CrystEngComm* (2014), **16**, 10804-10815.
103. Armstrong, E.; Khunsin, W.; Sotomayor Torres, C.M.; Osiak, M.; O'Dwyer, C., Synthetic Routes for the Preparation of Ordered Vanadium Oxide Inverted Opal Electrodes for Li-Ion Batteries. *ECS Transactions* (2014), **58**, 7-14.
104. Meseguer, F.; Blanco, A.; Míguez, H.; García-Santamaría, F.; Ibisate, M.; López, C., Synthesis of inverse opals. *Colloids Surf., A* (2002), **202**, 281-290.
105. Esmanski, A.; Ozin, G. A., Silicon Inverse-Opal-Based Macroporous Materials as Negative Electrodes for Lithium Ion Batteries. *Adv. Funct. Mater.* (2009), **19**, 1999-2010.
106. Rugge, A.; Becker, J. S.; Gordon, R. G.; Tolbert, S. H., Tungsten Nitride Inverse Opals by Atomic Layer Deposition. *Nano Lett.* (2003), **3**, 1293-1297.
107. Williams, V. O.; DeMarco, E. J.; Katz, M. J.; Libera, J. A.; Riha, S. C.; Kim, D. W.; Avila, J. R.; Martinson, A. B. F.; Elam, J. W.; Pellin, M. J.; Farha, O. K.; Hupp, J. T., Fabrication of Transparent-Conducting-Oxide-Coated Inverse Opals as Mesoporous Architectures for Electrocatalysis Applications: A Case Study with NiO. *ACS Appl. Mater. Interfaces* (2014), **6**, 12290-12294.
108. Collins, G.; Blömker, M.; Osiak, M.; Holmes, J. D.; Bredol, M.; O'Dwyer, C., Three-Dimensionally Ordered Hierarchically Porous Tin Dioxide Inverse Opals and Immobilization of Palladium Nanoparticles for Catalytic Applications. *Chem. Mater.* (2013), **25**, 4312-4320.
109. Yuan, Z.-Y.; Su, B.-L., Insights into hierarchically meso-macroporous structured materials. *J. Mater. Chem.* (2006), **16**, 663-677.
110. Liu, Y.; Qin, F.; Wei, Z.-Y.; Meng, Q.-B.; Zhang, D.-Z.; Li, Z.-Y., 10 fs Ultrafast All-optical Switching in Polystyrene Nonlinear Photonic Crystals. *Appl. Phys. Lett.* (2009), **95**, 131116.
111. Geng, C.; Wei, T.; Wang, X.; Shen, D.; Hao, Z.; Yan, Q., Enhancement of Light Output Power from LEDs Based on Monolayer Colloidal Crystal. *Small* (2014), **10**, 1668-1686.
112. Lu, L.; Joannopoulos, J. D.; Soljačić, M., Waveguiding at the Edge of a Three-Dimensional Photonic Crystal. *Phys. Rev. Lett.* (2012), **108**, 243901.
113. Nelson, E. C.; Dias, N. L.; Bassett, K. P.; Dunham, S. N.; Verma, V.; Miyake, M.; Wiltzius, P.; Rogers, J. A.; Coleman, J. J.; Li, X.; Braun, P. V., Epitaxial growth of

- three-dimensionally architected optoelectronic devices. *Nat. Mater.* (2011), **10**, 676-681.
114. Arsenault, A. C.; Puzzo, D. P.; Manners, I.; Ozin, G. A., Photonic-crystal full-colour displays. *Nat. Photonics* (2007), **1**, 468-472.
 115. Fenzl, C.; Hirsch, T.; Wolfbeis, O. S., Photonic Crystals for Chemical Sensing and Biosensing. *Angew. Chem., Int. Ed.* (2014), **53**, 3318-3335.
 116. Blanco, A.; Chomski, E.; Grabtchak, S.; Ibsate, M.; John, S.; Leonard, S. W.; Lopez, C.; Meseguer, F.; Miguez, H.; Mondia, J. P.; Ozin, G. A.; Toader, O.; van Driel, H. M., Large-scale synthesis of a silicon photonic crystal with a complete three-dimensional bandgap near 1.5 micrometres. *Nature* (2000), **405**, 437-440.
 117. Jin, F.; Shi, L.-T.; Zheng, M.-L.; Dong, X.-Z.; Chen, S.; Zhao, Z.-S.; Duan, X.-M., Lasing and Amplified Spontaneous Emission in a Polymeric Inverse Opal Photonic Crystal Resonating Cavity. *J. Phys. Chem. C* (2013), **117**, 9463-9468.
 118. Lee, Y. J.; Braun, P. V., Tunable Inverse Opal Hydrogel pH Sensors. *Advanced Materials* (2003), **15**, 563-566.
 119. Xue, F.; Meng, Z.; Qi, F.; Xue, M.; Wang, F.; Chen, W.; Yan, Z., Two-dimensional inverse opal hydrogel for pH sensing. *Analyst* (2014), **139**, 6192-6196.
 120. Barry, R. A.; Wiltzius, P., Humidity-Sensing Inverse Opal Hydrogels. *Langmuir* (2005), **22**, 1369-1374.
 121. Nakayama, D.; Takeoka, Y.; Watanabe, M.; Kataoka, K., Simple and Precise Preparation of a Porous Gel for a Colorimetric Glucose Sensor by a Templating Technique. *Angew. Chem., Int. Ed.* (2003), **42**, 4197-4200.
 122. Pernice, R.; Adamo, G.; Stivala, S.; Parisi, A.; Busacca, A. C.; Spigolon, D.; Sabatino, M. A.; D'Acquisto, L.; Dispenza, C., Opals infiltrated with a stimuli-responsive hydrogel for ethanol vapor sensing. *Opt. Mater. Express* (2013), **3**, 1820-1833.
 123. Hong, W.; Chen, Y.; Feng, X.; Yan, Y.; Hu, X.; Zhao, B.; Zhang, F.; Zhang, D.; Xu, Z.; Lai, Y., Full-color CO₂ gas sensing by an inverse opal photonic hydrogel. *Chem. Comm.* (2013), **49**, 8229-8231.
 124. Kim, S.; Mitropoulos, A. N.; Spitzberg, J. D.; Tao, H.; Kaplan, D. L.; Omenetto, F. G., Silk inverse opals. *Nat. Photonics* (2012), **6**, 818-823.
 125. Bonifacio, L. D.; Puzzo, D. P.; Breslav, S.; Willey, B. M.; McGeer, A.; Ozin, G. A., Towards the Photonic Nose: A Novel Platform for Molecule and Bacteria Identification. *Adv. Mater.* (2010), **22**, 1351-1354.
 126. Wang, H.; Zhang, K.-Q., Photonic Crystal Structures with Tunable Structure Color as Colorimetric Sensors. *Sensors* (2013), **13**, 4192-4213.
 127. Zhang, Y.; Qiu, J.; Gao, M.; Li, P.; Gao, L.; Heng, L.; Tang, B. Z.; Jiang, L., A visual film sensor based on silole-infiltrated SiO₂ inverse opal photonic crystal for detecting organic vapors. *J. Mater. Chem. C* (2014), **2**, 8865-8872.
 128. Blanford, C. F.; Schroden, R. C.; Al-Daous, M.; Stein, A., Tuning Solvent-Dependent Color Changes of Three-Dimensionally Ordered Macroporous (3DOM) Materials Through Compositional and Geometric Modifications. *Adv. Mater.* (2001), **13**, 26-29.
 129. Sharma, M.; Waterhouse, G. I. N.; Loader, S. W. C.; Garg, S.; Svirskis, D., High surface area polypyrrole scaffolds for tunable drug delivery. *Int. J. Pharm.* (2013), **443**, 163-168.
 130. João, C. F. C.; Vasconcelos, J. M.; Silva, J. C.; Borges, J. P., An Overview of Inverted Colloidal Crystal Systems for Tissue Engineering. *Tissue Eng., Part B* (2013), **20**, 437-454.
 131. Zhang, Y. S.; Choi, S.-W.; Xia, Y., Inverse opal scaffolds for applications in regenerative medicine. *Soft Matter* (2013), **9**, 9747-9754.

132. Rinnerbauer, V.; Ndao, S.; Yeng, Y. X.; Chan, W. R.; Senkevich, J. J.; Joannopoulos, J. D.; Soljacic, M.; Celanovic, I., Recent developments in high-temperature photonic crystals for energy conversion. *Energy Environ. Sci.* (2012), **5**, 8815-8823.
133. Arpin, K. Three-dimensional Metallic Architectures for Photonic and Energy Storage Applications. University of Illinois at Urbana-Champaign, 2013.
134. Arpin, K. A.; Losego, M. D.; Braun, P. V., Electrodeposited 3D Tungsten Photonic Crystals with Enhanced Thermal Stability. *Chem. Mater.* (2011), **23**, 4783-4788.
135. Denny, N. R.; Han, S. E.; Norris, D. J.; Stein, A., Effects of Thermal Processes on the Structure of Monolithic Tungsten and Tungsten Alloy Photonic Crystals. *Chem. Mater.* (2007), **19**, 4563-4569.
136. Han, S.; Stein, A.; Norris, D., Tailoring Self-Assembled Metallic Photonic Crystals for Modified Thermal Emission. *Phys. Rev. Lett.* (2007), **99**, 053906.
137. Park, Y.; Lee, J. W.; Ha, S.-J.; Moon, J. H., 1D nanorod-planted 3D inverse opal structures for use in dye-sensitized solar cells. *Nanoscale* (2014), **6**, 3105-3109.
138. Cheng-Yu, K.; Shih-Yuan, L., Fabrication of a multi-scale nanostructure of TiO₂ for application in dye-sensitized solar cells. *Nanotechnology* (2008), **19**, 095705.
139. Cho, C.-Y.; Moon, J. H., Hierarchical Twin-Scale Inverse Opal TiO₂ Electrodes for Dye-Sensitized Solar Cells. *Langmuir* (2012), **28**, 9372-9377.
140. Kang, D.-Y.; Lee, Y.; Cho, C.-Y.; Moon, J. H., Inverse Opal Carbons for Counter Electrode of Dye-Sensitized Solar Cells. *Langmuir* (2012), **28**, 7033-7038.
141. Varghese, L. T.; Xuan, Y.; Niu, B.; Fan, L.; Bermel, P.; Qi, M., Enhanced Photon Management of Thin-Film Silicon Solar Cells Using Inverse Opal Photonic Crystals with 3D Photonic Bandgaps. *Adv. Opt. Mater.* (2013), **1**, 692-698.
142. Mihi, A.; Zhang, C.; Braun, P. V., Transfer of Preformed Three-Dimensional Photonic Crystals onto Dye-Sensitized Solar Cells. *Angew. Chem., Int. Ed.* (2011), **50**, 5712-5715.
143. Osiak, M.; Geaney, H.; Armstrong, E.; O'Dwyer, C., Structuring Materials for Lithium-ion Batteries: Advancements in Nanomaterial Structure, Composition, and Defined Assembly on Cell Performance. *J. Mater. Chem. A* (2014), **2** 9433-9460.
144. Long, J. W.; Dunn, B.; Rolison, D. R.; White, H. S., Three-Dimensional Battery Architectures. *Chem. Rev.* (2004), **104**, 4463-4492.
145. Sakamoto, J. S.; Dunn, B., Hierarchical Battery Electrodes Based on Inverted Opal Structures. *J. Mater. Chem.* (2002), **12**, 2859-2861.
146. Ergang, N. S.; Lytle, J. C.; Yan, H.; Stein, A., Effect of a Macropore Structure on Cycling Rates of LiCoO₂. *J. Electrochem. Soc.* (2005), **152**, A1989-A1995.
147. Doherty, C. M.; Caruso, R. A.; Smarsly, B. M.; Drummond, C. J., Colloidal Crystal Templating to Produce Hierarchically Porous LiFePO₄ Electrode Materials for High Power Lithium Ion Batteries. *Chem. Mater.* (2009), **21**, 2895-2903.
148. Lu, J.; Tang, Z.; Zhang, Z.; Shen, W., Preparation of LiFePO₄ with inverse opal structure and its satisfactory electrochemical properties. *Mater Res Bull* (2005), **40**, 2039-2046.
149. Lu, J.; Tang, Z.; Zhang, Z.; Shen, W., Structural and Electrochemical Properties of Multihollow LiFePO₄ for Lithium Battery Cathodes. *Journal of The Electrochemical Society* (2005), **152**, A1441-A1444.
150. Ma, D. L.; Cao, Z. Y.; Wang, H. G.; Huang, X. L.; Wang, L. M.; Zhang, X. B., Three-dimensionally Ordered Macroporous FeF₃ and its In situ Homogenous Polymerization Coating for High Energy and Power Density Lithium Ion batteries. *Energy Environ. Sci.* (2012), **5**, 8538-8542.

151. Zakhidov, A. A.; Baughman, R. H.; Iqbal, Z.; Cui, C.; Khayrullin, I.; Dantas, S. O.; Marti, J.; Ralchenko, V. G., Carbon Structures with Three-Dimensional Periodicity at Optical Wavelengths. *Science* (1998), **282**, 897-901.
152. Lee, K. T.; Lytle, J. C.; Ergang, N. S.; Oh, S. M.; Stein, A., Synthesis and Rate Performance of Monolithic Macroporous Carbon Electrodes for Lithium-Ion Secondary Batteries. *Adv Funct Mater* (2005), **15**, 547-556.
153. Kang, D.-Y.; Kim, S.-O.; Chae, Y. J.; Lee, J. K.; Moon, J. H., Particulate Inverse Opal Carbon Electrodes for Lithium-Ion Batteries. *Langmuir* (2013), **29**, 1192-1198.
154. Song, T.; Jeon, Y.; Samal, M.; Han, H.; Park, H.; Ha, J.; Yi, D. K.; Choi, J.-M.; Chang, H.; Choi, Y.-M.; Paik, U., A Ge Inverse Opal with Porous Walls as an Anode for Lithium ion Batteries. *Energy Environ. Sci.* (2012), **5**, 9028-9033.
155. Kavan, L.; Zukalová, M.; Kalbáč, M.; Graetzel, M., Lithium Insertion into Anatase Inverse Opal. *J. Electrochem. Soc.* (2004), **151**, A1301-A1307.
156. Wu, M.-S.; Lin, Y.-P., Monodispersed macroporous architecture of nickel-oxide film as an anode material for thin-film lithium-ion batteries. *Electrochim. Acta* (2011), **56**, 2068-2073.
157. Zhang, H.; Yu, X.; Braun, P. V., Three-dimensional Bicontinuous Ultrafast-Charge and -Discharge Bulk Battery Electrodes. *Nat. Nanotechnol.* (2011), **6**, 277-281.
158. Zhang, H.; Braun, P. V., Three-Dimensional Metal Scaffold Supported Bicontinuous Silicon Battery Anodes. *Nano Lett.* (2012), **12**, 2778-2783.
159. Kim, D. Y.; Suk, J.; Kim, D. W.; Kang, Y.; Im, S. H.; Yang, Y.; Park, O. O., An electrochemically grown three-dimensional porous Si@Ni inverse opal structure for high-performance Li ion battery anodes. *J. Mater. Chem. A* (2014), **2**, 6396-6401.
160. Liu, H.; Cho, H.-M.; Meng, Y. S.; Li, Q., Engineering Three-Dimensionally Electrodeposited Si-on-Ni Inverse Opal Structure for High Volumetric Capacity Li-Ion Microbattery Anode. *ACS Applied Materials & Interfaces* (2014), **6**, 9842-9849.
161. Huang, X.; Chen, J.; Lu, Z.; Yu, H.; Yan, Q.; Hng, H. H., Carbon inverse opal entrapped with electrode active nanoparticles as high-performance anode for lithium-ion batteries. *Sci. Rep.* (2013), **3**.
162. Kim, J.-H.; Kim, J.-H.; Choi, K.-H.; Yu, H. K.; Kim, J. H.; Lee, J. S.; Lee, S.-Y., Inverse Opal-Inspired, Nanoscaffold Battery Separators: A New Membrane Opportunity for High-Performance Energy Storage Systems. *Nano Letters* (2014), **14**, 4438-4448.
163. Pikul, J. H.; Zhang, H. G.; Cho, J.; Braun, P. V.; King, W. P., High-power Lithium Ion Microbatteries from Interdigitated Three-dimensional Bicontinuous Nanoporous Electrodes. *Nat. Commun.* (2013), **4**, 1732-1736.

Chapter 3

Experimental

3.1 Introduction

In this chapter the methods employed for sphere assembly will be described including preparation of the different substrates used. The formation of inverse opal vanadium pentoxide (V_2O_5) through the infiltration of sphere templates with vanadium oxide precursors will then be outlined. The various characterisation techniques utilized will be explained, in particular, the use of angular resolved spectroscopy for probing of the PhC lattice structure, electron microscopy for topographical comparisons and Raman spectroscopy for vanadium oxide phase determination. The techniques and cell layout used for electrochemical characterisation of the vanadium oxide inverse opal structures will also be detailed.

3.2 Colloidal Sphere Assembly

3.2.1 Dip Coating

Dip coating was performed at a rate of 1.5 mm/hr on a motorized dip coating apparatus as described by Khunsin *et al.*, this was used both with and without the addition of acoustic vibrations. These vibrations were applied in the form of white noise at a frequency of 20 kHz through a loudspeaker beneath the colloidal suspension. Dip coating was performed at the faster rate of 1 mm/min using a MTI Corporation PTL-MM01 Dip Coater apparatus, shown in the photograph in Fig. 3.1(a). Dip coating or convective assembly was used for the assembly of both polystyrene (PS) and poly(methyl methacrylate) (PMMA) spheres on different substrates. The sensitivity of this method to various experimental circumstances was investigated by altering either solution or substrate conditions. Dip coating as outlined in Chapter 2 takes advantage of a moving meniscus line and the attractive capillary interactions between spheres. The spheres are drawn towards the air-water interface and assemble into

close packed arrays as the liquid bridge between neighbouring spheres evaporates (see Fig. 3.1 (b)).

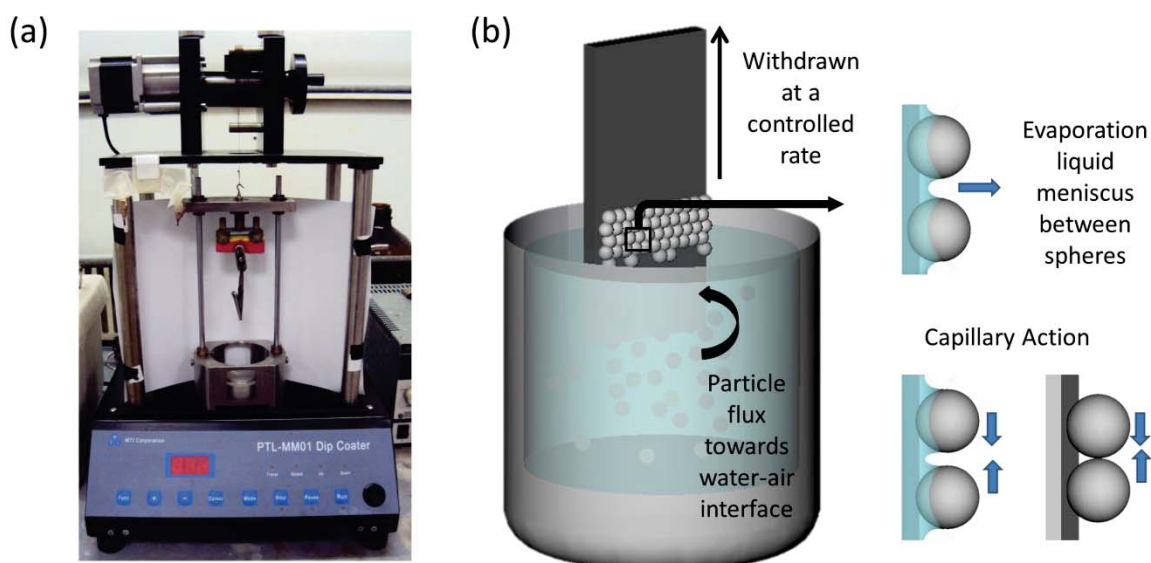


Fig. 3.1 (a) Schematic representation of the dip coating scenario for colloidal spheres (b) Photograph of the dip coater used at slow rate of 1 mm/min

The effects of substrate surface conditions on the order and thickness of the final sphere deposit was investigated using glass surfaces with differing levels of hydrophilicity. Glass substrates of approximately $2\text{ cm} \times 1\text{ cm}$ were cleaned by sonication in acetone, IPA and deionized water, dried in air and then subjected to two different additional cleaning treatments, using Piranha solution and O_2 Plasma respectively. Piranha solution is an etching solution for organic residue formed from a mixture of sulphuric acid and hydrogen peroxide, it was used here in the ratio of 3:1. O_2 Plasma was applied in a PVA TePla PS210 Microwave Plasma System. Contact angle measurements were taken for both samples on a Kruss Easy Drop measurement system using the static drop method. The glass substrates were then lowered into a 3 wt% solution of 700 nm PMMA spheres and removed at rate of 1.5 mm/hr while white noise at a frequency of 20 kHz was applied through a loudspeaker beneath the solution.

3.2.2. Surfactant-assisted Dip Coating

A surfactant is an organic molecule, used in affecting interface relationships or boundary conditions between two immiscible phases by adsorbing at particular surfaces or interfaces within a system. The name surfactant is itself a contraction of the term ‘surface active agent.’ Surfactants are normally amphiphilic compounds, meaning they consist of a lyophobic structural group and a lyophilic group, for example, for a surfactant in water, this signifies a hydrophobic end and a hydrophilic end. Surfactants are usually classed with respect to the nature of the hydrophilic group. With anionic surfactants, the hydrophilic end bears a negative charge, the surface active portion of cationic surfactants hold a positive charge, and non-ionic surfactants bear no charge. Surfactant monomers organize into micelles at concentrations above the critical micelle concentration (CMC), the hydrophilic heads orientate towards the polar solute, and the hydrophobic tails group together to form a hydrophobic core. These micelles are known to enhance certain aspects of a solution such as the solubility of hydrophobic materials, and alter other aspects such as viscosity and polarity.

Sodium dodecyl sulphate (SDS) is an anionic surfactant and dissociates in water to form negatively charged monomers. It is used in this work to alter the colloidal interactions and solution parameters in an aqueous solution of PMMA spheres with the aim of affecting or improving sphere assembly on hydrophobic gold-coated silicon surfaces when withdrawn at a relatively fast rate of 1 mm/min. At low concentrations these monomers adsorb along the water air interface with the insoluble hydrophobic group extended upwards out of the bulk water phase, thusly lowering the surface tension of a solution which in turn can cause a lengthening in the meniscus for any partially-submerged substrate. These monomers will arrange along the sphere-water interface as well, encapsulating the polymer spheres as though an oil droplet, where surfactant molecules act as a barrier delaying the coalescence of droplets by electrostatic and/or steric repulsion.¹ If the concentration increases beyond the

CMC for SDS of \sim of 2.3 mg ml^{-1} ($8.0 \times 10^{-3} \text{ mol dm}^{-3}$)² the formation of micelles begins. (See schematic Fig. 3.2).

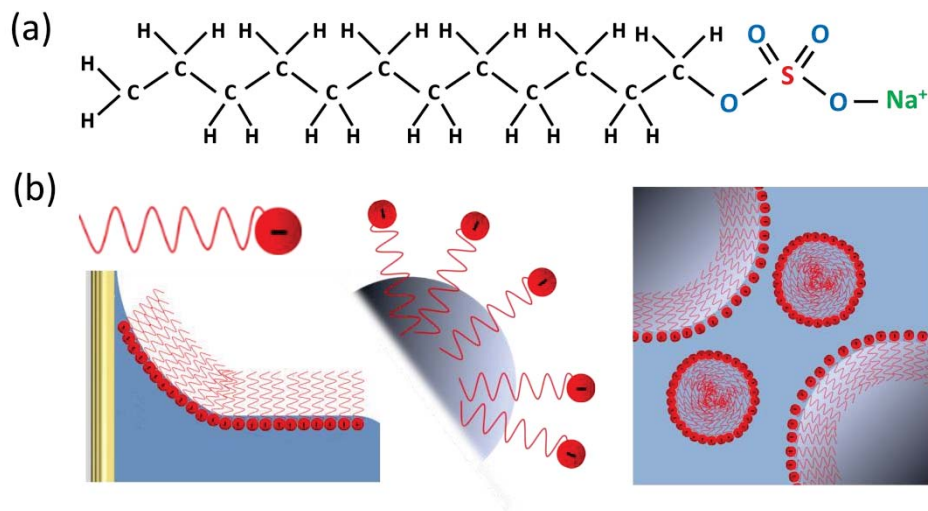


Fig. 3.2 (a) Molecular structure of the SDS molecule and (b) Schematic representations of the SDS monomer and its organization on addition to an aqueous solution of polymer spheres at a concentration above CMC.

In this work, a silicon wafer was cleaned in Ar⁺ plasma and coated with a 10 nm titanium adhesion layer and 100-150 nm gold by ion beam sputtering using an ATC Orion-5-UHV sputtering system. A piece of approximately 1 cm × 1 cm was then cleaned by sonication in acetone, IPA, rinsed with deionized water and dried in N₂. Mono-dispersed PMMA spheres with diameter $D \sim 700 \text{ nm}$, synthesized with altered concentrations according to the method outlined by Schroden,³ were centrifuged and dried at 50°C and redistributed in distilled water with a concentration of 5 wt%. SDS was added as received from Sigma-Aldrich, at a concentration of 8 mg ml^{-1} ($27.7 \times 10^{-3} \text{ mol dm}^{-3}$), greater than the theoretical critical micelle concentration (CMC) of 2.3 mg ml^{-1} ($8.0 \times 10^{-3} \text{ mol dm}^{-3}$) and stirred overnight.^{2, 4} The clean substrate was then settled vertically into the sphere solution for ~ 2 minutes and removed at the rate of 1 mm/min using a MTI Corporation PTL-MM01 Dip Coater apparatus. SDS used at this concentration resulted in a reduction in the overall

solution surface tension, encapsulation of the polymer spheres by the surfactant monomers much like they would an oil droplet and the likely formation of free standing micelle particles as well. All of which produced a monolayer of PMMA spheres on the gold coated silicon substrate at the comparatively fast rate of withdrawal of 1 mm/min.

3.2.3. Patterned Substrates

Patterned substrates were fabricated using electron beam lithography (EBL) (see Fig. 3.3(a)) with the aim of directing sphere assembly by limiting the allowed orientation. In this technique a focused beam of electrons is directed across an electron-sensitive material, known as a resist, in a predesigned, computer generated pattern.⁵ The electron beam, due to the inelastic collision of electrons and the resulting ionization of the resist, causes certain physico-chemical changes in the resist, changing the solubility of the exposed areas.⁶ Resists can be classed as either positive or negative, the solubility of a positive resist changes from low solubility to high solubility when exposed to electrons and the opposite is true for negative resists. The most commonly used positive resist is PMMA whose long polymer chain is broken in to more soluble fragments on exposure to a beam of electrons. An example of a negative resist is that of hydrogen silsesquioxane (HSQ), the electron beam causes a cross linking reaction combining smaller polymer parts into larger less soluble polymer chains.⁶ Development removes the fragmented polymers in the case of the positive resist or removes the non-cross-linked molecules in the case of negative resist. Development is effected by both duration and temperature, and must be correlated with exposure parameters to achieve the desired result. For example, high exposure and short development could be equivalent to a low, short exposure and longer development in achieving high resolution patterns. Developer usually consists of a mixture of solvents, for example in the case of PMMA, the developer is typically a 1:3 mixture of methyl isobutyl ketone (MIBK) with

isopropyl alcohol (IPA).

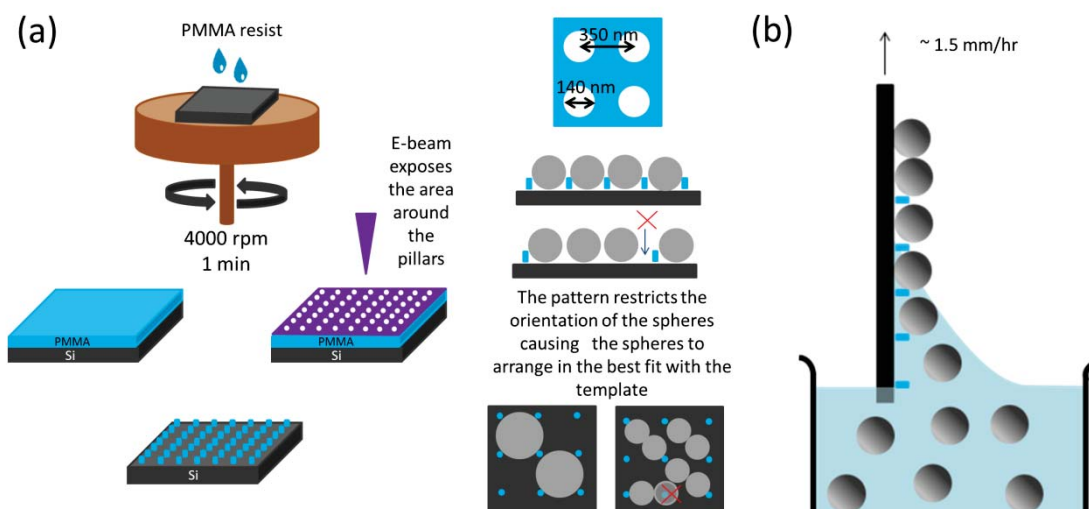


Fig. 3.3 Schematic representing (a) the template formation using electron beam lithography of spin-casted PMMA resist on silicon to produce a 2D array of pillars and a schematic representation of the desired effect on the orientation and ordering of then deposited spheres and (b) Dip-coating of 200 nm PS spheres

In this work, silicon wafer was cleaned by sonication in acetone, IPA and water, and dried in nitrogen. A 90 nm thick layer of poly-methacrylate (PMMA) 950K positive resist (AR-P 671.02) was applied by spin coating at a rate of 4000 rpm for 1 minute. 950K refers to the molecular weight of the PMMA and the lower this number the more sensitive the resist is to beam exposure. This was then baked at a temperature of ~ 180 °C for 5 minutes and patterned at 30 kV in an FEI Inspect F50 SEM equipped with a Raith EBL unit. Patterns were then developed in a 1:3 solution of Methyl isobutyl ketone (MIBK) and isopropanol (IPA) for 1 minute and rinsed in IPA for 1 minute. For imaging purposes templates were coated with ~ 4 nm gold. Unless stated otherwise, all write patterns were setup using an initial dose of $89.62 \mu\text{C}/\text{cm}^2$ and a dwell time of $0.4 \mu\text{s}$ then varied by the application of different dose factors to produce pillars of different definition for write field sizes of $200 \times 200 \mu\text{m}$, $50 \times 50 \mu\text{m}$ or $25 \times 25 \mu\text{m}$. Polystyrene spheres, with a diameter of 200 nm and a concentration of 2.5 wt%, used as received from Polysciences Inc., were then dip coated at a rate of ~ 1.5 mm/hr

using the home-made dipping apparatus, previously described by Khunsin *et al.*, but used here without noise assistance and outlined by the schematic in Fig. 3.3 (b).

3.2.4. Electrophoretic Deposition

Electrophoretic deposition (EPD) is the deposition of charged particles, dispersed and freely moving in a solvent, on to an oppositely charged electrode surface under the application of an electric field, schematically outlined in Fig. 3.4(a). It differs from electrodeposition and/or electroplating; these processes are more electrochemical in nature.⁷ They involve the diffusion and migration of individual ions or molecules within an electrolyte (usually an ionic salt solution) towards the deposition electrode and electrochemical conversion into the desired species in an insoluble form on the electrode surface. In electrophoretic deposition the particles to deposit already exist independently within the solvent. A number of factors influence EPD, particle and solvent parameters such as solution stability and the particle size, charge and subsequent mobility, and process.⁸

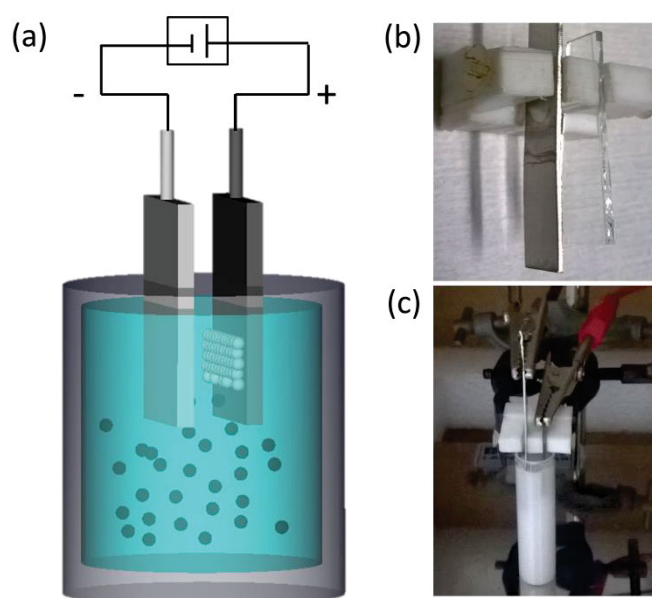


Fig. 3.4 (a) Schematic of the electrophoretic deposition (EPD) of PS spheres on to conductive substrates and photographs of the sample holder (b) and final setup (c).

In this work electrophoretic deposition using polystyrene (PS) spheres was performed similarly to the method described by Rogach *et al.*,⁹ in a cylindrical glass cell, with indium tin oxide (ITO) coated glass or stainless steel foil as the vertical anode and a stainless steel sheet as the counter electrode. Electrodes are held approximately 5 mm away from and directly in parallel with each other as shown in Fig. 3.4 (b) for an ITO-coated glass substrate as an example. The solution was prepared using 0.8 mL of the 2.5 wt% sulphated PS solution mixed with 4.3 mL ethanol, and ~ 80 μ L of 30% aqueous NH_4OH to ensure a pH of between 8 and 10. This produced a final concentration of spheres of ~0.4%. The electrophoretic deposition was carried out at 3 V for a variety of times in the setup shown in Fig. 3.4(c). This method was performed for PS spheres of 500, 350, and 200 nm in diameter purchased in 2.5 wt% aqueous solutions from Polysciences Inc., the 500 nm spheres had a slightly higher negative charge due to added surface functionalized with sulphate ions. The ITO coated glass was purchased from Sigma Aldrich and cut to approximately 8×25 mm pieces and cleaned by sonication in acetone, isopropanol (IPA) ethanol and deionized water. Stainless steel foil (SS316) was cut into rectangular pieces of ~ 2 cm \times 1 cm in size, and cleaned by sonication in acetone, IPA and DI water, and dried under N_2 . It is well known that heating stainless steel to high temperatures results in a colour change and this can be accompanied by slight changes in mass. Therefore in order to ensure mass consistency in determining deposited-material mass for later experiments, the stainless steel substrates were preheated to 300 $^\circ\text{C}$ (max. temp reached in overall experiments) for 24 h before sphere deposition. This resulted in a yellowing of the stainless steel foil.

3.3 Vanadium Pentoxide Precursor Infilling

Vanadium oxide inverted opals were formed by infiltrating the sphere templates, made by the methods described above, with vanadium pentoxide (V_2O_5) precursors. Two routes were

investigated, one involving the hydrolysis of vanadium triisopropoxide oxide precursor and another involving electrodeposition using a vanadium sulphate based electrolyte.

3.3.1 Drop Casting/Dip Coating

The opal templates were directly infiltrated with precursor solution by two methods. The precursor was formed from a mixture of IPA, deionized water, and vanadium triisopropoxide oxide ($\text{OV}(\text{OCH}(\text{CH}_3)_2)_3$). Firstly, a mixture of IPA and deionized water was formed in the ratio of 500:1 and a solution of IPA and vanadium triisopropoxide oxide in the ratio of 50:1, this solution was then added to the aqueous IPA for a final IPA: $\text{OV}(\text{OCH}(\text{CH}_3)_2)_3$ ratio of 100:1 and set stirring for ~30 minutes or until clear. This precursor was then directly applied to the opal templates by drop casting under a slight nitrogen overpressure as described in the schematic in Fig. 3.5(a) or by dip coating using an MTI Corporation PTL-MM01 Dip Coater. Drop-casting on monolayer, PMMA sphere templates created a basin-like morphology as schematically shown in Fig. 3.5(b) and the dip-coating of monolayer templates at a rate of 200 mm/min \times 10 times resulted in an overfilling effect to produce a hollow sphere morphology (Fig. 3.5(c)). Sphere removal was performed in a BINDER oven at 300 °C for 12 or 24 h. Removal of spheres was also carried out under UV Ozone in a Novascan PSD Pro Series digital UV Ozone system, for 12 h for the 2D IOs, followed by crystallization at 300 °C for 12 h in the oven with no discernible variation in morphology compared to the amorphous material structure.

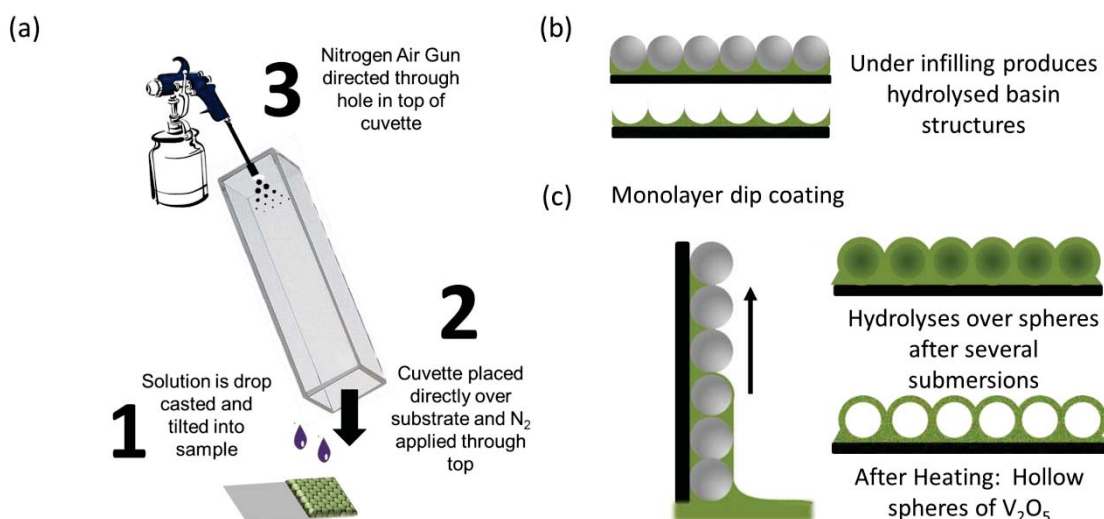
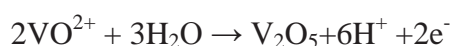


Fig. 3.5 Schematic diagram of template infilling by nitrogen-gun-assisted drop-casting of the 100:1 IPA:OV(OCH(CH₃)₂)₃ precursor solution (a) and of the resulting structure for under filling of a monolayer PMMA template by drop casting and the over filling for (c) dip coating at a rate of 200 mm/min × 10 times.

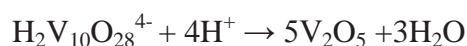
3.3.2 Electrodeposition

Infilling was also performed by electrodeposition in a three electrode cell at a constant voltage of 2V vs a saturated calomel reference electrode (SCE), a platinum mesh was used as counter electrode, as per the schematic and photograph in Fig. 3.6. All electrochemical work was carried out using a VersaSTAT3 Potentiostat. The working electrode consisted of PS sphere templates electrophoretically deposited on an area of ~ 1 cm × 1 cm of conductive substrates of stainless steel foil or ITO/FTO coated glass of ~ 2 cm × 1 cm total size. The electrolyte consisted of 0.25 M VOSO₄· γ H₂O solution in a 1:1 deionised water and ethanol mixture.^{10, 11} This was created by adding an amount of ~2.53 g VOSO₄· γ H₂O, used as purchased from Sigma Aldrich, to a mixture of 20 ml deionised water and 20 ml ethanol. The addition of ethanol to the solution reduces the surface tension between electrolyte and the PS template, increasing infiltration of the electrolyte to substrate surface. The electrodeposition of V₂O₅ from vanadyl sulphate solutions typically occurs through the reaction,



forming insoluble V_2O_5 at the electrode surface for a pH value of 1.8 at a voltage $> +1$ V.¹⁰

¹² For pH values greater than 1.8, Potiron *et al.* describes the process in two steps,¹³ firstly, oxidation into a soluble species and then precipitation at the electrode surface,



The electrolyte used here typically had a pH ~ 2.2 at room temperature. After deposition samples were heated to 300 °C for 24 h to remove the sphere templates and form crystalline V_2O_5 .

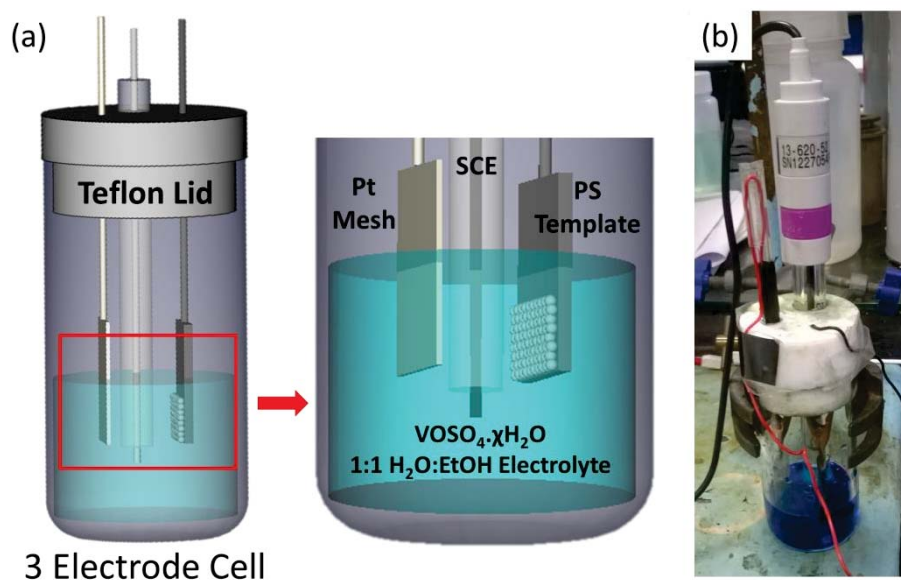


Fig. 3.6 The 3 electrode cell setup used in the electrodeposition of V_2O_5 (a) schematic and (b) photograph.

3.4 Structure and Elemental Characterisation Techniques

3.4.1 Reflectance/Transmission Spectroscopy

In this work, the PhC ordering was probed by non-destructive, static and/or angle-resolved spectroscopic techniques - reflection, transmission, or diffraction. Samples were mounted on a rotating stage and illuminated with white light from a Halogen bulb collimated to a beam

diameter of ~1 mm using a series of plano-convex lenses, as shown in Fig. 3.8(a). Dark and substrate background spectra were recorded and removed from the final processed sample spectra. Well-ordered PhCs produce stop bands at disallowed frequencies, exhibited as a peak in reflectance or minimum in transmission spectra. The position or dispersion of these resonances with respect to external angle of incidence θ can be compared with the Bragg law prediction for a FCC lattice, using the equation $\lambda = 2n_{\text{eff}}d_{hkl}\sqrt{(1 - (\sin \alpha_{hkl})^2)}$ where d_{hkl} is the inter-planer distance for the (hkl) planes, n_{eff} is the refractive index, and α_{hkl} is the angle between the incident light and the normal vector to the (hkl) plane. The internal angle of incidence α_{hkl} is related to the external angle θ using Snells law: $n_{\text{eff}} \sin(\alpha_{hkl}) = n_{\text{air}} \sin \theta$.¹⁴ The effective refractive index was calculated as $n_{\text{eff}} = 1.373$ assuming a filling fraction for an FCC crystal of 0.74 and this and $D = 700$ nm were used as fitting parameters for calculation of the Bragg fit. Transmission spectra as per Fig. 3.8 (b), for the multilayer PMMA structures formed on glass of different hydrophilicity were collected at intervals of 5° for light incident from $0-70^\circ$ using an a CCS200 Compact CCD spectrometer (Thorlabs) in the wavelength range 200 – 1000 nm and for higher wavelenths in the range 900-2100 nm with an Ocean Optics NIRQuest 256-2.1 spectrometer equipped with a 256-element InGaAs array detector.

The PMMA sphere monolayer deposits on gold coated silicon were investigated as 2D diffraction gratings. Diffraction from 2D structures manifests as peaks in diffraction spectra. Diffraction measurements were performed with fixed incident angles of 60° and 45° and spectra of the planar diffracted light were collected at an interval of 5° and an angular resolution of 2° using a CCS200 Compact CCD spectrometer (Thorlabs) in the wavelength range 200 – 1000 nm for the 2D monolayer PMMA samples on gold coated silicon. The planar grating equation, $\lambda = d[\sin(\alpha) + \sin(\beta + x)]$, where α is the angle of incidence, β is the angle of diffraction, d is the effective grating groove, which in the case of FCC (111) ordering corresponds to $\frac{\sqrt{3}}{2}D$, the half period of the trigonal lattice for the wave vector of

incident light propagating along the ΓK direction in the Brillouin zone (schematic Fig. 3.7 (c)) of a 2D hexagonal lattice, D is the sphere diameter, and x is a free constant.

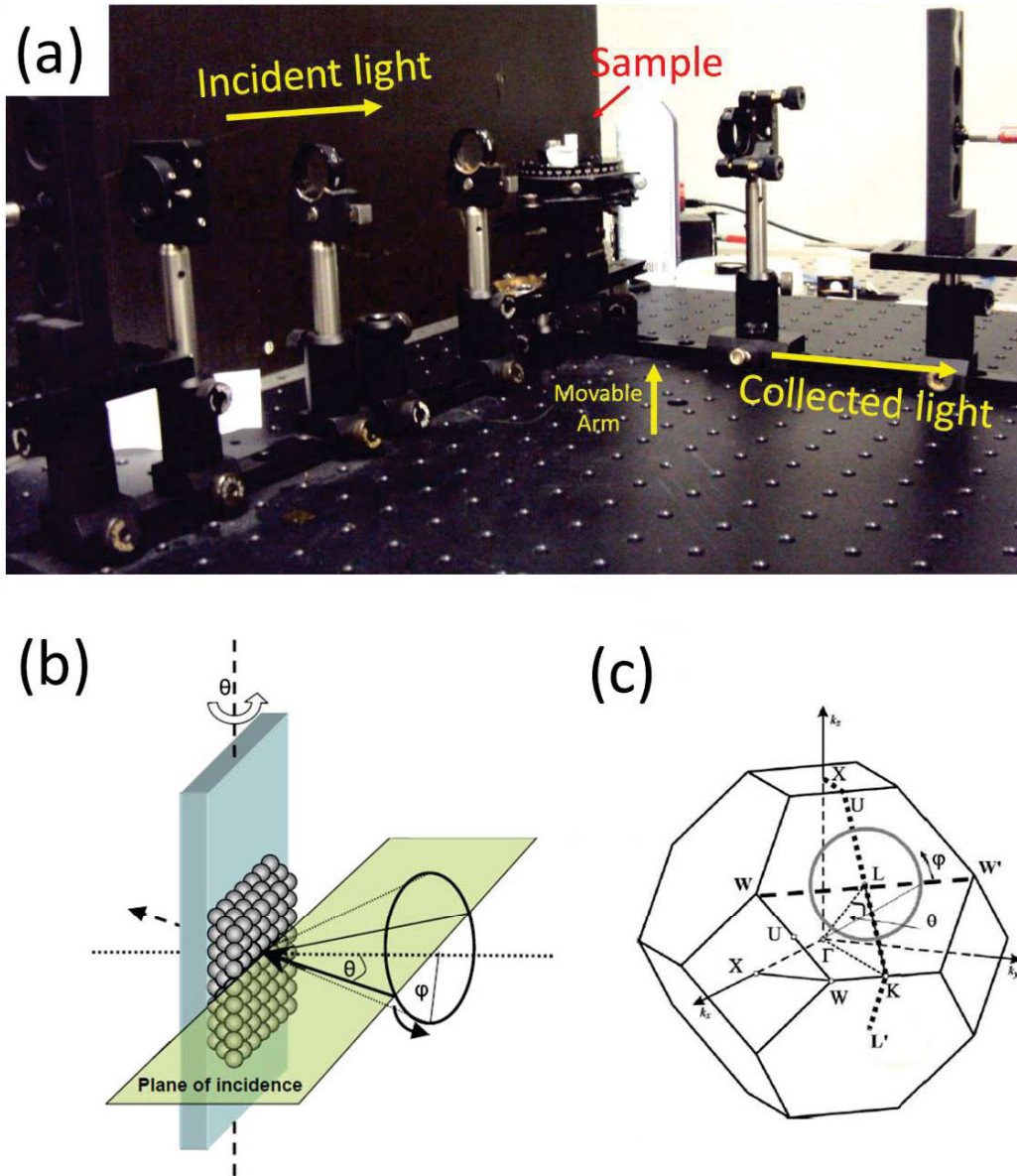


Fig. 3.7 (a) Photograph of spectroscopy setup (b) a schematic of a transmission measurement¹⁵ (c) shows the first Brillouin zone of an fcc lattice, where the dotted line indicates the plane of incidence.¹⁶

3.4.2 Electron Microscopy

Morphology and topology of samples were examined using scanning electron microscopy (SEM), performed on either a Hitachi S-4800 field emission or FEI Quanta 650 FEG high resolution scanning electron microscope. In SEM a focused beam of electrons is raster scanned across the sample surface and due to inelastic collisions within the material secondary electrons are released from the material surface and collected by a detector to produce a magnified image of the surface. The largest density of secondary electrons is ejected by the incident beam before it has a chance to spread within the material and so these have the highest spatial resolution of the signals generated. SEM is therefore best suited for topographical investigations. The sensitivity of secondary electrons to topology and interaction area effects image contrast. For example, a steep slope in topography increases the surface area of the interaction volume between sample and incident electrons, giving off more secondary electrons and therefore appearing brighter. Other information regarding composition for example can also be detected by SEM in the form of backscattered electrons and X-rays.¹⁷ SEM was typically used here to characterize opal templates and visualize the in-plane (top layer) ordering of the samples. It was later used to inspect the order and morphology of the vanadium oxide inverted opal structures and the effects of battery cycling on this morphology. SEM is best suited for features a few hundred nanometres to several microns in size and so for higher resolution imaging transmission electron microscopy (TEM) was conducted at 200 kV using a JEOL JEM-2100. In TEM a beam of focused electrons is transmitted through the sample under investigation and any variations in sample thickness and atomic composition are reflected in the scattering characteristics of the primary electron beam. In bright field imaging, the unscattered and inelastically scattered electrons are collected to form an image on a fluorescent screen or digital camera below the sample, and in

dark field imaging only widely scattered electrons are collected. TEM is the only analytical tool capable of atomic scale imaging.¹⁸

3.4.3 Raman Scattering Spectroscopy

Raman scattering is the inelastic scattering of photons, in the form of monochromatic light usually from a laser, on interaction with molecular vibrations or phonons within a material. Energy of the incident photons can be gained or lost so that the scattered photons are shifted in frequency. The scattering of light with no shift in frequency is known as Rayleigh scattering and Raman scattering with a change in frequency can be grouped into either Stokes or Anti-Stokes scatterings. Stokes scattering occurs when the photon is scattered at lower energies, and Anti-Stokes scattering, occurs for molecules at higher vibrations where the photon is scattered at higher energies and this is the weaker of the two. The change in energy of the photon can therefore be related to the nature of each bond or vibration within a material. Raman spectroscopy is highly selective and can therefore distinguish between molecules and chemical species that are very similar and can identify any changes in bond structures, that may occur for example due to phase changes, or stresses and strains within a crystal. Raman scattering spectroscopy was performed in this work using a Renishaw InVia Raman Spectrometer with a 514 nm 30 mW argon ion laser and spectra were collected using a RenCam CCD camera. The beam was focused onto the samples using a 50× objective lens.

3.4.4 X-ray Diffraction

X-ray diffraction (XRD) is a technique used in determining the atomic and molecular structure of a crystalline material. X-rays are a form of electromagnetic radiation with high energy and short wavelengths and a beam of X-rays incident on a crystalline material will be elastically scattered on interaction with the atomic structure. If Braggs law $n\lambda = 2d\sin\theta$ is

satisfied constructive interference will occur producing diffraction at an angle θ when the interplanar distance d in the crystal is of the order of the wavelength λ . The intensity of the diffracted beams can be measured by a detector producing a series of peaks versus the angle of reflection (2θ) associated with the different atomic planes within the crystal lattice. In this work, XRD was performed on a Philips Xpert PW3719 diffractometer using Cu K α radiation. High angle scans between 10° and 70° were performed on the vanadium oxide materials and the obtained pattern compared with the X'Pert HighScore software database. Samples deposited on stainless steel foil were examined using a monochromator detector in order to reduce effects due to fluorescence of the stainless steel foil under applied X-rays.

3.5 Electrochemical Characterisation

Prior to electrochemical testing the mass of deposited V₂O₅ was recorded by subtracting the substrate mass recorded earlier from the total mass. Electrochemical experiments were performed in half cell arrangements using a two-electrode split cell contained within an Argon atmosphere, as shown in Fig. 3.8 (a). Glass fiber separator was used as received from El-Cell and soaked with ~ 0.1 ml of electrolyte comprising 1 M LiPF₆ in a 1:1 (v/v) mixture of ethylene carbonate and diethyl carbonate. Lithium foil was used as the counter electrode and unless otherwise stated all electrochemical measurements are referenced to Li⁺/Li. The Li foil counter electrode in the form of circular disks of ~ 2 cm in diameter, were scraped until shiny in appearance, using stainless steel tweezers, prior to use. The half-cell was assembled in the split cell as per schematic in Fig. 3.8.

Measurements were recorded using a CHI 660B Potentiostat and a Biologic VSP. In galvanostatic chronopotentiometry testing a constant current is applied to the working electrode and the resulting potential is measured against a reference electrode as a function of time. The constant anodic or cathodic current applied to the electrode causes the electroactive

species to be oxidized or reduced at a constant rate, in the case of a cathode material, such as V_2O_5 used here, the cell is initially in a charged state. Galvanostatic testing was performed on samples in this work within a potential window of 4 V – 1.2 V at constant currents ranging between 30-200 μA . Initially, a negative current is applied to discharge the cell to the lower potential limit (~ 1.2 V), once the lower limit is reached polarity is reversed and the cell is charged under a positive current to the higher potential limit (~ 4 V). This type of galvanostatic testing is used to determine the electrochemical properties of insertion materials,^{19, 20} allowing the total quantity of electricity per unit mass of material available from a fully charged cell or storable in a fully discharged cell to be determined. This specific capacity is calculated from the charge transferred during the discharging (or charging) process in terms of C g^{-1} or mAh g^{-1} . It is also possible to determine the number of Li moles being intercalated into the active material during discharge for each potential. Cyclic voltammetry (CV) testing was also performed at a scan rate of 0.1 m V s^{-1} within the potential window of 4 V – 1.2 V.

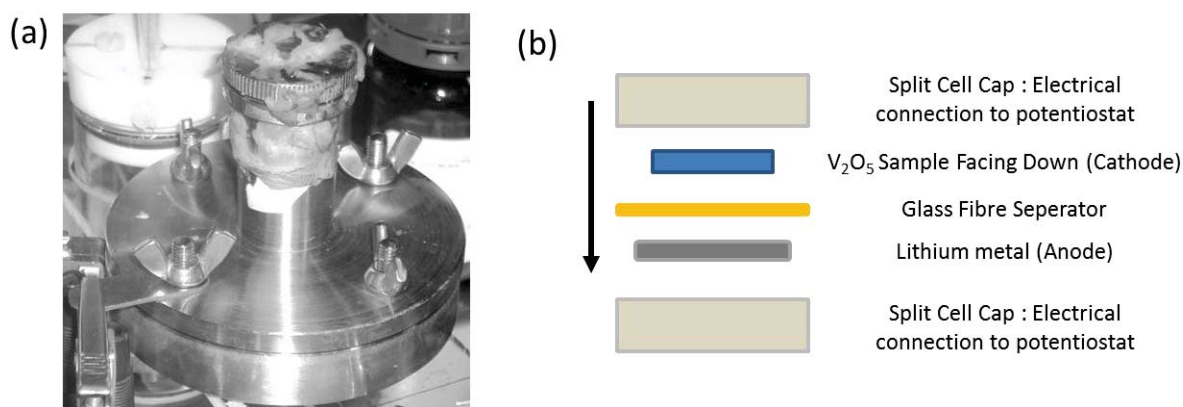


Fig. 3.8 (a) Photograph of the split cell used in electrochemical testing and (b) schematic illustration of the electrode arrangement within the cell.

3.6 References

1. James-Smith, M. A.; Alford, K.; Shah, D. O., A Novel Method to Quantify the Amount of Surfactant at the Oil/Water Interface and to Determine Total Interfacial Area of Emulsions. *J. Colloid Interface Sci.* (2007), **310**, 590-598.
2. Aniansson, E. A. G.; Wall, S. N.; Almgren, M.; Hoffmann, H.; Kielmann, I.; Ulbricht, W.; Zana, R.; Lang, J.; Tondre, C., Theory of the Kinetics of Micellar Equilibria and Quantitative Interpretation of Chemical Relaxation Studies of Micellar Solutions of Ionic Surfactants. *J. Phys. Chem.* (1976), **80**, 905-922.
3. Schroden, R. C.; Balakrishnan, N., *Inverse Opal Photonic Crystals: A Laboratory Guide*. University of Minnesota Materials Research Science and Engineering Center: University of Minnesota, Amundson Hall 491, 421 Washington Ave. SE, Minneapolis, MN 55455, (2001).
4. Lianos, P.; Zana, R., Fluorescence Probe Studies of the Effect of Concentration on the State of Aggregation of Surfactants in Aqueous Solution. *J. Colloid Interface Sci.* (1981), **84**, 100-107.
5. Altissimo, M., E-beam Lithography for Micro-/Nanofabrication. *Biomicrofluidics* (2010), **4**, 026503-1 - 026503-6.
6. Mohammad, M. A.; Muhammad, M.; Dew, S. K.; Stepanova, M., Fundamentals of Electron Beam Exposure and Development. In *Nanofabrication Techniques and Principles* Springer-Verlag/Wien: 2012; Vol. VIII, pp 11-41.
7. Van Tassel, J. J.; Randall, C. A., Mechanisms of Electrophoretic Deposition. *Key Eng. Mater.* (2006), **314**, 167-174.
8. Besra, L.; Liu, M., A Review on Fundamentals and Applications of Electrophoretic Deposition (EPD). *Prog. Mater. Sci.* (2007), **52**, 1-61.
9. Rogach, A. L.; Kotov, N. A.; Koktysh, D. S.; Ostrander, J. W.; Ragoisha, G. A., Electrophoretic Deposition of Latex-based 3D Colloidal Photonic Crystals: A Technique for Rapid Production of High-Quality Opals. *Chem. Mater.* (2000), **12**, 2721-2726.
10. Li, L.; Steiner, U.; Mahajan, S., Improved Electrochromic Performance in Inverse Opal Vanadium Oxide Films. *J. Mater. Chem.* (2010), **20**, 7131-7134.
11. Tong, Z.; Hao, J.; Zhang, K.; Zhao, J.; Su, B.-L.; Li, Y., Improved Electrochromic Performance and Lithium Diffusion Coefficient in Three-dimensionally Ordered Macroporous V₂O₅ Films. *J. Mater. Chem. C* (2014), **2**, 3651-3658.
12. da Silva, D. L.; Delatorre, R. G.; Pattanaik, G.; Zangari, G.; Figueiredo, W.; Blum, R.-P.; Niehus, H.; Pasa, A. A., Electrochemical Synthesis of Vanadium Oxide Nanofibers. *J. Electrochem. Soc.* (2008), **155**, E14-E17.
13. Potiron, E.; Le Gal La Salle, A.; Verbaere, A.; Piffard, Y.; Guyomard, D., Electrochemically Synthesized Vanadium Oxides as Lithium Insertion Hosts. *Electrochim. Acta* (1999), **45**, 197-214.
14. Romanov, S. G.; Bardosova, M.; Povey, I. M.; Pemble, M. E.; Sotomayor Torres, C. M., Understanding of Transmission in the Range of High-order Photonic Bands in Thin Opal Film. *Appl. Phys. Lett.* (2008), **92**, 191106-1 - 191106-3.
15. Khunsin, W.; Amann, A.; Kocher-Oberlehner, G.; Romanov, S. G.; Pullteap, S.; Seat, H. C.; O'Reilly, E. P.; Zentel, R.; Torres, C. M. S., Noise-Assisted Crystallization of Opal Films. *Adv. Funct. Mater.* (2012), **22**, 1812-1821.
16. Khunsin, W.; Kocher, G.; Romanov, S. G.; Sotomayor Torres, C. M. *Improving the Opal-based Photonic Crystals by Noise-assisted Crystallisation*, International

- Workshop and Conference on Photonics and Nanotechnology 2007, Proc. SPIE (2008); pp 67930B-67930B-12.
17. Zhou, W.; Apkarian, R.; Wang, Z.; Joy, D., Fundamentals of Scanning Electron Microscopy (SEM). In *Scanning Microscopy for Nanotechnology*, Zhou, W.; Wang, Z., Eds. Springer New York: 2007; pp 1-40.
 18. Williams, D. B.; Carter, B. C., *Transmission Electron Microscopy: A Textbook for Materials Science*. 2nd. ed. ed.; Springer: (2009).
 19. Pyun, S.-I.; Shin, H.-C.; Lee, J.-W.; Go, J.-Y., Electrochemical Methods. In *Electrochemistry of Insertion Materials for Hydrogen and Lithium*, Springer Berlin Heidelberg: 2012; pp 11-32.
 20. Bard, A. J.; Faulkner, L. R., *Electrochemical Methods: Fundamentals and Applications*. Wiley, (2000).

Chapter 4

Ordered 2D Colloidal Photonic Crystals on Gold Substrates by Surfactant-assisted Fast-rate Dip Coating

Abstract

The formation of monolayer 2D colloidal photonic crystals or templates on gold substrates by dip-coating poly(methyl methacrylate) (PMMA) spheres at fast (mm/min) withdrawal rates is demonstrated. Angle-resolved reflectance measurements confirm 2D light scattering characteristics from fast-rate dip-coated 2D PhCs with a high degree of surface ordering over large areas. The order was confirmed by scanning electron microscopy and is found to be facilitated when the micellar sodium dodecyl sulfate surfactant is used above its critical micelle concentration. The technique can also provide ordered 3D colloidal crystals on gold substrates, where the degree of template ordering is controlled by variation of surfactant concentration, withdrawal rate and sphere concentration. The method allows high surface area and high throughput templating of metallic substrates in 2D or 3D for application in photonics, and as functional material templates for energy storage or sensors.

4.1 Introduction

Photonic crystals¹ (PhCs) most commonly self-assembled from mono-dispersed colloidal particles have been heavily investigated over the past decade due to their wide ranging applications in optics and optoelectronics, and more recently in electrochemical systems such as Li-ion batteries and electrochromics.^{2,3} Now highly adopted as an inexpensive and reliable means for the formation of both two-dimensional (2D) and three-dimensional (3D) ordered structures,^{4,5} they have proven attractive as stable templates for the formation of waveguides,⁶ battery electrodes,^{7, 8} optical switches,⁹ and light-emitting diodes.¹⁰ A variety of well-controlled methods¹¹ can be used to form these arrays, such as spin-coating,¹² drop-casting,¹³ vertical deposition,¹⁴ electrophoretic deposition,¹⁵ dip-coating,^{16, 17} Langmuir Blodgett,¹⁸ layer-by-layer assembly¹⁹ or template directed growth.^{20,21} Advances in materials chemistry, that directly aid the assembly process, is critical for the function of templated 3D materials that are required for photonics, solar energy cells, and metamaterial constructs.

The requirements for near-perfection and zero defect tolerance is less stringent for some applications, particularly for templating materials for energy storage or sensing applications. Dip-coating is a widely used technique for the formation of colloidal 3D templates for functional porous materials, and is typically hindered from higher throughput by a slow rate of withdrawal. The control over evaporation rate and meniscus movement and characteristics are typically employed to ensure a well-ordered multilayer deposit of spheres.¹⁷ In combination with controllable variables, such as temperature,²² ionic strength control via charged colloids²³ or noise-induced stochastic resonance effect,²⁴ the coverage and long-range ordering can be improved, but all methods thus far rely on a very slow rate ($\mu\text{m}/\text{min}$) of withdrawal to achieve thick and uniform opal deposits. This is especially important for template or PhC formation on gold or metallic substrates, and when using large diameter spheres. Langmuir-Blodgett techniques also limit conformal coverage to flat, non-

curved substrates. At faster rates (mm/min), i.e. far from equilibrium condition,²⁴ the spheres lack sufficient time to achieve an ordered crystallization and good adhesion to the substrate. With a non-functionalized silica or polymer sphere, typically used in assembling 3D opal templates, short- and long-range attractive Van der Waals forces²⁵ dominate over repulsive interactions from an electrical double layer. With no natural repulsion to assist ordering, the crystallization inevitably leads to a disordered and patched coverage of opal deposits on the substrate.

Forming opal templates on metallic surfaces, particularly those that can hold surface plasmon polaritons (SPPs) is proving important in advancing light-matter interactions in applications of hybrid plasmonic-photonic crystals and other complex heterostructures that benefit from plasmonic coupling within photonic materials to a metallic substrate. Recent findings suggest that such metal-dielectric interfaces help reduce coupled light-leakage^{26, 27} with potential application in enhanced solar cells, offer improvements in the quality factor for index-guided optical modes by a factor of ~ 10 ,²⁸ and can enhance the light extraction efficiency of light emitters and the performance of photonic crystal based gas sensors^{28, 29}. Furthermore, this hybrid system finds beneficial applications as template for the fabrication of high-power, high rate battery electrodes,⁸ and as substrates for surface-enhanced Raman scattering (SERS) measurements, since the template that is eventually infilled is directly connected to the current collector (substrate).³⁰ However, coating of gold substrates with colloidal crystals is not favourable under ambient conditions. This is because a clean gold substrate, free of any type of contaminants and naturally hydrophilic, quickly turns hydrophobic even with a monolayer of carbonaceous contamination.³¹ As such, when in contact with air as in the most commonly used crystallization methods, the resulting structures are in most cases disordered crystals or amorphous structures.

Here, it is shown that surfactant functionalization of poly(methylmethacrylate) (PMMA) spheres of 700 nm in diameter allows a highly ordered 2D colloidal photonic crystal

(PhC) to form on a gold surface by dip-coating at rates between 20 and 40 times faster than previously reported^{23,24}. In the absence of the surfactant, however, an amorphous, potentially uncorrelated, overlapping opal film is formed. In addition, how to achieve a multi-layer colloidal crystal template with a similar light scattering ability and coverage during coating at slower rate of withdrawal, using a lower concentration of spheres and surfactant is demonstrated. As will be shown, surfactant-assisted dip-coating provides a route to high quality ordered 2D or 3D colloidal crystals or templates directly on metallic surfaces at fast dip-coating rates.

4.2 Results and Discussion

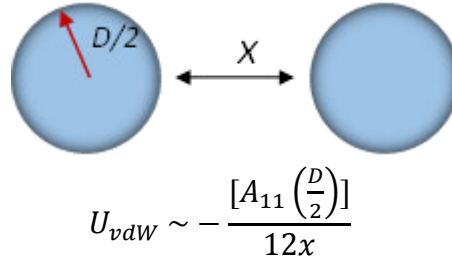
4.2.1 Morphological Effects of Sodium Dodecyl Sulphate Addition

As described in the experimental chapter, section 3.2.2, the amphiphilic anion sodium dodecyl sulphate (SDS), dissociates in water to form charged monomers. At a sufficiently high concentration, greater than the critical micelle concentration (CMC), these monomers orientate their hydrophilic heads towards the polar solute, and their hydrophobic tails group together to form a hydrophobic core. These particles, known as micelles are known to enhance certain aspects of a solution such as the solubility of hydrophobic materials, and alter other aspects such as viscosity and polarity.³² In our experiment, SDS was used at room temperature and at a concentration of 8 mg ml⁻¹, above the theoretical CMC for SDS of 2.3 mg ml⁻¹ (8.0×10^{-3} mol dm⁻³).³³ Fig. 4.1(a) summarizes the dip coating of PMMA PhC monolayers and Fig. 4.1-(1-3) illustrates the possible orientations of the SDS additive either in micellar and/or monomer form. At concentrations below CMC monomers of SDS are known to arrange along the water-air interface (Fig. 4.1-1) but at the concentration level used in our experiment micellization of the SDS within solution takes precedence (Fig. 4.1-2). At this point a transition from monomeric to micellized surfactant occurs at which point both

micelles and monomers co-exist within the solution^{34, 35} and any surfactant above CMC will lead to the formation of micelles.³⁶ These micelles much like SDS does on an oil droplet,³⁷ can settle between or adsorb onto the surface of the PMMA spheres. A combination between the repulsive electrostatic forces induced beyond the Debye screening length in the electrical double layer of the sphere and depletion force kinetics can then cause an ordering of the spheres on removal from solution. Using Derjaguin, Landau, Verwey and Overbeek (DLVO) theory³⁸ and assuming that it is uniquely the SDS in micellular form that causes a separation between otherwise directly touching spheres, it is possible to account for or predict that the inter-sphere separation is approximately a single micelle thick between the spheres at maximum packing using SDS just above CMC. The basis for this model is to determine if Derjaguin, Landau, Verwey and Overbeek (DLVO) theory can predict if single or multiple layers of spherical micelles form between SDS-functionalized PMMA spheres in water that accounts/predicts for the inter-sphere separation when deposited as an ordered assembly. Several assumptions were made in order to determine an approximation for this, firstly the basic assumption is taken that SDS exists in micellular form between the PMMA spheres (after removal from solution). The analysis assumes that only SDS causes a ‘gap’ between two spheres that would ordinarily touch, so that the distance between the sphere centres $d = 2(D/2)$, where d is the centre-to-centre distance between two identical spheres and D is the diameter of a sphere, increases to $d' = 2(D/2) + 2(2r_m)$, where r_m is the radius of a SDS micelle. It is also assumed that colloidal stability is present due to the balance of van der Waals (vdW) attractive forces and electrostatic and steric repulsions caused by the presence of micellular SDS. With an SDS-monomer-functionalised PMMA surface in water, the colloidal sphere is a sterically stabilised colloid. At the meniscus, just prior to deposition, the balance of forces is guided by evaporative self-assembly. The evaporation step is not assumed here to alter the final inter-sphere distance found at

maximum flocculation of the colloid in the SDS-containing solution above the SDS CMC.

The vdW pair potential describing interactions between two hard spheres separated by a distance x can be simplified from the full interaction pair potential in the case where spheres are close, to:



$$U_{vdW} \sim - \frac{[A_{11} \left(\frac{D}{2}\right)]}{12x}$$

where A_{11} is the Hamaker constant between PMMA sphere $\sim 6.3 \times 10^{-20}$ J (~ 15 k_BT). PS has a similar value of $6.5-9 \times 10^{-20}$ J.³⁹

In the case of SDS functionalised spheres, x is the distance between two sphere surfaces, i.e. thickness of film caused by micelles present, i.e. $x = \alpha r_m$, where $\alpha \in R$. If we can estimate x , it will be some factor of r_m and thus we can estimate the number of micelles between spheres. The electrostatic repulsion of SDS coated PMMA, which are not considered as charged spheres once SDS-functionalized, is given by

$$2\pi\epsilon\epsilon_0 \left(\frac{D}{2}\right) \psi_\delta e^{(-\kappa x)}$$

where ϵ is the relative permittivity of PMMA $\sim 78-82 \epsilon_0$ (value of 80 used), ψ_δ is surface (zeta) potential, usually $\geq \pm 30$ mV for a stable solution (value of -29.5 mV used),⁴⁰ and κ^{-1} is the Debye-Hückel screening length or double layer thickness given by

$$\kappa^{-1} = \sqrt{\frac{(2z^2 e^2 N_A C_0)}{(\epsilon\epsilon_0 k_B T)}}$$

where z is the net charge ($z = 1$ for a single negative charge of an SDS molecule in solution, and C_0 is its concentration ($> \text{CMC}$ in this case). More simply, it can be approximated quite well by $\kappa^{-1} = 0.3041/(\text{mod}(z)\sqrt{C_0}) \sim 3.4$ nm using C_0 as the SDS concentration used, e.g. 8×10^{-3} mol. The exponential can be expanded through Maclaurin series and limited to its first order, thus the balance of electrostatic/steric and vdW forces is

$$\frac{A_{11}\left(\frac{D}{2}\right)}{12x} = 2\pi\epsilon\epsilon_0\left(\frac{D}{2}\right)\psi_0^2(1 - \kappa x)$$

Rearranging, and obtaining the required root of x ,

$$x \sim \frac{1}{2\kappa} \pm \left[\frac{\sqrt{1 - 4\kappa N}}{2\kappa} \right],$$

where

$$N = \frac{A_{11}D}{24\pi\epsilon\epsilon_0 D\psi_0^2} \quad (N = 1.356 \times 10^{-9} \text{ JmF}^{-1}\text{V}^{-1})$$

$$x = 1.7 \pm 1.3 \times 10^{-9} \text{ m.}$$

The diameter of an SDS micelle is fundamentally given by 3.5 to 4 nm corresponding to estimated micelle radius of approximately 1.75 to 2 nm^{41, 42}. For either prolate or oblate shaped micelles, the average diameter is here assumed to account for either extensions beyond spherical at 298 K, and $r_m \sim 1.8$ nm. Essentially, the model predicts a film that is approximately a single micelle thick between the spheres at maximum packing for concentrations just above CMC.

The deposition was performed with a fast withdrawal rate of 1 mm/min, and SEM confirmed the resulting hexagonally packed monolayer of spheres. The sphere deposit exhibits large-scale surface coverage (over ~ 1 cm² of the substrate) of ordered domains (Fig. 4.1 (c)), a significant improvement over those achieved in the absence of SDS (Fig. 4.1(b)) which were not only entirely disordered, but also displayed weak adhesion to the gold

substrate. Micelle formation is expected and examinations of initial coagulation concentrations of SDS⁴³ show that the formation of a viscous mixture is possible and corresponds with the observation of improved order in deposits formed in the presence of micelles.

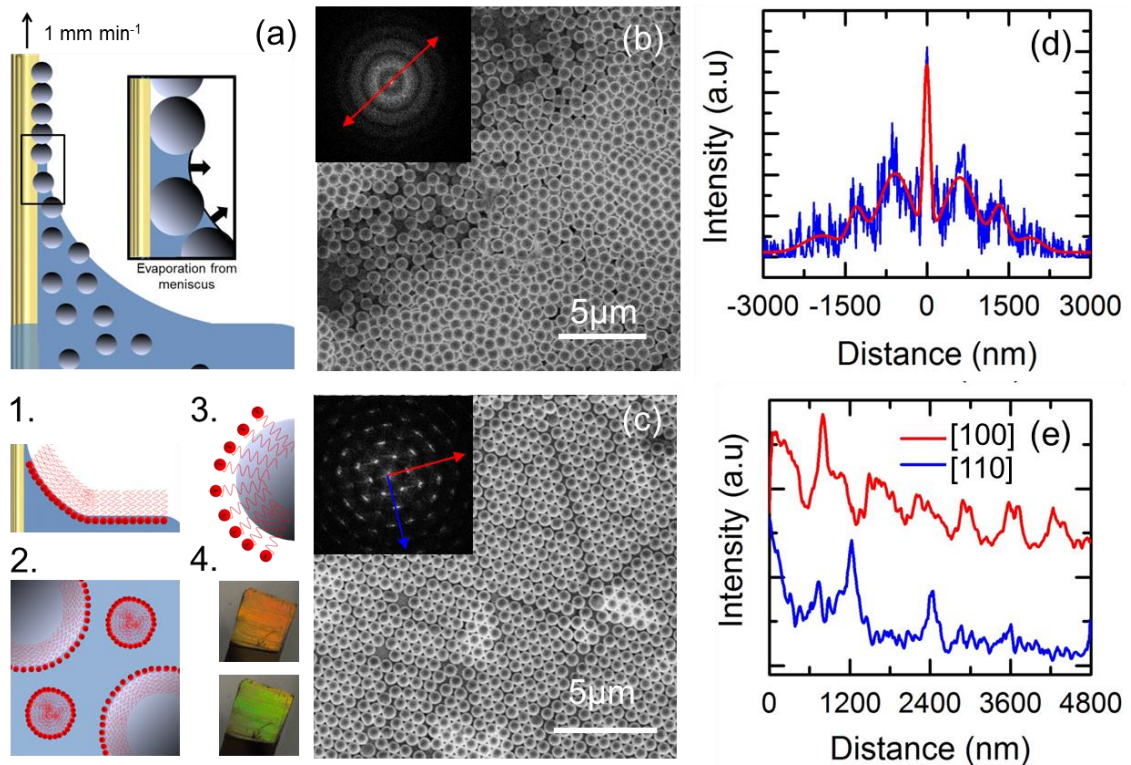


Fig. 4.1 (a) Diagram depicting the deposition mechanism of opal spheres by dip coating at a withdrawal rate of 1 mm/min. (1-4) Schematic representation of micellar SDS and functionalized PMMA and optical images of the angle-dependent scattering seen from PhC deposits formed using SDS. (b) SEM image and corresponding FFTs showing a 2D photonic glass monolayer (without SDS) and (c) a 2D monolayer photonic crystal (with SDS) and (d) and (e) are the FFT intensity profiles from (b) and (c) respectively. Profiles in (e) were acquired along the [100] and [110] directions, corresponding to the ΓX and ΓL directions in the Brillouin zone of a 2D hexagonal lattice.

Without SDS, a monolayer is demonstrated to form, but does so as an amorphous photonic glass (Fig. 4.1(b)). These deposits are also characterized by patchy coverage and regions of complete disorder. With SDS surfactant, the monolayer of 2D colloidal crystals can form from the fast rate (1 mm/min) of withdrawal with order and quality commensurate with the top surface ordering of multi-layered (3D) deposits reported previously for much slower

rates ($\mu\text{m}/\text{min}$).^{24, 44} In the present case, the SDS lowers the surface tension causing a lengthening and thinning of the meniscus,⁴⁵ which is believed to promote the adhesion and crystallization of the spheres at the fast withdrawal rate. Local lattice distortions or vacancy defects in the 2D order (see Fig. 4.1(c)) can be conveniently traced back to particle size distribution and shrinkage of the spheres during the drying process, a common cause of cracks⁴⁶ usually observed in 3D PhCs by colloidal self-assembly.

In addition to lattice distortion, lattice misalignments in the monolayer 2D PhC are found to be caused mainly by the line dislocations stemming from anomalies in the close-packed 2D assembly. In particular, for this monolayer-type structure, these line dislocations merge to form the boundaries for the individual domains. The domain structure, however, remains well ordered and few rotational boundaries are found. The degree of order, which is shown by the effectively long-range polycrystalline order observed by hexagonal pattern in FFTs of the assembly (Fig. 4.1(c)), is very high for a dip coating rate faster than typically used in dip-coating or Langmuir-Blodgett trough deposition. The 2D photonic glass monolayers (Fig. 4.1(b)), while disordered on larger length scales, do contain some degree of small domains of frustrated hexagonal order with close-packed disorder surrounding these domains, evidenced by the spots in the FFT pattern (Fig. 4.1(b)), that is largely characterized by diffuse rings symptomatic of a disordered (but not polycrystalline) arrangement.

4.2.2 Optical Characterisation

The unique optical characteristics of opal-type photonic crystal templates^{47, 48} allow for the investigation of their structural quality (assembly).^{49, 50} Well-ordered 3D PhC structures show a specific photonic band-gap (PBG), a feature which is observed at shorter wavelengths in the case of hexagonally ordered 2D opal PhCs, i.e. at $\lambda \approx D$, where D is the diameter of the spheres. These minima have been associated with excitation of 2D PhC optical eigenmodes that propagate along the plane of the monolayer opal.^{27, 51} It should be noted that the colloidal

crystals with thickness of a few monolayer are referred to as principally 2D structures, due to the absence of appreciable 3D-related reflectance maxima obtained from the sample. In general, reflectance from a true 3D opal is related to its film thickness via Bragg attenuation length. In opals assembled from PMMA spheres of 700 nm in diameter, used in this experiment, the Bragg attenuation length is of the order of 6.5 to 7 μm or approximately 12 monolayers of spheres.⁵² Furthermore, the presence of the reflectance maxima, i.e., photonic bandgap, quickly degrades in a disordered sample. It has been demonstrated with PMMA colloidal crystals that a defect vacancy of only 5% reduces the systems correlation length to a distance of $3D$, where D is the sphere diameter, resulting in the optical spectra being a simple incoherent scattering sum of individual Mie scatters without appreciable coherent PBG effect.⁵³ In our case of uncorrelated overlapping of 2D colloidal layers as seen in Fig. 1b, it is probably likely that the short correlation length due to large amount of defect vacancy present in the sample is the limiting factor to the absence of 3D optical feature.

The resonant scattering, thus formed by the coupling of the incident light with the guided mode of the 2D PhCs, provides an efficient and convenient means to characterize the 2D coverage and order within 2D opal films formed on a gold substrate at high drawing rate. The 2D PhCs, with thickness being far below the Bragg attenuation length, showed no three-dimensional order, as is evident by the lack of a photonic band gap within the expected range discussed above. Specifically, the corresponding 3D opal (111) plane stop band would appear at $\sqrt{8/3} D \sqrt{g\bar{\epsilon}_s + (1-g)\bar{\epsilon}_f} \approx 1.6 \mu\text{m}$, where $\bar{\epsilon}_s$ and $\bar{\epsilon}_f$ are the permittivity of PMMA and air between the spheres, and g is the maximum packing factor of $g = \pi/3\sqrt{2}$ for the fcc lattice. The 2D monolayer opal, however, does scatter light in the visible range (at $\lambda \approx D$) and can be conveniently detected with a Si CCD detector. Fig. 4.2(a) shows the angle-resolved diffraction measurement obtained at angular increments of 5° for light incident at 60° . It should be noted that the Fabry-Perot resonances are not observed from a single PhC layer as

they are typically weaker and broader than diffraction contributions. Additionally, resonances from plasmonic interactions from the gold surface and their coupling to the 2D PhC, typically observed at wavelengths less than the sphere diameter are not observed, which is probably due to non-corrugated gold surface and/or inefficient excitation of SPP at large incident angle.²⁷ It is worth noting, however, that the lack of SPP excitation facilitates direct analysis of light scattering from the 2D monolayer colloidal crystals without being obscured by dispersion and broadening of scattering spectra due to the presence of a SPP.⁵⁴

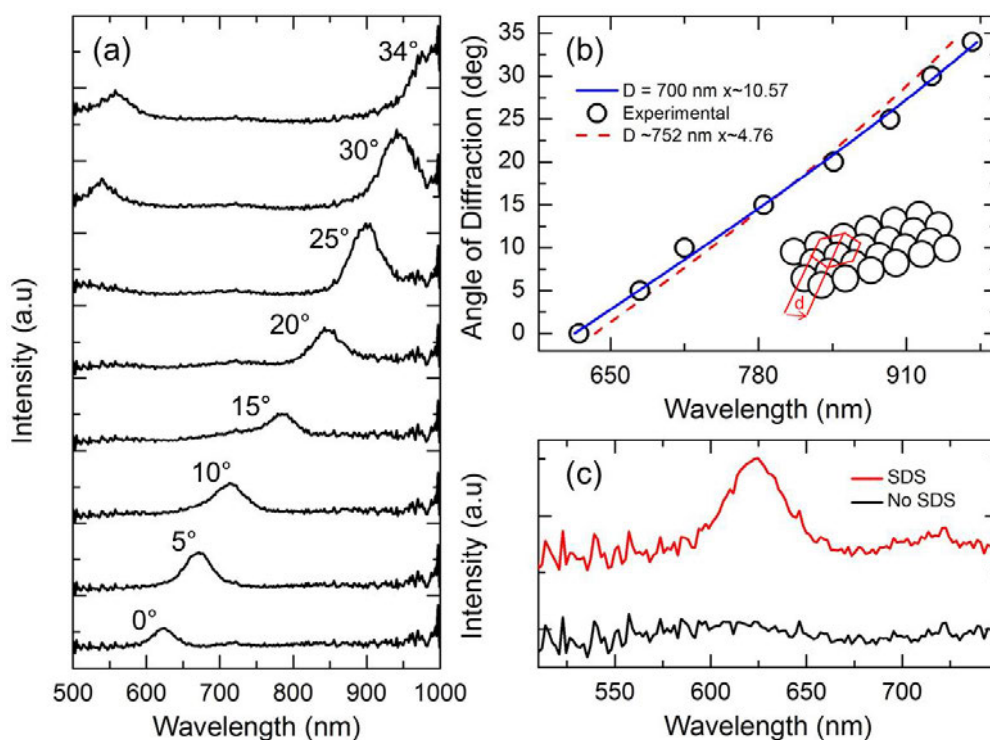


Fig. 4.2. Dispersion characterisation (a) Angle-resolved scattering for 5 wt% PMMA spheres with 8 mg ml^{-1} SDS at an incident angle of 60° . (b) The dispersion of the peak position compared with the theoretical dispersion and the schematic representation of the grating groove d , and (c) Light scattering normal to the surface (i.e. angle of diffraction = 0°) for light incident at 60° .

Confirmation of the structure of the 2D colloidal crystal formed is provided by analysis of the angle-resolved diffraction. The angular dispersion was fitted to the planar

grating equation, $\lambda = d[\sin(\alpha) + \sin(\beta + x)]$, where α is the angle of incidence, β is the angle of diffraction, d is the effective grating groove, which in this case corresponds to $\frac{\sqrt{3}}{2}D$, the half period of the trigonal lattice for the wave vector of incident light propagating along the ΓK direction in the Brillouin zone of a 2D hexagonal lattice. This is schematically represented in Fig. 1.2(b), where D is the sphere diameter, and x is a free constant. Fig. 4.2(b) shows the theoretical dispersion (blue line) calculated using the equation above with the nominal diameter of 700 nm for the spheres, as determined by SEM and dynamic light scattering, as an input parameter. The fitting procedure gives $x \sim 10.57$, the result of which is plotted against the experimental dispersions (black circles) taken from the experimental spectra shown in Fig. 4.2(a). The red dashed line indicates the ‘best fit’ theoretical dispersion i.e. when the diameter of the spheres is not fixed at 700 nm. This calculation suggests a slight increase in the diameter of the spheres which could be related to the SDS addition and its presence around the spheres.

Fig. 4.2(c) shows the light scattering behaviour for a fast-rate dip-coated 2D PhC monolayer formed with SDS surfactant at a diffraction angle of 0° , i.e. normal to the substrate, for light incident at 60° , and is compared to the same response for the photonic glass deposit in the absence of SDS (black line). In this latter case, no 2D scattering was observed. The scattering spectra of the PhC monolayer (red line) formed in the presence of SDS exhibited well-defined scattering characteristic of a 2D colloidal crystal at a reduced wavelength of $D/\lambda = 1.13$, close to the scattering resonance condition for the monolayer opal. The disordered monolayer breaks the Bragg scattering condition, causing additional background scattering components, which can be observed as a broadband, low-intensity peak shown in Fig. 4.2(c). The profile does follow somewhat the diffraction of the ordered 2D opal and is likely due to the small degree of ordering within several domains (see Fig. 4.1(b)).

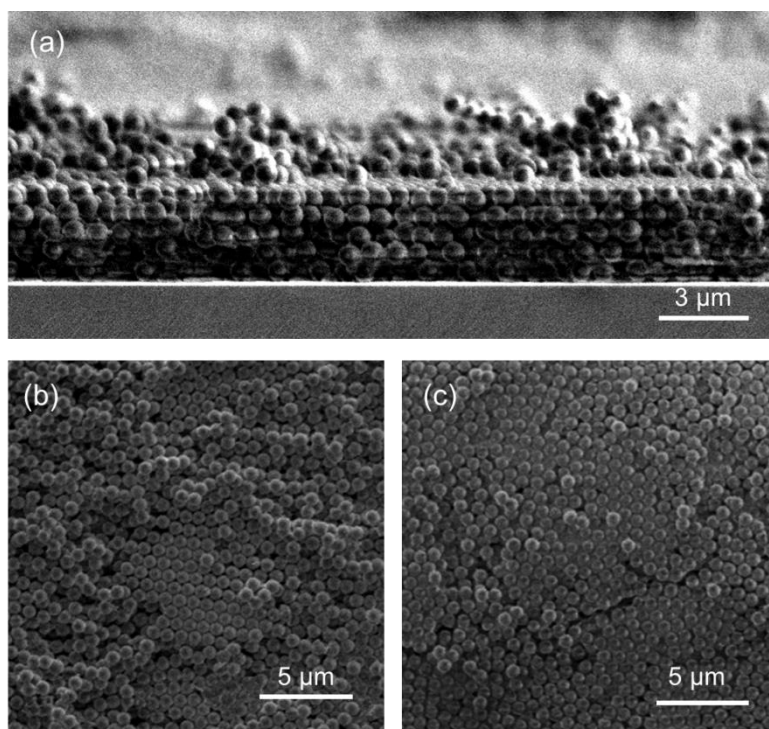


Fig. 4.3 SEM images the sample obtained when 5 wt% spheres with 8 mg ml^{-1} SDS is dip coated with a slow rate of withdrawal of $\sim 1 \text{ mm/hr}$, a multilayer sample is obtained as seen in (a) compared with the monolayer achieved with fast rate, as well while some order is evident in (b) a top layer of disorder is clearly visible and irregular clumping is also observed, in some areas as in (c) the effects of the large concentration of SDS is more visible than with the fast rate sample, thick clumped dispostis are observed with varying order.

Controlled experiments were performed at a slow rate of withdrawal, with and without SDS. In absence of SDS, no colloidal crystal formation on the gold substrate was observed. This is likely due to the difficulty of assembling on gold surfaces for PMMA spheres as mentioned above, greater than that observed for the faster rate of withdrawal, which is probably due to spontaneous fixing of the spheres onto the substrate by the fast advancing meniscus.⁵⁵ Dip coating experiments with the addition of SDS, identical to that reported in Fig. 4.1, but at a slow rate of $\sim 1 \text{ mm/hr}$ comparable to that reported by Khunsin *et al.*²⁴ produced a sample of patched coverage and poor order, the thickness of which varies across several areas of the sample to a greater extent than the fast rate sample (compare Fig. 4.1(c) and Fig. 4.3). Slower withdrawal from the same sphere-containing solution did not induce an

ordered opal monolayer. However, a reduction in sphere concentration by half with a parallel reduction in SDS concentration to 4 mg ml^{-1} , i.e. maintaining the same ratio of spheres to SDS as the fast rate sample, but still above critical micelle concentration, resulted in a better quality PhC structure, as shown in Fig. 4.4(b). The morphology is comparable to the monolayer formed at 1 mm/min with twice the concentration of spheres and SDS (Fig. 4.1(c)).

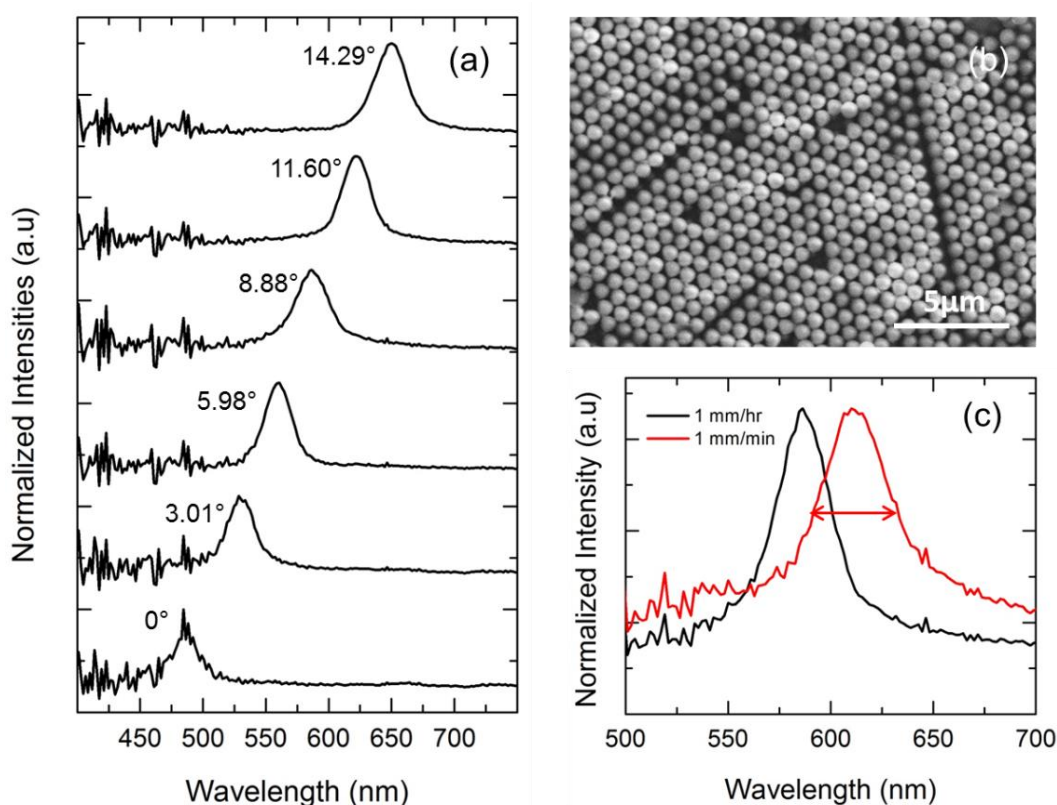


Fig. 4.4 (a) Angle resolved scattering from the 2D PhC formed from 2.5 wt% PMMA spheres with 4 mg ml^{-1} SDS dip coated at a slow rate ($\sim 1 \text{ mm/hr}$). Light was incident at 45° . (b) SEM image of the top surface of the 2D PhC. (c) Scattering at an angle of 8.88° for light incident at 45° for samples formed at fast rate with 5 wt% spheres and 8 mg ml^{-1} SDS (red), and for a sample formed at the slow rate where the concentrations of spheres and SDS are halved (black).

Scattering data acquired with light incident at 45° and a similar angular shift in peak position was measured indicating the presence of 2D order within the template, as shown in Fig. 4.4(a). A comparison of the scattering from the fast and slow rate 2D PhCs for light

incident at the same angle 45° is shown in Fig. 4.4(c), where the scattering peak for the fast rate sample is located at a wavelength of $D/\lambda = 1.13$, whereas that of a deposit formed with half the concentration of spheres and SDS is located at $D/\lambda = 1$. It is noted that the scattering peak for the fast rate sample is $\sim 15\%$ broader than the 2D PhC formed at the slow rate, which indicates a lesser degree of order in the fast rate sample. This might be due to larger crystal lattice distortion from dislocations and/or concentration gradients, i.e. non-uniform distribution of the spheres, and contributions from wider spaces between spheres in the case of fast rate sample with double the concentration of spheres and SDS.⁵⁶ It is noted, however, that the PhC achieved for the slow rate with reduced concentration is not a single monolayer of spheres as seen for the faster rate sample; the increase in thickness while not sufficient to produce a 3-dimensional structure provides an environment that is more conducive to crystallization of the spheres,²⁴ leading to extended long-range order for this slow rate sample and explains the lower relative bandwidth ($\Delta\lambda/\lambda$) of 0.052 compared with that of 0.067 for the fast rate dip-coated PhC (Fig. 4.4(c)).

The dispersion of the scattering maximum obtained from both samples show excellent agreement with calculated 2D diffraction from grating theory, as seen from the line fits in Fig. 4.5 (a) and 4.5 (b). However, two important differences between the two samples in the absolute position (wavelength) of the scattering maxima and the width of the resonances should be noted. The larger diffraction wavelengths, in the case of the slow rate sample, is due to two contributing factors: (1) larger effective diameter due to higher SDS concentration which leads to a thick coating of micellar SDS around the spheres (see Fig. 4.6), and (2) the increase in effective refractive index of the inter-sphere medium (which is nominally air) due to the coating of SDS. Fig. 4.5 (c) plots the dispersions of the ratio of the Full-Width Half-Maximum (FWHM) to the resonant wavelengths of the diffraction peaks as a function of diffraction angle for both the fast-rate sample, and the slow-rate sample. The lower overall ratio, i.e. narrower diffraction peaks, indicates less scattering from imperfection in the crystal

lattice and thus implies the improved order of the slow rate sample compared to the fast rate sample. Along the same line of the above arguments, we believe that the slow rate sample possesses better ordering due to a thinner and more uniform coating of SDS on the surface of the spheres than the fast rate sample. Further work into the optimum SDS concentration for the deposition of PMMA spheres on gold substrates is undergoing and will be reported elsewhere.

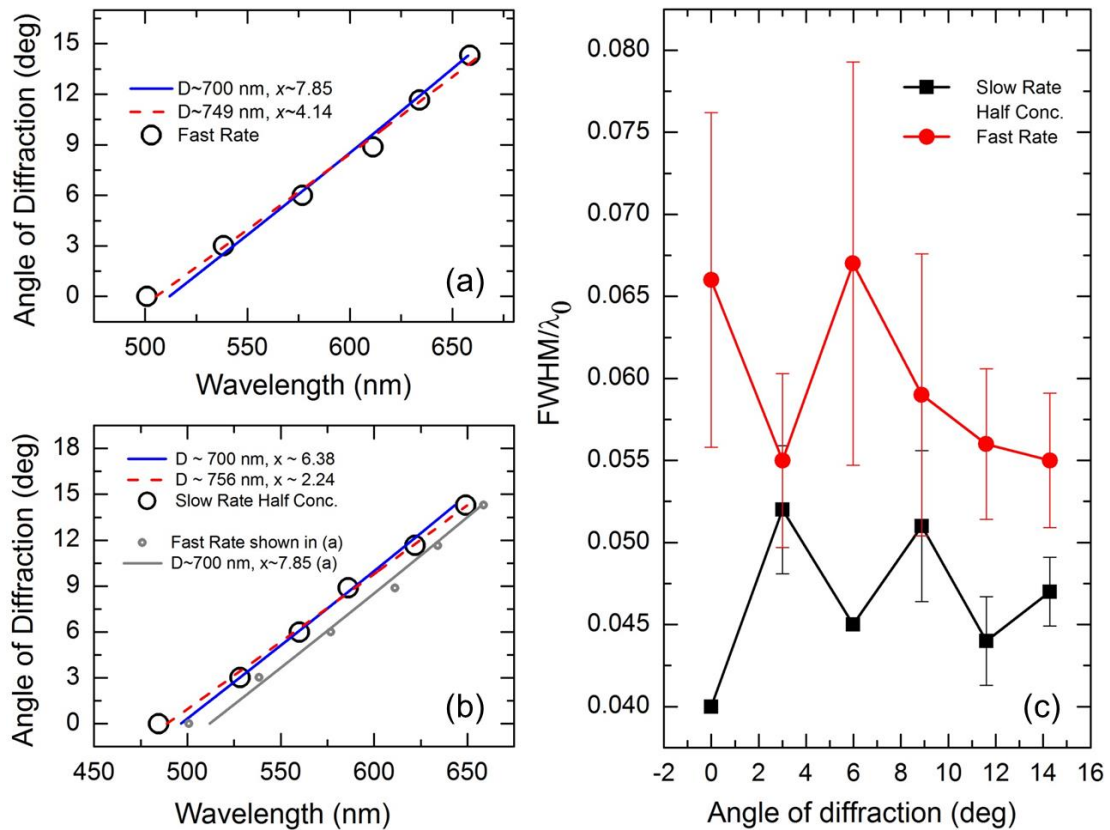


Fig. 4.5 (a) The dispersion relation for a sample made using 5 wt% PMMA spheres and 8 mg ml⁻¹ SDS withdrawn at a fast rate (~1 mm/min) when light is incident at 45°. (b) The dispersion relation for the scattering spectra shown in Fig. 4a (2.5 wt% PMMA spheres and 4 mg ml⁻¹ SDS), the grey line shows the plot in (a) again for comparison, it is proposed that the variation is due to the increased SDS concentration and (c) shows a plot of the ratio of the resonant wavelength to the FWHM for both samples.

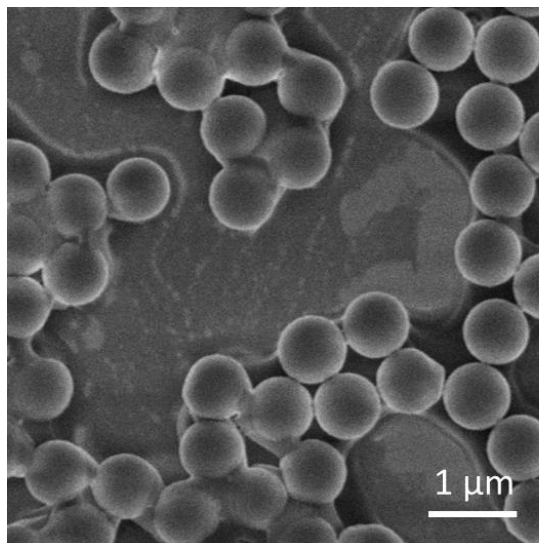


Fig. 4.6 Coating of spheres in an SDS residue at the high concentrations used is seen in certain areas of the sample which could be leading to lattice mismatches observed in the dispersion relationships.

4.3 Conclusion

To conclude, the fast-rate dip coating has been successfully demonstrated in the formation of an ordered 2D monolayer colloidal crystal of polymer (PMMA) spheres on a gold substrate when a surfactant such as SDS is mixed into the sphere solution *prior* to dipping. For the same concentration of spheres and SDS as is used when dip-coating at the faster rate, assembly of polymer (PMMA) spheres as a colloidal 2D PhC monolayer on gold coated silicon is less effective at a slow rate of withdrawal and typically results in a disordered monolayer. However, a reduction in the concentration of both spheres and SDS by 50% improves the deposition at a slow rate as evidenced by angle-resolved light scattering measurements, surpassing that obtained with the fast rate deposition. The findings demonstrate that higher quality 2D colloidal crystals of polymer spheres can be formed on gold substrates with the addition of SDS surfactant, when dip-coating at fast or slow rates, provided concentrations are controlled (in this case lowered) at slower rates, thus overcoming the difficulty associated with the hydrophobicity of the gold substrate at ambient conditions.

Our result may pave the way for the development of hybrid 2D and/or 3D opal photonic-plasmonic structures for applications in high-sensitivity bio- and chemical sensors, and as high-throughput templates on conductive surfaces for functional porous electrodes for energy storage/batteries, and as substrates for SERS experiments. Furthermore, the method can particularly be adapted to deposition methods of ordered monolayers that are typically limited to slower withdrawal or deposition rates.⁵⁷ The ability to control the assembled of 2- and 3D colloidal crystals may also aid the controlled evaporative self-assembly of binary or tertiary colloidal structures and photonic crystals composed of blends of templates and active emitters or absorbers, and do so on metallic surfaces that hold surface plasmon excitations for a wide variety of optical applications. Advances in template fabrication directly on metallic, conductive substrates at higher fabrication rates, without a reduction in ordering, are also particularly useful for sensing and energy storage architectures such as fast charging rate high power Li-ion microbatteries and related structures that rely on controlled porosity in the active materials.

4.4 References

1. Stein, A.; Schrodin, R. C., Colloidal Crystal Templating of Three-dimensionally Ordered Macroporous Solids: Materials for Photonics and Beyond. *Curr. Opin. Solid State Mater. Sci.* (2001), **5**, 553-564.
2. Galisteo-López, J. F.; Ibasate, M.; Sapienza, R.; Froufe-Pérez, L. S.; Blanco, Á.; López, C., Self-Assembled Photonic Structures. *Adv. Mater.* (2011), **23**, 30-69.
3. Stein, A.; Wilson, B. E.; Rudisill, S. G., Design and Functionality of Colloidal-crystal-templated Materials-Chemical Applications of Inverse Opals. *Chem. Soc. Rev.* (2013), **42**, 2763-2803.
4. López, C., Materials Aspects of Photonic Crystals. *Adv. Mater.* (2003), **15**, 1679-1704.
5. Braun, P. V., Materials chemistry in 3D templates for functional photonics. *Chem. Mater.* (2013), 277-286.
6. Lu, L.; Joannopoulos, J. D.; Soljačić, M., Waveguiding at the Edge of a Three-Dimensional Photonic Crystal. *Phys. Rev. Lett.* (2012), **108**, 243901.
7. Sakamoto, J. S.; Dunn, B., Hierarchical Battery Electrodes Based on Inverted Opal Structures. *J. Mater. Chem.* (2002), **12**, 2859-2861.
8. Zhang, H.; Yu, X.; Braun, P. V., Three-dimensional Bicontinuous Ultrafast-Charge and -Discharge Bulk Battery Electrodes. *Nat. Nanotechnol.* (2011), **6**, 277-281.
9. Liu, Y.; Qin, F.; Wei, Z.-Y.; Meng, Q.-B.; Zhang, D.-Z.; Li, Z.-Y., 10 fs Ultrafast All-optical Switching in Polystyrene Nonlinear Photonic Crystals. *Appl. Phys. Lett.* (2009), **95**, 131116.
10. Yablonovitch, E., Photonic band-gap structures. *J. Opt. Soc. Am. B* (1993), **10**, 283-295.
11. von Freymann, G.; Kitaev, V.; Lotsch, B. V.; Ozin, G. A., Bottom-up Assembly of Photonic Crystals. *Chem. Soc. Rev.* (2013), **42**, 2528-2554.
12. Pichumani, M.; Bagheri, P.; Poduska, K. M.; Gonzalez-Vinas, W.; Yethiraj, A., Dynamics, Crystallization and Structures in Colloid Spin Coating. *Soft Matter* (2013), **9**, 3220-3229.
13. Velev, O. D.; Furusawa, K.; Nagayama, K., Assembly of Latex Particles by Using Emulsion Droplets as Templates. 1. Microstructured Hollow Spheres. *Langmuir* (1996), **12**, 2374-2384.
14. Jiang, P.; Bertone, J. F.; Hwang, K. S.; Colvin, V. L., Single-Crystal Colloidal Multilayers of Controlled Thickness. *Chem. Mater.* (1999), **11**, 2132-2140.
15. Rogach, A. L.; Kotov, N. A.; Koktysh, D. S.; Ostrander, J. W.; Ragoisha, G. A., Electrophoretic Deposition of Latex-based 3D Colloidal Photonic Crystals: A Technique for Rapid Production of High-Quality Opals. *Chem. Mater.* (2000), **12**, 2721-2726.
16. Deleuze, C.; Sarrat, B.; Ehrenfeld, F.; Perquis, S.; Derail, C.; Billon, L., Photonic Properties of Hybrid Colloidal Crystals Fabricated by a Rapid Dip-coating Process. *Phys. Chem. Chem. Phys.* (2011), **13**, 10681-10689.
17. Dimitrov, A. S.; Nagayama, K., Continuous Convective Assembling of Fine Particles into Two-dimensional Arrays on Solid Surfaces. *Langmuir* (1996), **12**, 1303-1311.
18. Bardosova, M.; Hodge, P.; Pach, L.; Pemble, M. E.; Smatko, V.; Tredgold, R. H.; Whitehead, D., Synthetic Opals made by the Langmuir–Blodgett Method. *Thin Solid Films* (2003), **437**, 276-279.
19. Oh, J. R.; Moon, J. H.; Yoon, S.; Park, C. R.; Do, Y. R., Fabrication of Wafer-scale Polystyrene Photonic Crystal Multilayers *via* the Layer-by-layer Scooping Transfer Technique. *J. Mater. Chem.* (2011), **21**, 14167-14172.

20. Van Blaaderen, A.; Ruel, R.; Wiltzius, P., Template-Directed Colloidal Crystallization. *Nature* (1997), **385**, 321-324.
21. Jin, C.; McLachlan, M. A.; McComb, D. W.; De La Rue, R. M.; Johnson, N. P., Template-Assisted Growth of Nominally Cubic (100)-Oriented Three-Dimensional Crack-Free Photonic Crystals. *Nano Lett.* (2005), **5**, 2646-2650.
22. Fu, Y.; Jin, Z.; Liu, Z.; Liu, Y.; Li, W., Self-assembly of Colloidal Crystals from Polystyrene Emulsion at Elevated Temperature by Dip-drawing Method. *Mater. Lett.* (2008), **62**, 4286-4289.
23. Tan, K. W.; Koh, Y. K.; Chiang, Y.-M.; Wong, C. C., Particulate Mobility in Vertical Deposition of Attractive Monolayer Colloidal Crystals. *Langmuir* (2010), **26**, 7093-7100.
24. Khunsin, W.; Amann, A.; Kocher-Oberlehner, G.; Romanov, S. G.; Pullteap, S.; Seat, H. C.; O'Reilly, E. P.; Zentel, R.; Torres, C. M. S., Noise-Assisted Crystallization of Opal Films. *Adv. Funct. Mater.* (2012), **22**, 1812-1821.
25. Chen, J.; Anandarajah, A., Van der Waals Attraction between Spherical Particles. *J. Colloid Interface Sci.* (1996), **180**, 519-523.
26. Romanov, S. G.; Korovin, A. V.; Regensburger, A.; Peschel, U., Hybrid Colloidal Plasmonic-Photonic Crystals. *Adv. Mater.* (2011), **23**, 2515-2533.
27. Romanov, S. G.; Vogel, N.; Bley, K.; Landfester, K.; Weiss, C. K.; Orlov, S.; Korovin, A. V.; Chuiko, G. P.; Regensburger, A.; Romanova, A. S.; Kriesch, A.; Peschel, U., Probing Guided Modes in a Monolayer Colloidal Crystal on a Flat Metal Film. *Phys. Rev. B* (2012), **86**.
28. Yu, X. D.; Shi, L.; Han, D. Z.; Zi, J.; Braun, P. V., High Quality Factor Metalodielectric Hybrid Plasmonic-Photonic Crystals. *Adv. Funct. Mater.* (2010), **20**, 1910-1916.
29. López-García, M.; Galisteo-López, J. F.; Blanco, A.; Sánchez-Marcos, J.; López, C.; García-Martín, A., Enhancement and Directionality of Spontaneous Emission in Hybrid Self-Assembled Photonic-Plasmonic Crystals. *Small* (2010), **6**, 1757-1761.
30. Kubo, S.; Gu, Z.-Z.; Tryk, D. A.; Ohko, Y.; Sato, O.; Fujishima, A., Metal-Coated Colloidal Crystal Film as Surface-Enhanced Raman Scattering Substrate. *Langmuir* (2002), **18**, 5043-5046.
31. Smith, T., The Hydrophilic Nature of a Clean Gold Surface. *J. Colloid Interface Sci.* (1980), **75**, 51-55.
32. Ruiz, C. C., Micelle Formation and Microenvironmental Properties of Sodium Dodecyl Sulfate in Aqueous Urea Solutions. *Colloids Surf., A* (1999), **147**, 349-357.
33. Aniansson, E. A. G.; Wall, S. N.; Almgren, M.; Hoffmann, H.; Kielmann, I.; Ulbricht, W.; Zana, R.; Lang, J.; Tondre, C., Theory of the Kinetics of Micellar Equilibria and Quantitative Interpretation of Chemical Relaxation Studies of Micellar Solutions of Ionic Surfactants. *J. Phys. Chem.* (1976), **80**, 905-922.
34. Turro, N. J.; Yekta, A., Luminescent Probes for Detergent Solutions. A Simple Procedure for Determination of the Mean Aggregation Number of Micelles. *J. Am. Chem. Soc.* (1978), **100**, 5951-5952.
35. Freire, S.; Bordello, J.; Granadero, D.; Al-Soufi, W.; Novo, M., Role of Electrostatic and Hydrophobic Forces in the Interaction of Ionic Dyes with Charged Micelles. *Photochem. Photobiol. Sci.* (2010), **9**, 687-696.
36. Al-Soufi, W.; Piñeiro, L.; Novo, M., A Model for Monomer and Micellar Concentrations in Surfactant Solutions: Application to Conductivity, NMR, Diffusion, and Surface Tension Data. *J. Colloid Interface Sci.* (2012), **370**, 102-110.
37. James-Smith, M. A.; Alford, K.; Shah, D. O., A Novel Method to Quantify the Amount of Surfactant at the Oil/Water Interface and to Determine Total Interfacial Area of Emulsions. *J. Colloid Interface Sci.* (2007), **310**, 590-598.

38. Verwey, E. J. W.; Overbeek, J. T. G., *Theory of the Stability of Lyophobic Colloids*. Elsevier: Amsterdam, (1948).
39. Colloidal Dispersions, *Interparticle Forces and Dispersion Stability - Lecture 3*. (2005) <http://colloidaldispersions.com/resources/presentations/Dispersions%20in%20Nanotechnology/Lecture%203%20Dispersion%20Stability.pdf> (accessed 8th March).
40. Morales, V. L.; Parlange, J.-Y.; Wu, M.; Pérez-Reche, F. J.; Zhang, W.; Sang, W.; Steenhuis, T. S., Surfactant-Mediated Control of Colloid Pattern Assembly and Attachment Strength in Evaporating Droplets. *Langmuir* (2013), **29**, 1831-1840.
41. Molero, M.; Andreu, R.; González, D.; Calvente, J. J.; López-Pérez, G., An Isotropic Model for Micellar Systems: Application to Sodium Dodecyl Sulfate Solutions. *Langmuir* (2000), **17**, 314-322.
42. Bruce, C. D.; Berkowitz, M. L.; Perera, L.; Forbes, M. D. E., Molecular Dynamics Simulation of Sodium Dodecyl Sulfate Micelle in Water: Micellar Structural Characteristics and Counterion Distribution. *J. Phys. Chem. B* (2002), **106**, 3788-3793.
43. Umlong, I. M.; Ismail, K., Micellization behaviour of sodium dodecyl sulfate in different electrolyte media. *Colloids Surf., A* (2007), **299**, 8-14.
44. Khunsin, W.; Kocher, G.; Romanov, S. G.; Torres, C. M. S., Quantitative Analysis of Lattice Ordering in Thin Film Opal-based Photonic Crystals. *Adv. Funct. Mater.* (2008), **18**, 2471-2479.
45. H. H. Wickman; J. N. Korley, Colloid Crystal Self-Organization and Dynamics at the Air/Water Interface. *Nature* (1998), **393**, 445-447.
46. McLachlan, M. A.; Johnson, N. P.; De La Rue, R. M.; McComb, D. W., Domain Size and Thickness Control of Thin Film Photonic Crystals. *J. Mater. Chem.* (2005), **15**, 369-371.
47. John, S., Strong Localization of Photons in Certain Disordered Dielectric Superlattices. *Phys. Rev. Lett.* (1987), **58**, 2486-2489.
48. Yablonovitch, E., Inhibited Spontaneous Emission in Solid-State Physics and Electronics. *Phys. Rev. Lett.* (1987), **58**, 2059-2062.
49. Lozano, G.; Dorado, L. A.; Schinca, D.; Depine, R. A.; Míguez, H., Optical Analysis of the Fine Crystalline Structure of Artificial Opal Films. *Langmuir* (2009), **25**, 12860-12864.
50. Romanov, S. G.; Bardosova, M.; Pemble, M.; Torres, C. M. S., (2 + 1)-dimensional Photonic Crystals From Langmuir-Blodgett Colloidal Multilayers. *Appl. Phys. Lett.* (2006), **89**, 043105-3.
51. Peng, S.; Morris, G. M., Resonant Scattering from Two-dimensional Gratings. *J. Opt. Soc. Am. A* (1996), **13**, 993-1005.
52. Khunsin, W.; Romanov, S. G.; Torres, C. M. S.; Ye, J.; Zentel, R., Optical Transmission in Triple-film Hetero-opals. *J. Appl. Phys.* (2008), **104**, 013527.
53. Garcia, P. D.; Sapienza, R.; Toninelli, C.; Lopez, C.; Wiersma, D. S., Photonic Crystals with Controlled Disorder. *Phys. Rev. A* (2011), **84**, 023813-1- 023813-7.
54. Ding, B.; Bardosova, M.; Pemble, M. E.; Korovin, A. V.; Peschel, U.; Romanov, S. G., Broadband Omnidirectional Diversion of Light in Hybrid Plasmonic-Photonic Heterocrystals. *Adv. Funct. Mater.* (2011), **21**, 4182-4192.
55. Kralchevsky, P. A.; Denkov, N. D., Capillary Forces and Structuring in Layers of Colloid Particles. *Curr. Opin. Colloid Interface Sci.* (2001), **6**, 383-401.
56. Shimmin, R. G.; DiMauro, A. J.; Braun, P. V., Slow Vertical Deposition of Colloidal Crystals: A Langmuir-Blodgett Process? *Langmuir* (2006), **22**, 6507-6513.
57. Dai, Z.; Li, Y.; Duan, G.; Jia, L.; Cai, W., Phase Diagram, Design of Monolayer Binary Colloidal Crystals, and Their Fabrication Based on Ethanol-Assisted Self-Assembly at the Air/Water Interface. *ACS Nano* (2012), **6**, 6706-6716.

Chapter 5

Methods of Affecting and Directing Opal Growth by Dip Coating

Abstract

Routes towards improving opal order and thickness of colloidal spheres self-assembled by dip coating are demonstrated. Ordered poly(methyl methacrylate) (PMMA) templates are grown on hydrophilized glass substrates at slow rates by noise-assisted dip-coating. Using transmission spectroscopy better long range order is demonstrated for the sample grown on glass with the higher degree of hydrophilicity ($\sim 0^\circ$ contact angle). Applied heat is demonstrated as a route towards improving the order and thickness for PS spheres assembled on gold coated silicon when dip coating at fast rate (1 mm min^{-1}). The application of heat to PMMA sphere solutions is shown as a method for producing thicker, disordered photonic glasses at fast rate dip coating. The ability to predetermine sphere symmetry and order by dip coating e-beam patterned substrates is presented. Polymeric pillar patterns are used for the growth of an adsorbate unit cell of PS spheres a factor of $\sqrt{2}$ smaller than the substrate unit cell (pillars) in both directions, rotated by 45° with respect to the substrate fcc (100) unit cell. The possibilities of moving away from the usual particle-selected arrangement with the hexagonal (111) face parallel to the substrate are highlighted.

5.1 Introduction

Photonic crystals¹ (PhCs) have been intensely investigated over the last 50 years due to the significant design potential they provide for a host of science and engineering applications. The highly useful ability to direct and control the flow of light, ensures a continued and substantial interest into the design and fabrication of PhC-based structures and templates. Programmable and deterministic assembly in the growth of artificial opals and related structures through the assembly of silica, polystyrene (PS) or poly(methyl methacrylate) (PMMA) colloidal spheres benefits from the notional simplicity, low cost and design malleability afforded by this route compared with other more expensive and technically complicated top-down lithography techniques^{2, 3}. A large variety of methods already exist for the arrangement of these silica or polymer spheres into ordered 2- or 3-dimensional lattice structures, for example, drop-casting of the sphere solution⁴, dip coating^{5, 6}, spin coating⁷, vertical deposition⁸, electrophoretic deposition⁹, Langmuir-Blodgett^{10, 11} or layer-by-layer assembly¹². There is a continuous drive towards discovering not only the best technique but what environment, sample preparation and overall conditions are needed for achieving thick, well-ordered, high quality structures on desirable substrates, and with functional materials. The photonic properties of these materials are highly dependent on lattice structure and symmetry, therefore the ability to improve, control and direct the growth order, orientation and defect positioning^{13, 14} is highly desirable for a wide range of optical and optoelectronic devices,¹⁵⁻¹⁸ data storage¹⁹ and chemical sensors.^{20, 21} While energy storage and high surface areas technologies have less stringent requirements on the electronic and optical quality of the infilled materials, the porosity and arrangement is still a function of the quality of the original template. Long range order in the template, even if translate identically to the inverse opal material, may influence electronic connectivity and act as optical scattering centres.

5.1.1 Substrate Hydrophilicity and Temperature Effects on Order

Dip-coating facilitates opal formation on a range of substrates and substrate shapes with deposition control provided by parameters such as evaporation rate and meniscus shape, wettability, and colloid density and withdrawal rate. This makes dip-coating a versatile and highly utilized technique. It has proven to form well-ordered multilayer deposits of spheres as a PhC at a slow rate of withdrawal, and its simplicity and upscalable nature make it useful in an industrial setting⁶. Improvement in the coverage and long-range order of deposits has been achieved through the control and/or the addition of other variables such as temperature²², management of the ionic strength of the solution via the use of charged colloids²³, and noise-induced stochastic resonance effects that perturb deposits within the meniscus to ensure maximum surface packing.²⁴ A better understanding of how, and to what degree, dip-coating parameters influence the final deposit (controlling defect free, ordered vertical and lateral growth), can increase the quality and yield of consistent artificial opal templates.

In this chapter, we investigate methods of improving and controlling sphere adhesion and ordering, for PMMA and PS spheres, using already established growth techniques. The first investigation deals with the formation of 3D PhCs on glass substrates by dip-coating of 700 nm PMMA spheres with noise induced stochastic resonance. Second, a comparison of substrate cleaning methods and the influence of hydrophilicity on the degree of long range order in 3D PhCs is demonstrated. The findings highlight the sensitivity to, and importance of, hydrophilized surfaces for initial adsorption of the spheres onto the substrate surface.

As already discussed in the previous chapter, one of the limiting factors for opal growth by dip coating is the requirement of a relatively slow speed in order to achieve good opal order, and more significantly, high thickness. In Chapter 4 the details of an investigation

into the improvement of order in a monolayer of PMMA spheres at a relatively fast withdrawal rate by the addition of a surfactant was shown. Here, an alternative method is presented, whereby the application of heat to the sphere solution during dip-coating is used to improve opal order and thickness at faster withdrawal rates on conductive substrates of gold and ITO.

5.1.2 Patterning as a Route to Deterministic Assembly

Orientation of the spheres when self-assembled through dip-coating, and most other assembly routes mentioned above, is usually limited to the energetically favoured hexagonal close-packed lattice structure, with the (111) face parallel to the substrate. As well, prescribed defects (e.g. opal lattice vacancies) in the opal PhC that definitively alter the photonic stop bands are essential for both the trapping and guiding of light in some cases.²⁵⁻²⁹ However, poor control of sphere position can lead to order defects that act as optical scattering elements and perturb the order that defines the photonic band structure, erasing the benefits of as-deposited order, and indeed any written functional defect vacancies. The frequency and dimension of these defects can severely limit the long range order of the artificial opal.

Non-close packed spheres are useful too for a variety of applications, for example, nano-hole arrays for surface plasmonic devices,³⁰ nano-apertures for single quantum dot spectroscopy,³¹ and microwells for cell patterning in biology.³² Such structures may also allow for thicker infilling of other materials, or provide room for reversible swelling-mediated variation in the PBG. Certain devices such as bio-sensors,²⁰ patterned magnetic media,³³ and photonic and plasmonic waveguides,^{34, 35} require both long range order and precise pattern registrations, therefore control and selectivity of aperiodic structures or defects is greatly needed. The use of colloidal sphere arrays for solid surface patterning and particle growth direction, known as nanosphere lithography (NSL),^{36, 37} has been heavily

investigated throughout the last two decades as a reliable, inexpensive and scalable method for device design and fabrication at sub-micrometer and nanoscales.

For these reasons, a host of techniques have been investigated with the aim of controlling the order and orientation of spheres when they assemble, for example, the application of external electric or magnetic fields,³⁸⁻⁴⁰ or the use of patterned substrates by either chemical⁴¹⁻⁴³ or topographical⁴⁴⁻⁴⁹ means. Koumouto *et al.* used self-assembled monolayers (SAMs) of octadecyltrichlorosilane (OTS) modified by UV irradiation to produce regions of hydrophilic silanol groups, coupled with solvent chemistry to pattern silica spheres into close packed two-dimensional regions.⁴¹ Xia *et al.* presented the assembly of polymer spheres into complex aggregates (polygonal and polyhedral clusters) by physical confinement into a 2D array of holes patterned into a layer of photoresist on glass and removal of the photoresist.⁵⁰ This bears some resemblance to the graphoepitaxy of self-assembled spherical block copolymers (BCP),⁵¹ which Bitai *et al.* performed on two dimensional periodically patterned substrates, where-by polymer posts act as surrogates for the minority domains of the block copolymer. Essentially, by governing the order and orientation of the spherical micro-domains by the commensurability between the BCP period and the period of the template, they achieve the formation of a single-grain BCP lattice with reduction in overall defect density.

Here, this same methodology is applied to polymer sphere self-assembly, partially combining the methods of Xia and Bitai mentioned above, and using the patterned resist directly to structurally orientate spheres as they assemble. In this work, the patterned substrate is a 2D array of pillars created in the shape of a square lattice, non-commensurate with the energetically favoured hexagonal ordering of colloidal spheres, formed using scanning-electron beam lithography of a 90 nm thick poly-methacrylate (PMMA) resist layer on a silicon substrate. Development reveals the exposed pillars, without requiring furthering

etching or processing, unlike other template assembly where the template is etched into the substrate proper. We show that these pillars, if appropriately sized and spaced, can template the assembly of polymer spheres into a lattice arrangement of chosen orientation and periodicity. Three-dimensional inverse opals are formed by the infilling of templates with a chosen material, of a high refractive index for optical applications, or an electrochemically active material for energy-storage applications. The formation of non-close packed arrays of sphere templates with tuneable lattice orientations and order would allow variations in infill material thickness and structure, ideal for optical analysis of the characteristics of functional materials and material architectures for example. Templated 3D spatial constraints of various geometries are demonstrated and compared with direct colloidal crystal assembly, formed by dip-coating. With this bottom-up topographical approach, the opal structure and periodicity can be manipulated to form single crystals with reduced lattice constants in fcc (100) adlayers, or crystals with a spatially defined change in structure and order over a wide range of length-scales on e-beam written templates formed by various resist exposure and sensitivity.

5.2 Results and Discussion

5.2.1 Colloidal Photonic Crystal Dip Coating on Hydrophilized Glass

The deposition of 700 nm PMMA spheres on glass substrates by noise-assisted dip coating at a rate of withdrawal of $\sim 1.5 \text{ mm hr}^{-1}$ is outlined schematically in Fig. 5.1. The application of acoustic vibrations to the colloidal solution during deposition prevents both the sedimentation of the spheres over time increasing uniformity in thickness and, as determined by Khunsin *et al.* who developed the technique,^{24, 52} improves order by increasing the effective crystallization time in the meniscus, lowering the stress to the deposited lattice.

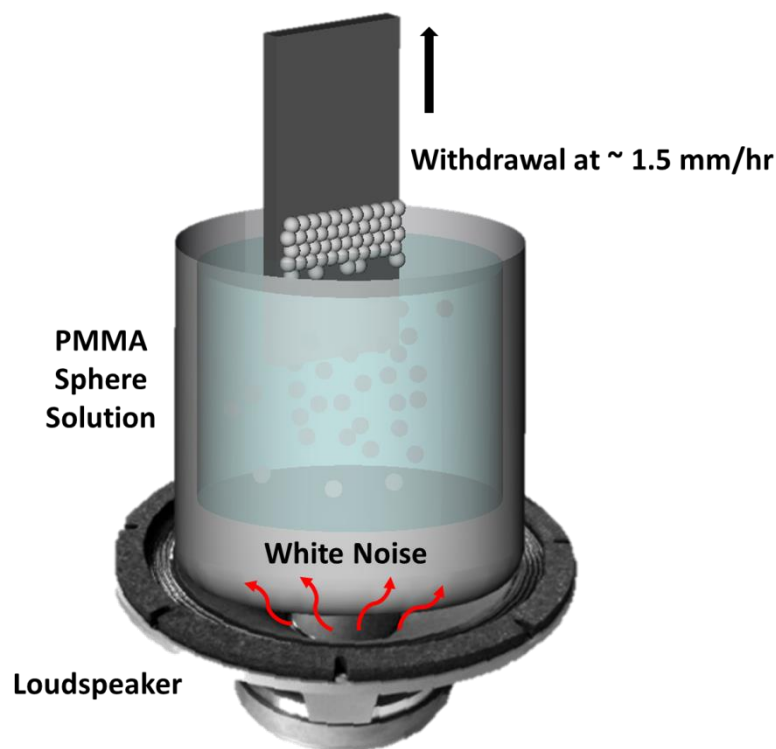


Fig. 5.1 Schematic representation of dip-coating under acoustic vibrations, through the loudspeaker placed beneath the PS sphere solution.

The glass substrates of approximately 2.5×1 cm were cleaned by sonication in acetone, IPA and DI water. Following this usual solvent cleaning technique, the glass substrates were subjected to different subsequent cleaning: one was submerged for approximately 5 minutes in Piranha solution, prepared using hydrogen peroxide and sulfuric acid, in the ratio of 1:3, the second method involved cleaning by O_2 Plasma on PVA TePla PS210 Microwave Plasma System. Contact angle measurements were acquired for both sample cleaning methods on a Kruss Easy Drop measurement system. Measurements revealed both cleaning methods to induce high degrees of hydrophilicity. The contact angle for the O_2 Plasma-cleaned glass indicated a more substantial improvement. The Piranha cleaned glass produced a substrate with a contact angle of approximately 32.5° and the O_2 plasma clean gave a contact angle of approximately 0° , indicating an almost perfect hydrophilic surface, as shown in the insets of Figs 5.2 (a) and (d).

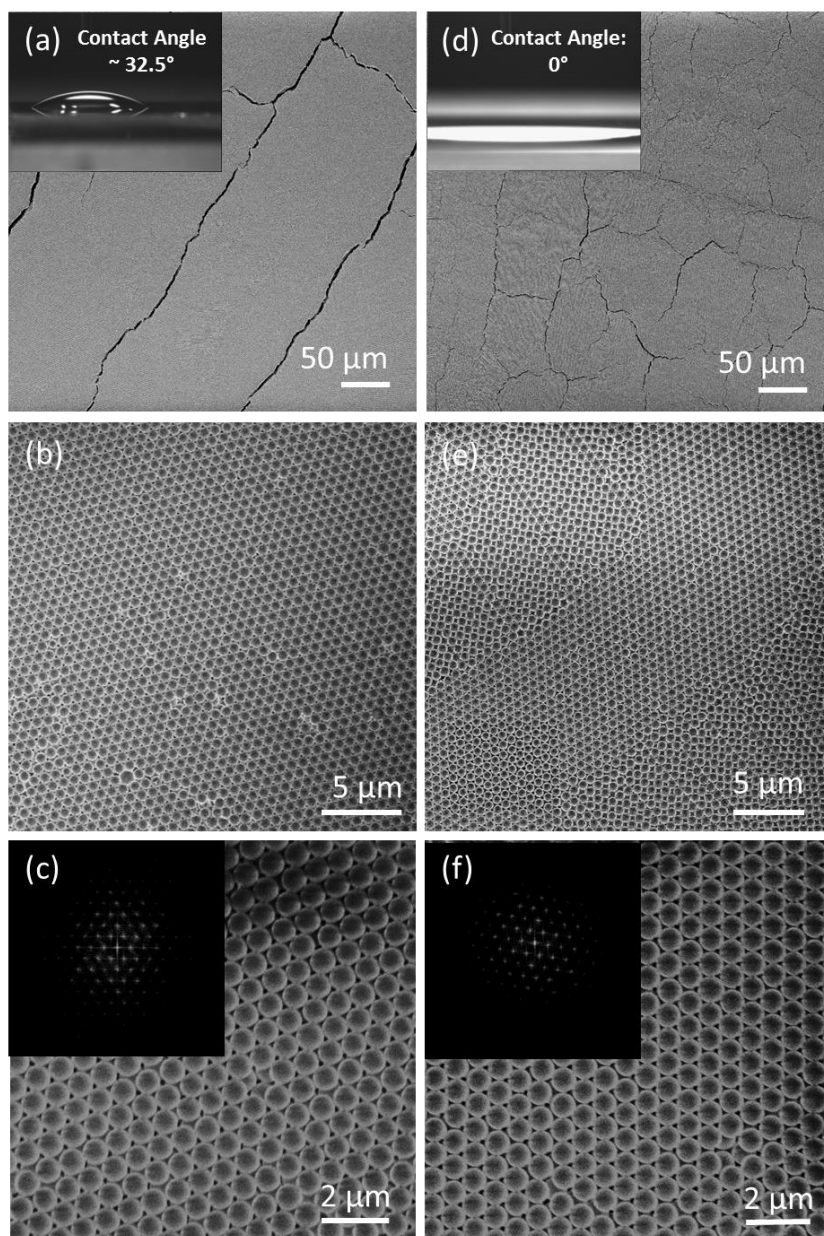


Figure 5.2. SEM images of inverted opals prepared by noise-assisted dip-coating of 500 nm PS spheres onto glass substrates cleaned by (a-c) Piranha solution and (d-f) O_2 plasma. Inset of (a) shows the contact angle measurement on Piranha cleaned glass and Inset of (d) shows contact angle measurement on O_2 plasma cleaned glass. Inset of (c) FFT of SEM image shown in (c) and Inset of (f) FFT pattern of SEM image in (f).

The opal PhC template that formed on the Piranha cleaned glass is shown in Figs 5.2(a)-(c), and a similarly deposited opal formed on the O_2 plasma cleaned glass can be seen in Figs 5.2 (d)-(f). Both samples show fcc ordering in the sphere arrangement on either surface. The colloidal crystal opal formed on the piranha cleaned glass appears to contain larger but fewer cracks than the O_2 plasma cleaned sample, which shows smaller, rounder

domains. However, less variation in relative domain orientation is seen on Piranha cleaned substrates (Fig. 5.2 (b)). Domains with different relative orientations bounded by lateral stacking faults could be seen in the sample formed on the O₂ plasma cleaned substrate, as shown in Fig. 5.2 (e). The square packing of the spheres is indicative of a domain with (100) orientation at the surface, while the surrounding areas demonstrate the typical packing with (111) orientation. While Fig. 5.2 (b) illustrates a number of single-sphere vacancies in the packing order common in many artificial opals, the film appears more consistently fcc since vacancies do not disrupt the ordering by forming boundaries; rotational and disorder-induced boundaries and domain formation are found to be more prevalent in opals formed on an O₂ plasma cleaned glass. However, both samples have good local crystalline ordering indicated by the FFT of the domain structure shown in Figs 5.2 (c) and (f).

In Fig. 5.3 the plot profiles along one direction are shown for both a sample on piranha cleaned glass (Fig. 5.3 (a)) and a sample on O₂ plasma cleaned glass (Fig. 5.3 (b)). These profiles correspond to a line of spheres in the SEM images shown in Fig. 5.3 (c) and Fig. 5.3 (d) marked by the black arrow in each. The peak intensities are related to the bright outer edges of each sphere and therefore peak to peak distance corresponds to a sphere diameter, and trough to trough corresponds to the centre to centre spacing. As is observed along a well ordered line the peak to peak distance approximates to the 700 nm PMMA sphere diameter, indicating a highly close packed structure. It should be noted however, that this method has a low sensitivity to disorder as is shown for an example area of the sample on piranha cleaned glass in the SEM images of Fig. 5.3 (e). The stacked plot profiles in Fig. 5.3 (e) are related to the same coloured arrows in the accompanying SEM images. The upper graph shows the profile across three ordered spheres, the lower graph shows the profile across two spheres separated by a void. The void defect causes a discrepancy in the peak to peak distance but a low intensity peak is still observed, corresponding to the underlayer

structure observable through the void. A statistical characterization was carried out in order to better quantify the defects across a larger sample area. A statistical model that employs a Delaunay triangulation^{53, 54} was used with Matlab® to analyse a collection of SEM images in every direction and not just along a single line for samples grown on both glass substrates. In this way, spheres were categorised by the number of neighbouring spheres allowing defects to be identified by any discrepancies. The distance between the neighbouring spheres was determined for several SEM images and averaged, the average distribution is shown in Fig. 5.3(f) for the sample on piranha cleaned glass and in Fig. 5.3 (g) for the sample on O₂ plasma cleaned glass. The centre to centre spacing distribution was then fitted using the Gaussian function where the full width half maximum (FWHM) served as an indicator of the number of defects due to variations in sphere-sphere distances. The smaller the FWHM the lower the distribution of spacing distances. As is observed in the distribution plots some spheres are separated by wider distances/defects and this constitutes the right wing variation from Gaussian form in both samples. The measurements of centre to centre spacing using this statistical method are comparable to those made along a single direction using plot profiles, but take a wider area into account. The Gaussian curves (average FWHM of ~ 50-70) for both samples were comparable, suggesting a similar top layer close packing and apparent level of defects for both samples. However, probing of the internal structure of the opals grown on piranha cleaned glass and O₂ plasma cleaned glass using transmission spectroscopy illustrated a deeper variation in long range order.

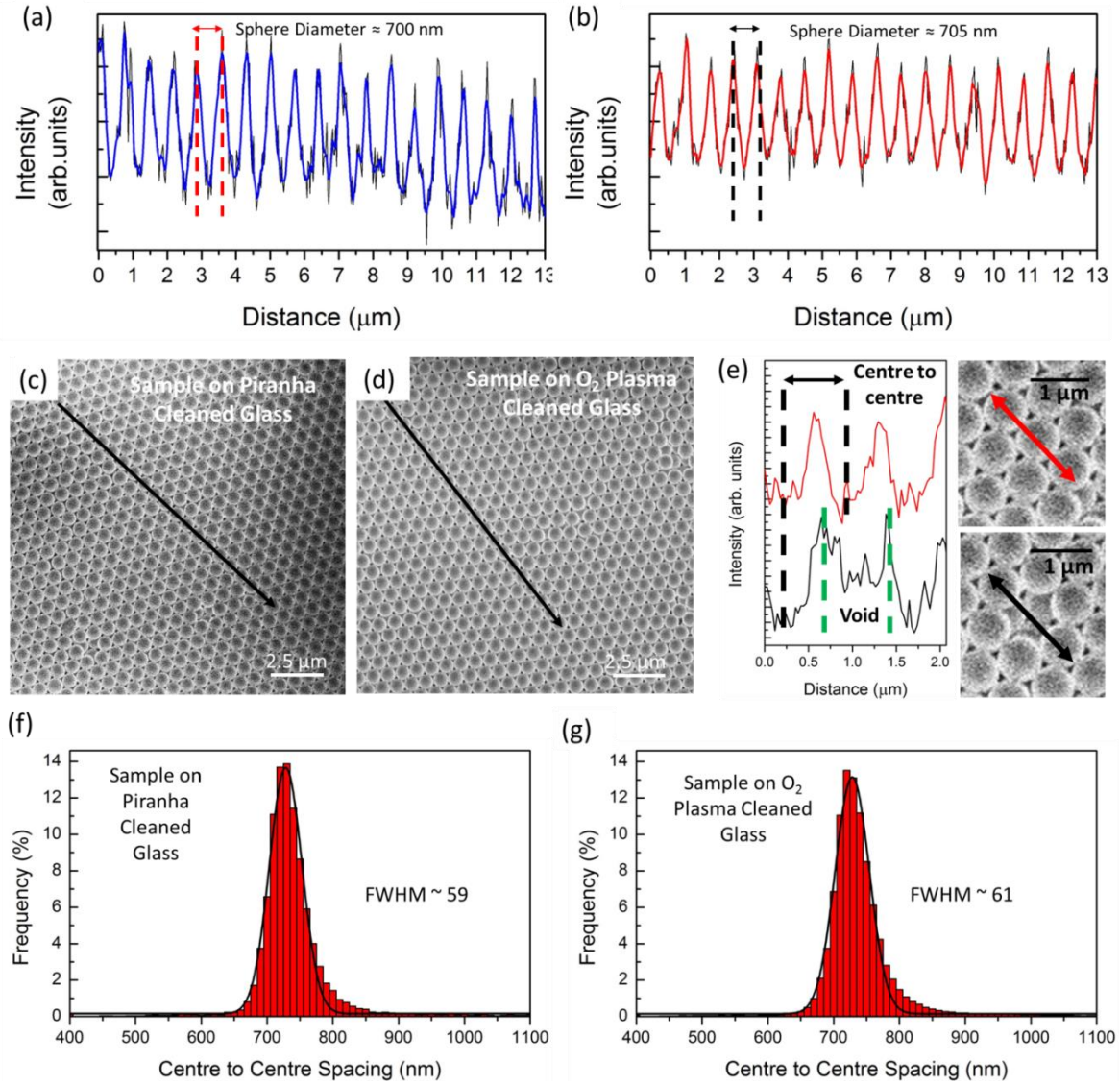


Fig. 5.3 Plot profiles for an opal grown on piranha cleaned glass (a) and O₂ plasma cleaned glass (b) along the black arrows in SEM images of top layer of the opal on (c) piranha cleaned glass and (d) O₂ plasma cleaned glass. (e) Plot profile for an area of the sample on piranha cleaned glass showing the profile variation for ordered spheres (red) and spheres separated by a void (black). (f) Average Gaussian distribution for sphere centre to centre spacing measured across a ~ 8 SEM images for the sample on piranha cleaned glass (f) and O₂ plasma cleaned glass (g).

Optical transmission spectra for the 3D PhCs formed on each surface are shown in Fig. 5.4 for light incident at 5° increments, for angles 0°-70°. Transmission spectra were taken using a CCS200 Compact CCD spectrometer (Thorlabs) for wavelengths within the visual range, and for higher, near-infrared wavelengths between 900-2100 nm with an Ocean Optics NIRQuest 256-2.1 spectrometer as is outlined in Chapter 3 Section 3.4.1. A photonic

bandgap (PBG) was observed for opals grown on the hydrophilized surfaces prepared using both cleaning treatments, confirming 3D order in the assembly of the template. The colloidal crystal shows a transmission minimum centered at $\lambda_{(111)} \approx 1620$ nm. The angle-resolved shift in the transmission minima for different angles of incident light for the sample formed on the Piranha cleaned glass is shown in Fig. 5.4 (a) and (c) and Fig. 5.4 (b) and (d) shows the angle resolved shift for the sample on the O₂ plasma cleaned glass.

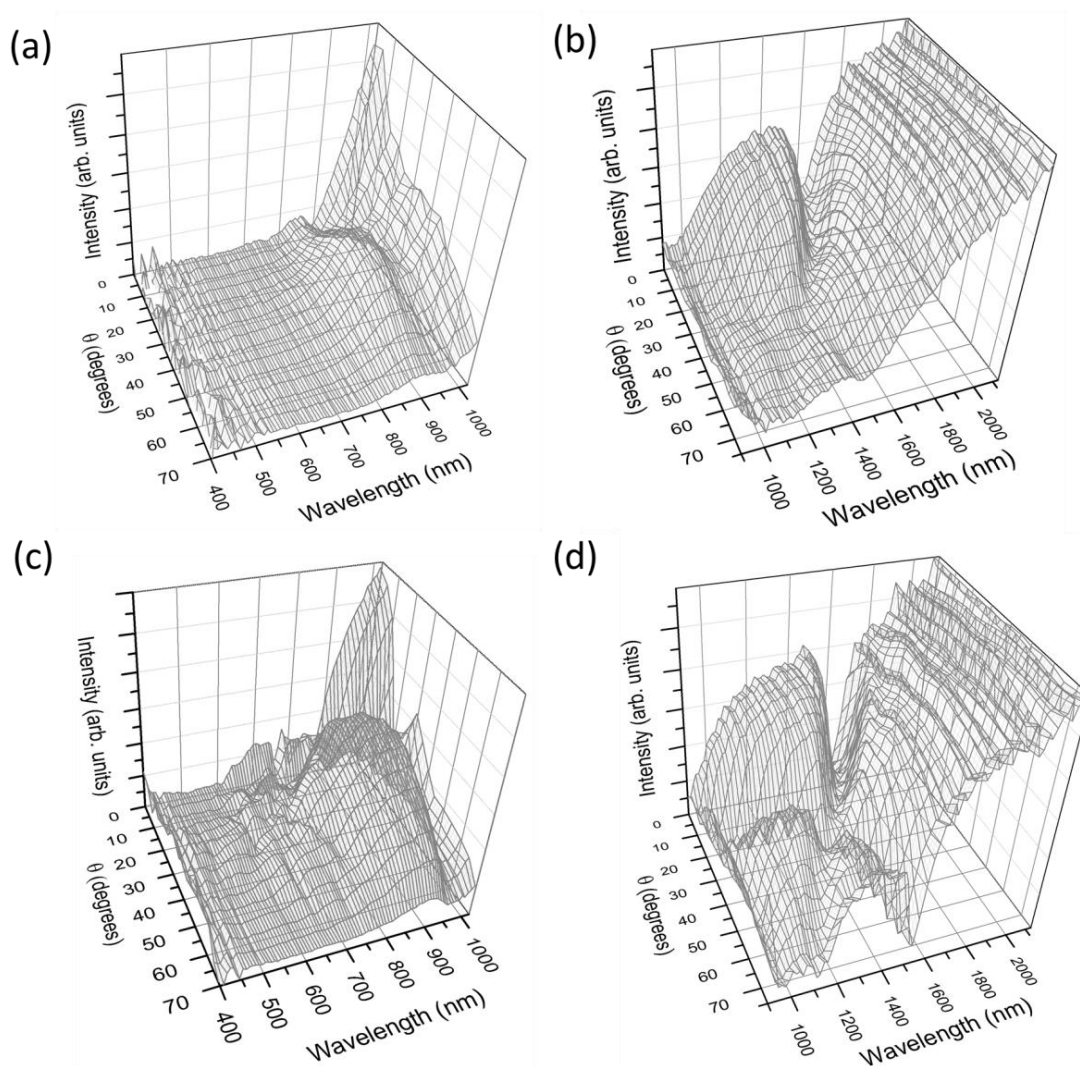


Figure 5.4 Angle-resolved transmission from the artificial opal formed on the piranha-cleaned glass within the visual-wavelength range (a) and near-infrared wavelength range (b) and the transmission data for the sample on O₂ plasma-cleaned glass in the visual range (c) and near-infrared (d).

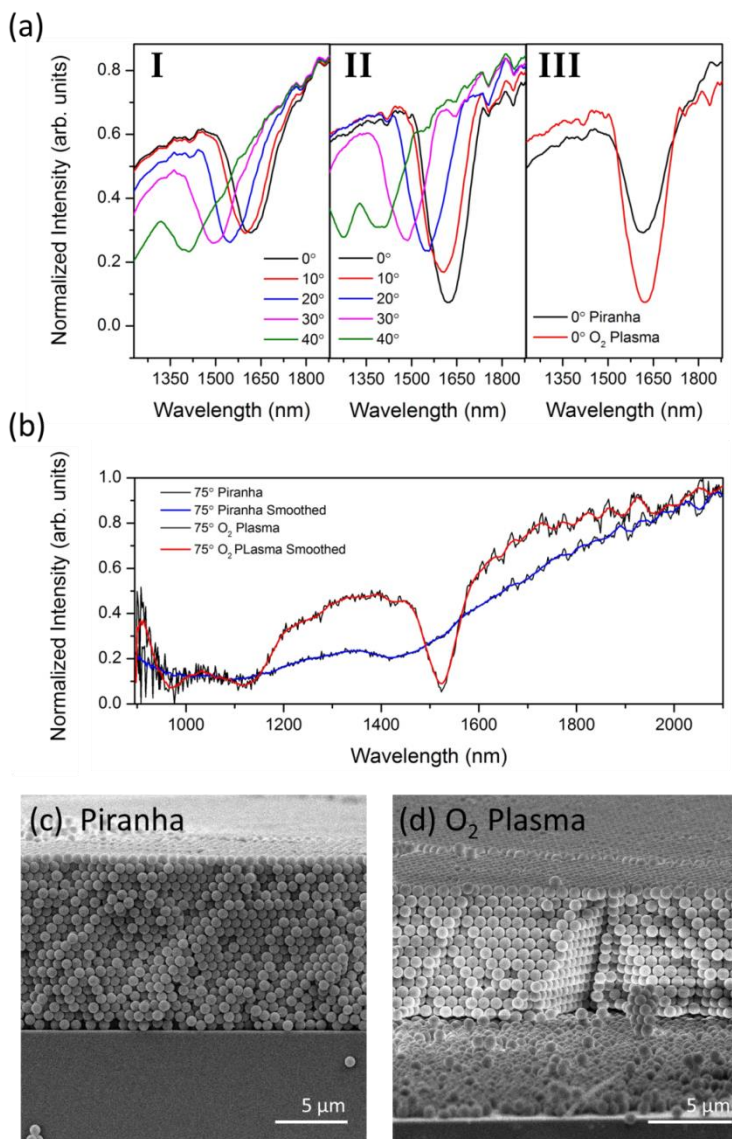


Fig. 5.5 Close-up inspection of angle dependent movement of the λ_{111} resonant peak for light incident at 0° , 10° , 20° , 30° and 40° as an example range for the PMMA spheres on (I) piranha cleaned glass and on (II) the O_2 plasma cleaned glass and a comparison between the λ_{111} peak at 0° for both glass types in (III) highlighting the difference in the two deposits. A comparison is also made between the transmission spectra attained for light incident at the higher angle of 75° for both type deposits in (b) highlighting the increased signature witnessed in the sample formed on the O_2 plasma cleaned glass (red) compared with the sample on piranha cleaned glass (blue) and cross sectional SEM images of the opals formed on the (a) piranha cleaned glass and (b) the O_2 plasma cleaned glass.

The movement of the PBG (λ_{111}) is more easily observed in Fig. 5.5 (a) for the sample on the piranha cleaned glass (I) and for the sample on the O_2 plasma cleaned glass (II). The transmission minimum for the sample on the more hydrophilic surface is deeper, more

symmetric and well defined than observed for the opal formed on the piranha cleaned glass, as shown in Fig. 5.5 (a) III. In transmission spectra of opals, the degree of transmission attenuation is a function of the structural disorder; the PBG minima become less pronounced, with a background signal attenuation at lower wavelengths, and a larger FWHM as disorder increases. This variation is especially pronounced at higher angles of incidence. At 75° shown in Fig. 5.5 (b), a greater number and more defined minima are observed that follow the theoretical dispersion for an FCC opal of 700 nm spheres. This serves as an indication of improved long ranging order in the sample formed on the more hydrophilic surface.⁵⁵

Fitting of the dispersions for the transmission resonance wavelengths for different planes of the opal lattice for samples on both glass surfaces were compared with the Bragg law prediction for a FCC lattice, using the equation $\lambda = 2n_{eff}d_{hkl}\sqrt{1 - (\sin \alpha_{hkl})^2}$, where d_{hkl} is the inter-planer distance for the (hkl) planes given by $\sqrt{2D^2/(h^2 + k^2 + l^2)}$, n_{eff} is the effective refractive index, and α_{hkl} is the angle between the incident light ($\sin \theta$) and the normal vector to the (hkl) plane within the PhC. α_{hkl} is related to the angle of incident of the light through Snell's law according to $n_{eff} \sin \alpha_{hkl} = n_{med} \sin \theta$, where n_{med} is the refractive index of the surrounding medium, in this case air. A value of $n_{eff} = 1.373$ and $D = 700$ nm were used as fitting parameters for calculation of the Bragg fit. The experimental dispersion data, taken from both the visual wavelength range data (blue) and near-infrared wavelength range data (red), are shown in Fig. 5.6 where the dispersion for the (111) plane is shown to fit very well with the theoretical dispersion for the piranha cleaned sample Fig. 5.6 (a) and the sample on the O₂ plasma cleaned glass Fig. 5.6 (b). A slight variation is observed for the (11-1) resonance minimum in the sample on the O₂ plasma cleaned glass (Fig. 5.6 (b)) which suggests a small variation in the inter-plane distance. This is attributed to the stretching of the lattice during dip-coating. The capillary force, which is accelerated by pulling the sample out of the suspension, will exert a force that packs the spheres denser in the direction of

drawing/pulling.⁵² This deviation from the theoretical dispersion is more pronounced for the sample on the O₂ plasma cleaned glass. One possible reason for this is the higher degree of hydrophilicity, which in lengthening the meniscus could be increasing the stretching distance. The hydrophilicity helps push spheres further out of the meniscus as the substrate is being drawn out and with the added noise vibration, external perturbation is given to supply spheres to the drying front, which under a very thin layer of water (due to hydrophilicity of the substrate), anchors the spheres onto the substrate.

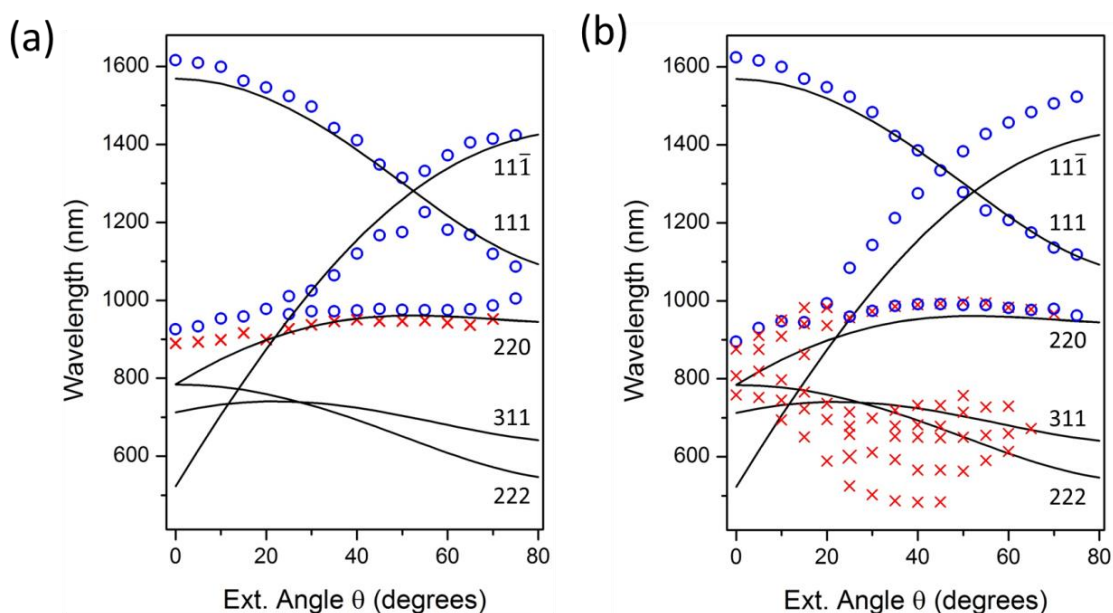


Figure 5.6 Dispersion of the transmission minima for the sample formed on (a) the piranha cleaned glass and on (b) the O₂ plasma cleaned glass, compared against the theoretical Bragg law dispersions for a 3D photonic crystal with sphere size of $D = 700$ nm.

A greater number of transmission minima are observed at lower wavelengths for the O₂ plasma sample than are seen in sample on Piranha where only the (220) resonance can be seen. These minima partially follow the (311) and (222) theoretical resonances, but they cannot be unambiguously assigned. Such scattered minima have been reported previously and attributed to variations in inter-planar distances and the possibilities of new lattice planes due to lattice distortion on growth.⁵² However, the very presence of such minima, likely related to

the (311) and (222) resonances, highlights the improved order in the sample on the O₂ plasma cleaned glass compared with the sample on the piranha cleaned glass from which only the (220) dispersion and no other lower wavelength dispersions were observed.

Therefore, in order to improve deposition by dip coating on glass substrates, the substrate surfaces should be made as hydrophilic as possible to promote ordered assembly with long range order at several angles of incident light. However, assembly on conductive substrates is more beneficial for many functional materials that rely on a defined template to create electrically addressable, active, porous structures. The assembly of the spheres on gold-coated silicon substrates was also investigated using faster rate dip-coating, for the increased withdrawal rate of 1 mm min⁻¹. What we observed was at faster rates of withdrawal, far from the equilibrium condition, with non-functionalized spheres such as the PMMA used here, short- and long-range van der Waals forces⁵⁶ dominate over the repulsive interactions of the particles and so there is insufficient time to achieve the ordered crystallization. Thus unlike perturbative noise-assisted assembly at much slower rates, very limited order for these non-functionalized spheres is found on glass at faster withdrawal rates. At the faster rate, with no natural repulsion to assist with ordering, the crystallization inexorably leads to a disordered and patched coverage of opal deposits on the substrate, particularly for a metallic surface, which has become hydrophobic in air.

5.2.2 Dip-coating with Applied Heat

The application of heat to a solution of spheres during dip coating has the effect of altering a number of solution parameters. In particular, temperature affects the floatation force near the meniscus, the evaporation rate and the kinetic energy of the spheres. Increasing the temperature during the vertical deposition of colloidal spheres is not uncommon, increasing the evaporation along the meniscus for a substrate held in a stationary position, vertically in a

solution will increase the rate of meniscus movement and hence assembly of the spheres. However, tuning of the temperature has not been as widely applied to dip-coating techniques due in large part to the slow rate of withdrawal typically used and difficulties associated with increased evaporation rates that can cause instabilities in the opal growth⁶ and less control over thickness and uniformity of coatings. It remains to be seen however, whether increased temperature can compensate for the faster withdrawal rate by increasing the meniscus evaporation rate and the particle flux towards the solution surface.

Here, the deposition of PS spheres on conductive substrates of gold coated silicon and ITO-coated glass by dip coating at the faster rate of 1 mm min^{-1} , compared to the 1 mm hr^{-1} of the previous experiments on glass (discussed above), is compared to the deposition of the same kind but at an increased temperature. Although the rate is quite fast, the concentration of spheres at the meniscus allows the system to evolve similar to a liquid film under capillary forces, i.e. a higher sphere density at elevated temperature ensure sphere deposition at faster rates before gravity drainage effects are observed, which is common for dilute systems at fast rates. Firstly, ITO-coated glass, cleaned by sonication in acetone, IPA and deionised water and of approximately $2 \text{ cm} \times 1 \text{ cm}$ in size, was withdrawn from a 2.5 wt% aqueous solution of 500 nm PS spheres at a rate of 1 mm min^{-1} . At this rate, no sphere assembly was observed on the surface of the ITO-coated glass, however, the spheres did appear to assemble along the thin edge of the substrate, as is observed in the photograph of Fig. 5.7 (a), and the SEM image in Fig. 5.7 (b). However, heating of the solution of spheres to $\sim 50 \text{ }^\circ\text{C}$ produced a marked improvement in the deposit thickness, and in the order observed therein, as is highlighted in the SEM image of Fig. 5.7 (c) and at higher magnification in Fig. 5.7 (d). The FFT of this area is shown in Fig. 5.7 (e) illustrating the high degree of crystallinity visible on the top surface of this colloidal assembly. The regularity within the structure is further

illustrated by the line profile in Fig. 5.7 (f) taken along the red arrow of Fig. 5.7 (e), the peaks, indicating the high intensity spots off the FFT, are uniformly positioned.

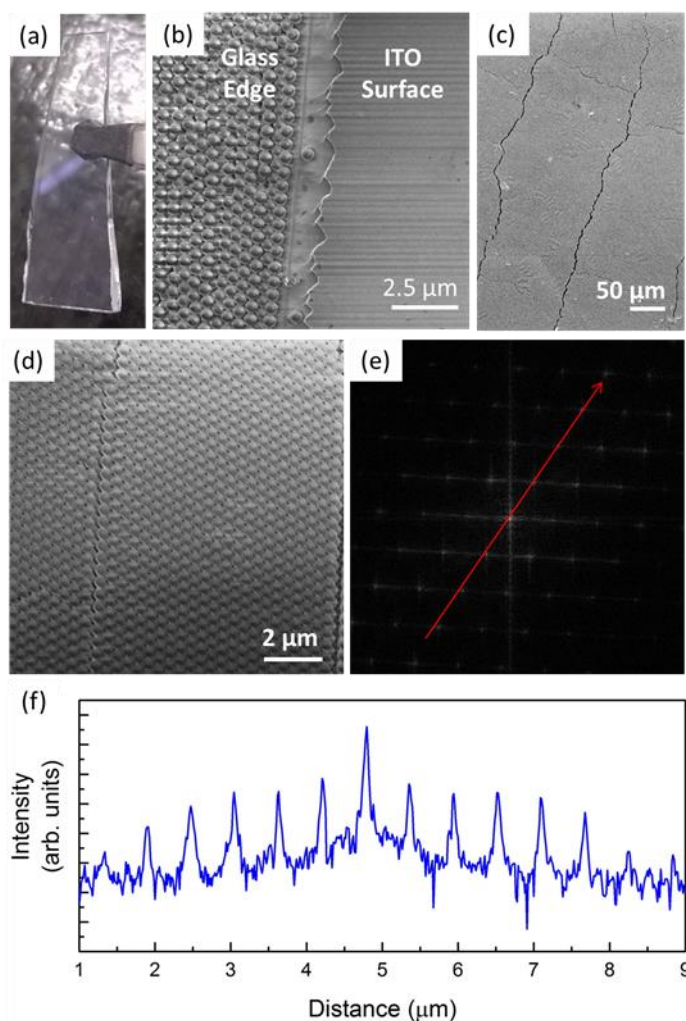


Fig. 5.7 (a) Photograph of ITO-coated glass dip coated at a rate of 1 mm/min into a 2.5 wt% aqueous solution of 500 nm PS spheres and SEM images of (b) the lack of spheres deposited on the larger surface area of the substrate but only along the narrow edge (c) an ITO-coated glass substrate dip-coated at the rate of 1 mm min⁻¹ into a 2.5 wt% aqueous solution of 500 nm PS spheres heated to a temperature of ~50 °C, highlighting large scale domain cracking indicative of high thickness and (d) the increased order achieved at this higher temperature shown at higher magnification. (e) FFT of (d) indicating high crystalline like order and (e) line profile along the red line shown in (e) showing the consistent, periodic order.

On contact with air, gold surfaces which are initially hydrophilic quickly turn hydrophobic⁵⁷ and this presents a major difficulty for colloidal crystal assembly directed at hybrid plasmonic-photonic crystal^{34, 35, 58} applications. Metal-dielectric interfaces hold a lot of potential within a range of functional devices, including electrochemically active

electrodes.⁵⁹ The ability to assemble artificial opal structures on a conductive substrate as templates for electrically addressable continuously interconnected porous materials is therefore of critical importance. However, due to the hydrophobic nature of gold surfaces in air, dip-coating of PS spheres can be problematic. Gold-coated silicon substrates, cleaned with acetone, IPA and deionized water and dried in nitrogen, were dip-coated into a 2.5 wt% aqueous solution of 500 nm PS spheres at room temperature. This produced a poorly ordered patchy deposit as shown by the SEM images in Fig. 5.8 (a) and (b), with little to no adhesion of the spheres on to the gold surface no diffraction is observed from the less ordered deposit as shown by the inset photograph of Fig. 5.8 (a).

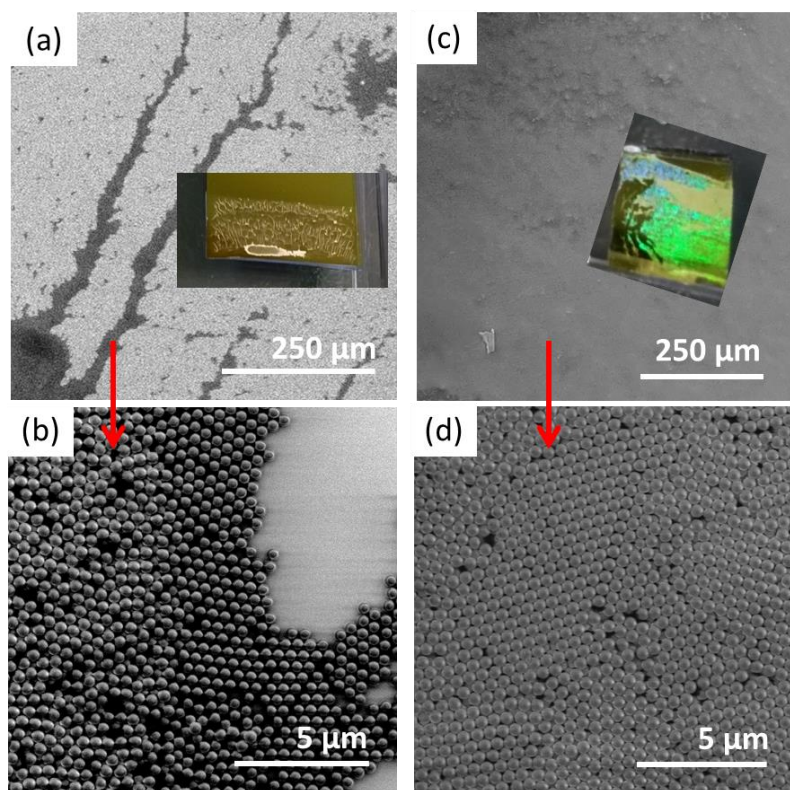


Fig. 5.8 SEM images of 2.5 wt% 500 nm PS spheres dipcoated at a rate of 1 mm/m on gold-coated silicon substrates at (a) room temperature (c) room temperature at higher magnification (c) $\sim 50^{\circ}\text{C}$ and (d) at higher magnification. Inset photographs of (a) and (b) illustrate corresponding sample overviews depicting levels of reflectivity.

The application of heat to the sphere solution, up to a temperature of $\sim 50^\circ\text{C}$ increased the particle flux within the solution, resulting in a greater number of spheres directed towards the water-air interface. This caused in an increased thickness of spheres available for assembly at the liquid-substrate contact line while compensating for the faster withdrawal rate. The increase in evaporation rate also has the effect of lowering surface tension. As is observed in the SEM images of Fig. 5.8 (c) and (d), the order for spheres deposited at 50°C shows an improved uniformity in coverage, thickness, and in crystalline order, characterized by the high reflectivity from the surface of the material as seen for the photograph in the inset image of Fig. 5.8 (c).

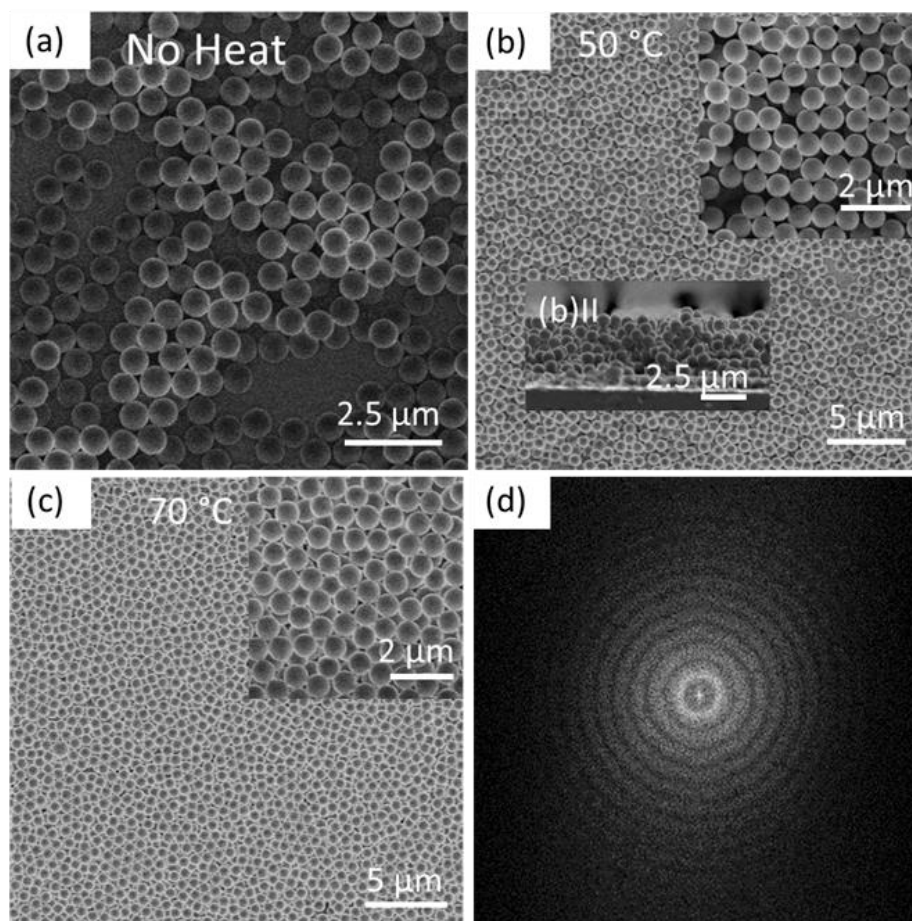


Fig.5.9 SEM image of 700 nm PMMA spheres dip coated at a rate of 1 mm/min at (a) room temperature (b) 50°C and inset (b)II cross section of (b) highlighting thickness (c) 70°C and (d) the FFT of the surface shown in (c) indicating amorphous-like structure.

Next, 700 nm PMMA spheres at a concentration of 5 wt% were dip-coated at a rate of 1 mm min⁻¹ on to gold-coated silicon substrates. As observed, in Fig. 5.9 (a) this resulted in a sparse, poorly ordered deposit. Heating the sphere solution to a temperature of ~50 °C achieved a notable increase in thickness and packing but the structure maintained a relatively poor level of order, producing an amorphous photonic glass compared with the ordered crystalline structure achieved for the PS equivalent discussed above. An additional increase in temperature to ~70 °C saw a further increase in thickness and packing as seen for Fig. 5.9(c). However, as evident by the amorphous pattern of its FFT spectrum in Fig. 5.9(d), the structure continued to hold a high level of disorder.

The self-assembly of colloidal spheres into ordered arrays occurs through the interaction of a number of colloidal forces, and it is by the manipulation of these attractive, compacting and repulsive forces that assembly can be controlled and improved.⁶⁰ The primary model for explaining the influence of a number of experimental parameters on colloidal interactions in the assembly of colloidal crystals through dip coating is well known from the work of Dimitrov and Nagayama.⁶ They estimate the number of layers assembled k to be a result of a number of experimental properties related by,

$$k = \frac{\beta l J_e \varphi}{0.605 d v_w (1 - \varphi)} \quad \text{Eqn. 5.1}$$

Here, J_e is the water evaporation rate, φ is the particle volume fraction, d is the particle diameter, v_w is the rate of withdrawal, and βl is an experimental constant: l is the evaporation length and β is the ratio of the particle velocity to the velocity of the solvent (water) molecules. This value depends on particle-particle and particle-substrate interactions and can vary between 0 (stronger interactions) and 1 (weakest interaction). For electrostatically stable particles and dilute solutions $\beta \rightarrow 1$. The problem encountered at faster

withdrawal rates is illustrated by Eq. 5.1; an increase in the rate of withdrawal v_w will result in a decrease in the number of assembled layers at maximum packing. However, also illustrated is the potential compensation afforded by an increase in the evaporation rate J_e . A higher evaporation rate should increase the number of arrays formed for a given rate of withdrawal, thereby effectively balancing Eq 5.1, at least qualitatively.

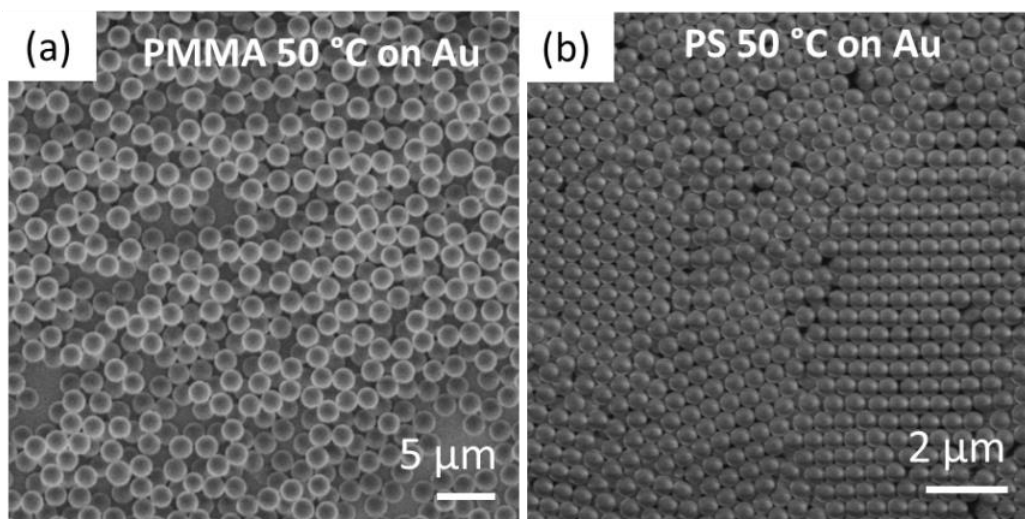


Fig. 5.10 SEM images of a) 700 nm PMMA and (b) 500 nm PS spheres dip-coated at 50 °C on to gold coated silicon substrates at a rate of 1 mm/min.

Variations between the PMMA spheres and PS spheres deposited at 50 °C are more comparable in Fig. 5.10. Regardless of the slight variations in diameter between the PS and PMMA spheres used (which is compensated by the variation in volume fraction and higher density of PMMA), stand-alone comparisons for each type of spheres indicate improved order for the PS spheres between room temperature and heated deposition, and no clear improvement in order for the PMMA spheres. The purchased PS spheres are more electrostatically stable than the synthesized PMMA spheres characterized by low stability in resting solution and this can account for the discrepancy. PMMA sphere deposition increased only in thickness; while the higher evaporation rate increased particle flux towards the air-liquid interface thereby increasing the number of spheres available for deposition, weaker repulsive forces allowed the attractive van der Waals forces between particles to command

assembly, thus producing a disordered and randomly deposited structure. The observations show that an increased meniscus flux does not allow sufficient time for an ordered opal layer to form or for the spheres to reach their most energetically favoured arrangement before other spheres reach the interface, leading to lack of uniformity and order. In the self-assembly of colloidal spheres on a substrate, lateral capillary interactions play an enormous role. These are influenced by the wetting properties of the particle surface, namely the position of the liquid contact line and magnitude of the contact angle, which are in turn are determined by particle separation, radius, and the surface tension of the liquid.⁶¹

5.2.3 Dip Coating of Artificial Opals on e-Beam Patterned Substrates

Substrates, prepared with a 90 nm thick layer of PMMA 950K positive resist (AR-P 671.02) and patterned using e-beam lithography, as outlined in Fig. 5.11 (a) and described in detail in the Chapter 3 Section 3.2.1., were withdrawn at a rate of $\sim 1.5 \text{ mm hr}^{-1}$ (Fig. 5.11 (b)) from an aqueous solution of PS sphere. The pillars of polymer resist on the substrate acted as pattern constraints during sphere assembly.

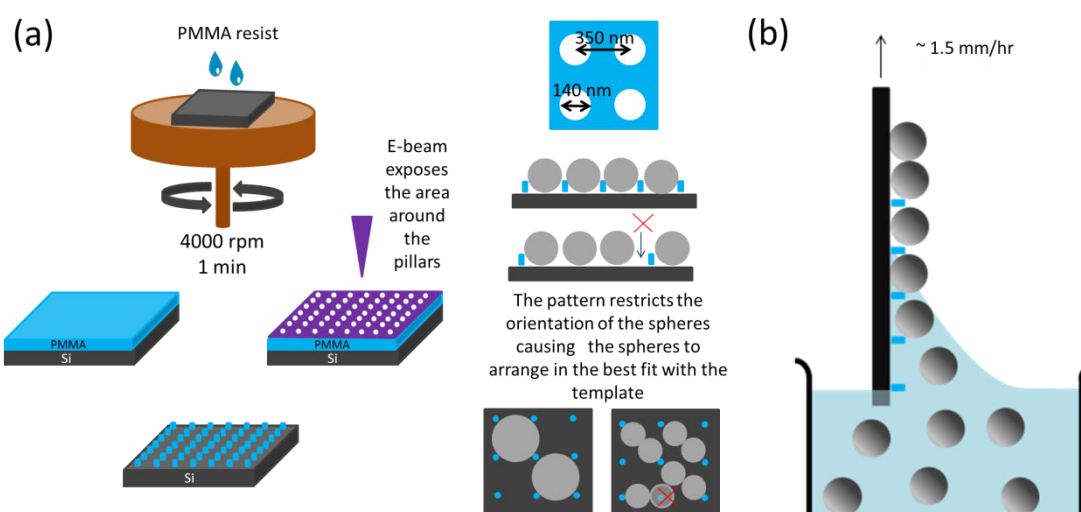


Fig. 5.11 Schematic representing (a) the template formation using electron beam lithography of spin-casted PMMA resist on silicon to produce a 2D array of pillars and a schematic representation of the desired effect on the orientation and ordering of then deposited spheres and (b) Dip-coating of 200 nm PS spheres.

The effect of pattern design methods on the final write pattern is highlighted by Fig. 5.12(a). The pattern blueprint was designed using a series of square-hole patterns then reproduced to form a pattern of consecutive square-hole patterns to fit the desired write field size. This design leaves some areas of unexposed resist at the edges of each square. This is particularly prominent at low doses, whereas for the same effective write-field area at higher doses, remnant resist is exposed and removed, as seen when comparing Fig. 5.12(c) at $\approx 134 \mu\text{C}/\text{cm}^2$ and (d) at $\approx 179 \mu\text{C}/\text{cm}^2$. It is possible however to achieve increased uniformity in writing at low doses by using smaller write-field areas, this lessens the need of beam deflection and thusly increases the effective dose by a factor of $2\times$ for the write field size of $25 \mu\text{m}$ in Fig. 5.12 (b) compared to $50 \mu\text{m}$ in Fig. 5.12 (a).

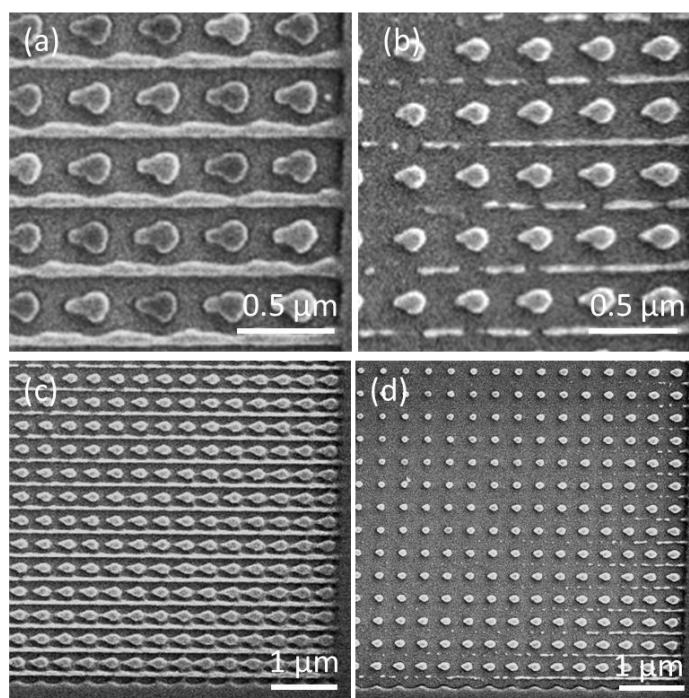


Fig. 5.12 SEM images of pillars patterned using a dose of $89.628 \mu\text{C}/\text{cm}^2$ at 30 kV with applied dose factors of (a) 1.7 for a $50 \mu\text{m} \times 50 \mu\text{m}$ write field area and (b) 1.7 for a $25 \mu\text{m} \times 25 \mu\text{m}$ write field area (c) 1.5 for a $25 \mu\text{m} \times 25 \mu\text{m}$ write field area and (d) 2.0 for a $25 \mu\text{m} \times 25 \mu\text{m}$ write field area, indicating the variations observed in feature resolution and quality and the high sensitivity to pattern blueprint design.

Also shown in Fig. 5.12 is the appearance of tails on some pillar structures leading to non-concentric pillars, this can be attributed as an artefact of faster write speeds at lower

doses. Higher exposure dose values produced fewer speed-triggered tail formations likely due to the slower write speed and the proximity effect at higher doses. The proximity effect is a prominent problem when forming nested features, such as this array of pillars, however, in this case the effective ‘spill-over’ of the beam of electrons whose mean-free path within the interaction volume in the polymer is not limited by causing chain scission during exposure of adjacent regions, could be diffusing to expose and reduce the presence of tail features on nearby pillars i.e. the proximity effect acts as an advantage.

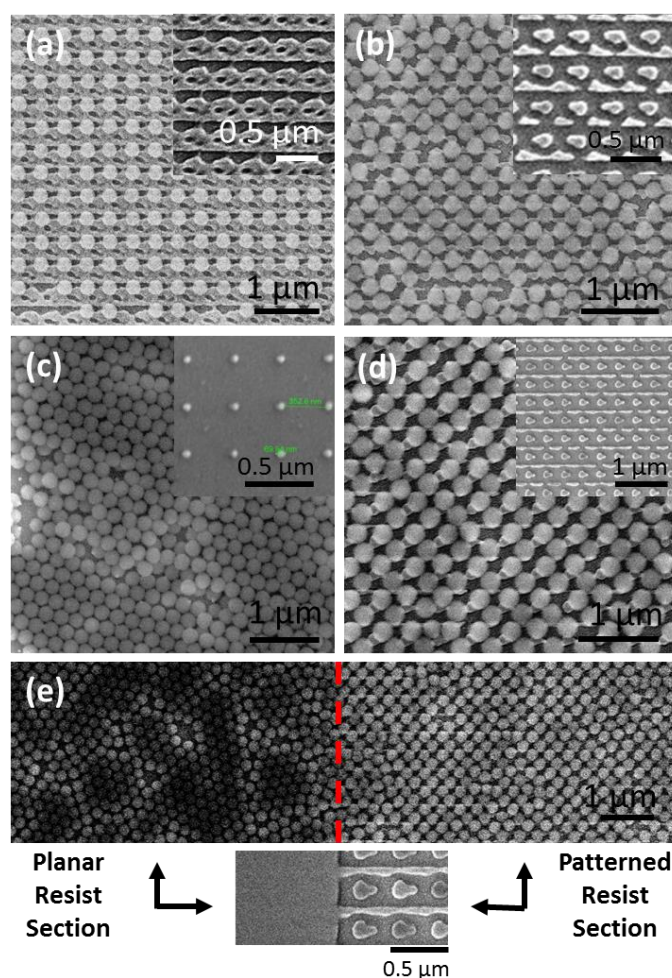


Fig. 5.13 SEM image of 200 nm PS spheres deposited on patterns formed with dose factors of (a) 1.0 and (b) 1.5 for a write field size of $200 \times 200 \mu\text{m}$ and (c) 2.2 and (d,e) 1.7 for a write field size of $50 \times 50 \mu\text{m}$. (e) SEM image showing the disparity between sphere order on the unpatterned and patterned resist with the interface outlined by the red dashed line.

Spheres with a diameter smaller ($\sim 57\%$) than the inter-sphere distance outline by the pattern blueprint were used in order to introduce a size mismatch between the pattern

dimension and the sphere size in each pattern shown in Fig. 5.13. On inspection, spheres were seen to deposit in primarily monolayer arrangements among the patterned resist and also on the planar (non-patterned) resist of the same material. On underexposed patterns, spheres were seen to arrange in a non-close packed, fcc (100) square symmetry, matching that of the substrate unit cell, as is shown in Fig. 5.13 (a). The inset shows the pattern before sphere assembly. An increase in dose factor from 1.0 to 1.5 produces a template with an inter-pillar space in the x-direction of approximately 142 nm, and between 220-230 nm in the y-direction (Fig. 5.13(b)). This pattern is shown to accommodate the 200 nm spheres in a different arrangement to that of Fig. 5.13 (a). The remaining resist left in a grid like pattern around the pillars, shown in the inset of Fig. 5.13 (b), greatly influences the sphere placement by acting as pillars themselves. During dip-coating the spheres organize around the lithographically defined pillars and remaining periodic resist, introducing an ordering that can be described using Woods notation⁶² for overlayer ordering as a c(1×1) fcc (100) or $(\frac{1}{\sqrt{2}} \times \frac{1}{\sqrt{2}})$ R45 order or structure, i.e. a factor of $\sqrt{2}$ smaller than the substrate unit cell and rotated by 45 ° (explained schematically in Fig. 5.16).

The size of the pattern features also has an influence on sphere ordering. As shown in Fig. 5.13 (c), pillars reduced in height and diameter by e-beam exposure to only a dot pattern of PMMA had no visible effect on assembly of the relatively larger spheres, which assembled into their favoured hexagonal (111) ordering on top of the over-exposed pattern. A lower dose exposure for the same size write field produces a pattern which, as per the SEM image in Fig. 5.13 (d), organizes the spheres into $(\frac{1}{\sqrt{2}} \times \frac{1}{\sqrt{2}})$ R45 structure once again.

This variation in sphere organization compared to the more prevalent (111) hexagonal ordering is most noticeable in Fig. 5.13 (e), which shows the interface between planar, un-patterned resist and the patterned region from Fig. 5.13 (d). On the planar resist layer, the spheres adopt their energy minimized order similar to a bare substrate. Sphere self-assembly

is altered once the spheres meet the patterned substrate and immediately adopts a pattern commensurate with the underlying pattern. Importantly, the transition to a different packing structure is sharply defined. SEM images of these two differently ordered areas are shown again in Fig. 5.14 (a) and (b) with their corresponding fast Fourier transforms (FFT) in Fig. 5.14 (c) and (d), respectively showing the difference in the 2D film symmetry and ordering. The FFT of the patterned region is more defined and follows an fcc (100) type lattice. The pattern observed for the area on the planar resist tends more toward long range six-fold symmetry, but currently limited by a large density of defects. The patterned and non-patterned regions are simultaneously in contact with the meniscus line as the substrate is removed from solution therefore coating of the two regions occurs at the same time.

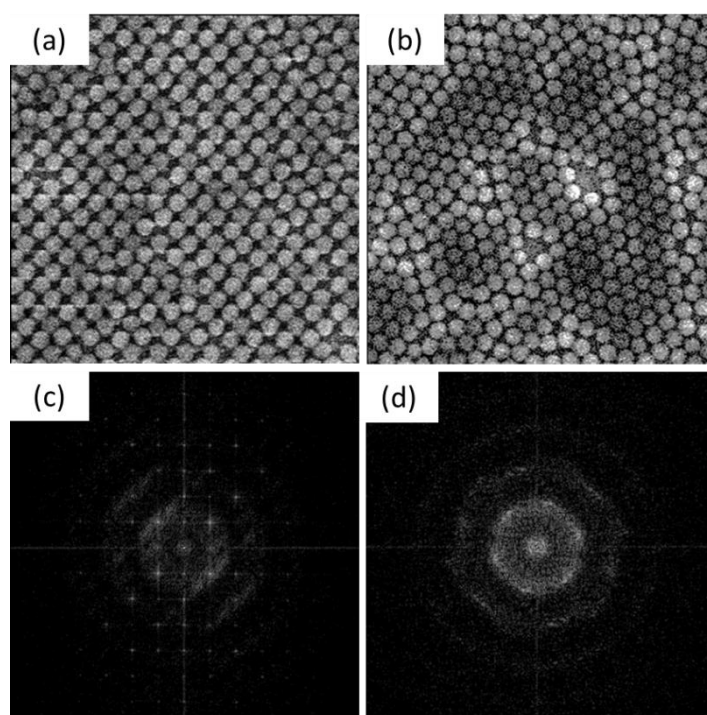


Fig. 5.14 SEM images of spheres ordered on (a) the pattern designed with dose factor 1.7 for a write field size of $50 \times 50 \mu\text{m}$ and (b) on planar resist alongside patterned region and (c) FFT of area shown in (a) and (d) the FFT of area shown in (b).

Variations in beam exposure and proximity effects, discussed previously, can cause discrepancies between outer regions of patterned areas and the centre of these patterns and this can effect sphere organization across the pattern. The dependence of the sphere ordering

to the relative pitch and spacing of pillars (that are large enough to influence sphere position) was examined and shown in Fig. 5.15. During dip-coating, the spheres begin to organize to suit one type of patterned substrate but must be accommodated differently when wider spaced pillars are encountered further into the pattern. Figure 5.15 (b) and (c) outline the differences in the patterns beneath the spheres. In Fig. 5.15 (a), the pattern consists of an area of pillars with a vertical pitch of ~ 250 nm and a lateral pitch providing ~ 200 nm accessible for sphere positioning.

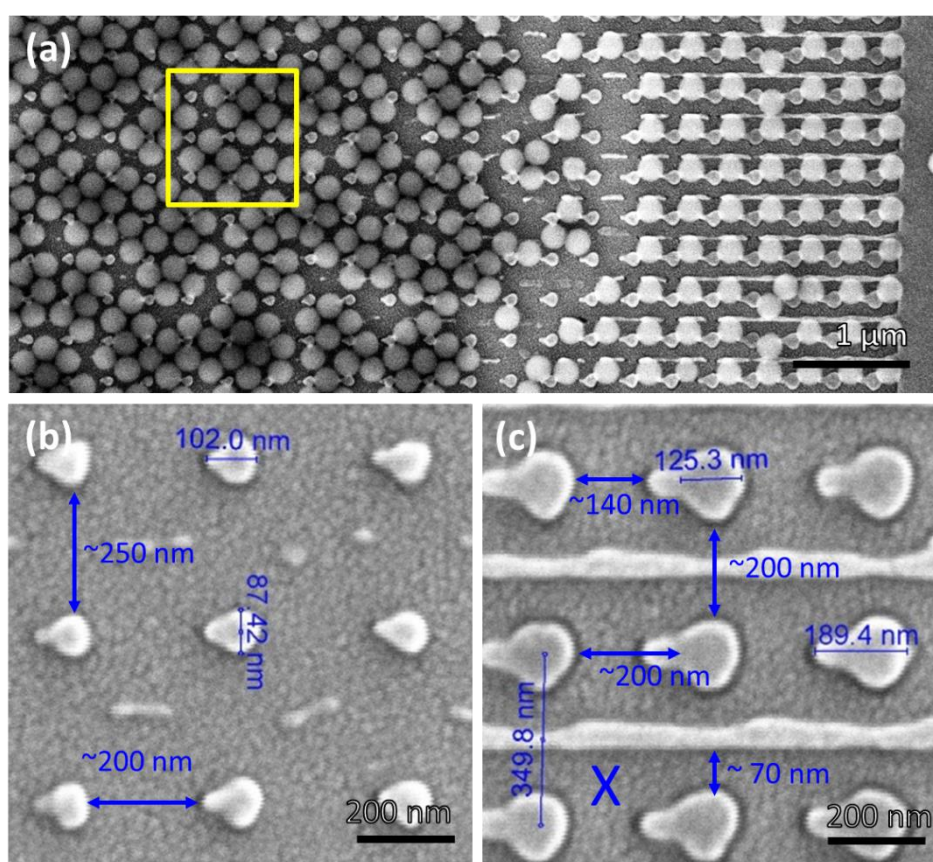


Fig. 5.15 SEM images showing the variation in ordering for 200 nm PS spheres (a) deposited on a pattern exposed with a dose factor of 1.9 to produce variable features due to differences between beam exposure caused by proximity effects and beam levels of deflection towards the centre of the pattern (b) near the outer edge of the pattern (c).

In this region the higher dose exposure and proximity effect closer to pattern centre reduces pillar diameter and removes the linear stripes of resist (seen at the edge of the pattern), providing a square array pattern with inter-pillar distances amenable to sphere positioning. In this region spheres, given the allowed space for deposition, begin to pack as

per the $c(1\times 1)$ fcc (100) or $(\frac{1}{\sqrt{2}} \times \frac{1}{\sqrt{2}})$ R45 order (see yellow box Fig. 5.15(a)). However, along the outer regions of the pattern, the presence of tail features on the edge of the pillars reduces the horizontal pitch between pillars from ~ 200 nm (ideal for the 200 nm spheres used) to ~ 140 nm. The vertical pitch is also obstructed by lines of residual resist on either side of the pillar arrays, reducing the vertical pitch from ~ 200 nm to only ~ 70 nm either side of the linear stripes. In these regions spheres settle atop the pattern in the regions with the most available space for sphere deposition, for example, that marked by the blue X in Fig. 5.15(c). This highlights the sensitivity of sphere deposition and order to substrate characteristics and feature sizes. In order to achieve cohesive ordering on a large scale, pattern development must be of a high quality, consistent and uniform so as to maintain equal ordering.

5.2.4 Binary-like Colloidal PhC using Patterned Substrates

The PMMA pillars can also effectively act as the first adlayer of spheres, and provide an alternative packing structure to create a binary PhC following sphere deposition. In the more widely spaced pillar-patterns similar to that shown in Fig. 5.15 (b), 2D non-closed packed sphere arrangements can be formed. The top surface, shown in Fig. 5.16 (a) indicates spheres in a $(\frac{1}{\sqrt{2}} \times \frac{1}{\sqrt{2}})$ R45 arrangement. This pattern is formed within a pattern unit cell. However, by comparison to the underlying e-beam pattern, the sphere adsorbate unit cell has unit cell dimensions rotated by 45° with respect to the substrate fcc (100) unit cell. As the e-beam patterned PMMA pillar dimensions are $\sim 0.5D$ and thus not crystallographically equivalent, the spheres deposit assembles in the form of a $(\frac{1}{\sqrt{2}} \times \frac{1}{\sqrt{2}})$ R45 structure, i.e. a factor of $\sqrt{2}$ *smaller* than the substrate unit cell (outlined in the schematics I and II in Fig. 5.16). The 200 nm spheres have a size comparable though slightly smaller than the distances between pillars (pattern shown Fig. 5.16 (b)) and therefore must be organized in a square diamond orientation

around each pillar, as shown by the schematic in Fig. 5.16 (c). The pillars take the place of a centre sphere of dimension $D/2$, thus providing a packing density in fcc (100) ordering that is not possible during dip-coating onto unpatterned substrates, nor with binary systems containing two different sphere sizes formed bottom-up. Patterning the substrate with similar polymers facilitates a binary 2D PhC with a higher packing factor per unit area.

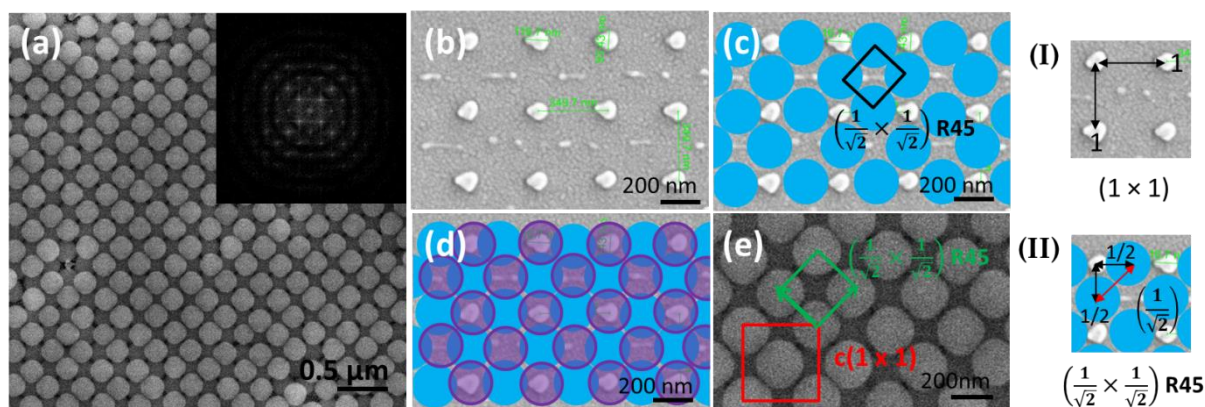


Fig. 5.16 SEM image of (a) 200 nm PS spheres deposited on (b) a template patterned with a DF of 2.0 and schematic depicting (c) the assumed first layer sphere arrangement and (d) second layer sphere arrangement and (e) a high magnification SEM image of the observable top surface structure with the Woods notation for overlayer ordering depicted by the red and green boxes. Inset in (a) is FFT pattern for the area shown in (a) highlighting high degree of symmetry.

To form a 3D artificial opal with this alternative fcc structure, a second layer of spheres, outlined by the schematic Fig. 5.16 (d) is organized on top of the pillars to produce the arrangement shown at high magnification in Fig. 5.16 (e). This indicates the potential of patterned substrates in directing the sphere ordering and opal assembly into periodic structures that differ from the more energetically favoured arrangement of the hexagonal (111) plane parallel to the substrate. By forming a higher packing factor fcc (100) 2D binary PhC using the smaller periodic pillars, the successive layers follow the pattern of the dip-coated spheres. Importantly, this demonstrates the fcc(100) 3D PhC with altered periodicity and structure can be formed using a single sphere size.

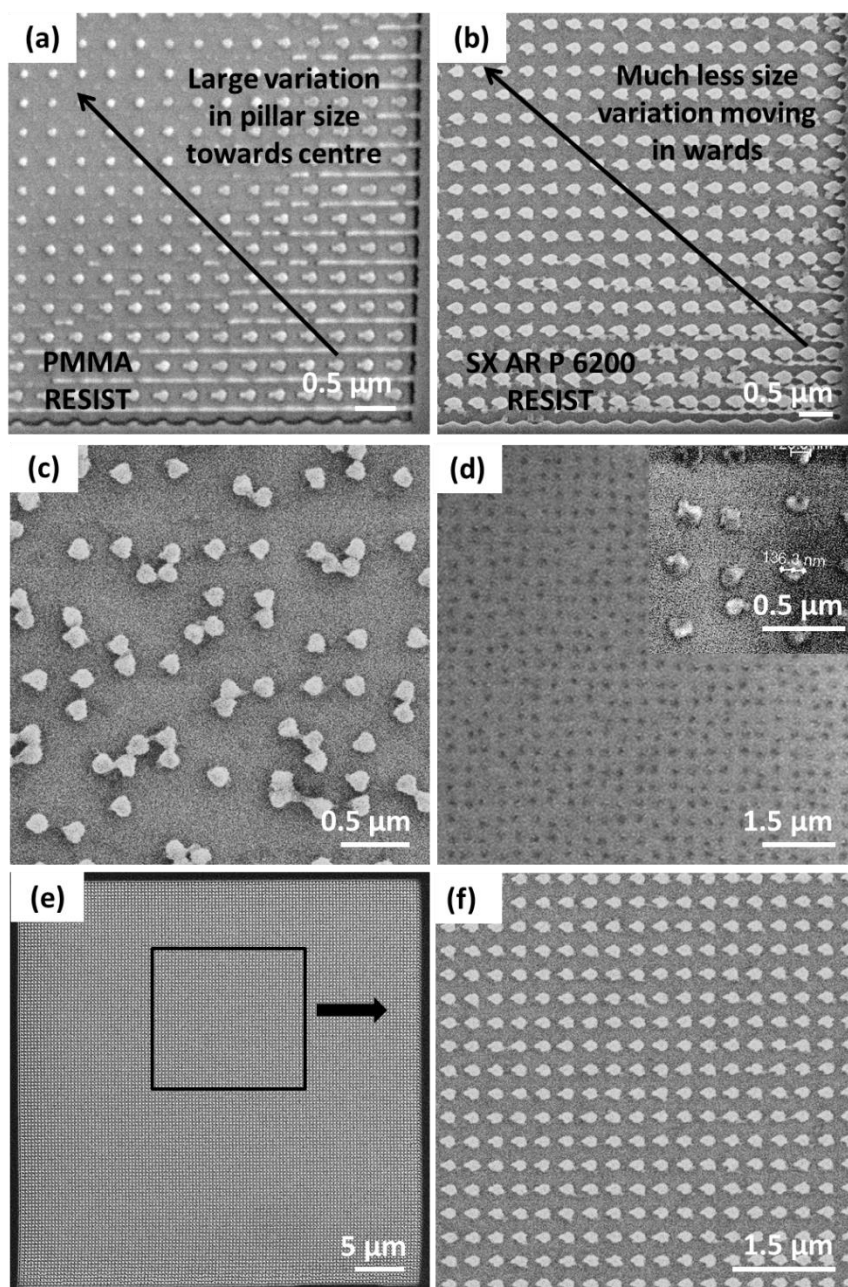


Fig. 5.17 SEM images of the pillars patterned on (a) PMMA resist at a dose of $\approx 197 \mu\text{C}/\text{cm}^2$ and on (b) the higher sensitivity SX AR P 6200 resist at a dose of $44 \mu\text{C}/\text{cm}^2$. Higher dose levels of (c) $51 \mu\text{C}/\text{cm}^2$ and (d) $60 \mu\text{C}/\text{cm}^2$ produced badly formed regions on the sensitive resist but the lower dose $\approx 46 \mu\text{C}/\text{cm}^2$ produced uniform pillar pattern as shown (d) and at higher magnification in (e).

One option for improving initial pattern formation is the use of a resist of higher sensitivity. To investigate this, the resist SXARP6200, also a positive resist, was prepared for beam exposure by the same method outlined in Fig. 5.11. As can be observed in Fig. 5.17, this resist produces much less variation throughout a single write field than the PMMA resist

at a dose value lower ($\approx 44 \mu\text{C}/\text{cm}^2$) than that used with the PMMA resist. As is observed in Fig. 5.17 (c) and (d), a higher dose with this more sensitive resist produces disparities within the template write field. This is shown in Fig. 5.17 (c) where at the higher dose of $\approx 51 \mu\text{C}/\text{cm}^2$, it appears as though in places the pillars detach fully from the substrate once developed and move position within the write field leading to high levels of disorder. This is likely caused by undercutting by the exposure beam, and increased proximity effects for the high sensitivity resist. If the exposure is too high ($\approx 60 \mu\text{C}/\text{cm}^2$), the area is completely overexposed resulting in no pattern, shown in Fig. 5.17 (d). This effect is reduced at lower doses as shown by the SEM images in Fig. 5.17 (e) and (f), producing a nicely uniform pattern for an exposure of $\approx 46 \mu\text{C}/\text{cm}^2$ only. However, the ability to create uniform patterns at lower dose levels could benefit investigations into fast and low impact fabrication routes for the uniform pre-patterning of substrates for sphere assembly by dip-coating. The variable packing order in 2D monolayer artificial opal formation could provide possibilities for tuning the order and arrangement of the spheres across the one device. Depending on the application, a variation in complex photonic band structures are possible using 2D monolayer artificial opal assemblies.

5.3 Conclusions

5.3.1 Substrate Hydrophilicity and Increased Temperature

In summary, 3D photonic crystals were prepared on glass with different degrees of hydrophilicity by noise-assisted dip-coating and a greater level of long-range order was observed in the film formed on the more hydrophilic substrate. Temperature-assisted fast rate dip coating was performed for PS spheres on ITO-coated glass and gold-coated silicon substrates, the increased temperature promoted layer growth on the surface of the solution as the flux of particles towards the air-water interface increased. This resulted in improved

overall adsorption of spheres to the ITO surface and produced artificial opals with improved thickness and order compared with the deposition performed at room temperature. A similar result was observed for PS spheres deposited on gold surfaces at fast rate with improved reflectivity from the opal deposit representative of higher levels of 2D order compared with the patchy deposit observed at room temperature. The added heat was less beneficial for PMMA spheres deposited on gold coated silicon substrates, while increasing thickness, this method is more suited to the formation of thick photonic glasses as opposed to well-ordered opal structures. The lower solution stability of the PMMA spheres compared with the stability of the purchased PS sphere solution leaves insufficient time at the higher temperatures for the spheres to reach energetically favoured ordered arrangements before aggregation occurs. Increased thickness during fast rate dip coating is achievable by controlling the temperature, however, too high an evaporation rate will cause irregularities in the array growth and therefore further exploration is needed to determine the ideal evaporation rate needed to compensate for a particular increase in rate of withdrawal. It is also important to note that this is highly sensitive to both substrate type and sphere type. Polymers are more sensitive to environmental variations than silica spheres for example, and therefore too high a temperature (close to T_g) could cause the polymer spheres to deform.

5.3.2 Patterning

We have shown the sensitivity of opal assembly to substrate orientation and the ability to template PS spheres both in-between and atop patterned PMMA resist. In this way it was possible to demonstrate the subsequent sensitivity of the substrate pattern to the size of the spheres then assembled. Spheres with a diameter of 200 nm, somewhat smaller than the predetermined inter-pillar distance outlined in the blueprint, assembled around the pillars in a diamond like shape with a second layer mimicking the pillar pattern directly. This produced

an adsorbate unit cell a factor of $\sqrt{2}$ smaller than the substrate unit cell in both directions and also rotated by 45° with respect to the substrate fcc (100) unit cell. This highlights the possibilities of moving away from the usual particle-selected arrangement with the hexagonal (111) face parallel to the substrate. The use of PMMA in the pattern formation could allow the possibility of controlled defect introduction into PhCs if the technique is developed further, whereby lattice orientation could be designed so as to allow defect introduction by selective dry etch methods so as to remove the PMMA posts once the spheres are assembled, producing a defect in a specified area. This chapter demonstrated that a polymer pattern as a concept could be used to dip-coat an ordered binary 2D PhC. Second, subsequent growth into a 3D PhC was possible, forming a 3D PhC with a smaller periodicity, using a single sphere size for the 3D opal. Such an arrangement, including the fcc(100) arrangement are not possible with a single sphere size without a smaller secondary sphere/feature. Future efforts could explore combined topographical and chemically patterned techniques, modifying the pillar surfaces with material selective SAMs and using different sphere types, one type of sphere could then be selectively removed or altered to create the desired pattern. A more sensitive resist produced pillar patterns at lower exposures that showed a reduction in proximity effect, improving the pillar uniformity within the one template. Provided dose characteristics are tuned to suit the higher sensitivity and scanning direction and exposure mode explored as possible paths to improvement more perfect pillar patterns could be established to suit specific device requirements. The work has shown the sensitivity of dip-coated spheres to substrate topography, and in turn the sensitivity of surface patterns to sphere size. This type of directed-growth without a need for substrate manipulation beyond removing the resist following assembly could be particularly useful in device designs in need of larger, micro-sized features but is viable for nanoscale features also.

5.4 References

- Galisteo-López, J. F.; Ibisate, M.; Sapienza, R.; Froufe-Pérez, L. S.; Blanco, Á.; López, C., Self-Assembled Photonic Structures. *Adv. Mater.* (2011), **23**, 30-69.
- Braun, P. V., Materials chemistry in 3D templates for functional photonics. *Chem. Mater.* (2013), 277-286.
- Stein, A.; Wilson, B. E.; Rudisill, S. G., Design and Functionality of Colloidal-crystal-templated Materials-Chemical Applications of Inverse Opals. *Chem. Soc. Rev.* (2013), **42**, 2763-2803.
- Denkov, N. D.; Velev, O. D.; Kralchevsky, P. A.; Ivanov, I. B.; Yoshimura, H.; Nagayama, K., Mechanism of Formation of 2-Dimensional Crystals from Latex-Particles on Substrates. *Langmuir* (1992), **8**, 3183-3190.
- Deleuze, C.; Sarrat, B.; Ehrenfeld, F.; Perquis, S.; Derail, C.; Billon, L., Photonic Properties of Hybrid Colloidal Crystals Fabricated by a Rapid Dip-coating Process. *Phys. Chem. Chem. Phys.* (2011), **13**, 10681-10689.
- Dimitrov, A. S.; Nagayama, K., Continuous Convective Assembling of Fine Particles into Two-dimensional Arrays on Solid Surfaces. *Langmuir* (1996), **12**, 1303-1311.
- Pichumani, M.; Bagheri, P.; Poduska, K. M.; Gonzalez-Vinas, W.; Yethiraj, A., Dynamics, Crystallization and Structures in Colloid Spin Coating. *Soft Matter* (2013), **9**, 3220-3229.
- Jiang, P.; Bertone, J. F.; Hwang, K. S.; Colvin, V. L., Single-Crystal Colloidal Multilayers of Controlled Thickness. *Chem. Mater.* (1999), **11**, 2132-2140.
- Rogach, A. L.; Kotov, N. A.; Koktysh, D. S.; Ostrander, J. W.; Ragoisha, G. A., Electrophoretic Deposition of Latex-based 3D Colloidal Photonic Crystals: A Technique for Rapid Production of High-Quality Opals. *Chem. Mater.* (2000), **12**, 2721-2726.
- Bardosova, M.; Hodge, P.; Pach, L.; Pemble, M. E.; Smatko, V.; Tredgold, R. H.; Whitehead, D., Synthetic Opals made by the Langmuir–Blodgett Method. *Thin Solid Films* (2003), **437**, 276-279.
- van Duffel, B.; Ras, R. H. A.; De Schryver, F. C.; Schoonheydt, R. A., Langmuir-Blodgett Deposition and Optical Diffraction of Two-dimensional Opal. *J. Mater. Chem.* (2001), **11**, 3333-3336.
- Oh, J. R.; Moon, J. H.; Yoon, S.; Park, C. R.; Do, Y. R., Fabrication of Wafer-scale Polystyrene Photonic Crystal Multilayers *via* the Layer-by-layer Scooping Transfer Technique. *J. Mater. Chem.* (2011), **21**, 14167-14172.
- Mishchenko, L.; Hatton, B.; Kolle, M.; Aizenberg, J., Patterning Hierarchy in Direct and Inverse Opal Crystals *Small* (2012), **8**, 1904-1911.
- Aizenberg, J.; Muller, D. A.; Grazul, J. L.; Hamann, D. R., Direct Fabrication of Large Micropatterned Single Crystals. *Science* (2003), **299**, 1205-1208.
- Geng, C.; Wei, T.; Wang, X.; Shen, D.; Hao, Z.; Yan, Q., Enhancement of Light Output Power from LEDs Based on Monolayer Colloidal Crystal. *Small* (2014), **10**, 1668–1686.
- Liu, Y.; Qin, F.; Wei, Z.-Y.; Meng, Q.-B.; Zhang, D.-Z.; Li, Z.-Y., 10 fs Ultrafast All-optical Switching in Polystyrene Nonlinear Photonic Crystals. *Appl. Phys. Lett.* (2009), **95**, 131116.
- Yablonovitch, E., Photonic band-gap structures. *J. Opt. Soc. Am. B* (1993), **10**, 283-295.
- Lu, L.; Joannopoulos, J. D.; Soljačić, M., Waveguiding at the Edge of a Three-dimensional Photonic Crystal. *Phys. Rev. Lett.* (2012), **108**, 243901.

19. Paquet, C.; Kumacheva, E., Nanostructured polymers for photonics. *Mater Today* (2008), **11**, 48-56.
20. Fenzl, C.; Hirsch, T.; Wolfbeis, O. S., Photonic Crystals for Chemical Sensing and Biosensing. *Angew. Chem., Int. Ed.* (2014), **53**, 3318-3335.
21. Wang, H.; Zhang, K.-Q., Photonic Crystal Structures with Tunable Structure Color as Colorimetric Sensors. *Sensors* (2013), **13**, 4192-4213.
22. Fu, Y.; Jin, Z.; Liu, Z.; Liu, Y.; Li, W., Self-assembly of Colloidal Crystals from Polystyrene Emulsion at Elevated Temperature by Dip-drawing Method. *Mater. Lett.* (2008), **62**, 4286-4289.
23. Tan, K. W.; Koh, Y. K.; Chiang, Y.-M.; Wong, C. C., Particulate Mobility in Vertical Deposition of Attractive Monolayer Colloidal Crystals. *Langmuir* (2010), **26**, 7093-7100.
24. Khunsin, W.; Amann, A.; Kocher-Oberlehner, G.; Romanov, S. G.; Pullteap, S.; Seat, H. C.; O'Reilly, E. P.; Zentel, R.; Torres, C. M. S., Noise-Assisted Crystallization of Opal Films. *Adv. Funct. Mater.* (2012), **22**, 1812-1821.
25. John, S., Strong Localization of Photons in Certain Disordered Dielectric Superlattices. *Phys. Rev. Lett.* (1987), **58**, 2486-2489.
26. Yablonovitch, E., Inhibited Spontaneous Emission in Solid-State Physics and Electronics. *Phys. Rev. Lett.* (1987), **58**, 2059-2062.
27. Mekis, A.; Chen, J.; Kurland, I.; Fan, S.; Villeneuve, P.; Joannopoulos, J., High Transmission through Sharp Bends in Photonic Crystal Waveguides. *Phys. Rev. Lett.* (1996), **77**, 3787-3790.
28. Yan, Q.; Wang, L.; Zhao, X. S., Artificial Defect Engineering in Three-Dimensional Colloidal Photonic Crystals. *Adv. Funct. Mater.* (2007), **17**, 3695-3706.
29. Tétreault, N.; Mihi, A.; Míguez, H.; Rodríguez, I.; Ozin, G. A.; Meseguer, F.; Kitaev, V., Dielectric Planar Defects in Colloidal Photonic Crystal Films. *Adv. Mater.* (2004), **16**, 346-349.
30. Jiang, P., Surface-Templated Nanostructured Films with Two-Dimensional Ordered Arrays of Voids. *Angew. Chem., Int. Ed.* (2004), **43**, 5625-5628.
31. Ulf, H.; Jonas, P.; Filip, P.; Hans, S.; Lars, M.; Mikael, K. J. J., Nano-aperture Fabrication for Single Quantum Dot Spectroscopy. *Nanotechnology* (2003), **14**, 675.
32. Ren, Z.; Li, X.; Zhang, J.; Li, W.; Zhang, X.; Yang, B., Tunable Two-Dimensional Non-Close-Packed Microwell Arrays Using Colloidal Crystals as Templates. *Langmuir* (2007), **23**, 8272-8276.
33. Ross, C., Patterned Magnetic Recording Media. *Annu. Rev. Mater. Res.* (2001), **31**, 203-235.
34. Yu, X. D.; Shi, L.; Han, D. Z.; Zi, J.; Braun, P. V., High Quality Factor Metallo-dielectric Hybrid Plasmonic-Photonic Crystals. *Adv. Funct. Mater.* (2010), **20**, 1910-1916.
35. Romanov, S. G.; Korovin, A. V.; Regensburger, A.; Peschel, U., Hybrid Colloidal Plasmonic-Photonic Crystals. *Adv. Mater.* (2011), **23**, 2515-2533.
36. Haynes, C. L.; Van Duyne, R. P., Nanosphere Lithography: A Versatile Nanofabrication Tool for Studies of Size-Dependent Nanoparticle Optics. *J. Phys. Chem. B* (2001), **105**, 5599-5611.
37. Ye, X.; Qi, L., Two-dimensionally patterned nanostructures based on monolayer colloidal crystals: Controllable fabrication, assembly, and applications. *Nano Today* (2011), **6**, 608-631.
38. Ge, J.; He, L.; Hu, Y.; Yin, Y., Magnetically induced colloidal assembly into field-responsive photonic structures. *Nanoscale* (2011), **3**, 177-183.

39. He, L.; Wang, M.; Ge, J.; Yin, Y., Magnetic Assembly Route to Colloidal Responsive Photonic Nanostructures. *Acc. Chem. Res.* (2012), **45**, 1431-1440.
40. He, L.; Hu, Y.; Kim, H.; Ge, J.; Kwon, S.; Yin, Y., Magnetic Assembly of Nonmagnetic Particles into Photonic Crystal Structures. *Nano Lett.* (2010), **10**, 4708-4714.
41. Masuda, Y.; Itoh, T.; Koumoto, K., Self-Assembly Patterning of Silica Colloidal Crystals. *Langmuir* (2005), **21**, 4478-4481.
42. Chen, K. M.; Jiang, X.; Kimerling, L. C.; Hammond, P. T., Selective Self-Organization of Colloids on Patterned Polyelectrolyte Templates. *Langmuir* (2000), **16**, 7825-7834.
43. Masuda, Y.; Tomimoto, K.; Koumoto, K., Two-Dimensional Self-Assembly of Spherical Particles Using a Liquid Mold and Its Drying Process. *Langmuir* (2003), **19**, 5179-5183.
44. Dziomkina, N. V.; Vancso, G. J., Colloidal Crystal Assembly on Topologically Patterned Templates. *Soft Matter* (2005), **1**, 265-279.
45. Ye, Y.-H.; Badilescu, S.; Truong, V.-V.; Rochon, P.; Natansohn, A., Self-assembly of Colloidal Spheres on Patterned Substrates. *Appl. Phys. Lett.* (2001), **79**, 872-874.
46. Dziomkina, N. V.; Hempenius, M. A.; Vancso, G. J., Symmetry Control of Polymer Colloidal Monolayers and Crystals by Electrophoretic Deposition on Patterned Surfaces. *Adv. Mater.* (2005), **17**, 237-240.
47. Van Blaaderen, A.; Ruel, R.; Wiltzius, P., Template-Directed Colloidal Crystallization. *Nature* (1997), **385**, 321-324.
48. Wang, D.; Mohwald, H., Template-directed Colloidal Self-assembly - The Route to 'Top-down' Nanochemical Engineering. *J. Mater. Chem.* (2004), **14**, 459-468.
49. Hoogenboom, J. P.; Rétif, C.; de Bres, E.; van de Boer, M.; van Langen-Suurling, A. K.; Romijn, J.; van Blaaderen, A., Template-Induced Growth of Close-Packed and Non-Close-Packed Colloidal Crystals during Solvent Evaporation. *Nano Lett.* (2004), **4**, 205-208.
50. Yin, Y.; Lu, Y.; Gates, B.; Xia, Y., Template-Assisted Self-Assembly: A Practical Route to Complex Aggregates of Monodispersed Colloids with Well-Defined Sizes, Shapes, and Structures. *J. Am. Chem. Soc.* (2001), **123**, 8718-8729.
51. Bitá, I.; Yang, J. K. W.; Jung, Y. S.; Ross, C. A.; Thomas, E. L.; Berggren, K. K., Graphoepitaxy of Self-Assembled Block Copolymers on Two-Dimensional Periodic Patterned Templates. *Science* (2008), **321**, 939-943.
52. Khunsin, W.; Kocher, G.; Romanov, S. G.; Torres, C. M. S., Quantitative Analysis of Lattice Ordering in Thin Film Opal-based Photonic Crystals. *Adv. Funct. Mater.* (2008), **18**, 2471-2479.
53. Protonotarios, E. D.; Baum, B.; Johnston, A.; Hunter, G. L.; Griffin, L. D., An Absolute Interval Scale of Order for Point Patterns. *J. R. Soc. Interface* (2014), **11**.
54. Mulchrone, K. F., Application of Delaunay triangulation to the nearest neighbour method of strain analysis. *Journal of Structural Geology* (2003), **25**, 689-702.
55. Romanov, S. G.; Sotomayor Torres, C. M., Forward Scattering of Light in Thin Opal Films. *Phys. Rev. E* (2004), **69**, 046611.
56. Chen, J.; Anandarajah, A., Van der Waals Attraction between Spherical Particles. *J. Colloid Interface Sci.* (1996), **180**, 519-523.
57. Smith, T., The Hydrophilic Nature of a Clean Gold Surface. *J. Colloid Interface Sci.* (1980), **75**, 51-55.
58. Ding, B.; Bardosova, M.; Pemble, M. E.; Korovin, A. V.; Peschel, U.; Romanov, S. G., Broadband Omnidirectional Diversion of Light in Hybrid Plasmonic-Photonic Heterocrystals. *Adv. Funct. Mater.* (2011), **21**, 4182-4192.

59. Zhang, H.; Yu, X.; Braun, P. V., Three-dimensional Bicontinuous Ultrafast-Charge and -Discharge Bulk Battery Electrodes. *Nat. Nanotechnol.* (2011), **6**, 277-281.
60. von Freymann, G.; Kitaev, V.; Lotsch, B. V.; Ozin, G. A., Bottom-up Assembly of Photonic Crystals. *Chem. Soc. Rev.* (2013), **42**, 2528-2554.
61. Kralchevsky, P. A.; Nagayama, K., Capillary Forces between Colloidal Particles. *Langmuir* (1994), **10**, 23-36.
62. Department of Chemistry, Q. M. U. o. L. 6.1 Classification of Overlayer Structures. http://www.chem.qmul.ac.uk/surfaces/scc/scat6_1.htm (accessed 5th December 2014).

Chapter 6

2D and 3D Vanadium Oxide Inverse Opals and Hollow Sphere Arrays

Abstract

High quality 2D and 3D inverse opals and hollow sphere arrays of vanadium oxide are grown on conductive substrates from colloidal polymer sphere templates formed by electrophoretic deposition or surfactant-assisted dip-coating. Inverse opals (IOs) are formed using variants of solution drop-casting, N₂-gun assisted infiltration and high-rate (200 mm/min) iterative dip-coating methods. Through Raman scattering, transmission electron microscopy and optical diffraction, it is shown how the oxide phase, crystallinity and structure are inter-related and controlled. Opal template removal steps are demonstrated to determine the morphology, crystallinity and phase of the resulting 2D and 3D IO structures. The ability to form high quality 2D IOs is also demonstrated using UV Ozone removal of poly(methyl methacrylate) PMMA spheres. Rapid hydrolysis of the alkoxide precursor allows the formation of 2D arrays of crystalline hollow spheres of V₂O₅ by utilizing over-filling during iterative dip-coating. The methods and crystallinity control allow 2D and 3D hierarchically structured templates and inverse opal vanadium oxides directly on conductive surfaces. This can be extended to a wide range of other functional porous materials for energy storage and batteries, electrocatalysis, sensing, solar cell materials and diffractive optical coatings.

6.1 Introduction

Photonic Crystals (PhCs),¹ the basis for many of nature's colour schemes (butterfly wings, dragonflies, beetles etc.),² have proven highly useful for many applications throughout optics and optoelectronics.^{3, 4} Artificial PhCs, formed through the self-assembly of silica or polymer spheres (PS, PMMA), are becoming widely accepted as low cost and stable templates for the formation of three-dimensional (3D) and two-dimensional (2D) ordered structures.⁵⁻⁸ For example, waveguides,⁹ optical switches,¹⁰ and light-emitting devices¹¹ with enhanced output power and external quantum efficiency have all been successfully produced using artificial opal templates. A growing area of interest however, is the potential these structures hold for the formation of three-dimensionally ordered macroporous (3DOM) or inverse opal battery electrodes.¹²⁻¹⁴ Inverse opals, as the name suggests, are formed by the infiltration of a PhC template or artificial opal with a material precursor and removal of the template. These structures have the advantage of periodicity in all three dimensions and the consequent possibility for a full photonic bandgap. These structures therefore, through template design and choice of infill material, allow the optical characteristics or phenomena of a material system to fit the desired application. The variety of assembly routes¹⁵ available for the formation of these templates, such as spin coating,¹⁶ drop casting,¹⁷ electrophoretic deposition,¹⁸ Langmuir-Blodgett,¹⁹ vertical deposition or dip coating,^{20, 21} make it a well-controlled and easily adapted method for template design and formation.²²

The open and interconnected architectures have been shown to improve battery performance through increased conductivity and better electrolyte infiltration, providing substantial improvements in both power and rate capabilities.^{13, 23} These properties have also been shown to extend to electrocatalysts, allowing a hierarchically

porous host structure that incorporates efficient catalytic nanocrystals.^{24, 25} IO structures could provide that continuously sought after duplex of abilities; the battery that not only stores large amounts of energy in a light weight, binder free mouldable material can exhibit the power density capabilities of super-capacitors with the energy density of Li-ion batteries, required by the growing number of high power applications.^{12, 14, 26-29} Controlled porosity in functional materials has been continuously pursued for a wide range of materials in an effort to understand their synthesis, crystallization and their properties.³⁰⁻³²

Vanadium oxides, in their various phases, have been employed in catalysis, energy storage and supercapacitors,^{10, 33, 34} photovoltaics,³⁵ thermochromic and electrochromic devices,³⁶⁻⁴⁰ as well as sensing^{41, 42} and field emission devices.^{43, 44} Developing methods towards structuring vanadium oxide into ordered and optically significant architectures has the potential therefore to advance several types of functional devices. Vanadium oxide has long been a potential replacement cathode material for use in rechargeable lithium ion batteries due primarily to its layered geometry for cation intercalation, high theoretical specific capacity and low cost.⁴⁵⁻⁴⁸ Silver vanadium oxides are the primary materials for medical device batteries.^{49, 50} When the c-axis of its unit cell structure is minimized, it has been shown to withstand high rates of intercalation allowing fully reversible charge discharge performance.⁵¹⁻⁵³ Most recently, it has proven successful for use in sodium ion batteries, a potential alternative to Li-ion technologies.⁵⁴ Some success has been made in combining the structural advantages of the 3-dimensionally ordered macroporous (3DOM) architecture with V_2O_5 to form a continuous network of porous V_2O_5 material with the aim of tackling the limited electronic conductivity issue faced by most V_2O_5 materials. Recent alternative methods have successfully demonstrated how mesocrystals of V_2O_5 can form using liquid crystals-based phases known as tactosols.

Vanadium oxide inverted opals (IOs) have primarily been formed as non-crystalline aerogel vanadium oxide synthesized from precursor infiltration and solvent exchange methods. Investigations in using electrodeposited crystalline V_2O_5 have also been made, quite often concentrating on electrochromic performance in 3D IOs.^{55, 56} Recently, a thin layer of V_2O_5 was successfully electrodeposited on a 3D aluminum electrode for application as a Li-ion microbattery.⁵⁷ Controlling the phase, crystallinity and order in high quality IOs is critical for correlating structural changes, material and interface composition, electrochemical activity and electrical connection. In optical applications, the requirements for a high degree of order in the crystalline material would benefit from improvements in the methods of their synthesis and formation. Control in under- and over-infiltration methods by altering the influence of strong capillary forces through lowered viscosity and dip-coating for example, also provide opportunities for inverse opals as well as close-packed arrays of hollow spheres. Amorphous 2D structures can demonstrate controlled lasing and somewhat ordered 3D arrays can realize colour arrays independent of reflection angle for example.

Here, several routes for the formation of crystalline or amorphous 2D and 3D V_2O_5 inverse opals and hollow sphere arrays by low temperature crystallization of liquid precursor infiltrated colloidal crystal opal templates formed by electrophoretic deposition are presented. Two alternative methods of precursor infilling are demonstrated and thickness disparities and morphological variations are distinguished by particularly distinct Raman scattering responses and crystalline quality after equal heat treatments. The investigations uncover the specific phase transitions occurring during 3D IO formation. Methods towards the formation of amorphous and crystalline 2D V_2O_5 IOs on conductive substrates are also outlined.

6.2 Results and Discussion

6.2.1 Methods for 2D and 3D Opal Template Formation

The formation of the multilayer PS or PMMA sphere template on ITO glass by electrophoretic deposition is schematically represented in Fig. 6.1(a) and discussed in more detail in chapter 3, section 3.2.4. The resulting polymer sphere deposit is shown in Fig. 6.1(b) with the (111) plane of the colloidal crystal observed parallel to the substrate. This arrangement has the lowest free energy (maximum packing) for spherical colloids and therefore tends to form preferentially to other planes. At longer times the ordering can vary between domains due to the speed of sphere deposition and varying E-field strength.

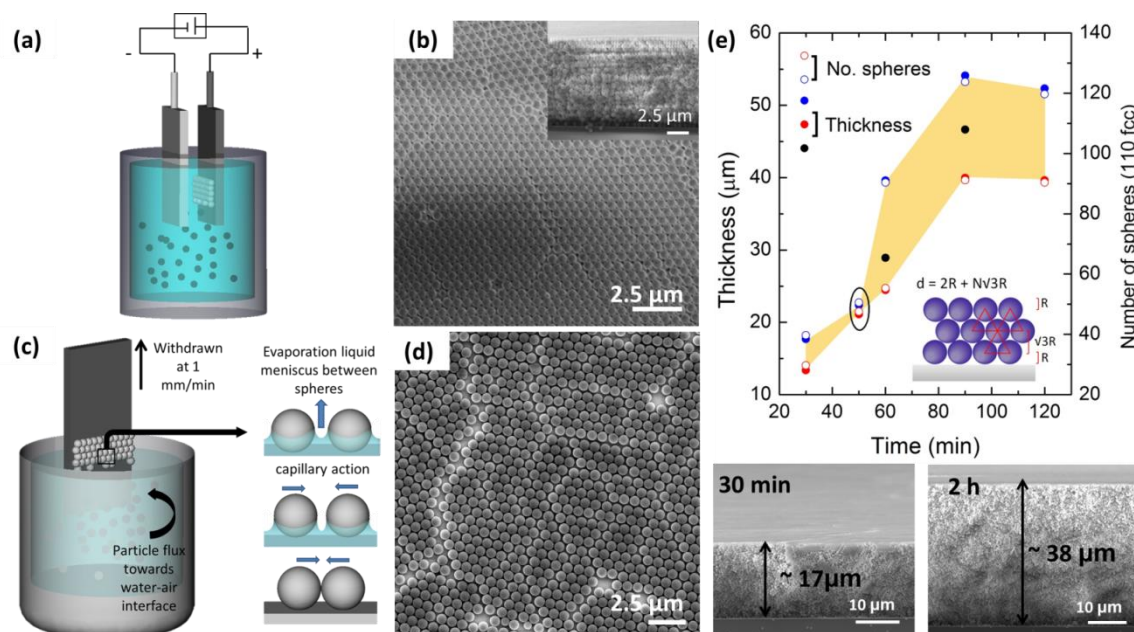


Fig. 6.1 (a) Schematic of the EPD technique. (b) SEM image of the top surface of the multilayer PS sphere template formed by the EPD technique after 10 min at 3 V. Inset shows cross section indicating multilayer thickness. (c) Schematic of the surfactant assisted dip-coating process for PMMA monolayer formation on gold surfaces. (d) SEM image of the top surface of the 2D monolayer PMMA sphere template with inset showing the monolayer with substrate clearly visible (through voids in the film). (e) Variation in EPD opal thickness as a function of deposition time for sulphated PS spheres on gold-coated silicon substrate.

Surfactant-assisted dip coating with PMMA spheres, described in chapter 3, section 3.2.2 and outlined in the schematic Fig. 6.1(c), produces a monolayer of PMMA spheres on gold coated silicon substrates, with a (111)-terminated surface shown in Fig. 6.1(d) similar to EPD deposited 3D opals. The cross-section of a sample prepared by this method (inset of Fig. 6.1(d)), shows a 2D opal from a single layer of spheres. Usually, gold surfaces quickly turn hydrophobic on interaction with air from any carbonaceous contamination, causing difficulties for ordered sphere deposition. The addition of the SDS surfactant to the solution at a concentration above its critical micelle concentration (CMC) causes the formation of micelles of SDS within solution. These micelles, comprising monomers of SDS with the hydrophilic heads orientated towards the polar solute and hydrophobic tails grouped into a hydrophobic core, allow more time for the spheres to reach an ordered organization at the air-liquid interface by reducing the surface tension, which subsequently reduces the evaporation rate. With the high concentration of 8 mg ml^{-1} ($27.7 \times 10^{-3} \text{ mol dm}^{-3}$) of SDS, and consequential formation of micelles in the solution, the horizontal component of the capillary forces between the spheres is increased due to the increase in ionic strength and surface compression of the solution.⁵⁸ Micelles then interact with the spheres and the strong lateral forces push the spheres together as an assembly. As outlined in the previous chapter, it is possible using Derjaguin, Landau, Verwey and Overbeek (DLVO) theory⁵⁹ and some assumptions, to predict that a separation of approximately one micelle thick can occur between neighbouring spheres when SDS above the CMC is used. The spheres' colloidal stability in the presence of SDS at the air-liquid interface within the meniscus and substrate-liquid-air interfaces allows a close-packed ordered monolayer of PMMA spheres that behaves as a 2D diffraction grating.²¹

With respect to the electrophoretic deposition route, as the template deposition time increases the deposited spheres will begin to screen the charge from the electrode,

weakening the attractive forces induced on the negatively charged spheres by reduction of the electric field influencing the electrophoresis. Therefore, the deposition rate will decrease with time and reach a plateau at very high deposition times.⁶⁰ Direct measurements of the thickness of sulphated PS sphere templates on gold-coated silicon substrates for various EPD times at 3 V are shown in Fig. 6.1 (e), with each dark circle corresponding to a sample from which ~3 measurements were taken across between 3 and 5 different cross-sectional SEM images of the sample. Thickness variations between samples as a result of thickness variations between the top and lower areas on the substrate, contribute to the average values.

At longer deposition times, sphere settlement under gravity can create thickness gradients in the resulting opal deposit, evident by the larger variation between data points in Fig. 6.1(e) after longer EPD times. At 3 V, an optimum deposition time (thickness) to form a well ordered stable template on gold coated silicon using sulphated PS spheres without thickness gradients is between 30-50 minutes, highlighted by the black oval in Fig. 6.1(e). The overall mass deposit is directly proportional to the electric field E and the deposition time t , and can also be represented in terms of the opal template thickness d resolved by the number of spheres comprising the deposit as an fcc lattice (see Fig. 6.1(e) inset), such that $E = V/d$, where $d = (2R + N\sqrt{3}R)$, where V is the applied voltage, R is the sphere radius and N the number of spheres stacked in an fcc lattice viewed along the (110) plane. The E-field is shielded preventing further deposition at 3 V after ~90 mins, which corresponds to a threshold E-field for EPD of $\sim 6.5 \times 10^4$ V/m at a final thickness of ~ 45 μm or ~ 103 spheres (Fig. 6.1(e)) in height. Electrophoretic deposition of the spheres is possible on any conductive substrate and on a planar surface, the deposited spheres maintain the (111) plane parallel to the substrate as shown in Fig. 6.2.

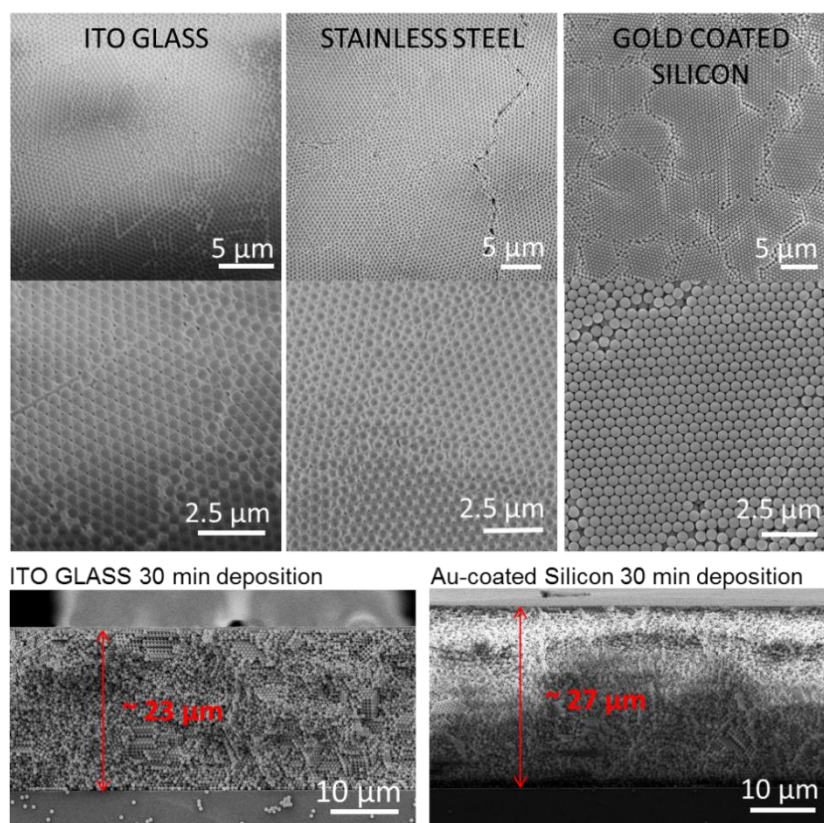


Fig. 6.2 SEM images of sphere templates deposited by electrophoretic deposition at 3V for 30 min on (a) ITO coated glass (b) Stainless Steel and (c) gold-coated Silicon showing domains of spheres arranged with the (111) plane parallel to the substrate. Bottom images indicating high level of thickness achieved for both ITO glass and Au-coated Silicon substrates.

6.2.2 Methods for 2D and 3D Inverse Opal Formation

Through condensation reactions and hydrolysis the liquid precursor solidifies into a rigid, amorphous V_2O_5 network of material when exposed to moisture in the air, once the added IPA is allowed to evaporate. The application of high temperature should then lead to crystallization of the V_2O_5 material. The method of precursor application and the following heat treatment can greatly influence the morphology and crystallinity of the resulting inverse opals. One of the methods developed in this work is schematically represented in Fig. 6.3(a). The 100:1 precursor solution was drop cast on to a multi-layered PS sphere template, covered with a cuvette and using a nitrogen gun, a light

flow of nitrogen gas was applied through the top of the cuvette, as is described in the experimental chapter, in section 3.3.1. The template was then heated for 12 h at 300 °C to simultaneously remove the spheres and crystallize the vanadium oxide. Higher temperatures (~450°C) are often used for the crystallization of vanadium oxide from liquid precursors, however, the vanadium oxide was found to grow to sizes and shapes that obscured the inverse opal morphology at those higher temperatures (See Fig. 6.4).⁶¹ However, when a lower temperature of 300 °C is used for the longer time of 12 h compared to 5-8 h frequently used at the higher temperature, and the nitrogen assisted infiltration is used as opposed to drop casting by other methods, well-ordered porous structures are achievable as shown in Fig. 6.5. This lower temperature crystallization is also mentioned as an alternate route to vanadium oxide porous structures by Stein *et al.* but dismissed due to poor ordering within the structure, it is believed that this something which is alleviated here by the applied pressure during infiltration and hydrolysis.⁶¹

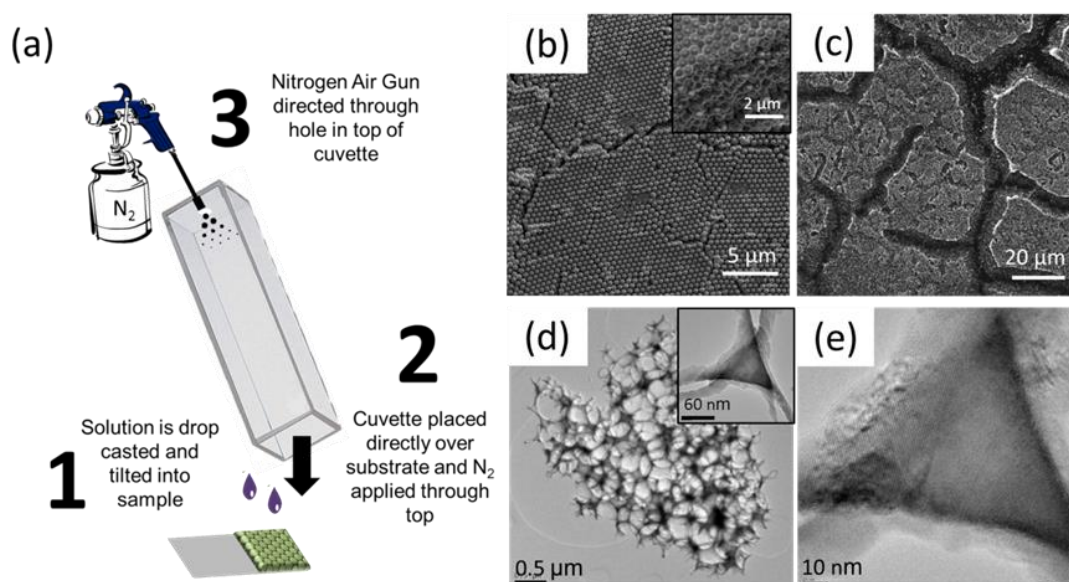


Fig. 6.3 (a) Schematic diagram of drop casting of precursor solution and the nitrogen-gun-assisted infilling of the template and SEM images of (b) infilled template with inset highlighting the infilling of the precursor to under layers and (c) the overall island morphology due to shrinking of material on drying. TEM image of a section of V₂O₅ thin walled IO with the inset highlighting the distinctive triangular wall region between the macro-pores characteristic of hexagonally ordered structures (f) and of the crystalline planes in the triangular section (e).

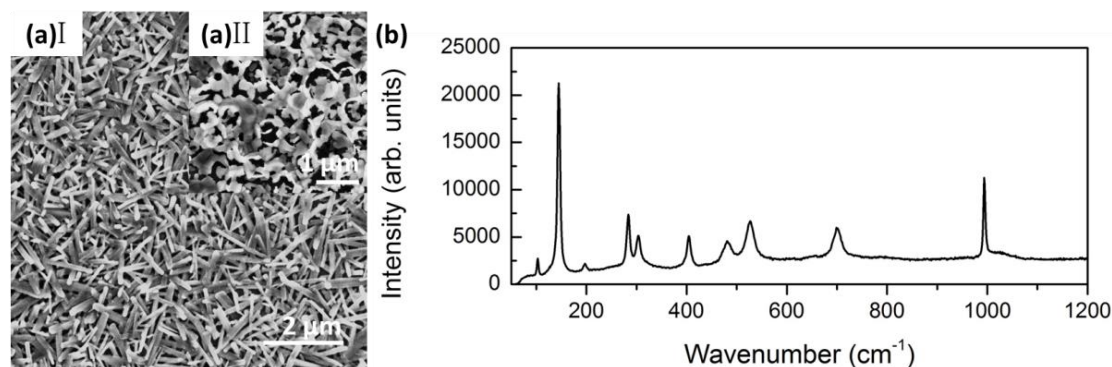


Fig. 6.4 (a)I SEM image of 100:1 IPA:OV(OCH(CH₃)₂)₃ precursor solution drop-cast with 20 s sonication, and then allowed to hydrolyse in air, and heated at 450 °C for 5 hours in a furnace oven (a)II SEM image of another area on same sample highlighting the non-uniformity of infiltration and crystallization by this method (b) Raman spectrum of (a) showing peaks at 103, 145, 197, 285, 304, 405, 483, 526, 703, and 994 cm⁻¹ indicating the formation of crystalline orthorhombic V₂O₅

A common problem for IO formation is crack propagation in the porous materials which can occur on evaporation of infiltrated solution and shrinkage during sphere removal. Large-scale growth of cracks along large domain boundaries of the starting opal template can lead to islands of IO material that mirror the grain shapes of the parent opal. The similarity in the shape and directional growth of the cracks and island boundaries in the IO material compared to the grain boundaries in an opal template can be observed in Fig. 6.3(b) and (c). The application of a steady flow of nitrogen air pressure during solidification increases the infiltration of the precursor through the close packed template as seen in the inset of Fig. 6.3(b). A crystalline IO structure is obtained as indicated by the TEM images shown in Figs 6.3(d) and (e). The nitrogen-containing flow directly above the substrate slows the hydrolysis of the precursor to solid vanadium oxide, improving precursor infiltration through the layers of the template. After 12 h at 300 °C, sphere removal is confirmed by SEM, by which an IO structure comprising two different morphologies is observed, as shown in Fig. 6.5 (a) and Fig. 6.5 (b). The variation in morphology and wall thickness can be attributed to a varied degree of precursor infilling before calcination. Used N₂ flow with slight

overpressure, while successful in retarding hydrolysis, can apply uneven pressure over the template causing infiltration of more material in certain areas. Crystallization by heating to these two areas for an equal amount of time produced IOs at different stages of crystallization with different morphological characteristics. The characteristic Raman modes at 103, 145, 197, 285, 304, 405, 483, 526, 703, and 995 cm^{-1} are clearly visible for both regions in the Raman scattering spectra taken over both areas of morphology and shown in Fig. 6.5 (c). These vibrational modes can be indexed to the orthorhombic structure of crystalline V_2O_5 with a space group $Pm\bar{m}n$ and D_{2h} point symmetry. Thus, when acoustic modes are ignored, the optical modes (21 in total) are defined as: $\Gamma_{\text{opt}} = 7A_g + 7B_{1g} + 3B_{2g} + 4B_{3g} + 3A_u + 3B_{1u} + 6B_{2u} + 6B_{3u}$. In both regions the stretching mode associated with the A_g symmetric vibrations of the short vanadyl $\text{V}=\text{O}$ bond, with the bond length 1.58 Å, is consistent at 995 cm^{-1} , and the skeleton bent vibration at 145 cm^{-1} , evidence of the layered structure of the V_2O_5 , is predominant in both spectra.^{62, 63} Variations in the two spectra however are more easily observed in Figs 6.5 (I)-(III). In these spectra, there are Raman modes visible that are not normally associated with purely crystalline V_2O_5 . A low frequency mode at 167 cm^{-1} (Fig. 6.5(I)) and the higher frequency vibrations at 847, 880 and 936 cm^{-1} (Fig. 6.5(II)) are found for the IO. Another peak is visible at 1033 cm^{-1} (Fig. 6.5(III)), particularly in the spectrum of the wider walled morphology (Fig. 6.5(a)). It is known that several growth mechanisms can occur for different morphologies of vanadium oxide that produce different Raman scattering responses.⁶⁴ In some cases, the peaks at ~167, 848, 880 and 936 cm^{-1} have been described as artefactual,⁶⁵ but have been observed in several reports involving the synthesis of vanadium oxide structures, as a mixed phase with crystalline V_2O_5 .⁶⁶

The peaks at 848 and 936 cm^{-1} were previously assigned by Su et al. to a mode of VO_2 and the peak at 167 cm^{-1} discussed as a result of a VO_x layered structure.⁶⁴

Several reports have considered these peaks as a characteristic of VO_x nanotubes (VONTs),⁶⁶ or a phase seen in VONTs at low annealing temperatures before the nanotube structure is decomposed and re-arranged to form V_2O_5 .^{67, 68} However, Manning *et al.* observed similar Raman scattering spectra in V_2O_5 thin films prepared from VOCl_3 and from XRD analysis suggests that this mixed phase is V_6O_{13} and V_2O_5 .⁶⁹ XRD analysis of a sample which is seen to exhibit the foreign Raman peaks, did not yield an XRD pattern conducive with a presence of V_6O_{13} . The pattern, shown in Fig. 6.5 (f), can be indexed to crystalline orthorhombic V_2O_5 with space group *Pmmn* but does not clearly show any alternative phase of vanadium oxide. Some peaks are observed that could represent tetragonal V_2O_5 and these are indicated by the star symbol in Fig. 6.5(f). The V-O-V in-plane mode depicted in Fig. 6.5(II) can theoretically exhibit an antiphase stretch with B_{2g} symmetry. This mode is a pseudo centro-symmetric bending in pristine orthorhombic, layered $\text{V}_n\text{O}_{2n-1}$. This mode is predicted at $\sim 848 \text{ cm}^{-1}$ when the centro-symmetry is broken and the resulting Raman intensity greatly increases. Therefore the peak at 848 cm^{-1} while present in the Raman scattering response of V_6O_{13} , could also be related to the curved nature of the crystalline structure found in the IO structures⁶⁹⁻⁷¹. The intensities of these extra peaks, relative to the predominant 145 cm^{-1} and 995 cm^{-1} peaks of the pristine V_2O_5 structure, are lower for defined IO walls, as would be expected if pseudo centrosymmetry is returned for thinner, less curved IO features. Defined and thinner opal walls are not as widely curved and possess more linearity (Fig. 6.5b) than seen for the wider walled regions. Their intensity is markedly increased in the wider walled morphology where a much greater quantity of curved crystalline V_2O_5 regions are observed, but may also include a mixed oxide phase.

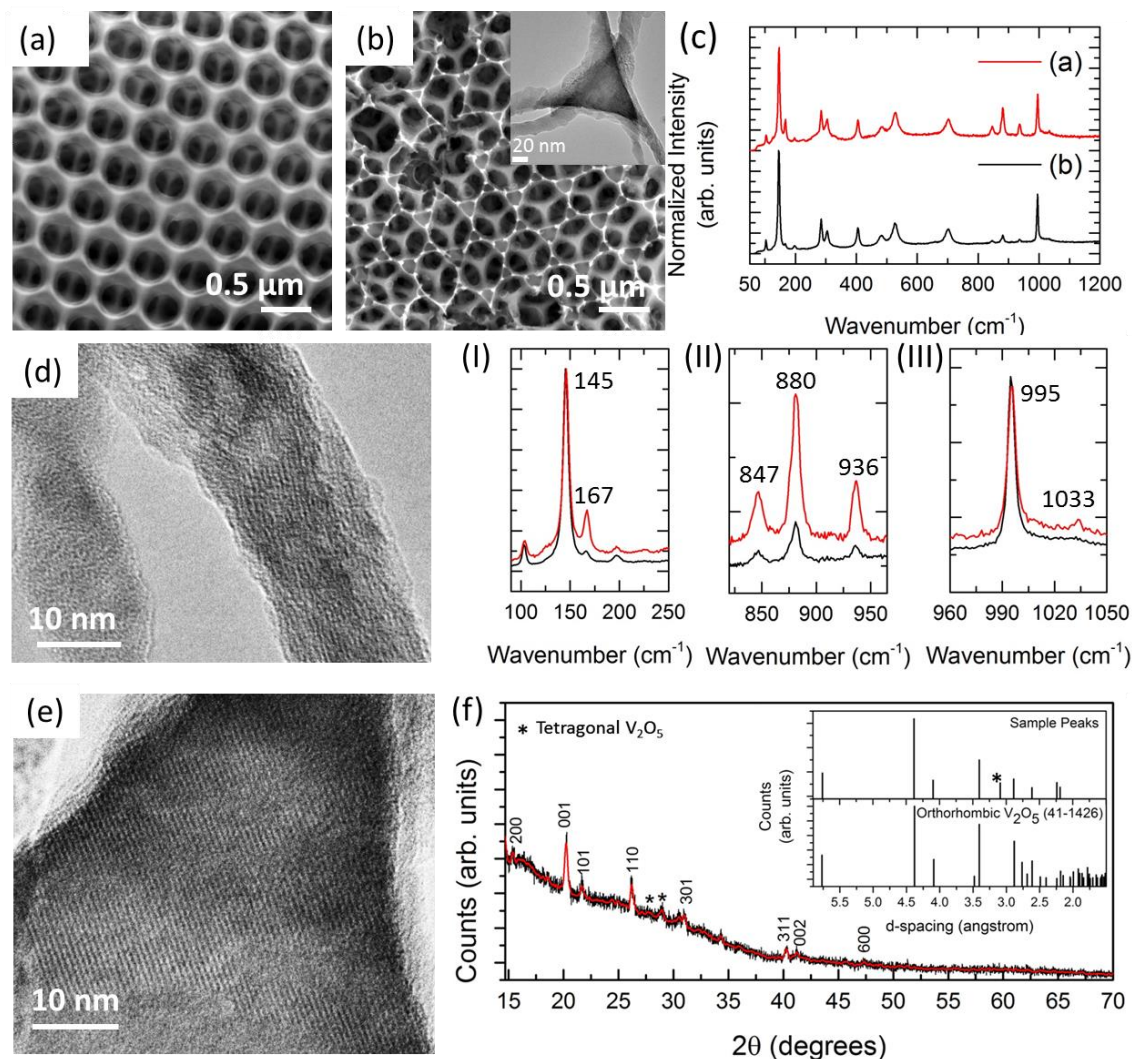


Fig. 6.5 SEM image of (a) wide walled IO structure and (b) thin walled IO structure seen within the same sample formed from the drop casted 100:1 IPA:OV(OCH(CH₃)₂)₃ precursor solution with air-gun assisted infilling and heating for 12 h at 300 °C. (c) Raman scattering for these two different morphologies indicating the greater presence of the minority phase vanadium oxide in the wider walled structure as indicated by the relative intensities of the peaks at (I) 167 cm⁻¹ (II) 847, 880, 936 cm⁻¹ and (III) 1033 cm⁻¹. TEM images of IO walls (d) and part of a triangular inter-pore partition (e). (f) XRD pattern of IOs indexed to orthorhombic V₂O₅ with some reflections indexed to tetragonal V₂O₅.

For the multi-layered (3D opal) templates dip-coated with precursor solution, thin, IO structures are observed in many areas. However, the morphology of the material in many areas in this sample is less defined than in the drop cast sample, with the appearance of precursor over-filling in many areas (see inset Fig. 6.6). Saturation of the top layers, where the precursor completely surrounds individual spheres and

hydrolyses before material can penetrate further into the template, could account for this effect. The IO structures are very thin and have smooth, wider walls that appear less uniform in morphology than those seen in the drop cast sample. The relative thinness of this IO structure, seemingly only one layer of material, compared with the drop cast sample can be explained by a lesser degree of template infilling in the absence of the added nitrogen pressure.

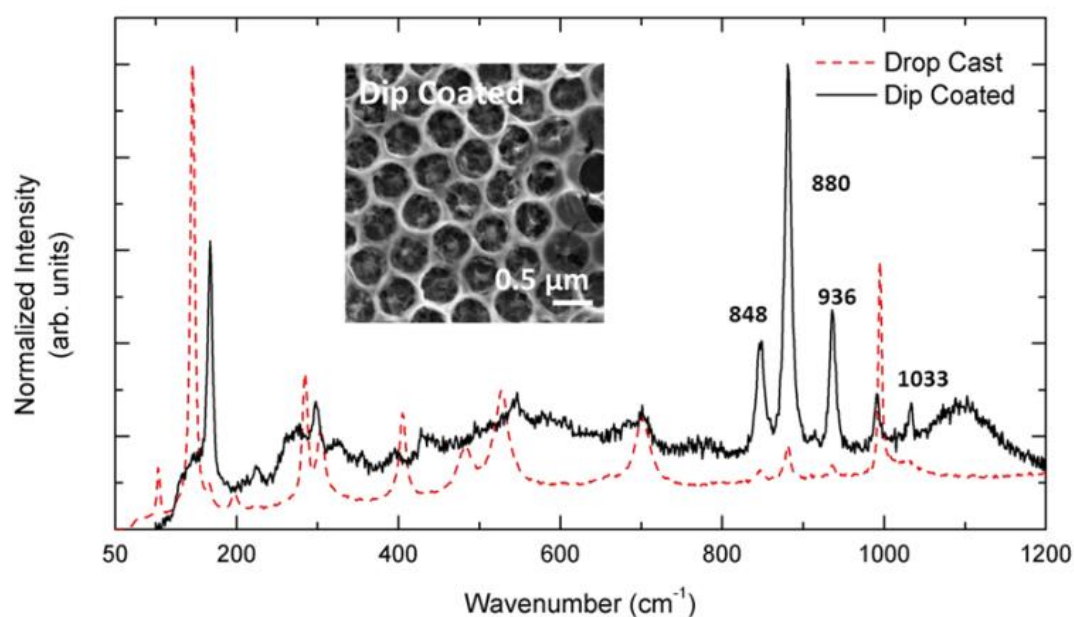


Fig. 6.6 Raman scattering of dip coated multi-layer template (black line) showing the predominance of the V_6O_{13} phase compared to the spectrum (red dashed line) from the drop cast V_2O_5 IO. Inset SEM image of resulting structure after heat treatment at 300 °C for 12 h of the dip coated precursor.

Raman scattering data for the multi-layered template dip-coated with the 100:1 precursor solution, shown in Fig. 6.6, was used to probe the crystal structure and composition simultaneously. The dominant Raman signature observed is identical to the minority phase of vanadium oxide seen in the spectrum in Fig. 6.5 for the drop-cast IO, most likely V_6O_{13} . The strongest peaks are the vibrations at 167, 848, 880 and 936 cm^{-1} and the peaks associated with crystalline V_2O_5 , most importantly the vibrations at 145 and 995 cm^{-1} , associated with long range order within the V_2O_5 planes and the

$V^{5+}=O$ bond respectively, are not seen. However, low intensity broad peaks are observed at ~ 224 , 298, 428, and 546 cm^{-1} , which are characteristic of the bending vibrations of V_2O_5 . The mode at 224 cm^{-1} is often found only when the modes associated with a frustrated or curved V_2O_5 crystal are found. The peak observed at $\sim 701\text{ cm}^{-1}$ is the classic in-plane antiphase V-O stretching vibration of V_2O_5 . The peak observed at $\sim 991\text{ cm}^{-1}$ likely represents the stretching vibration of $V^{4+}=O$ bond, before complete oxidation to $V^{5+}=O$, indicating a presence of more V^{4+} ions than V^{5+} . This Raman signature is identical to that presented by Huotari *et al.* for VO_x -NT, referred to as the VO_x -NT phase (curved or scrolled oxide).⁶⁶ The Raman shift associated with bond order = 2 for the V=O bond can be expressed semi-empirically as $\nu = 21349 \exp(-1.9176R)$ where R is the bond length.⁷² For all 3D and 2D IOs and hollow sphere arrays in this work, this bond is unique to V_2O_5 with a shift close to 1000 cm^{-1} and confirms V_2O_5 formation (see Table S1). Curvature or change in phase must also be those that contain a vanadyl oxygen that is unconstrained at a similar frequency.

The 100:1 precursor solution was drop-cast on a multilayer template and subjected to $300\text{ }^\circ\text{C}$ for the longer time of 24 h also. The resulting inverted structure can be seen in Fig. 6.7(a) and at higher magnification in (b). The resulting IOs exhibit long range crystalline order. IOs with well-defined, circular pores are observed with walls that are smooth and somewhat thicker than the thin walled area shown in the sample heated for 12 h (Fig. 6.5(b)). After 24 h crystallization, the sensitivity of material crystallization to the precursor infilling and resultant IO thickness is also observed, shown in Figs 6.7 (c)-(f). It is evident through SEM inspection that the wall thickness and the presence of the mixed phase vanadium oxide is not solely dependent on heating time but on precursor hydrolysis and crystallization, with the mixed Raman response (Fig. 6.7(c)) more prevalent in areas of greater material thickness and better inverted opal structure.

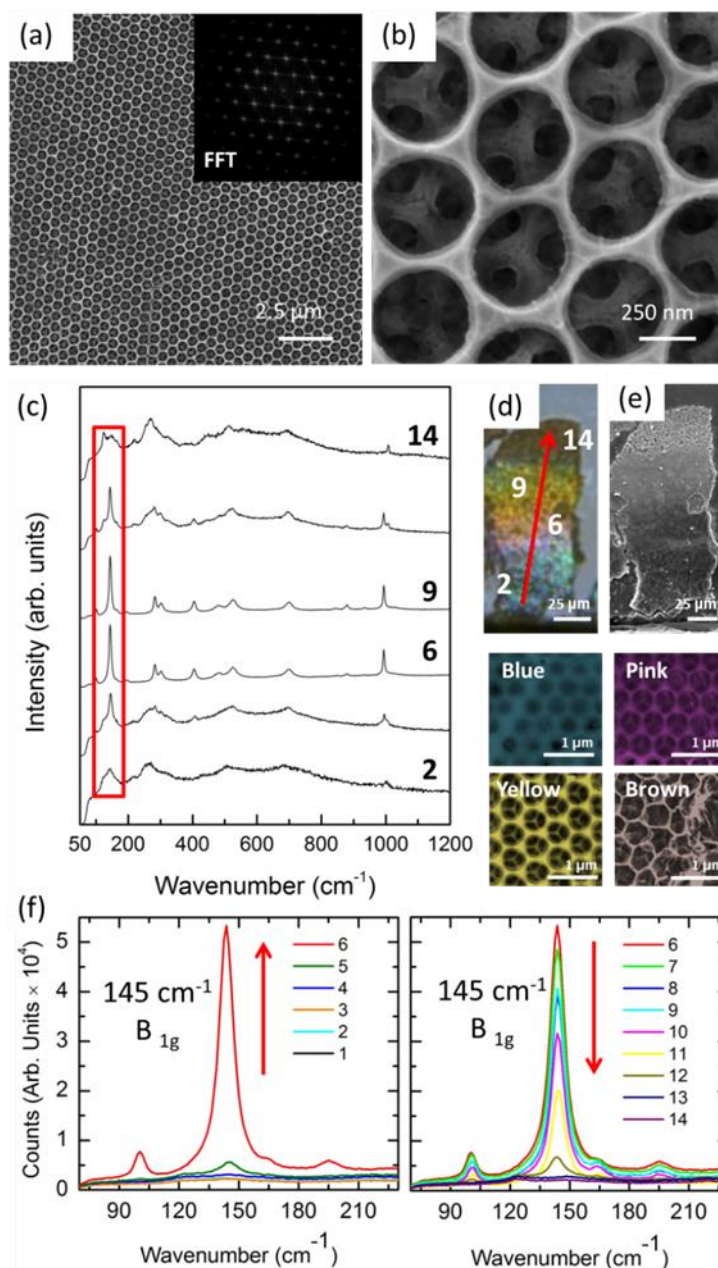


Fig. 6.7 SEM images (a) and (b) of the structure formed from drop cast 100:1 IPA:OV(OCH(CH₃)₂)₃ precursor solution and N₂-gun assisted infilling with heating for 24 h at 300 °C. (Inset (a)) FFT of the IO structure. (c) Raman scattering data across a region of differing structure and thickness as indicated by accompanying SEM images which correspond to the different colour of light reflected in the optical image in (d) where the red arrow indicates the direction where Raman scattering data was obtained. (e) SEM image of region shown in (d). (f) Evolution of the 145 cm⁻¹ peak along the direction indicated by the arrow.

The change in the wall thickness and thus the periodicity of the IO causes a change in the wavelength of the primary diffraction, or color, as observed in Fig. 6.7(d,e). Differing degrees of crystallization and spectral purity can be seen in the Raman

signatures across the area (Fig. 6.7(c)). Fig. 6.7(f) highlights the 145 cm^{-1} (B_{1g}) mode from all 14 spectra taken along the arrow in Fig. 6.7(d). This is shown to approach higher intensity (spectra 1-6) where it approaches the ‘pink’ region indicative of high structural order, and then decreases in intensity (spectra 6-14) as the IO reduces in thickness, characterized by a poorly structured material shown as the brown area in Fig. 6.7 (d). The same intensity variation is also found in the peak at 995 cm^{-1} ($V=O$) proving that structural changes, both internal crystalline changes and external macro-structure changes, can correlate to different diffraction in the IOs. In such a scenario, hydrolysing alkoxide may pool and begin to solidify affecting the thickness or concentration of material between the spheres when hydrolysis occurs. Some methods have been proposed where vacuum infiltration can greatly improve the overall infiltration⁷³. This however, is suitable for liquid precursors that solidify and crystallize upon heating after full infiltration. Preventing hydrolysis on surfaces with large surface area is less simplistic. This sensitivity of the Raman characterization to thickness variations and the mixed phase relationship to the amount of precursor present is shown throughout Fig. 6.7.

The Raman response previously discussed as either associated with VONTs-like curved V_2O_5 or a mixture of V_2O_5 polymorphs are observed in the areas on this sample corresponding to the IO structures with the highest order and regularity, comprised of defined walls and ordered sub-surface. The fact that these peaks are observed in the areas of darkest colour and best defined in structure further suggests these features could be both material and structurally dependent – a higher portion of curved crystalline V_2O_5 contributes to the Raman tensor where the V-O bond polarizability is increased. This occurs when the pseudo-centrosymmetric structure of the in-plane V-O-V bond is broken due to curvature in the layered structure. The minority phase peaks, occur in the wider walled morphologies uniquely, pointing further towards their

dependence on the arrangement of the vanadium oxide layers in the network of material during hydrolysis and crystallization and an increased level of precursor settlement in those areas. Through TEM, Fig. 6.5 and Fig. 6.8, the crystalline nature of all materials is evident, though complete 3D lattice structures are not easily resolved due to the curvature of the materials.

Crystallinity is more distinct in the inter-pore triangular partitions, seen in the TEM images for the drop cast precursor under nitrogen flow and heated for 12 h at 300 °C shown in Fig. 6.2 and 6.5 (e), and for the dip coated sample shown in Fig. 6.8 (a). The IO walls for both the dip coated sample (Fig. 6.8 (b)) and drop cast samples (Fig. 6.5(d), Fig. 6.8(c) and (d)) are shown by TEM imaging to be crystalline regardless of slight variations in crystal structure observed in their Raman responses.

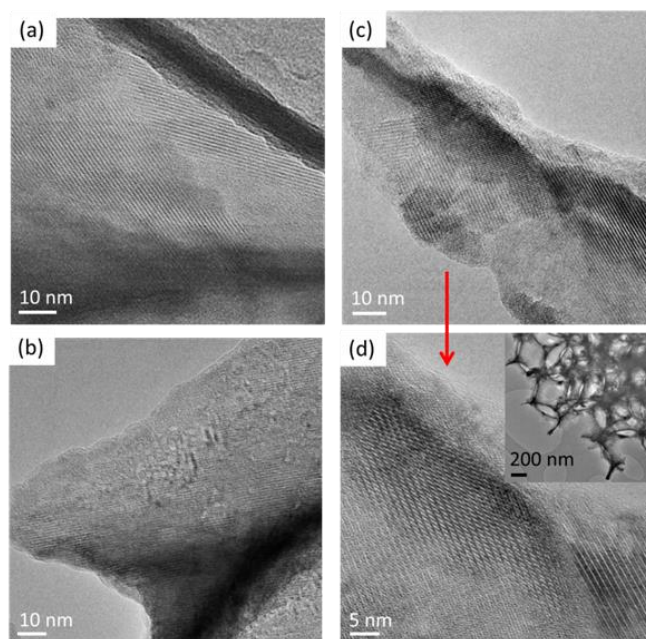


Fig. 6.8 TEM images indicating the crystalline walls of the IO structures formed from the dip coated multi-layer template (a) and (b) and the drop cast 100:1 IPA:OV(OCH(CH₃)₂)₃ precursor solution and air-gun assisted infilling with heating for 24 h at 300 °C (c) and (d).

In order to determine if the crystallization of the amorphous, hydrolysed material, deposited in the multilayer templates by the two infilling techniques, affected the

dimensions of the resulting IOs, line profiles from SEM images of the different structures were taken and are shown in Fig. 6.9. The templates were formed using 500 nm PS spheres and a plot profile for a typical top surface of such a template is shown in Fig. 6.9(a). The peak to peak distance can be taken as a representation of the diameter of the spheres, however, due to secondary electron contrast variations it can more accurately be used as a simple comparison between the plot profile of a closely packed template and the plot profiles taken for the inverted structures shown below this in Fig. 6.9(b)-(e). All data indicate an average value for the pores very close to the diameter of the spheres (500 nm). The average pore diameter for structures formed after drop casting and 24 h heating at 300 °C is ~505 nm, a broad short intensity peak is also visible in between the more defined peaks of the top surface walls, which are due to the structures visible in the second layer. However, the larger width of these peaks compared with that of the higher intensity peaks indicates a variation (increase) in wall thickness deeper into the structure.

Comparing Fig. 7(c) and (d) the differences between the two morphologies observed in the drop cast sample with nitrogen assisted infilling, and heating for only 12 h at 300 °C, can be more closely realized. The average pore diameter for Fig. 7(d) is ~ 480 nm, this is 20 nm less the average diameter calculated for the plot profile of Fig. 7(e) of ~500 nm. This, combined with the broader, high intensity peaks observed in Fig. 7(d) suggests the wall variation is ~20 nm between this morphology and the thinner walled morphology of the highly defined structure shown in Fig. 7(d). However, both these plot profiles produce low intensity peaks, characteristic of the IO walls on the layer beneath the top surface and seen between the pores, exactly midway between the high intensity peaks, (~240 nm and ~250 nm respectively) revealing a very well-ordered structure in both cases.

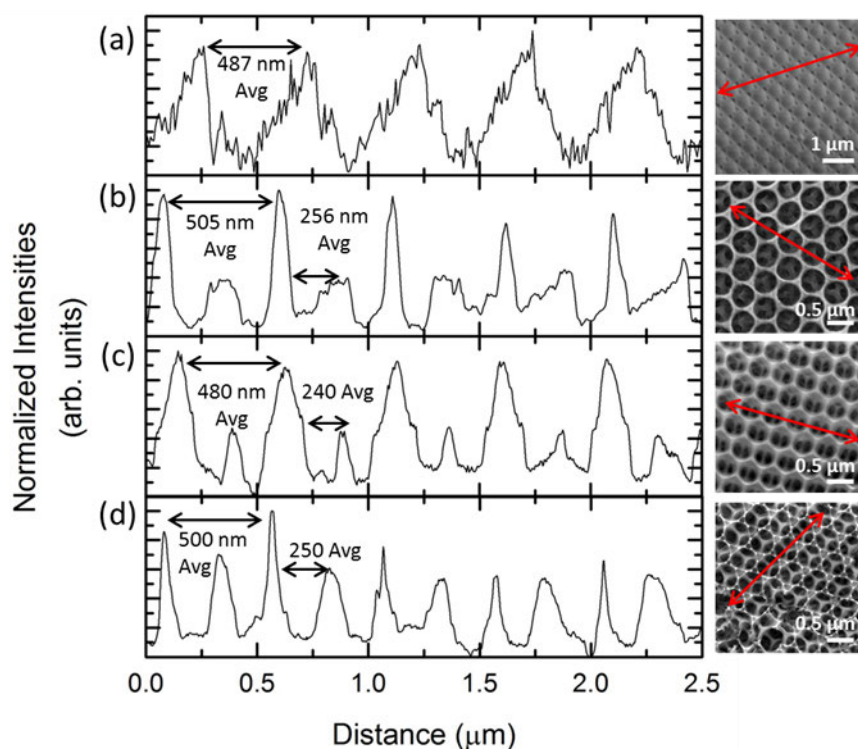


Fig. 6.9 Plot profiles and corresponding SEM images for a multilayer template of 500 nm spheres deposited by EPD on ITO glass (a) and 100:1 IPA:OV(OCH(CH₃)₂)₃ precursor solution drop cast with N₂-gun assisted infilling and heating for 24 h at 300 °C (b) dip coated at a rate of 200 mm/min × 10. (c) Drop cast with N₂-gun assisted infilling and heating for 12 h at 300 °C producing the wide walled morphology (d) and thin walled morphology (e).

Examining the plot profiles, it is clearly observed that the superior IOs are attained for the drop cast precursor with hydrolysis under applied nitrogen. However, this method of infiltration can produce areas of uneven infilling which can lead to variations in morphology and crystallinity within the one template outlined in Fig. 6.5 and Fig. 6.7. This could be beneficial in applications where variations in material phase, structure or crystallinity are desirable. By controlling the thickness and amount of material deposited, the length and temperature of the applied heat, different phases of the same material can be synthesized in one step and as part of the same structure. Thin walled structures are only attained after sufficient calcination time under temperature, however wider walled structures are also achieved in areas where it is

possible more material hydrolysed out of solution. This is also likely controllable by using a different precursor with a slower rate of hydrolysis or by varying the ratio of IPA to undiluted precursor, a smaller ratio will produce more crystalline V_2O_5 for a given area, but in this case hydrolysis will occur faster on exposure to air and moisture. These samples present possibilities for further investigations into the origin of the peaks sometimes seen in VONTs and their structural dependence, the arrangement of the vanadium oxide layers in the wider-walled IOs may be comparable to the walls of VONTs, unlike the mono-layered or thin-walled IOs.

6.2.3 2D Monolayer Vanadium Oxide IOs and Hollow Sphere Arrays

Monolayer templates of PMMA spheres were formed by surfactant assisted dip-coating as outlined in our previous work,²¹ whereby the spheres, due to micellar interactions, exhibit better order at higher withdrawal rates. This produced order similar to that of a 2D diffraction grating as shown by the light scattered normal to the surface when incident at 60° as shown in Chapter 4 Fig. 4.2. 2D monolayer templates prepared in this way were then infiltrated using the same two methods used for the multilayer samples. The resulting formations can be seen in Fig. 6.10 (a-e). Due to the thin nature of the monolayer templates the precursor, when drop cast and subjected to nitrogen air flow for infiltration assistance, pooled beneath the spheres between the substrate surface and sphere resulting in basin-like structures shown in plan-view in Fig. 6.10(a) with the cross-section shown in Fig. 6.10(d). Hydrolysis within a confined inter-sphere spacing solidifies into a solid but at the expense of a reduced volume, causing defects within the structure.

The over-filling effect discussed for the multi-layer dip-coated sample (summarised schematically in Fig. 6.10(b)) was more pronounced in 2D monolayer-templated structures, leading to alternative structure formation. In such cases an array of hollow

spheres of V_2O_5 are formed as seen in Fig. 6.10(c) and Fig. 6.10(e). It is postulated that hollow sphere 2D arrays could form as a consequence of the instability of PMMA in IPA, leading to their breakdown with each successive dip-coating in conjunction with continuing material hydrolysis. This would account for the absence of the spheres after heating without appreciable breakdown in the individual crystalline hollow spheres. Alternatively, the spheres may decompose with evolving CO and CO_2 escaping through voids in the structure. Future research may provide routes for optimizing single and multilayer hollow sphere arrays.

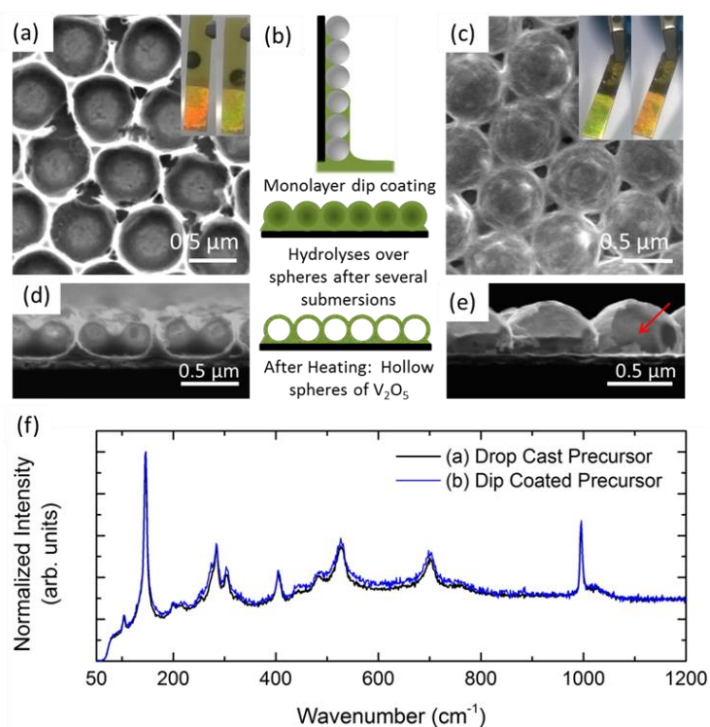


Fig. 6.10 SEM image of the structure formed when precursor is drop cast with nitrogen assisted infilling and heated at 12 h for 300 °C (b) Schematic outlining the dip coating of a monolayer PMMA template with precursor solution and (c) SEM image of a monolayer PMMA template when dip coated at a rate of 200 mm/min \times 10 times (d) Cross section of the structure shown in (a). (e) Cross section of the hollow spheres shown in (c). The red arrow indicates the hollow internal structure. Insets of (a) and (c) show optical image of the visible diffraction from these 2D structures. (f) Raman scattering of both (a) and (b) confirming V_2O_5 crystal structure.

Both the drop cast and dip coated monolayer templates when heated at 300 °C for 12 h produced crystalline V_2O_5 as evidenced by the Raman scattering shown in Fig.

6.10(f). The characteristic peaks of the 145 cm^{-1} and 995 cm^{-1} , indicative of the layered structure and V=O short-length bond are well defined. Mixed phases of vanadium oxide are not observed in either of the monolayer IOs. This provides further evidence that template thickness influences crystallization; 12 h at $300\text{ }^{\circ}\text{C}$ is insufficient for complete crystallization to orthorhombic V_2O_5 but is sufficient for these thinner material deposits in 2D IOs.

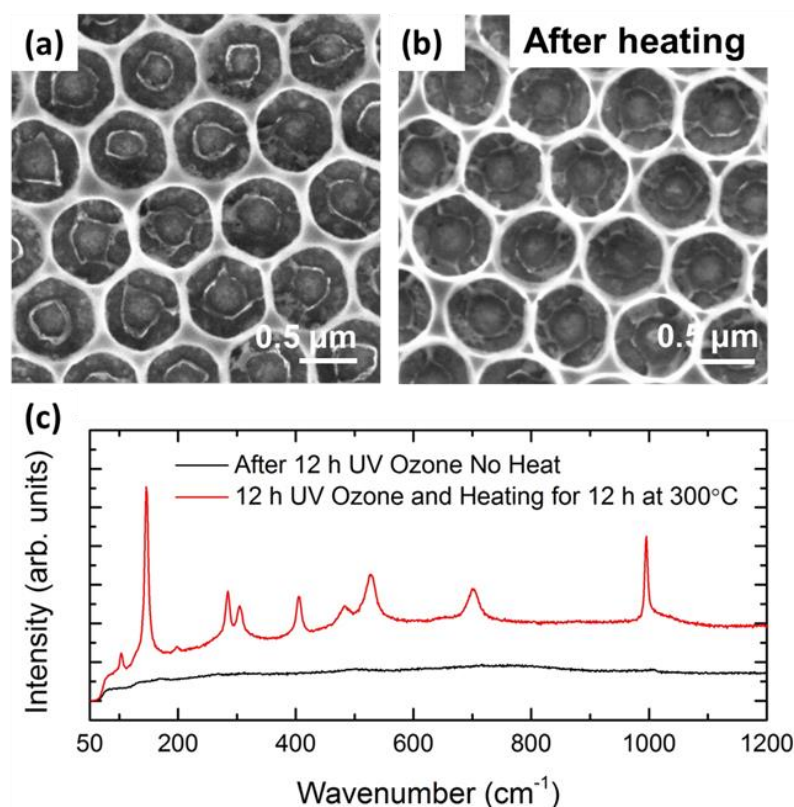


Fig. 6.11 SEM images of (a) amorphous vanadium oxide after dip coating with 100:1 IPA:OV(OCH(CH₃)₂)₃ precursor at a rate of $150\text{ mm/min} \times 8$ times and treated with UV Ozone for 12 h and (b) following heating for 12 h at $300\text{ }^{\circ}\text{C}$. (c) Raman scattering spectrum of the crystallized vanadium oxide following the heat treatment compared with the amorphous spectrum of the material after UV Ozone treatment only.

A monolayer template dipped at a rate of $150\text{ mm/min} \times 8$ into precursor solution and subjected to UV Ozone for an extended period of 12 h, produced 2D IO structures of amorphous vanadium oxide, shown in Fig. 6.11(a), i.e. removing the sphere template without crystallizing the vanadium oxide precursor. This results in a high quality, ordered 2D vanadium oxide IO with smooth walls. After heating for 12 h at

300 °C to crystallize the material, the structure shows negligible deformation, shown in Fig. 6.11(b) and is confirmed as crystalline V_2O_5 as indicated by the Raman scattering spectrum shown in Fig. 6.11(c) thus indicating UV Ozone is a viable route for amorphous IO structures that do not experience further growth or modifications to overall arrangement during heating and crystallization. Due to the monolayer nature of the template, infilling is possible after fewer coats. These structures have extremely thin walls due to the ratio of alkoxide in the IPA diluted precursor and subsequent low filling factor after only one dip at a very high withdrawal rate of 150 mm/min (see Fig. 6.12).

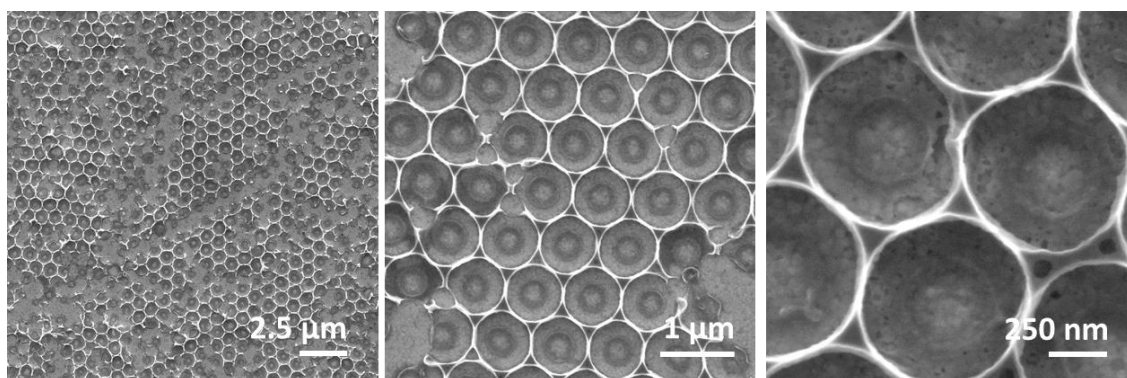


Fig. 6.12 SEM images at different magnification of the IO structure formed from dip coating a monolayer template in the 100:1 IPA:OV(OCH(CH₃)₂)₃ precursor solution, only once at the rate of 150 mm/min showing effects of low filling factor.

The thickness of the multilayer samples and the close-packed arrangement presented a difficulty in complete infiltration of precursor and the resulting IO can often lose up to 70% in thickness after sphere removal. This could be reduced with further study into concentration and type of precursor solution. However, it has been shown that the synthesis of ordered IOs of crystalline vanadium oxide are possible when using liquid precursor and infilling is assisted by some applied pressure and slowed hydrolysis. Crystallization is then performed at a lower temperature and a longer time than most

other methods so as to prevent over-growth of the vanadium oxide and loss of the ordered structure.

6.3 Conclusions

This work has demonstrated how 2D and 3D opals and corresponding vanadium oxide IOs can be formed from electrophoretically deposited templates and subsequent infilling methods. The formation and crystallization of the 2D and 3D V_2O_5 inverse opals was followed in detail through Raman scattering and it was demonstrated that the type of precursor deposition and subsequent treatment and removal of the sphere template greatly influences the morphology, crystallinity and phase of the resulting IOs structures. The ability to form high quality 2D IOs using UV Ozone removal of PMMA sphere templates was also demonstrated. Where rapid hydrolysis can occur, the formation of 2D arrays of crystalline hollow spheres of V_2O_5 is possible using iterative coating of opal templates. These methods provide viable routes for amorphous IO materials that optically diffract as a grating that can later be crystallized without major changes to the IO structure, and can likely be generalized to any template structure that uses polymeric templates capable of decomposition under UV-ozone exposure. The infiltration methods described here have the advantage of simplicity and low cost, with samples subjected to less strenuous synthetic methods, compared to other methods, such as CVD, ALD, PLD or electro-deposition, which is desirable for up-scaled charge storage, sensing, electrochromic and optoelectronic applications involving ordered or porous materials that behave as photonic crystals or 2D diffraction gratings. Very large-area templating on planar and curved metallic surfaces augers well for applications that require a conductive contact to the functional porous materials.

6.4 References

1. Stein, A.; Schrodin, R. C., Colloidal Crystal Templating of Three-dimensionally Ordered Macroporous Solids: Materials for Photonics and Beyond. *Curr. Opin. Solid State Mater. Sci.* (2001), **5**, 553-564.
2. Vukusic, P.; Sambles, J. R., Photonic Structures in Biology. *Nature* (2003), **424**, 852-855.
3. Osiak, M.; Geaney, H.; Armstrong, E.; O'Dwyer, C., Structuring Materials for Lithium-ion Batteries: Advancements in Nanomaterial Structure, Composition, and Defined Assembly on Cell Performance. *J. Mater. Chem. A* (2014), **2** 9433-9460.
4. Stein, A.; Wilson, B. E.; Rudisill, S. G., Design and Functionality of Colloidal-crystal-templated Materials-Chemical Applications of Inverse Opals. *Chem. Soc. Rev.* (2013), **42**, 2763-2803.
5. López, C., Materials Aspects of Photonic Crystals. *Adv. Mater.* (2003), **15**, 1679-1704.
6. Braun, P. V., Materials chemistry in 3D templates for functional photonics. *Chem. Mater.* (2013), 277-286.
7. Hatton, B.; Mishchenko, L.; Davis, S.; Sandhage, K. H.; Aizenberg, J., Assembly of Large-area, Highly Ordered, Crack-free Inverse Opal Films. *Proc. Natl. Acad. Sci. U. S. A.* (2010), **107**, 10354-10359.
8. Aizenberg, J.; Muller, D. A.; Grazul, J. L.; Hamann, D. R., Direct Fabrication of Large Micropatterned Single Crystals. *Science* (2003), **299**, 1205-1208.
9. Lu, L.; Joannopoulos, J. D.; Soljačić, M., Waveguiding at the Edge of a Three-Dimensional Photonic Crystal. *Phys. Rev. Lett.* (2012), **108**, 243901.
10. Liu, Y.; Qin, F.; Wei, Z.-Y.; Meng, Q.-B.; Zhang, D.-Z.; Li, Z.-Y., 10 fs ultrafast all-optical switching in polystyrene nonlinear photonic crystals. *Appl. Phys. Lett.* (2009), **95**, 131116.
11. Geng, C.; Wei, T.; Wang, X.; Shen, D.; Hao, Z.; Yan, Q., Enhancement of Light Output Power from LEDs Based on Monolayer Colloidal Crystal. *Small* (2014), **10**, 1668-1686.
12. Zhang, H.; Braun, P. V., Three-Dimensional Metal Scaffold Supported Bicontinuous Silicon Battery Anodes. *Nano Lett.* (2012), **12**, 2778-2783.
13. Pikul, J. H.; Zhang, H. G.; Cho, J.; Braun, P. V.; King, W. P., High-power Lithium Ion Microbatteries from Interdigitated Three-dimensional Bicontinuous Nanoporous Electrodes. *Nat. Commun.* (2013), **4**, 1732-1736.
14. Zhang, H.; Yu, X.; Braun, P. V., Three-dimensional Bicontinuous Ultrafast-Charge and -Discharge Bulk Battery Electrodes. *Nat. Nanotechnol.* (2011), **6**, 277-281.
15. von Freymann, G.; Kitaev, V.; Lotsch, B. V.; Ozin, G. A., Bottom-up Assembly of Photonic Crystals. *Chem. Soc. Rev.* (2013), **42**, 2528-2554.
16. Pichumani, M.; Bagheri, P.; Poduska, K. M.; Gonzalez-Vinas, W.; Yethiraj, A., Dynamics, Crystallization and Structures in Colloid Spin Coating. *Soft Matter* (2013), **9**, 3220-3229.
17. Velev, O. D.; Furusawa, K.; Nagayama, K., Assembly of Latex Particles by Using Emulsion Droplets as Templates. 1. Microstructured Hollow Spheres. *Langmuir* (1996), **12**, 2374-2384.
18. Rogach, A. L.; Kotov, N. A.; Koktysh, D. S.; Ostrander, J. W.; Ragoisha, G. A., Electrophoretic Deposition of Latex-based 3D Colloidal Photonic Crystals: A Technique for Rapid Production of High-Quality Opals. *Chem. Mater.* (2000), **12**, 2721-2726.
19. van Duffel, B.; Ras, R. H. A.; De Schryver, F. C.; Schoonheydt, R. A., Langmuir-Blodgett Deposition and Optical Diffraction of Two-dimensional Opal. *J. Mater. Chem.* (2001), **11**, 3333-3336.
20. Khunsin, W.; Amann, A.; Kocher-Oberlehner, G.; Romanov, S. G.; Pullteap, S.; Seat, H. C.; O'Reilly, E. P.; Zentel, R.; Torres, C. M. S., Noise-Assisted Crystallization of Opal Films. *Adv. Funct. Mater.* (2012), **22**, 1812-1821.

21. Armstrong, E.; Khunsin, W.; Osiak, M.; Blömker, M.; Torres, C. M. S.; O'Dwyer, C., Ordered 2D Colloidal Photonic Crystals on Gold Substrates by Surfactant-Assisted Fast-Rate Dip Coating. *Small* (2014), **10**, 1895-1901.
22. Mandlmeier, B.; Minar, N. K.; Feckl, J. M.; Fattakhova-Rohlfing, D.; Bein, T., Tuning the Crystallinity Parameters in Macroporous Titania Films. *J. Mater. Chem. A* (2014), **2**, 6504-6511.
23. Ma, D. L.; Cao, Z. Y.; Wang, H. G.; Huang, X. L.; Wang, L. M.; Zhang, X. B., Three-dimensionally Ordered Macroporous FeF₃ and its In situ Homogenous Polymerization Coating for High Energy and Power Density Lithium Ion batteries. *Energy Environ. Sci.* (2012), **5**, 8538-8542.
24. Collins, G.; Blömker, M.; Osiak, M.; Holmes, J. D.; Bredol, M.; O'Dwyer, C., Three-Dimensionally Ordered Hierarchically Porous Tin Dioxide Inverse Opals and Immobilization of Palladium Nanoparticles for Catalytic Applications. *Chem. Mater.* (2013), **25**, 4312-4320.
25. Dusastre, V., Inverse Opal Catalysts. *Nat. Mater.* (2013), **12**, 1080.
26. Kang, B.; Ceder, G., Battery materials for ultrafast charging and discharging. *Nature* (2009), **458**, 190-193.
27. Tarascon, J.-M.; Armand, M., Issues and challenges facing rechargeable lithium batteries. *Nature* (2011), **414**, 359-367.
28. Vu, A.; Qian, Y.; Stein, A., Porous Electrode Materials for Lithium-Ion Batteries – How to Prepare Them and What Makes Them Special. *Adv. Energy Mater.* (2012), **2**, 1056-1085.
29. Stein, A., Energy storage: Batteries take charge. *Nat. Nanotechnol.* (2011), **6**, 262-263.
30. Wei, D.; Scherer, M. R. J.; Bower, C.; Andrew, P.; Ryhänen, T.; Steiner, U., A Nanostructured Electrochromic Supercapacitor. *Nano Lett.* (2012), **12**, 1857-1862.
31. Armatas, G. S.; Kanatzidis, M. G., Hexagonal Mesoporous Germanium. *Science* (2006), **313**, 817-820.
32. Warren, S. C.; Messina, L. C.; Slaughter, L. S.; Kamperman, M.; Zhou, Q.; Gruner, S. M.; DiSalvo, F. J.; Wiesner, U., Ordered Mesoporous Materials from Metal Nanoparticle-Block Copolymer Self-Assembly. *Science* (2008), **320**, 1748-1752.
33. Bao, J.; Zhang, X.; Bai, L.; Bai, W.; Zhou, M.; Xie, J.; Guan, M.; Zhou, J.; Xie, Y., All-solid-state flexible thin-film supercapacitors with high electrochemical performance based on a two-dimensional V₂O₅·H₂O/graphene composite. *J. Mater. Chem. A* (2014), **2**, 10876-10881.
34. Zhu, J.; Cao, L.; Wu, Y.; Gong, Y.; Liu, Z.; Hoster, H. E.; Zhang, Y.; Zhang, S.; Yang, S.; Yan, Q.; Ajayan, P. M.; Vajtai, R., Building 3D Structures of Vanadium Pentoxide Nanosheets and Application as Electrodes in Supercapacitors. *Nano Lett.* (2013), **13**, 5408-5413.
35. Bitai, I.; Yang, J. K. W.; Jung, Y. S.; Ross, C. A.; Thomas, E. L.; Berggren, K. K., Graphoepitaxy of Self-Assembled Block Copolymers on Two-Dimensional Periodic Patterned Templates. *Science* (2008), **321**, 939-943.
36. Aizenberg, J.; Braun, P. V.; Wiltzius, P., Patterned Colloidal Deposition Controlled by Electrostatic and Capillary Forces. *Phys. Rev. Lett.* (2000), **84**, 2997-3000.
37. Granqvist, C. G., Electrochromics for Smart Windows: Oxide-based Thin Films and Devices. *Thin Solid Films* (2014), **564**, 1-38.
38. Kats, M. A.; Sharma, D.; Lin, J.; Genevet, P.; Blanchard, R.; Yang, Z.; Qazilbash, M. M.; Basov, D. N.; Ramanathan, S.; Capasso, F., Ultra-thin Perfect Absorber Employing a Tunable Phase Change Material. *Appl. Phys. Lett.* (2012), **101**, -.
39. Kats, M. A.; Blanchard, R.; Zhang, S.; Genevet, P.; Ko, C.; Ramanathan, S.; Capasso, F., Vanadium Dioxide as a Natural Disordered Metamaterial: Perfect Thermal Emission and Large Broadband Negative Differential Thermal Emittance. *Phys. Rev. X* (2013), **3**, 041004.
40. Prum, R. O.; Quinn, T.; Torres, R. H., Anatomically diverse butterfly scales all produce structural colours by coherent scattering. *J. Exp. Biol.* (2006), **209**, 748-765.

41. Li, Z.; Hu, Z.; Peng, J.; Wu, C.; Yang, Y.; Feng, F.; Gao, P.; Yang, J.; Xie, Y., Ultrahigh Infrared Photoresponse from Core–Shell Single-Domain-VO₂/V₂O₅ Heterostructure in Nanobeam. *Adv. Funct. Mater.* (2014), **24**, 1821-1830.
42. Nicholas, F.; Sean, M. P.; Mark, W. H.; Bharadwaja, S. S. N., Electrical Properties of Vanadium Oxide Thin Films for Bolometer Applications: Processed by Pulse dc Sputtering. *J. Phys. D: Appl. Phys.* (2009), **42**, 055408.
43. Kim, G. T.; Muster, J.; Krstic, V.; Park, J. G.; Park, Y. W.; Roth, S.; Burghard, M., Field-effect Transistor made of Individual V₂O₅ Nanofibers. *Appl. Phys. Lett.* (2000), **76**, 1875-1877.
44. Zhai, T.; Liu, H.; Li, H.; Fang, X.; Liao, M.; Li, L.; Zhou, H.; Koide, Y.; Bando, Y.; Golberg, D., Centimeter-Long V₂O₅ Nanowires: From Synthesis to Field-Emission, Electrochemical, Electrical Transport, and Photoconductive Properties. *Adv. Mater.* (2010), **22**, 2547-2552.
45. Whittingham, M. S., Lithium Batteries and Cathode Materials. *Chem. Rev.* (2004), **104**, 4271-4301.
46. O'Dwyer, C.; Lavayen, V.; Tanner, D. A.; Newcomb, S. B.; Benavente, E.; González, G.; Torres, C. M. S., Reduced Surfactant Uptake in Three Dimensional Assemblies of VO_x Nanotubes Improves Reversible Li⁺ Intercalation and Charge Capacity. *Adv. Funct. Mater.* (2009), **19**, 1736-1745.
47. Wang, Y.; Takahashi, K.; Lee, K.; Cao, G. Z., Nanostructured Vanadium Oxide Electrodes for Enhanced Lithium-ion Intercalation. *Adv. Funct. Mater.* (2006), **16**, 1133-1144.
48. Vernardou, D.; Louloudakis, D.; Spanakis, E.; Katsarakis, N.; Koudoumas, E., Electrochemical Properties of Vanadium Oxide Coatings Grown by Hydrothermal Synthesis on FTO substrates. *New J. Chem.* (2014), **38**, 1959-1964.
49. Takeuchi*, K. J.; Marschilok, A. C.; Davis, S. M.; Leising, R. A.; Takeuchi*, E. S., Silver Vanadium Oxides and Related Battery Applications. *Coord. Chem. Rev.* (2001), **219–221**, 283-310.
50. Leising, R. A.; Takeuchi, E. S., Solid-State Synthesis and Characterization of Silver Vanadium Oxide for Use as a Cathode Material for Lithium Batteries. *Chem. Mater.* (1994), **6**, 489-495.
51. Chan, C. K.; Peng, H.; Twisten, R. D.; Jarausch, K.; Zhang, X. F.; Cui, Y., Fast, Completely Reversible Li Insertion in Vanadium Pentoxide Nanoribbons. *Nano Lett.* (2007), **7**, 490-495.
52. Sakamoto, J. S.; Dunn, B., Hierarchical Battery Electrodes Based on Inverted Opal Structures. *J. Mater. Chem.* (2002), **12**, 2859-2861.
53. Rolison, D. R.; Long, J. W.; Lytle, J. C.; Fischer, A. E.; Rhodes, C. P.; McEvoy, T. M.; Bourg, M. E.; Lubers, A. M., Multifunctional 3D Nanoarchitectures for Energy Storage and Conversion. *Chem. Soc. Rev.* (2009), **38**, 226-252.
54. Tepavcevic, S.; Xiong, H.; Stamenkovic, V. R.; Zuo, X.; Balasubramanian, M.; Prakapenka, V. B.; Johnson, C. S.; Rajh, T., Nanostructured Bilayered Vanadium Oxide Electrodes for Rechargeable Sodium-Ion Batteries. *ACS Nano* (2012), **6**, 530-538.
55. Li, L.; Steiner, U.; Mahajan, S., Improved Electrochromic Performance in Inverse Opal Vanadium Oxide Films. *J. Mater. Chem.* (2010), **20**, 7131-7134.
56. Scherer, M. R. J.; Li, L.; Cunha, P. M. S.; Scherman, O. A.; Steiner, U., Enhanced Electrochromism in Gyroid-Structured Vanadium Pentoxide. *Adv. Mater.* (2012), **24**, 1217-1221.
57. Rehnlund, D.; Valvo, M.; Edström, K.; Nyholm, L., Electrodeposition of Vanadium Oxide/Manganese Oxide Hybrid Thin Films on Nanostructured Aluminum Substrates. *J. Electrochem. Soc.* (2014), **161**, D515-D521.
58. Marquez, M.; Grady, B. P., The Use of Surface Tension to Predict the Formation of 2D Arrays of Latex Spheres Formed via the Langmuir–Blodgett-Like Technique. *Langmuir* (2004), **20**, 10998-11004.
59. Verwey, E. J. W.; Overbeek, J. T. G., *Theory of the Stability of Lyophobic Colloids*. Elsevier: Amsterdam, (1948).
60. Besra, L.; Liu, M., A Review on Fundamentals and Applications of Electrophoretic Deposition (EPD). *Prog. Mater. Sci.* (2007), **52**, 1-61.

61. Holland, B. T.; Blanford, C. F.; Do, T.; Stein, A., Synthesis of Highly Ordered, Three-Dimensional, Macroporous Structures of Amorphous or Crystalline Inorganic Oxides, Phosphates, and Hybrid Composites. *Chem. Mater.* (1999), **11**, 795-805.
62. Baddour-Hadjean, R.; Pereira-Ramos, J. P.; Navone, C.; Smirnov, M., Raman Microspectrometry Study of Electrochemical Lithium Intercalation into Sputtered Crystalline V₂O₅ Thin Films. *Chem. Mater.* (2008), **20**, 1916-1923.
63. Glynn, C.; Thompson, D.; Paez, J.; Collins, G.; Benavente, E.; Lavayen, V.; Yutronic, N.; Holmes, J. D.; Gonzalez, G.; O'Dwyer, C., Large Directional Conductivity Change in Chemically Stable Layered Thin Films of Vanadium Oxide and a 1D Metal Complex. *J. Mater. Chem. C* (2013), **1**, 5675-5684.
64. Su, Q.; Huang, C. K.; Wang, Y.; Fan, Y. C.; Lu, B. A.; Lan, W.; Wang, Y. Y.; Liu, X. Q., Formation of Vanadium Oxides with Various Morphologies by Chemical Vapor Deposition. *J. Alloys Compd.* (2009), **475**, 518-523.
65. Souza Filho, A. G.; Ferreira, O. P.; Santos, E. J. G.; Mendes Filho, J.; Alves, O. L., Raman Spectra in Vanadate Nanotubes Revisited. *Nano Lett.* (2004), **4**, 2099-2104.
66. Huotari, J.; Lappalainen, J.; Puustinen, J.; Lloyd Spetz, A., Gas Sensing Properties of Pulsed Laser Deposited Vanadium Oxide Thin Films with Various Crystal Structures. *Sens. Actuators, B* (2013), **187**, 386-394.
67. Lavayen, V.; O'Dwyer, C.; Cárdenas, G.; González, G.; Sotomayor Torres, C. M., Towards Thiol Functionalization of Vanadium Pentoxide Nanotubes using Gold Nanoparticles. *Mater. Res. Bull.* (2007), **42**, 674-685.
68. O'Dwyer, C.; Lavayen, V.; Newcomb, S. B.; Santa Ana, M. A.; Benavente, E.; González, G.; Sotomayor Torres, C. M., Vanadate Conformation Variations in Vanadium Pentoxide Nanostructures. *J. Electrochem. Soc.* (2007), **154**, K29-K35.
69. Krumeich, F.; Muhr, H. J.; Niederberger, M.; Bieri, F.; Schnyder, B.; Nesper, R., Morphology and Topochemical Reactions of Novel Vanadium Oxide Nanotubes. *J. Am. Chem. Soc.* (1999), **121**, 8324-8331.
70. O'Dwyer, C.; Gannon, G.; McNulty, D.; Buckley, D. N.; Thompson, D., Accommodating Curvature in a Highly Ordered Functionalized Metal Oxide Nanofiber: Synthesis, Characterization, and Multiscale Modeling of Layered Nanosheets. *Chem. Mater.* (2012), **24**, 3981-3992.
71. Gannon, G.; O'Dwyer, C.; Larsson, J. A.; Thompson, D., Interdigitating Organic Bilayers Direct the Short Interlayer Spacing in Hybrid Organic-Inorganic Layered Vanadium Oxide Nanostructures. *J. Phys. Chem. B* (2011), **115**, 14518-14525.
72. Hardcastle, F. D.; Wachs, I. E., Determination of Vanadium-Oxygen Bond Distances and Bond Orders by Raman Spectroscopy. *J. Phys. Chem.* (1991), **95**, 5031-5041.
73. Chen, X.; Li, Z.; Ye, J.; Zou, Z., Forced Impregnation Approach to Fabrication of Large-Area, Three-Dimensionally Ordered Macroporous Metal Oxides. *Chem. Mater.* (2010), **22**, 3583-3585.

Chapter 7

Electrodeposited Vanadium Oxide Inverse Opal Lithium-ion Battery Cathodes

Abstract

Crystalline V_2O_5 inverse opal electrodes were synthesised by electrodeposition at constant voltage vs SCE from an aqueous solution of $VOSO_4 \cdot xH_2O$ into a stainless steel supported PS template (deposited by EPD). The electrodeposition growth process was compared with that of material deposited directly on bare stainless steel substrates with no template. Using the current-time transients it was confirmed that diffusion controlled growth occurs in both cases and the template presence has no noticeable effect on nucleation process. The performance of these V_2O_5 structures were then analysed and compared through rate capability test against the performance of V_2O_5 formed by drop cast infiltration with IPA diluted oxytriisopropoxide precursor. Electrodeposited IOs show good capacity retention over 100 cycles and high good coulombic efficiency per individual cycle. V_2O_5 still suffers a high degree of structural deformation on increasing lithium content which is illustrated using Raman scattering and XRD characterisation after discharge to different voltages at a 0.1 mV/s scan rate. Overall, the rate capability and cycling stability of both IO materials, and the as deposited electrodeposited material is shown to outperform that of bulk V_2O_5 powder.

7.1 Introduction

With the rapid and ever increasing growth in portable electronics and the growing need for electric and hybrid powered vehicles, the demand for light weight, high performance batteries with high power and energy densities, has never been more prevalent. Rechargeable lithium ion batteries (LIBs), which offer specific energies higher than other electrochemical power sources,¹ have become the leading battery type for many of these applications. LIBs typically consist of a positive and negative electrode, the cathode and anode respectively, and electrolyte with a separator (usually a polymer membrane) to electrically isolate the anode and cathode from each other, preventing short circuits. It is the nature of these components that determines the performance of the battery, including the cell kinetics, cycle life and energy and power densities. The active material electrodes currently used in most LIBs often suffer performance issues due in some part to the disordered and brittle nature of these materials. For this reason, a substantial amount of research is currently underway to find materials and material architectures that can deliver the desired improvements in battery performance.²⁻⁷

Recently, three dimensional macroporous or mesoporous (3DOM) architectures, inverse opal (IO) architectures in particular,⁸⁻¹⁰ have shown a lot of potential for providing a large active surface area within a continuously-interconnected electrode structure.¹¹⁻¹⁶ Lithium cobalt oxide (LiCoO_2) is currently the most commonly used cathode material in commercial LIBs. However, its increasing scarcity, high cost and poor cycle life has led to a growing interest into finding a replacement cathode material that is low in cost and can provide high specific capacity values while withstanding high charge/discharge rates. One such material receiving a lot of attention as a replacement cathode material, due to its low cost, availability and high energy density, is that of vanadium pentoxide (V_2O_5).

Vanadium is a material whose multiple valence states allow the formation of a number of oxides. In particular, Vanadium pentoxide (V_2O_5) has a particularly attractive mixed valence, V^{4+} and V^{5+} , making it an ideal candidate for a large number of redox-dependent applications. Orthorhombic crystalline V_2O_5 consists of layers of VO_5 square pyramids that share edges and corners. This layered geometry makes it highly suited to the reversible intercalation of mobile guest species, such as metal ions.¹⁷ Intercalation of this kind, into a crystalline material with available and appropriately sized lattice sites, where the structural integrity of the host lattice is theoretically maintained, will cause certain changes to occur, including changes to material phase, and the inter-layer spacing.¹⁸ For this reason, interest into the development and synthesis of three-dimensional, nanostructured, porous V_2O_5 materials that can provide the desired surface area while accommodating foreign species with limited structural deformation, is important. The growth of metal oxide films through electrochemical oxidation is a well-established route and while V_2O_5 can be synthesised by a number of techniques, including hydrothermal synthesis, sol gel techniques, chemical vapour deposition, and atomic layer deposition, the electrodeposition of vanadium oxides from $VOSO_4$ aqueous solutions has the benefit of low cost and simplicity.

In recent years, the combination of the inverse opal architecture with electrodeposited V_2O_5 has in particular shown a lot of potential for both electrochromics and electrochemistry.^{19, 20} Engineered nanoscale materials that have 3D porosity can in principle accommodate electrolyte within the material and provide shorter diffusion pathways for efficient lithiation of the active material.^{9, 12, 21} A key challenge that is a basis for the use of ordered material approaches, is the problem of sluggish ionic and electronic transport kinetics in standard battery materials, especially if higher charge rates are required.^{3-5, 9, 16, 21-23} Reductions in the characteristic dimensions of the active material in an electrode are more effective in improving battery cycling rates than increases in ion diffusivity D , because the

characteristic time constant t for diffusion is proportional to the square of the diffusion length L ($t \sim L^2/D$).³ Furthermore, if the rate of lithiation can be increased, structural changes to the active material can be reduced under normal charging conditions to predefined depths of discharge. With respect to inverse opals, three-dimensionally interconnected macropores facilitate the rapid flux of liquid electrolyte solutions, such that, in a Carbon IO material for example $100 \text{ m}^2 \text{ g}^{-1}$ of electrode interfaces are simultaneously accessible to Lithium or other mobile ionic charges. This degree of macropore interconnectivity is intentionally tailored into PhCs from self-assembled close-packed templates. For example, the ionic conductivity of a 1 M LiPF_6 liquid electrolyte solution is only impeded by a factor of two when ion transport occurs through the interconnected macropores of monolithic carbon inverse opals (electrode thicknesses: $300 \text{ }\mu\text{m}$ – 3 mm).^{24, 25}

In this chapter the formation of inverse opal vanadium oxide structures through electrodeposition on to PS templates suspended on a variety of substrates is presented. The use of different substrates and times, and the subsequent growth kinetics is briefly examined. The electrochemical performance of a V_2O_5 IO formed using one set of conditions is then assessed and compared to bulk and electrodeposited non IO examples.

7.2 Results and Discussion

7.2.1 Electrodeposition of V_2O_5

As described in Chapter 6, colloidal crystal templates were formed on conductive substrates of stainless steel, ITO-coated glass, or FTO-coated glass by electrophoretic deposition of 350 nm PS spheres at 3V for 50 minutes, described schematically in Fig. 3.4 of Chapter 3. This produced multilayer PS templates with the hexagonal (111) plane grown parallel to the substrate surface. Templates were then annealed for ~2 hours at 70°C to promote adhesion and structural stability. Vanadium oxide was infilled using electrodeposition at room

temperature with a constant potential of 2 V versus a saturated calomel (SCE) reference electrode in a three-electrode cell with a platinum mesh as counter electrode (Fig. 7.1 (a)).¹⁹ After deposition, samples were heated to 300°C for 24 hours to remove the spheres, resulting in the formation of a network of crystalline V₂O₅. The electrodeposition of vanadium oxide was performed for PS templates on ITO-coated glass, FTO-coated glass and stainless steel foil substrates. For comparison, vanadium oxide was also electrodeposited under similar conditions on to substrates without PS templates in place. These as-deposited samples were also heated at 300°C for 24 hours to form crystalline V₂O₅. The mass of stainless steel changes slightly on heating due to oxide formation, and so all stainless steel substrates were therefore pre-heated to 300°C and allowed to cool before sphere deposition to improve the accuracy of the mass calculation for the electrodeposited active material.

The current-time relationship shown in Fig. 7.1(b) is characteristic of 3D growth and nucleation. The current initially rises as the size and/or number of growth nuclei increases thus expanding the electroactive area. The current begins to decrease once the electrode surface becomes saturated and the rate of nucleation and growth gradually lowers towards steady state growth. The deposition profile observed for the PS templates is much like that of a bare substrate but due to a lower active surface area and electrode screening by the spheres, current values are lower than on the bare substrates. Oscillations in the current-time transient characteristic of electrodeposition into a sphere template were observed and are shown in the magnified region of the current-time transient in the bottom inset of Fig. 7.1 (b).²⁶ In a simple diffusion controlled process the Cottrell equation,²⁷

$$I = \frac{nFAD^{1/2}C_0^*}{(\pi t)^{1/2}} \quad \text{Eqn. 7.1}$$

can be used to describe the current-time relationship and to determine a value for the diffusion coefficient, where I is the current, n is the number of electrons transferred, F is

Faradays constant, A is the area of the electrode, C_0^* is the concentration of the electroactive species, t is the time and D is the diffusion coefficient for the electro-active species.^{28, 29}

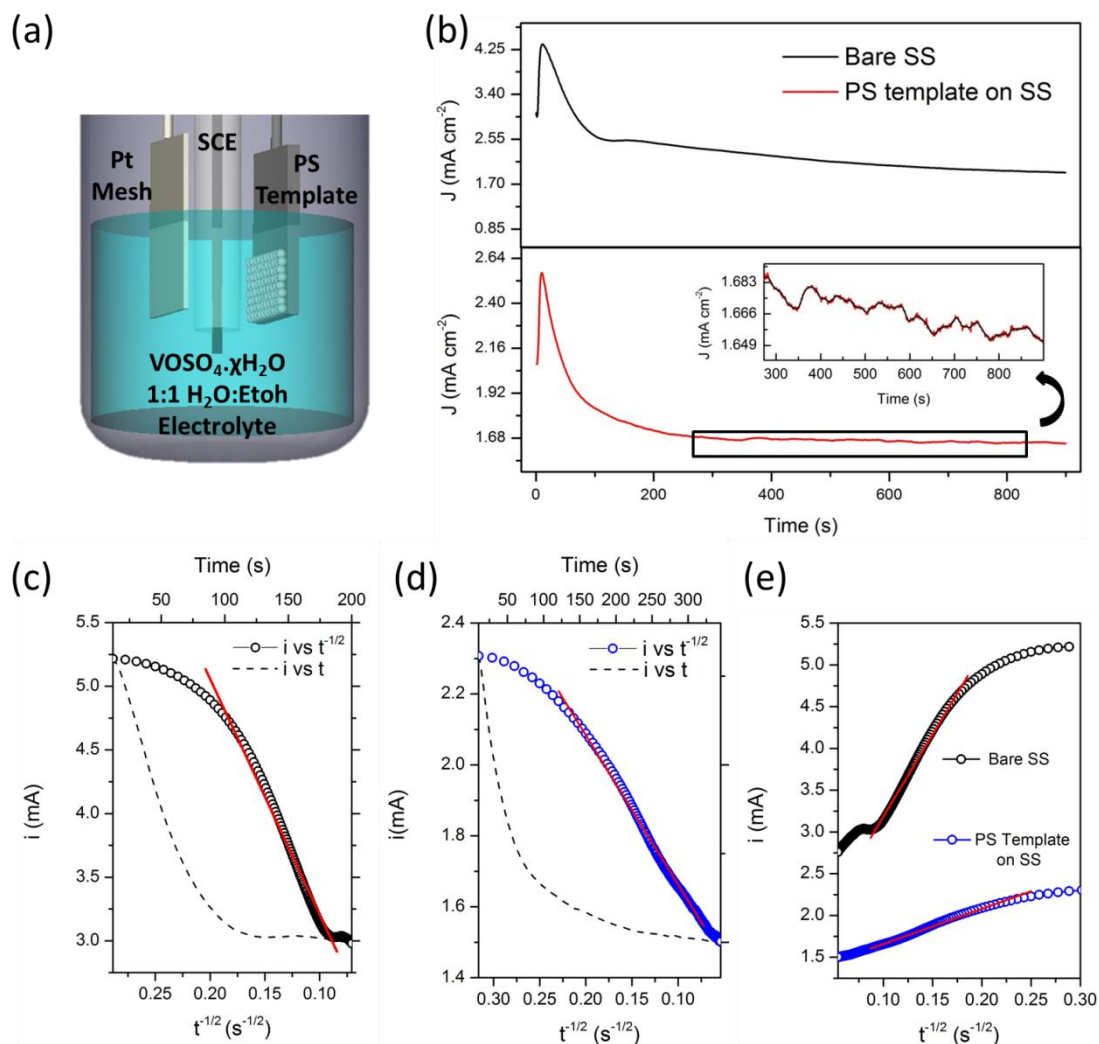


Fig. 7.1 (a) Schematic diagram of the three electrode cell used for the electrodeposition of vanadium oxide and (b) the characteristic current density versus time chronoamperograms observed for deposition on bare stainless-steel foil substrates (Bare SS), and PS sphere templates supported on stainless steel foil substrates (PS template on SS). (c) Current versus $t^{-1/2}$ for the decreasing portion of the i vs t transient (dotted line) for electrodeposition on bare stainless steel and (d) for the case of a PS template on stainless steel at 2 V for 15 minutes. (e) i vs $t^{-1/2}$ for both depositions plotted according to Cottrell equation with positive slope.

In an electrodeposition process the electrodeposited area continuously changes with time following initial nucleation of the V_2O_5 . The trends observed for both planar and templated V_2O_5 electrodeposition in Fig. 7.1 confirm a diffusion controlled growth. The

Cottrell equation can be applied to the decreasing portion (after the current peak) of the current-time transient by plotting the current density i vs $t^{-1/2}$, and the linear relationship is indicative of a diffusion limited process in this region. Mass transport of reactants is thus limited by the diffusion constant with the double layer at the surface of the growing V_2O_5 . A similar trend is shown in Fig. 7.1(c) for electrodeposition onto the bare stainless steel substrate (SS Bare) and in Fig. 7.1(d) for the stainless steel foil with a PS opal template on top. In Fig. 7.1 (e) the two Cottrell plots are shown together for comparison. As is observed, while the slope differs as expected due to the variation in growth parameters caused by the template presence, the process of deposition into the template is also diffusion controlled, highlighting that the presence of the template does little to effect method of material nucleation and serves as a structural mould for shaping the growth.

7.2.2 Structure of Electrodeposited V_2O_5 Inverse Opals

The bottom-up filling of the sphere template can be an advantage in preparing IOs. Material congestion in the upper layers of the template, problematic in some top down infilling techniques is not an issue with electrodeposition. Improved infilling and thicker deposits are therefore possible with electrodeposition compared with some top down methods such as alkoxide drop-casting described in chapter 6. However, the bottom up approach provides other challenges. Material formation occurs at the electrode surface i.e. those areas of the substrate in contact with electrolyte. When using a sphere template atop a conductive substrate the available electrode surface are interstitial sites within the opal template and in the preferred case, growth and nucleation continues around and within the template.^{30, 31} It is possible however, for growth to occur destructively towards the template, growing parallel to the substrate beneath the template, reducing sphere adhesion, leading to separation from the substrate before complete infiltration can happen. Detachment from the substrate is also seen

when material thickness grows to a large mass, effectively pulling the template from the substrate. This was particularly prevalent for depositions of ≥ 1 hour (corresponding to thickness $> 18 \mu\text{m}$) on all substrates investigated. Deposition time must therefore be calibrated to suit the template thickness, too long results in an overfilling of the template, producing a porous IO structure trapped beneath dense layers of material, as shown for samples on ITO-coated glass in the SEM images in Fig. 7.2.

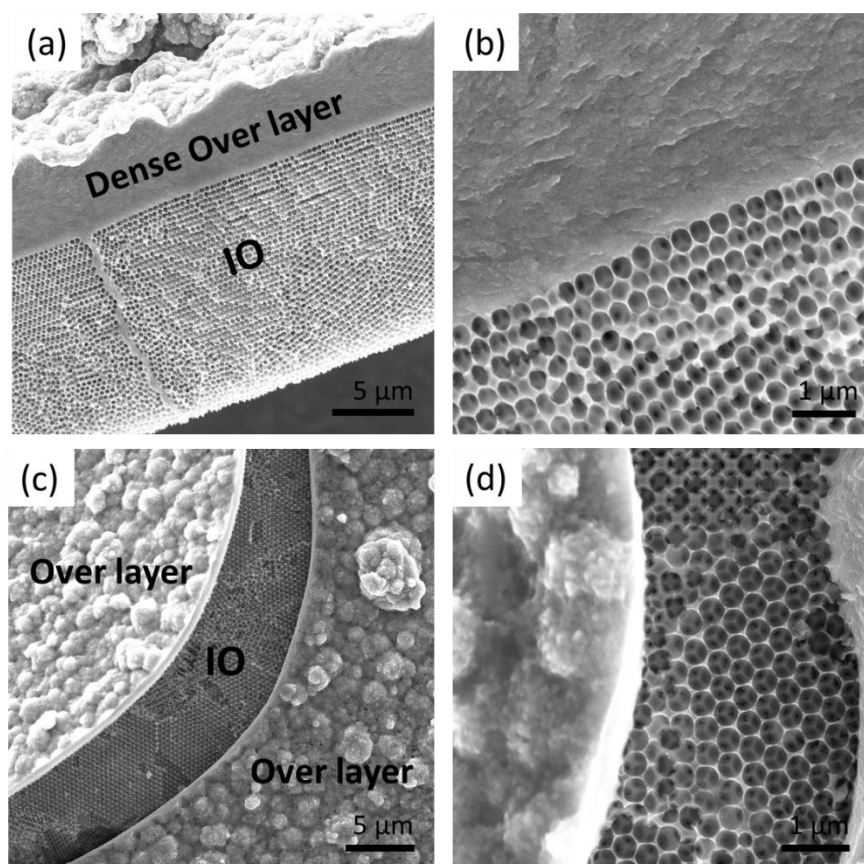


Fig.7.2 SEM images of the resulting V_2O_5 IO structure observed after infilling of PS sphere templates on ITO-coated glass by electrodeposition at 2 V for (a) and (b) 1 hour and (c) and (d) for 30 min. Note the excess material atop the IO structure, resultant from an extended infill time.

To reduce the possibilities of template overfilling and/or detachment from the substrate, deposition times were restricted to 15 min. At this time, templates (electrophoretically deposited at 3 V for 20 min) usually filled to a level below the total template thickness (see Fig. 7.3 (a)), leaving the template surface visible after removal from the electrolyte. In this way open IO structures which are more conducive to electrolyte

infiltration were allowed to form with thickness of $\sim 10\text{--}12\ \mu\text{m}$, see cross section Fig. 7.3 (b). Unless otherwise stated, electrochemical analysis as a Li-ion battery cathode was performed using IO structures prepared at 2 V for 15 min on stainless steel foil substrates due to the suitability of this substrate to the battery cell arrangement.

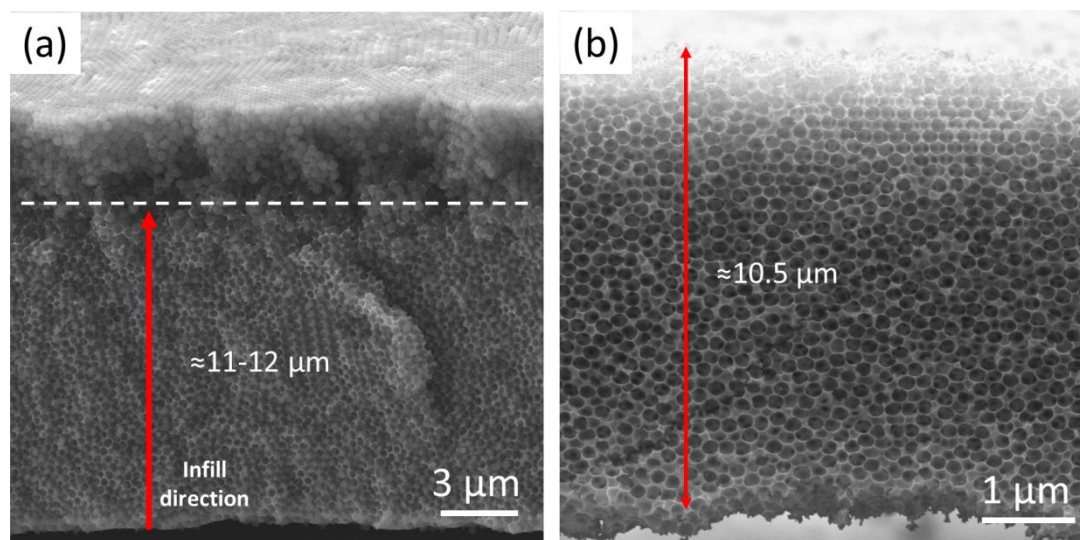


Fig. 7.3 Cross sectional SEM images of (a) a PS template on stainless steel substrate infilled at 2 V for 15 min before removal of the spheres, indicating only a partially filled template with a remaining area of unfilled sphere layers along the sample top (above white dashed line) and (b) the resulting IO structure after removal of the spheres and material crystallization after ~ 24 h at $300\ ^\circ\text{C}$.

The two central morphologies observed in an IO structure formed at 2 V for 15 min on stainless steel foil are presented in Fig. 7.4. SEM analysis revealed the formation of three-dimensional macroporous structures separated into an island like arrangement by structural voids characteristic of crack propagation and material contraction that occurs during sphere removal and sample drying.^{32, 33} Islands of networked material close to the centre of the template appeared more disordered (Fig. 7.4 (a)-(c)) than those formed near the meniscus line and outer edges of the sample, which were able to maintain the structural order of the opal template (Fig. 7.4 (d)-(e)). It is unclear whether the disorder within the sample structure is as a result of the deposition process or as result of sphere removal. At regions along the

meniscus, template thickness is often thinner than the template bulk due to a thin liquid region within a meniscus, thus reducing the density of spheres available for deposition during EPD as well as overall solution settlement during the process. The removal of the remaining, unfilled layers of spheres along the surface of the sample could therefore be disrupting the order of the regions below, unlike areas at the meniscus that were more fully filled within the 15 min deposition time. The disordered upper regions may not extend fully within the sample structure, as is suggested by the SEM image in Fig. 7.5 (a) for a sample formed on ITO-coated glass, which indicates better opal order. This further suggests the disordered regions are a product of the under-filling technique employed. Overfilling results in coverage of the surface by V_2O_5 with an overlayer that negates the benefit of a porous, open access to the material. Accurate filling of a self-assembled opal template of indeterminate thickness (or variable thickness) may require further work for accurate control of electrodeposition kinetics and time. However, it is also possible that disorder occurs due to the growth of the electrodeposited material. As discussed above, nucleation below the template could have a disruptive effect on the ordering of the spheres before they become enclosed by the growing deposit, and as such, fundamentally decrease the degree of ordering with time prior to the final stages of electrodeposited infilling near the surface.

The force of the sphere shrinking and liquid removal at high temperature was observed to cause the islands of IO material to contract together, folding upwards from the substrate, typically at edges of domains of infilled opal, as is shown in the SEM images in Fig. 7.5 (b) and more closely in Fig. 7.5 (c). The inconsistency of occurrence for this folding effect could suggest an environmental factor, changes in humidity or temperature during synthesis. The effect could also be attributed to levels of sphere packing and domain structuring, a slower rate of heating could alleviate the strain on the sample domains as the spheres shrink. However, the active V_2O_5 remains interconnected electrically within each

domain, and each domain is electrically addressable with the stainless steel substrate. Thus, under mild compression in a Li-ion cell, and also as a native electrodeposited materials soaked in an electrolyte, no delamination of the material occurs.

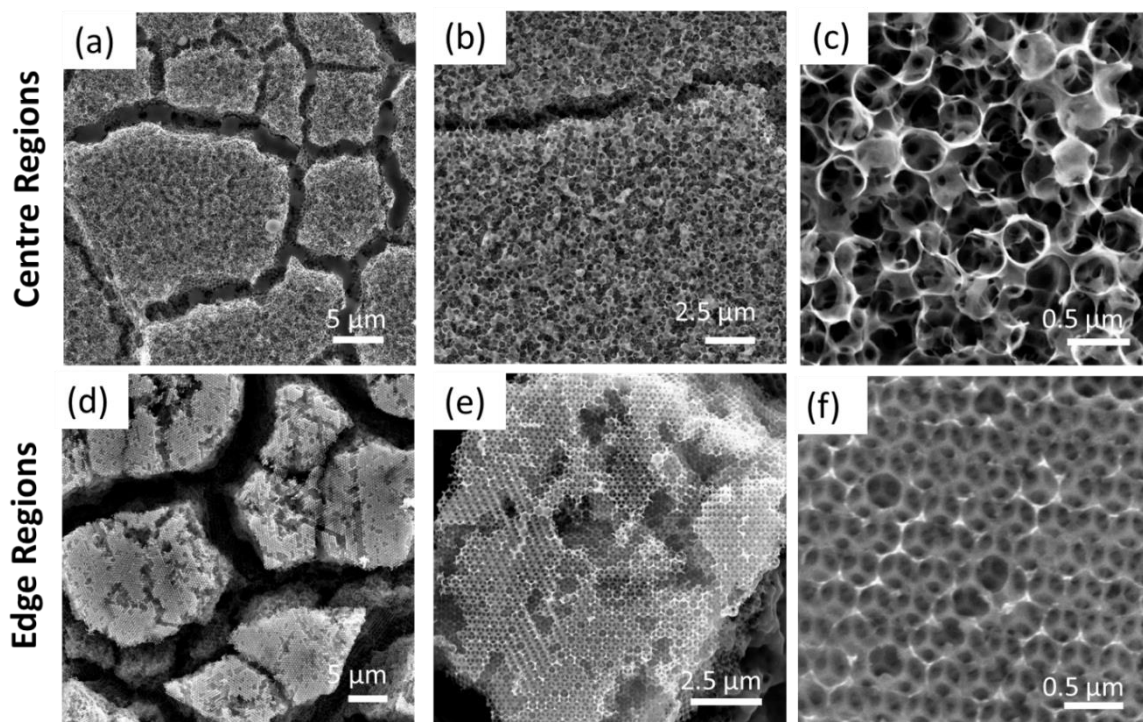


Fig. 7.4 SEM images of the disordered but highly porous network of material observed at regions near the centre of the sphere template (a-c) and the areas near the top and side edges of the template that maintained better structural order producing an inverse opal – like island morphology (d-e) for PS templates on stainless steel infilled by electrodeposition at 2 V for 15 min and heated at 300°C for 24 h.

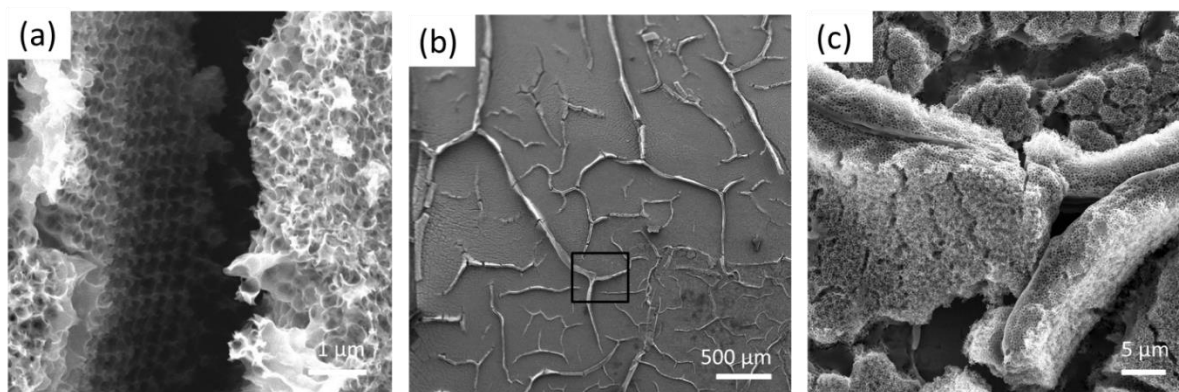


Fig. 7.5 SEM images of (a) a seemingly ordered IO network maintained beneath the disordered top-layers of an IO formed on ITO-coated glass after infilling at 2 V for 15 min and heating at 300°C for 24 hours and the material folding defects at (b) low and (c) high magnification seen throughout samples formed at 2 V for 15 min, attributed to material contraction on drying and sphere removal.

7.2.3 Electrochemical Characterisation – IOs as Lithium-ion Battery Cathodes

Electrochemical analysis was carried out in a half cell arrangement as outlined in the experimental description in Chapter 3. In this split cell (similar to a coin cell) lithium foil was used as the counter and reference electrode and glass fiber separator was soaked with 0.1 ml of electrolyte - a 1 M solution of LiPF_6 salts in a 1:1 (v/v) mixture of ethylene carbonate in diethyl carbonate. The V_2O_5 IO electrode completed the sandwich structure of the battery cell, assembled in a water and oxygen-free Argon atmosphere. In order to compare the fundamental charge/discharge behaviour of the electrodeposited V_2O_5 IO with the crystallized as-deposited and bulk V_2O_5 material, no conductive additives or binders were added to the prepared cathode materials. In some cases the battery performance of V_2O_5 IOs formed by drop casting 100:1 IPA:Alkoxide precursor solution under nitrogen pressure, described in the previous chapter, are also compared. Galvanostatic cycling was typically performed within a potential window of 4.0-1.2 V and the potential difference between the working and counter electrodes was measured as a function of time.

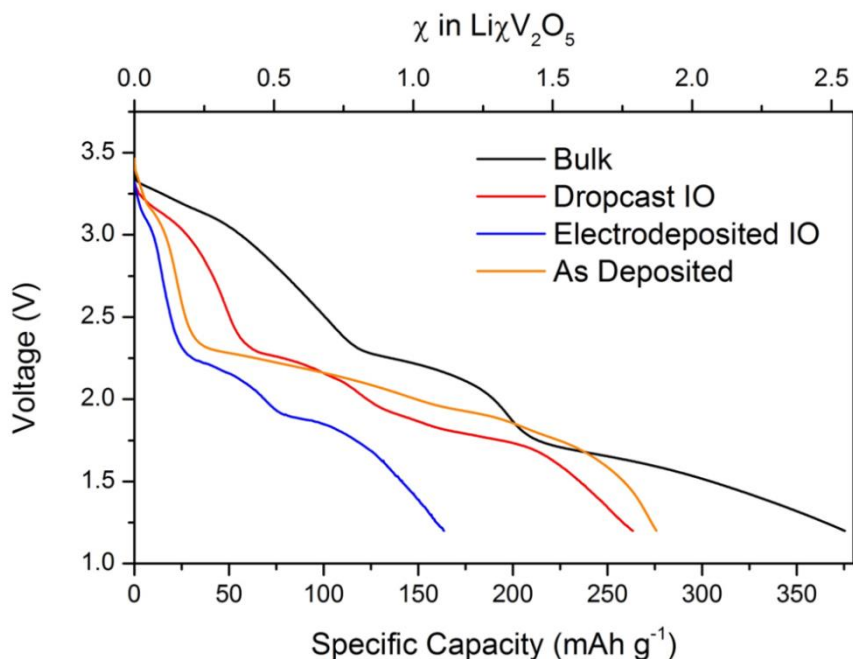


Fig. 7.6 The first discharge curves for IO samples formed by electrodeposition (blue) and dropcasting (red) compared with those of the as deposited material electrodeposited without a template (orange), and bulk V_2O_5 powder dropcast on stainless steel foil (black) showing specific capacity (bottom axis) and number of moles of intercalated Li (top axis) as a function of voltage when discharged at a constant current of $50 \mu\text{A}$ within a potential window of $4.0 - 1.2 \text{ V}$.

In Fig. 7.6, the initial discharge curve for samples cycled at a constant current of $\pm 50 \mu\text{A}$ within a potential window of $4.0-1.2 \text{ V}$ are shown. As reported by Whittingham the interactions and cell reactions between lithium and V_2O_5 produces ternary $\text{Li}_\chi\text{V}_2\text{O}_5$ phases.³⁴ These phase transitions during discharge correspond to different fractions of intercalated lithium (χ) and are reflected by distinct changes in the shape profile of the discharge curve, as the potential (V) varies. For bulk V_2O_5 , the α phase occurs for $\chi < 0.01$ and results in little distortion of the V_2O_5 structure, for χ between 0.35 and 0.7 a puckering of the layered structure of this material begins and the interlayer spacing widens in what is known as the ϵ -phase. At $\chi = 1$, the δ phase is reached which usually instigates a sudden decrease in cell potential. Beyond this serious structural changes begin to occur as the γ phase ($\chi = 2$) and the irreversible ω phase, are reached ($\chi = 3$). It has been suggested however, that due to the diffusion based nature of lithium insertion into V_2O_5 active material at the electrolyte

interface, lithium intercalating can occur earlier than regions at the current collector. This could cause several phases to co-exist at different stages during discharge for various amounts of intercalated lithium.^{18, 34} By introducing a porous inverse opal structure that accommodates electrolyte, the issues of slower cation diffusion and multiple phase formation over time in thick, coherent films, is reduced and beneficial for repeated cycling at the expense of higher gravimetric energy densities.

The discharge curve for the electrodeposited IO structure is plotted in Fig. 7.6, with those of the orthorhombic bulk V_2O_5 , the drop cast IO structure and the as deposited material, against the number of lithium moles intercalated per mole of V_2O_5 (χ in $Li\chi V_2O_5$) and the specific capacity of the material in $mAh\ g^{-1}$. The value χ was calculated for the mass m of active V_2O_5 material, discharged for a time t at a constant current I using the equation,

$$\chi = \frac{ItM}{mF} \quad \text{Eqn. 7.2}$$

where M refers to the molar mass of V_2O_5 and F to Faradays constant. The mass of the active material was calculated by recording the mass of the stainless steel substrate before template formation and subtracting this from the mass of the final sample after heating at 300 °C for ~ 24 h. Specific capacity is a measure of the amount of charge stored per unit mass of material,

$$SC = \frac{It}{m} \quad \text{Eqn. 7.3}$$

where m is the mass of active material charged or discharged for a time t at a constant current of I . The profile for the first discharge curve is similar across all samples and the phase transitions were found to occur at similar potentials. Some variation is observed, for example, the phase transition at ~2.298 V in the bulk powder sample occurs at the slightly lower potential of ~2.258 V in the electrodeposited structure. Fewer discrete phase changes are visible in the discharge curve of the as deposited material, suggesting perhaps a lower level of

crystallinity in this sample compared with the bulk and IO samples. Similar smooth cycling curves were reported for vanadium oxide xerogels heated to 300 °C.^{18, 35} Importantly for reversible and efficient deintercalation, the mole fraction of lithium in the IO structure is lower than for bulk at an equal depth of discharge. While the specific capacity is lower, the thinner walls of the IO structure prevent solid state diffusion limitations and the formation of phases that cause large scale crystal structure changes or irreversible deintercalation during subsequent charging ($\delta \rightarrow \omega$ phase transitions).

In Fig. 7.7 the specific capacity (bottom axis) and fraction of intercalated lithium (top axis) is examined as a function of the 2nd, 5th and 10th charge/discharge cycle in order to compare the relative cycling performance of the different electrode architectures. Samples were cycled 10 times at a constant current of 50 μ A within the potential window of 4.0-1.2 V. The shape of the discharge/charge curves can aid in understanding the mechanism of lithium insertion and removal that occurs for each sample. The mole fraction of lithium inserted into all samples shown, the electrodeposited IO (Fig. 7.7(a)), the drop cast IO sample (Fig. 7.7(b)) and the as deposited material (Fig. 7.7(c)) does not exceed an amount greater than $\chi \approx 1$ mol. The phase transitions seen in the discharge curve of these samples correspond to the ϵ - phase (typically $0.35 < \chi < 0.7$) and the δ -phase which can occur between 0.9 and 1.0 mol Li in $\text{Li}\chi\text{V}_2\text{O}_5$. A larger amount of lithium is intercalated into the dropcast IO structure. However, the amount of intercalated lithium is seen to increase slightly from the 2nd to 10th cycle for both the electrodeposited IO structure (Fig. 7.7(a)) and the electrodeposited as-deposited material (Fig. 7.7(c)). This may be due to a number of reasons. The increased thickness of these samples compared with the drop cast IO material may delay diffusion of the lithium to the lower regions of the material (a function of depth into the structure, not the thickness of the walls of the structure). Successive cycling (longer times at corresponding voltages) allows intercalation into material deeper into the structure. It could be a factor of electrolyte soakage

or simply temperature fluctuations during testing.

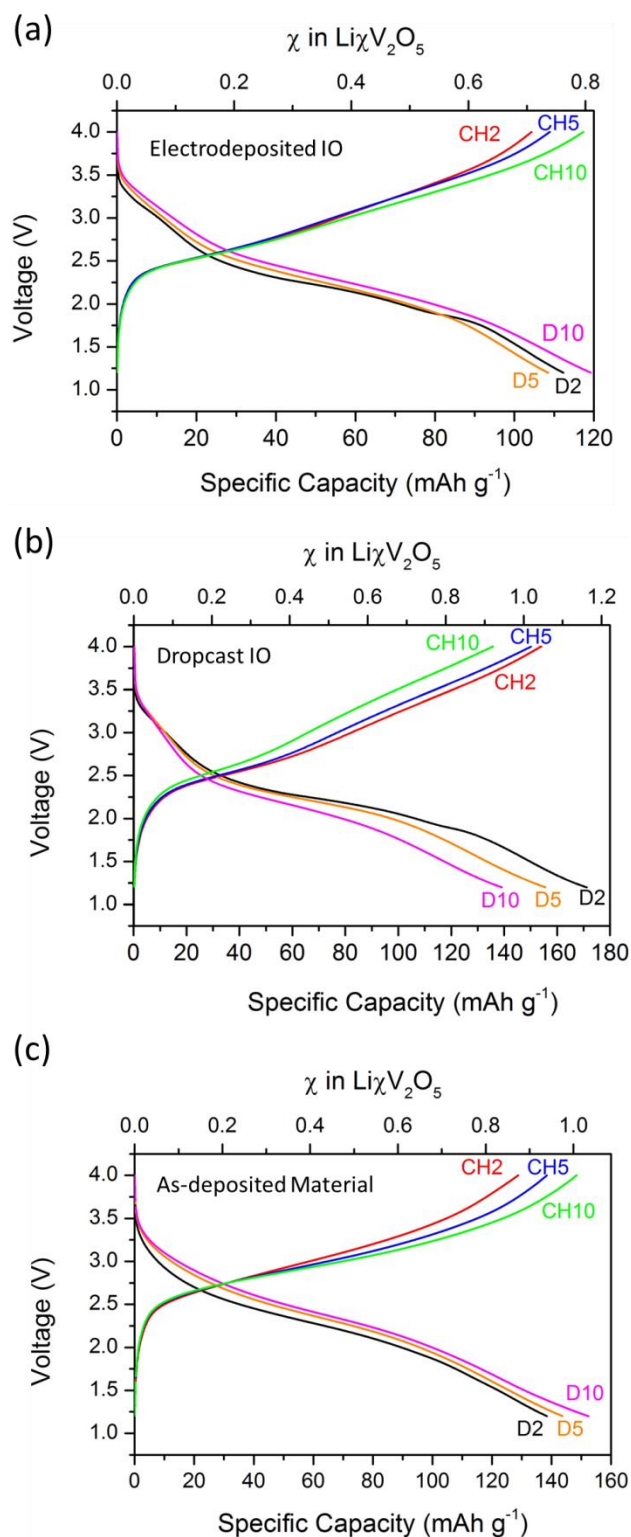


Fig. 7.7 2nd, 5th and 10th discharge/charge curves for the (a) electrodeposited IO (b) dropcast IO and (c) as-deposited material after heating to 300 °C for a constant current of 50 μA within a potential window of 4.0-1.2 V

While initial discharge capacity values are highest for the bulk V_2O_5 , the subsequent decrease in this value, seen in all vanadium oxide materials and many positive electrode materials after the first discharge, is much larger than the decrease seen for the electrodeposited IO, dropcast IO and the as deposited samples. Figure 7.8 shows the discharge capacities for all samples as a function of cycle number. Assuming similar electrochemical processes and materials, the large irreversible capacity loss is generally greater for systems limited by ionic solid state diffusion. The chemical potential, surface reactivity, electrolyte stability, and changes in electrical conductivity upon lithiation are not dominant factors for first cycle capacity loss in cathodes at potentials far from 0 V vs Li^+/Li . For the same materials with different degrees of porosity and size (microscale versus nanoscale) the irreversible capacity loss is reduced by preventing large structural changes and irreversible phase formation (maintaining a lower Li mole fraction) on deep discharge in the first cycle. Narrow walled IO structures also reduce diffusion limitations to lithium removal on the first charge cycle.^{11, 36, 37} The IO V_2O_5 structure exhibits excellent Coulometric efficiency and capacity stability during cycling form Fig. 7.8; bulk material specific capacity continuously decrease by comparison.

The lowest capacity values are seen for the bulk V_2O_5 , compared with these values both the electrodeposited, the drop-cast IO and the as-deposited material all demonstrate superior cycling stability and efficiency. After the second discharge the specific capacities for the electrodeposited and drop-cast IO samples are $\sim 112 \text{ mAh g}^{-1}$ and $\sim 171 \text{ mAh g}^{-1}$ respectively. Due to variations in mass loading the capacity values for the drop cast IO are not fully comparable to those of the electrodeposited IO and it cannot be unequivocally stated that the drop-cast IO performs better of the two. The discharge capacities for the drop-cast and bulk materials show a steady decline with increasing cycle number, as expected if structural integrity is worsened with increased cycling.

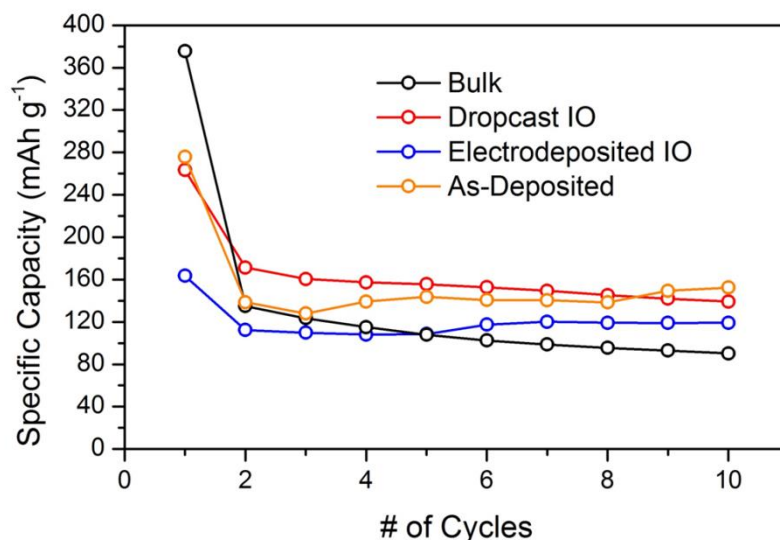


Fig. 7.8 Discharge capacities for the electrodeposited IO, dropcast IO, as-deposited material electrodeposited without a template and bulk V_2O_5 powder over 10 cycles. The enlarged initial capacities seen for the first cycle is a common characteristic for V_2O_5 materials and capacity stability should therefore be determined from subsequent cycles.

However, the capacity values for the electrodeposited materials, both the as-deposited and IO structures, show a larger variation in capacity values over the 10 cycles, improving in both cases from values of 112 and 138 mAh g^{-1} respectively after the 2nd discharge to values of 119 and 152 mAh g^{-1} respectively in the 10th cycle. This increase in specific capacity occurs between the 5th and 6th cycle for the electrodeposited IO, this is between approximately the 17th and 21st hours of cycling. The increase occurs sooner for the as deposited material, from the 3rd to 4th discharge, between ~ 15 and 20 hours into cycling. The higher overall capacities for the as deposited material may be due to better contact with the current collector compared with the IO structures. A number of reasons could account for the *increase* in specific capacity values for the electrodeposited materials. Structural changes that form defect sites within the material crystal structure have been reported to contribute pseudocapacitance to the overall measured charge capacity. In this first possible contributory case, the material is generally small or thin (on the nanoscale) and has undergone heating that can result in thermal removal of oxygen atoms by calcination in humid O_2/H_2O atmospheres

leaving proton-stabilized cation vacancies. In such systems, the typical increase was about 23% over the entire cycle lifetime. The second contribution could be space charge pseudocapacitance, but this effect is typically a mass transport limitation effect from varying the potential at fast rates – in charge-discharge curves, a constant current is applied and so this charge contribution is not likely to contribute. Exfoliation or widening of inter-planar distances within the walls of the IO may also contribute some improvement or maintenance of charge capacity observed in these coulometrically stable IO materials.

The specific capacity for the electrodeposited IO was monitored over 100 cycles at a constant current of 30 μA in a potential window of 4.0 – 1.2 V as shown in Fig. 7.9 (a). The smaller oscillations in the specific capacity values in the data are due to temperature fluctuations within the lab environment, between night and day. After 100 cycles the specific capacity has faded to $\sim 51 \text{ mAh g}^{-1}$ which amounts to a decrease of $\sim 33\%$ from value obtained for the second discharge of $\sim 151 \text{ mAh g}^{-1}$. Coulombic efficiency is ratio of the charge in to the charge out after equal discharge-charge times (equivalent depth of discharge and state of charge). The average coulombic efficiency from the 2nd to the 100th cycle was $\sim 96\%$. This indicates that the intercalation of lithium ions into the electrodeposited V_2O_5 IO for a single discharge-charge cycle appears highly reversible however, it is important to note that the capacity retention of $\sim 33\%$ over 100 cycles intimates that this cannot be equally said from one cycle to the next, i.e. over the complete range of cycles. SEM images of the sample following 100 cycles, are shown in Fig. 7.9 (b)-(c). Comparing these to the images shown in Fig. 7.4, the effect of the lithium intercalation in disturbing the material structure and IO order on the macro-level can be seen.

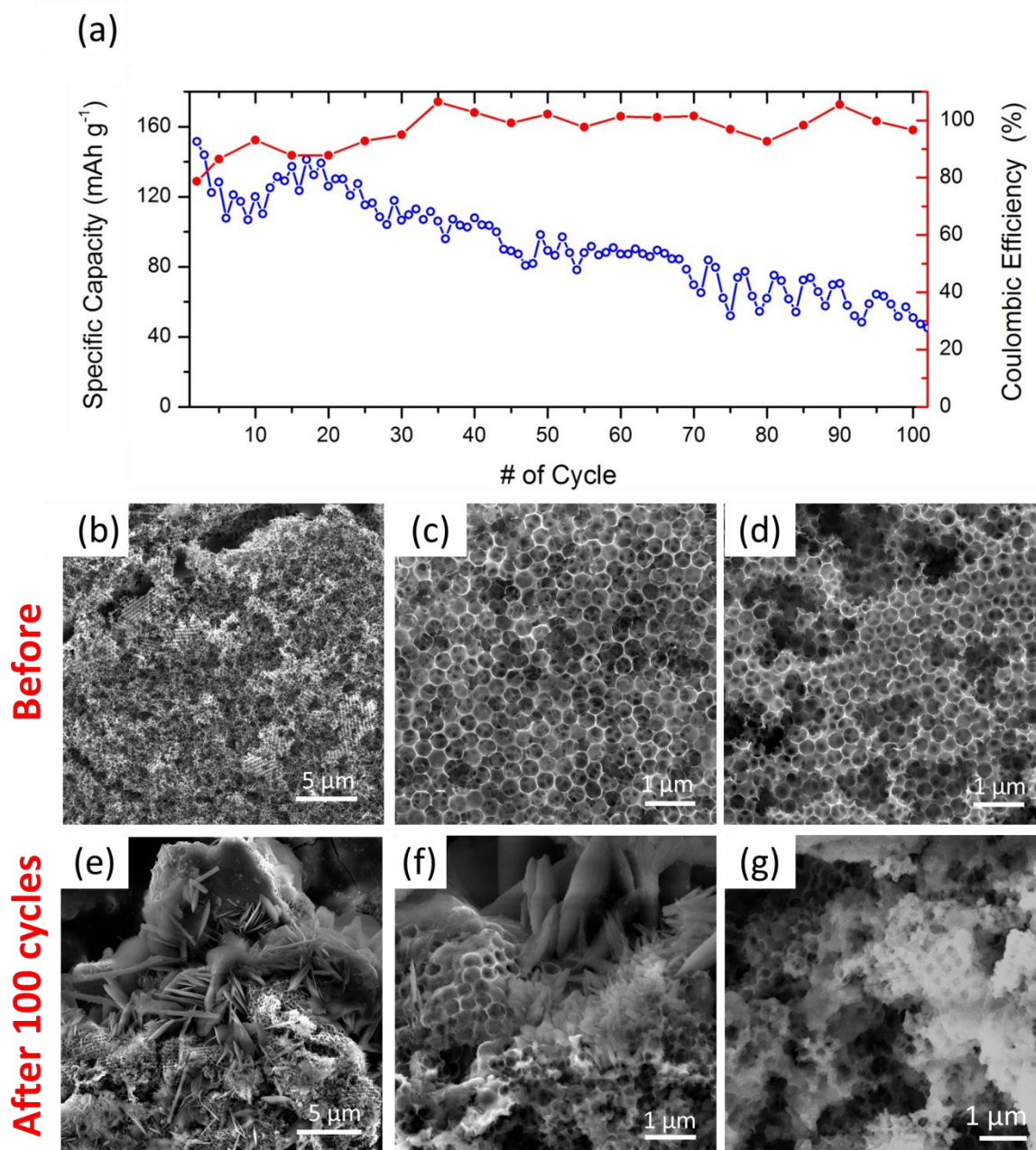


Fig. 7.9 (a) Specific capacities for the electrodeposited IO material over 100 cycles at a constant current of $30 \mu\text{A}$ within the potential window of $4.0 - 1.2 \text{ V}$ and the corresponding coulombic efficiency calculated for every 5 cycles (b)-(d) SEM images representative of the IO morphology before electrochemical cycling and (e)-(g) SEM images representative of the material morphology after 100 cycles.

Rate capability testing, in a potential window of $4.0 - 1.2 \text{ V}$, was performed to further investigate the performance of the IO materials and their response to high rates of charge and discharge. This was done by changing the applied current every 10 cycles from $50 \mu\text{A} \rightarrow 100 \mu\text{A} \rightarrow 150 \mu\text{A} \rightarrow 200 \mu\text{A} \rightarrow 50 \mu\text{A}$. Porous architectures have been reported to demonstrate

improved cycle ability compared with bulk materials, attributed to better accommodation of volume changes during lithiation/delithiation and the shorter diffusion lengths provided by the nanowalled architecture.^{38 39}

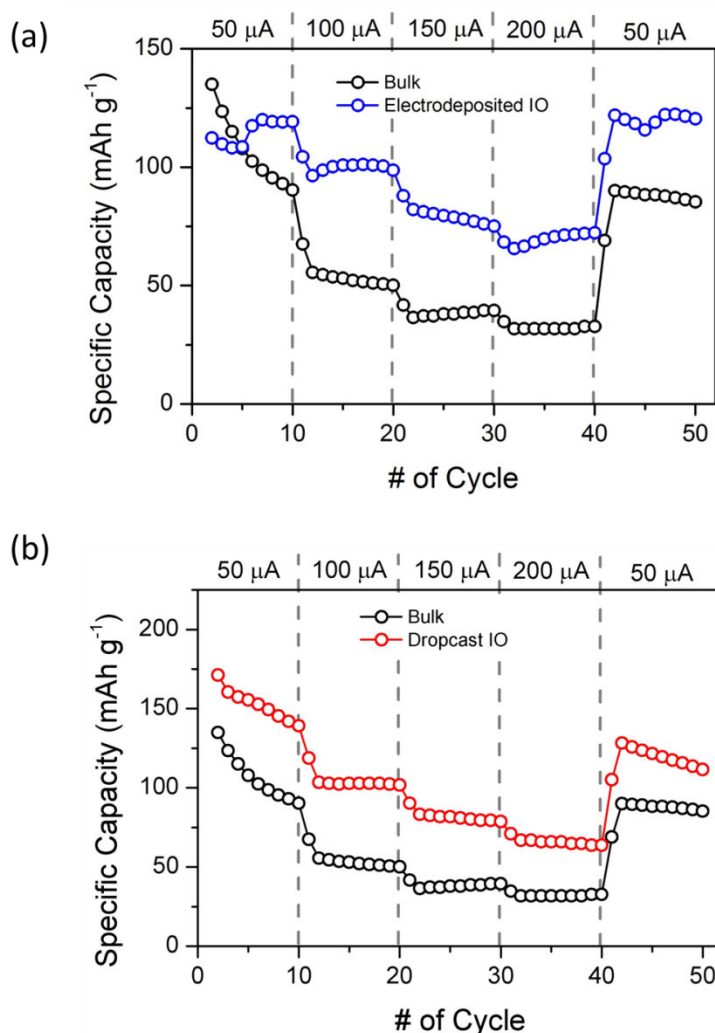


Fig. 7.10 Rate capability tests for the (a) electrodeposited IO and (b) drop casted IO compared with the rate capability of bulk V_2O_5 for current values as indicated.

The specific capacities for the electrodeposited IO and for the drop-cast IO during the rate testing are shown in Fig. 7.10 both against the rate test for bulk V_2O_5 . Both IO materials are shown to perform better than bulk V_2O_5 . With respect to the electrodeposited IO material Fig. 7.10 (a) shows an increase in applied current from $\pm 50 \mu A$ to $\pm 100 \mu A$ after the first 10 cycles caused a decrease in specific capacity from $\sim 104.4 \text{ mAh g}^{-1}$ to $\sim 96.4 \text{ mAh g}^{-1}$. For an

applied current of 150 μA the specific capacity decreased to a value of 82.1 mAh g^{-1} and a further increase in current to 200 μA resulted in a decrease in specific capacity to $\sim 65.6 \text{ mAh g}^{-1}$. However, when the current was decreased back to its initial value of 50 μA the specific capacity increased to $\sim 121.90 \text{ mAh g}^{-1}$. From the 10th cycle at $\pm 50 \mu\text{A}$ to the 41st cycle a minor increase in specific capacity of $\sim 16 \%$ was observed. This recovery in specific capacity to the values at or above the original values indicates a high degree of stability for the electrodeposited V_2O_5 IO as a cathode material.

For the IO material formed by drop casting, the rate capability is outlined in Fig. 7.10 (b). An increase in applied current to 100 μA saw a decrease in specific capacity from $\sim 118.8 \text{ mAh g}^{-1}$ to 103.4 mAh g^{-1} . For an applied current of 150 μA the specific capacity decreased to a value of $\sim 83.3 \text{ mAh g}^{-1}$ and an increase to 200 μA decreased the specific capacity to $\sim 66.9 \text{ mAh g}^{-1}$. However, similar to the behaviour of the electrodeposited IO, once the applied current was returned to $\pm 50 \mu\text{A}$ the specific capacity after cycle 40 rose to a value of $\sim 128.34 \text{ mAh g}^{-1}$, $\sim 8 \%$ higher than the value after at the 10th cycle, indicating a high degree of stability as a cathode material. The rate performance of these two structures is compared with that of bulk and the as deposited material in Fig. 7.11. The as deposited material indicates a similar increase in specific capacity values on return to 50 μA rate after the 40th cycle. However, the stability of these values appears lower than the capacity values for the IO structure, indicating perhaps a lower degree of structural stability or higher degree of sensitivity to the temperature fluctuations in the outside environment. Observable in all cases is the increased stability at higher currents for all samples compared with measurement at the lower current of 50 μA . Also clear, is the higher specific capacity values observed for the IO and as deposited material compared with the bulk V_2O_5 powder.

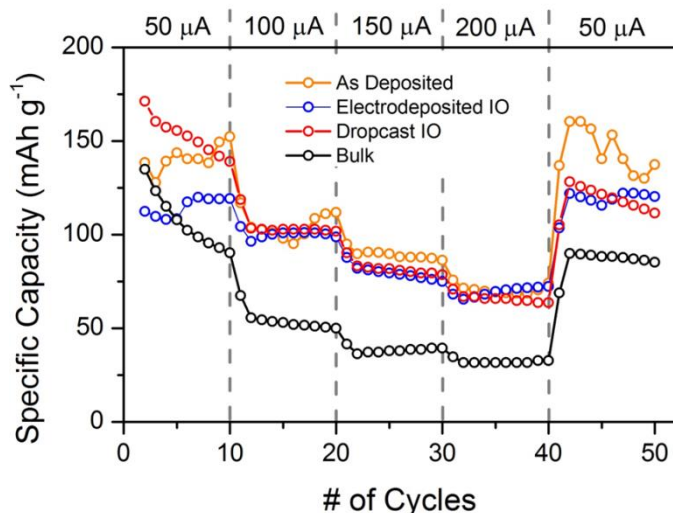


Fig. 7.11 Comparison of the rate performance for all sample types indicating slightly improved specific capacity values after rate changes in both the as-deposited (after heating to 300 °C) material (orange) and the electrodeposited IO material (blue).

Cyclic voltammetry was performed on the electrodeposited V_2O_5 IO and as deposited material at a scan rate of 0.1 mV/s for 10 cycles within the potential range of 4.0-1.2 V. A comparison between the first cycle of the IO and as deposited material is shown in Fig. 7.12(a). In the first discharge, the shape, as per galvanostatic measurements, is highly indicative of the phase and structural transitions within the material due to lithium insertion. In Fig. 7.12 (b) and (c) the cyclic voltammograms for the 2nd, 5th and 10th cycles for both the IO and as deposited material, respectively are shown. The differences in the changes occurring to the structure/phase of the two materials are immediately clear. In Fig. 7.12 (a) reduction peaks are observed at ~ 3.359, 3.142, 2.217 and 1.851 V for the IO structure. The last two peaks at ~ 2.217 V and 1.851 V correspond well with the potential plateau regions in the galvanostatic discharge curves shown in Fig. 7.6. These two peaks are also present in the as deposited material. The reduction peaks seen in the first discharge remain partially visible in the 2nd cycle for the IO sample but at more positive currents. These two peaks at ~3.359 V and 3.142 V are also seen in the 2nd discharge of the as deposited material.

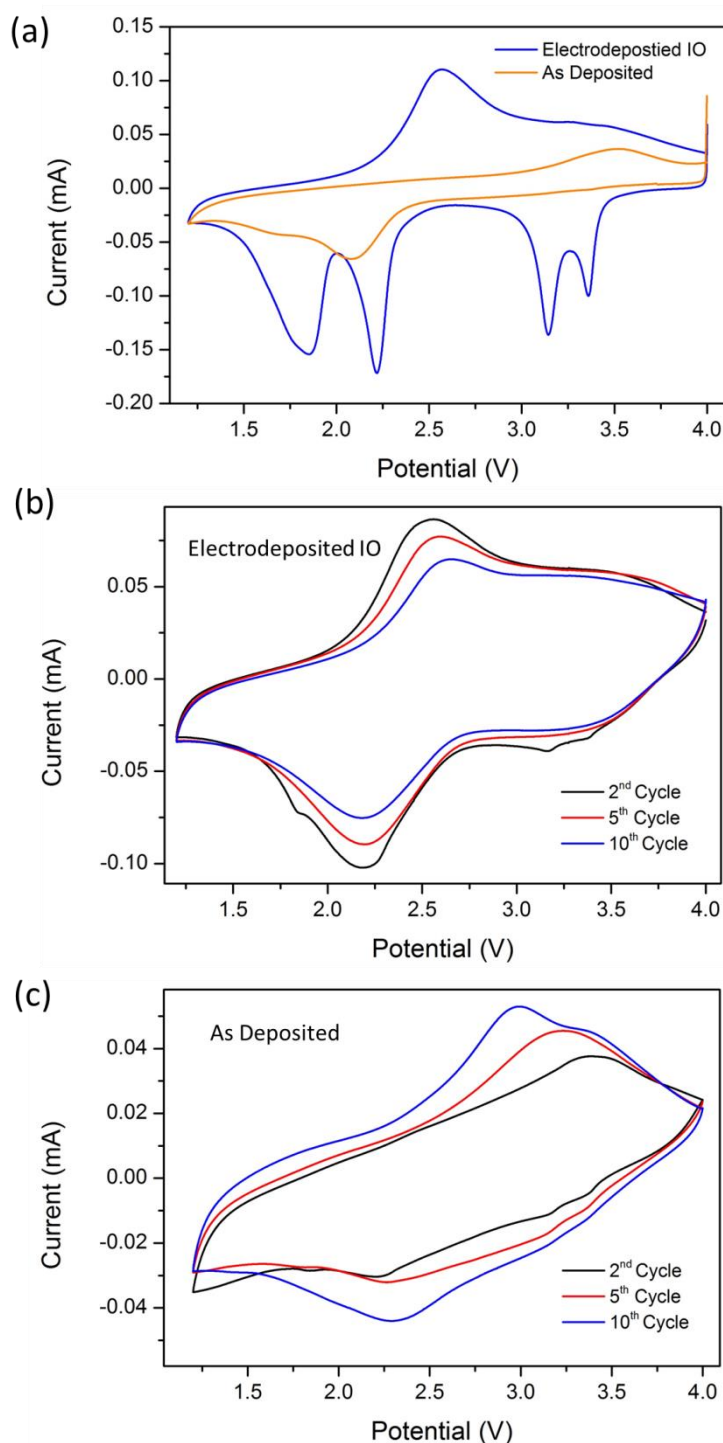


Fig. 7.12 Cyclic voltammograms of the electrodeposited IO sample and electrodeposited as-deposited sample at a rate of 0.1 mV s^{-1} (a) first cycle comparisons (b) the 2nd, 5th and 10th cycle for the IO material and (c) the 2nd, 5th and 10th cycle for the as-deposited material.

The integrated area (charge) in cyclic voltammogram over a certain potential range can be used to determine specific capacity values, though this method can give heightened values and is therefore less reliable than galvanostatic measurements for specific capacity

determination. For example, discharge specific capacities were calculated as $\sim 241 \text{ mAh g}^{-1}$ for the electrodeposited IO and $\sim 171 \text{ mAh g}^{-1}$ for the as deposited material after the 10th CV cycle. These values far exceed those seen in galvanostatic testing. The area for the as deposited sample increases from the 2nd to the 10th suggesting, as was observed in the galvanostatic testing, an increase in the amount of lithium intercalated and subsequent specific capacity between the 2nd and 10th cycle.

7.2.4 Structural Characterisation of Li Intercalated IOs

In order to better understand the structural changes occurring in the IO material, linear sweep voltammograms were conducted from 4 V to the reduction peak voltages V_p observed in the initial cyclic voltammograms i.e. $V_p = 3.359, 3.142, 2.217$ and 1.851 V . At these voltages samples were removed from the split cell and both Raman scattering and XRD measurements were performed to characterize any changes to the IO atomic and/or molecular structure. The initial Raman spectra for the electrodeposited IO, shown in Fig. 7.13 (a), matches that of orthorhombic V_2O_5 with a space group $Pmmn$ and D_{2h} point symmetry with the characteristic Raman modes at 102, 145, 196, 285, 304, 404, 482, 526, 701, and 994 cm^{-1} , identical to the drop-cast structures discussed in Chapter 6. On lithium insertion, one of the first noticeable changes in the Raman signature for the sample removed at 3.359 V, is the change in the skeleton bent vibration at 145 cm^{-1} evidence of the layered structure of the V_2O_5 . This peak begins to lower in intensity indicative of a decrease in structural order a slight shift towards a lower wavenumber of 143 cm^{-1} is also seen which is contrary to other reports on lithium insertion effects which report an increase in wavenumber.^{40, 41} However, this increase is later seen, in the samples removed at lower voltages, i.e. those intercalated for a longer time with lithium inserted to a higher mole fraction. The internal modes associated with the O-V-O and V-O-V bending vibrations and V-O stretching vibrations between wavenumbers $200\text{-}700 \text{ cm}^{-1}$

¹ are also seen to deform and shift in wavenumber. The peaks at 285 and 304 cm⁻¹ shift to lower wavenumbers, of 282 and 299 cm⁻¹ respectively, the peak at 404 cm⁻¹ previously assigned to a V-O-V stretch, moves towards a higher wavenumber of 407 cm⁻¹. The Raman modes at 482, 526 and 701 cm⁻¹ appear to shift towards lower wavenumbers. The formation of ϵ phase Li χ V₂O₅ has previously been reported with movement of the 483, 526 and 404 cm⁻¹ Raman modes towards higher wavenumbers, associated with oxygen displacement along the a-axis of the unit cell.^{41, 42} A shift in the stretching mode associated with the A_g symmetric vibrations of the short vanadyl V=O bond, initially with a bond length of ~ 1.58 Å, located at 994 cm⁻¹, shifts towards a lower wavenumber of 992 cm⁻¹. This is characteristic of a lengthening of this bond as lithium enters the interlayer spacing and has previously been associated with the ϵ phase.⁴⁰⁻⁴⁴ The sample removed at 3.359 V likely represents an intermediate phase, moving towards the transition to the ϵ phase.

The Raman signature for the sample discharged to 3.142 V shows the formation of a new peak at 957 cm⁻¹ and a further reduction in the V=O stretching mode frequency to 978 cm⁻¹. Low wavenumber vibrations are observed at 96, 123, and 169 cm⁻¹, the disappearance of the 196 cm⁻¹ mode and the progressive loss in intensity for these low wavenumber modes indicates a significant increase in local disorder within the layers. The modes associated with the bending and stretching vibrations of the weak V-O bonds, appear at 271, 327, 534, 641, and 720 cm⁻¹, the 404 cm⁻¹ mode disappears. Little difference is observed between the spectra at 3.142 V and 2.217 V. At 1.851 V, the peaks become broader and lower further in intensity, a new peak is observed at 412 cm⁻¹. The behaviour described here for the Raman characteristics of IO V₂O₅ intercalated with increasing amounts of lithium are mainly associated with the ϵ phase of LiV₂O₅ as has been reported for crystalline thin films elsewhere.⁴⁰⁻⁴² This suggests that lithium insertion into the crystalline V₂O₅ in IO form occurs similarly to that of a thin film material but across the increased surface area of the IO. It

should be noted that in most cases minor differences in spectra were observed throughout a single structure, characteristic of the presence of multiple phases.

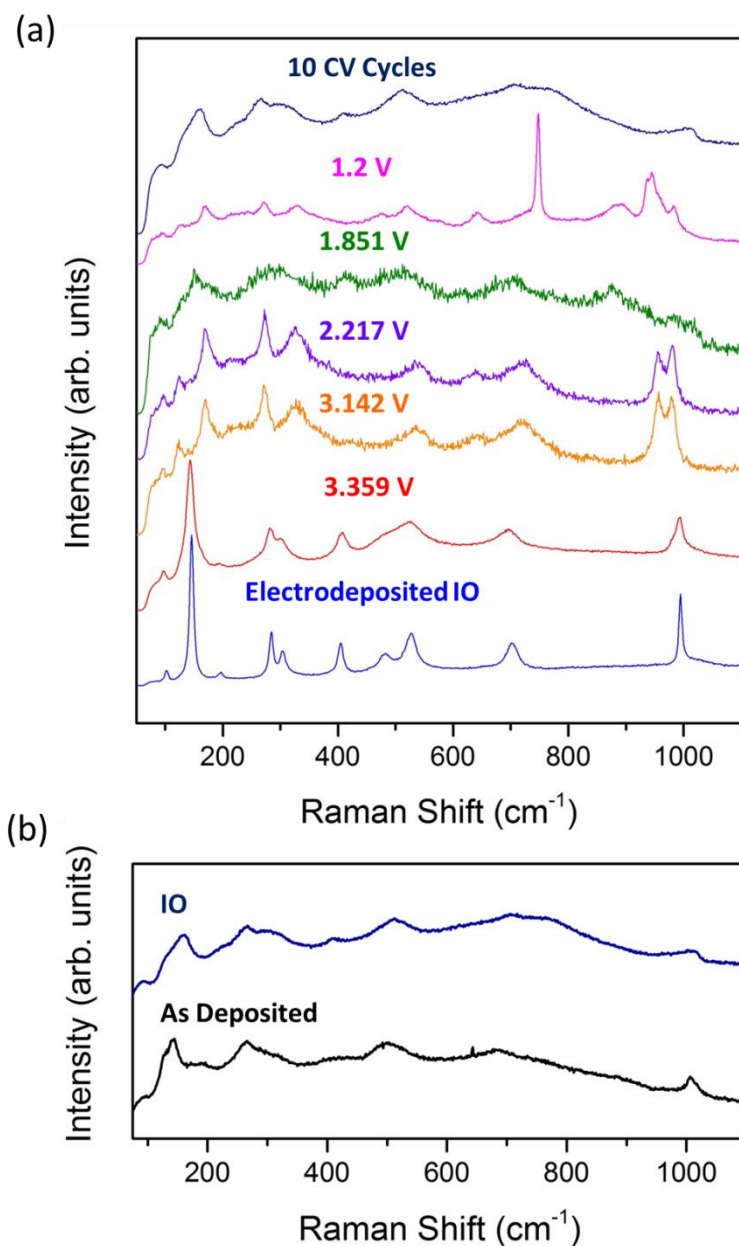


Fig. 7.13 (a) Raman scattering comparing the before spectra of an electrodeposited V₂O₅ IO structure to the spectra observed when potentiostatically swept at a rate of 0.1 mV s⁻¹ from 4.0 V to 3.359, 3.142, 2.217, 1.851 and 1.2 V, and after 10 cycles at a rate of 0.1 mV s⁻¹ in the potential window of 4 – 1.2 V and (b) a comparison of the IO and as deposited material after 10 cycles at 0.1 mV s⁻¹ between 4.0-1.2 V.

Generally, similar Raman characteristics are common to all the potential sweeps with the central differing factor being the disintegrating local order, and the lengthening and/or weakening of the V=O stretching mode. After 10 cycles, several low intensity broad peaks remain visible but extremely poor order within the $\text{Li}_x\text{V}_2\text{O}_5$ structure is probable. Interestingly the IO structure is still visible after 10 cycles. As is shown in Fig. 7.14, the IO structure before cycling is comparable to that seen after 10 cycles, order is relatively maintained after cycling though the material itself appears altered in composition evident by increased transparency and sensitivity under the electron beam. The splitting of the 957 and 978 cm^{-1} peaks has been suggested as resultant of two different vanadium atoms explained by a higher depth of discharge causing a change in electron localization.⁴¹ The similar Raman signatures for the as deposited and IO structures following successive cycling (10 cycles), shown in Fig. 7.13(b), suggests a similar structural deformation process in both samples, which is interesting given the initial differences seen in their CV profiles.

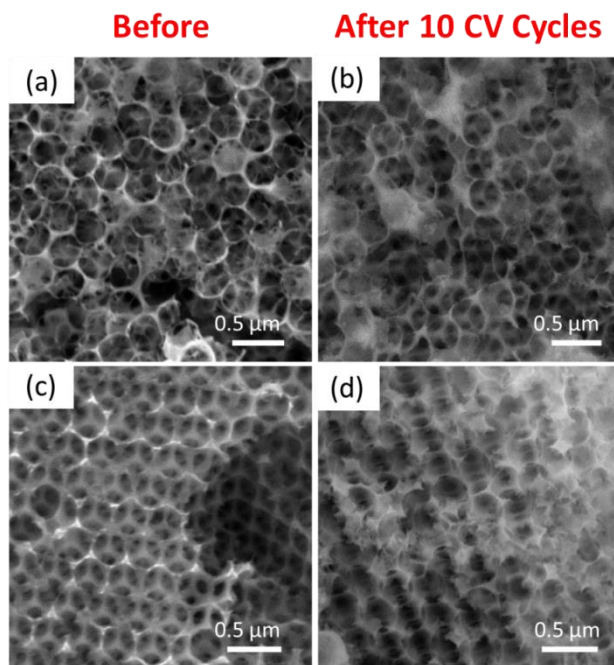


Fig. 7.14 SEM images representative of the IO morphology before (a) and (c) and after 10 cyclic voltammetry cycles (b) and (d) illustrating that the IO structure is still visible after 10 cycles though the IO walls appear rougher and more transparent under the beam.

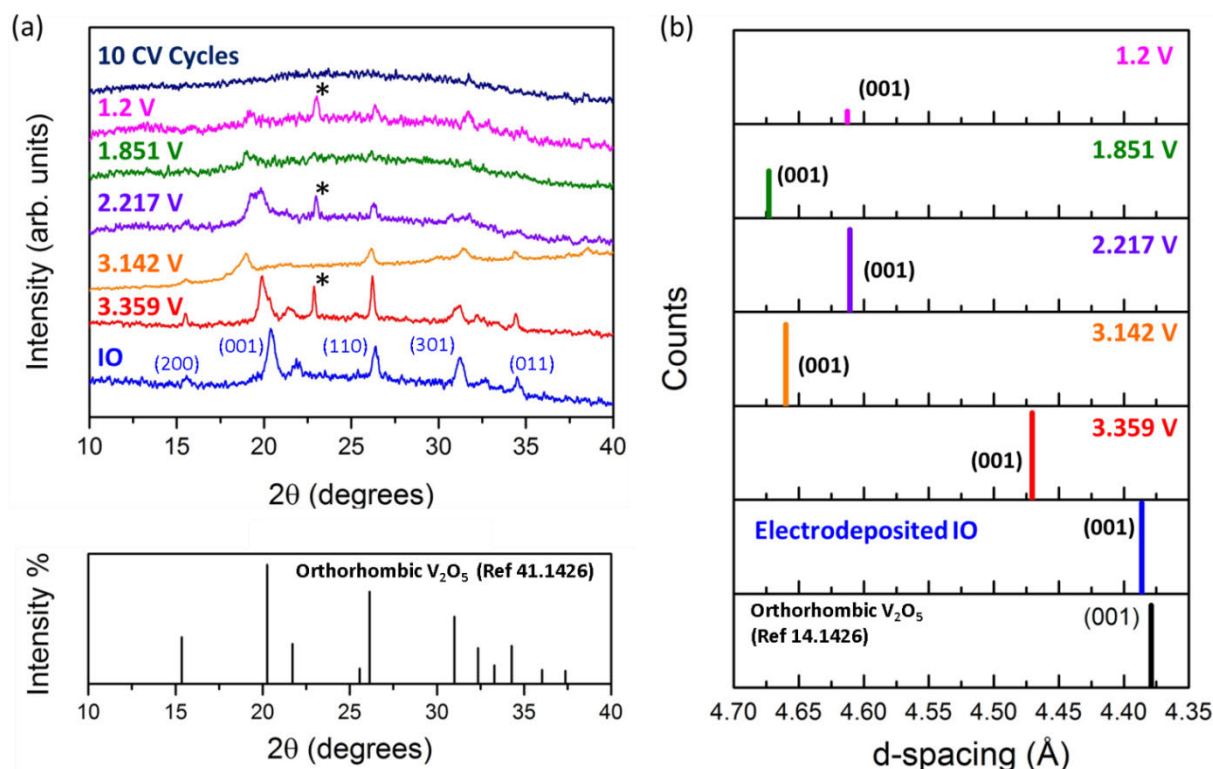


Fig. 7.15 (a) XRD spectra for the electrodeposited IO structure, before and after discharge at a rate of 0.1 mV s^{-1} to voltages corresponding to the reduction peaks seen in the cyclic voltammograms and after 10 discharge/charge cycles at a rate of 0.1 mV s^{-1} from 4.0-1.2 V. (b) Stick pattern corresponding to the peak position of the 001 peak, illustrating its variation in position and intensity caused by intercalating lithium.

The disintegration in local order in the layered structure of the V_2O_5 IO is further corroborated by XRD, shown in Fig. 7.15. The XRD pattern observed for the electrodeposited IO structure corresponds to orthorhombic V_2O_5 , with space group $Pmnm$, with the (001) peak at $2\theta \approx 20.37^\circ$. This (001) resonant peak shifts to lower angles and broadens as the discharge voltage decreases which is indicative of a widening of the crystal planes within the solid material regions of the lamellar structure as a consequence of the intercalation of the lithium ions between the V_2O_5 planes.⁴⁵⁻⁴⁷ A greater number of lithium ions cause a puckering of the layers and an increase in the interlayer spacing. The progression of the XRD spectra is directly correlated with the Raman spectra, showing gradual decrease in crystalline order as the material is discharged to 1.851 V, then a slight recovery at 1.2 V as

the lithium begins to leave the structure on charging. The final spectra taken after 10 cycles in both the Raman scattering data and XRD shows a lacking of any crystalline order present. The d-spacing decreases slightly between the sample at 3.142 V and 2.217 V and between 1.851 and 1.2 V. This could suggest a slight recovery in layer structure or, as has been proposed in dedicated HRTEM analysis of in-situ electrochemical modifications to vanadium oxide, a lithiation-induced electrochemical ‘welding’ of regions caused by phase change inclusions (localised regions of different phase) throughout the structure. However, considering these measurements were not conducted *in-situ*, slight variations in sample structure and thickness could account for the discrepancies in peak movement patterns, and specifically, the change in space group of the V_2O_5 structure as a function of the mole fraction of intercalated Li. A diffraction peak is observed at $\sim 22.8^\circ$ (* in Fig. 7.15 (a)) for the samples swept to 3.359 V, 2.217 V and 1.2 V, it is unclear as to the origin of this peak but one possibility is recrystallization of salts in residual electrolyte.

7.2.5 Flooded Cell Measurements

Galvanostatic testing was also performed in a 3 electrode flooded glass cell, to examine the possibility of optical characterization of porous IO materials deposited on ITO and FTO as transparent Li-ion battery electrodes, and to assess the usability of this cell setup. Measurements were performed under the same conditions as the split cell test – at a constant current of $\pm 30 \mu\text{A}$ in a potential window of 4.0-1.2 V with lithium foil as the counter and reference electrodes.

The specific capacity values obtained for the sample tested in the flooded cell correlate well with those obtained in the split cell as is shown in Fig. 7.16. The capacity in the flooded cell does not appear to suffer the same capacity fading, as is observed by the slight separation in trend around the 40th cycle. This may be due to a drying out of the separator in

the split cell arrangement, which is not a factor in a flooded cell. It could also be attributed to an increased electrolyte soakage for the flooded cell arrangement. This preliminary test to a significant number of cycles is promising for developing diffractive optical analytical method for examining changes to the photonic band gap and bias-dependent electrochromic responses of 3D structured porous materials as ion-intercalation electrodes.

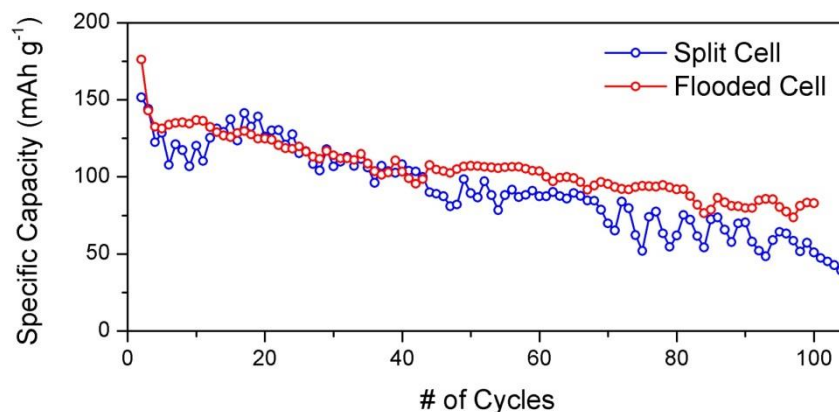


Fig. 7.16 Specific capacity as a function of cycle number for an electrodeposited V_2O_5 IO on stainless steel foil, tested in a potential window of 4.0-1.2 V, at a constant current of $30 \mu A$ over 100 cycles in a flooded cell and split cell arrangement.

7.3 Conclusions

Inverse opal vanadium oxide cathode architectures were synthesised using PS sphere templates and electrodeposition from a vanadate sulphate aqueous solution. Electrodeposition time was limited to 15 min to prevent overfilling the IO structure. Electrochemical characterization was performed using a split cell arrangement against a lithium anode. Galvanostatic measurements were performed at a constant current of $50 \mu A$ within a potential window of 4-1.2 V. Results indicate that the IO structures formed by electrodeposition and alkoxide drop-casting present promising initial capacities of ~ 160 and 109 mAh g^{-1} for the drop-cast and electrodeposited IO respectively, compared with bulk V_2O_5 . The discharge profile for the as deposited material suggests a partially amorphous structure this may allude

to a need for further, longer crystallization, perhaps at higher temperature, due to the dense packing of the as deposited material compared with the porous IO structure. This could also be accounted for by the presence of a lower oxidation state of vanadium oxide, possibly due also to the post deposition sample treatment. However, the as deposited material displayed capable performance, suggesting perhaps that partially amorphous materials could be beneficial for lithium intercalation. The IO and as deposited materials all presented good rate stability. Raman scattering and XRD characterization was performed to help determine the structural and phase alterations on lithium insertion and to what level structural degradation occurs. This process highlighted the stress incurred by the interlayer widening and formation of the $\epsilon\text{-Li}_x\text{V}_2\text{O}_5$ phase. In order to better determine performance ability between the different structures, further investigation needs to be made better accounting for mass loading between samples. In situ measurements would also provide an increased understanding of both macro-structure changes to the IO order and phase changes in the V_2O_5 structural order during intercalation. For this reason the transferability of the sample performance to a flooded glass cell is promising towards accommodating and developing *in-situ* measurement methods.

7.4 References

1. Tarascon, J. M.; Armand, M., Issues and Challenges Facing Rechargeable Lithium Batteries. *Nature* (2001), **414**, 359-367.
2. Scrosati, B.; Garche, J., Lithium batteries: Status, prospects and future. *J. Power Sources* (2010), **195**, 2419-2430.
3. Roberts, M.; Johns, P.; Owen, J.; Brandell, D.; Edstrom, K.; El Enany, G.; Guery, C.; Golodnitsky, D.; Lacey, M.; Lecoeur, C.; Mazor, H.; Peled, E.; Perre, E.; Shaijumon, M. M.; Simon, P.; Taberna, P.-L., 3D Lithium ion Batteries-from Fundamentals to Fabrication. *J. Mater. Chem.* (2011), **21**, 9876-9890.
4. Rolison, D. R.; Long, J. W.; Lytle, J. C.; Fischer, A. E.; Rhodes, C. P.; McEvoy, T. M.; Bourg, M. E.; Lubers, A. M., Multifunctional 3D Nanoarchitectures for Energy Storage and Conversion. *Chem. Soc. Rev.* (2009), **38**, 226-252.
5. Van Gough, D.; Juhl, A. T.; Braun, P. V., Programming Structure into 3D Nanomaterials. *Mater. Today* (2009), **12**, 28-35.
6. Ergang, N. S.; Lytle, J. C.; Lee, K. T.; Oh, S. M.; Smyrl, W. H.; Stein, A., Photonic Crystal Structures as a Basis for a Three-Dimensionally Interpenetrating Electrochemical-Cell System. *Adv. Mater.* (2006), **18**, 1750-1753.
7. Ergang, N. S.; Fierke, M. A.; Wang, Z.; Smyrl, W. H.; Stein, A., Fabrication of a Fully Infiltrated Three-Dimensional Solid-State Interpenetrating Electrochemical Cell. *J. Electrochem. Soc.* (2007), **154**, A1135-A1139.
8. Sakamoto, J. S.; Dunn, B., Hierarchical Battery Electrodes Based on Inverted Opal Structures. *J. Mater. Chem.* (2002), **12**, 2859-2861.
9. Lytle, J., Inverse Opal Nanoarchitectures as Lithium-Ion Battery Materials. In *Nanotechnology for Lithium-Ion Batteries*, Abu-Lebdeh, Y.; Davidson, I., Eds. Springer US: 2013; pp 13-41.
10. Kang, D.-Y.; Kim, S.-O.; Chae, Y. J.; Lee, J. K.; Moon, J. H., Particulate Inverse Opal Carbon Electrodes for Lithium-Ion Batteries. *Langmuir* (2013), **29**, 1192-1198.
11. Li, X.; Dhanabalan, A.; Gu, L.; Wang, C., Three-Dimensional Porous Core-Shell Sn@Carbon Composite Anodes for High-Performance Lithium-Ion Battery Applications. *Adv. Energy Mater.* (2012), **2**, 238-244.
12. Zhou, W.; Lin, L.; Wang, W.; Zhang, L.; Wu, Q.; Li, J.; Guo, L., Hierarchical Mesoporous Hematite with "Electron-Transport Channels" and Its Improved Performances in Photocatalysis and Lithium Ion Batteries. *J. Phys. Chem. C* (2011), **115**, 7126-7133.
13. Doherty, C. M.; Caruso, R. A.; Smarsly, B. M.; Drummond, C. J., Colloidal Crystal Templating to Produce Hierarchically Porous LiFePO₄ Electrode Materials for High Power Lithium Ion Batteries. *Chem. Mater.* (2009), **21**, 2895-2903.
14. Zhang, H.; Braun, P. V., Three-Dimensional Metal Scaffold Supported Bicontinuous Silicon Battery Anodes. *Nano Lett.* (2012), **12**, 2778-2783.
15. Zhang, H.; Yu, X.; Braun, P. V., Three-dimensional Bicontinuous Ultrafast-Charge and -Discharge Bulk Battery Electrodes. *Nat. Nanotechnol.* (2011), **6**, 277-281.
16. Osiak, M.; Geaney, H.; Armstrong, E.; O'Dwyer, C., Structuring Materials for Lithium-ion Batteries: Advancements in Nanomaterial Structure, Composition, and Defined Assembly on Cell Performance. *J. Mater. Chem. A* (2014), **2**, 9433-9460.
17. Wang, Y.; Cao, G., Synthesis and Enhanced Intercalation Properties of Nanostructured Vanadium Oxides. *Chem. Mater.* (2006), **18**, 2787-2804.

18. McNulty, D.; Buckley, D. N.; O'Dwyer, C., Synthesis and electrochemical properties of vanadium oxide materials and structures as Li-ion battery positive electrodes. *J. Power Sources* (2014), **267**, 831-873.
19. Tong, Z.; Hao, J.; Zhang, K.; Zhao, J.; Su, B.-L.; Li, Y., Improved Electrochromic Performance and Lithium Diffusion Coefficient in Three-dimensionally Ordered Macroporous V₂O₅ Films. *J. Mater. Chem. C* (2014), **2**, 3651-3658.
20. Li, L.; Steiner, U.; Mahajan, S., Improved Electrochromic Performance in Inverse Opal Vanadium Oxide Films. *J. Mater. Chem.* (2010), **20**, 7131-7134.
21. Vu, A.; Qian, Y.; Stein, A., Porous Electrode Materials for Lithium-Ion Batteries – How to Prepare Them and What Makes Them Special. *Adv. Energy Mater.* (2012), **2**, 1056-1085.
22. Goodenough, J. B.; Kim, Y., Challenges for Rechargeable Li Batteries. *Chem. Mater.* (2009), **22**, 587-603.
23. Stein, A., Energy storage: Batteries take charge. *Nat. Nanotechnol.* (2011), **6**, 262-263.
24. Lee, S. W.; Yabuuchi, N.; Gallant, B. M.; Chen, S.; Kim, B.-S.; Hammond, P. T.; Shao-Horn, Y., High-power Lithium Batteries from Functionalized Carbon-Nanotube Electrodes. *Nat Nanotechnol.* (2010), **5**, 531-537.
25. Arico, A. S.; Bruce, P.; Scrosati, B.; Tarascon, J.-M.; van Schalkwijk, W., Nanostructured Materials for Advanced Energy Conversion and Storage Devices. *Nat. Mater.* (2005), **4**, 366-377.
26. Sapoletova, N.; Makarevich, T.; Napolskii, K.; Mishina, E.; Eliseev, A.; van Etteger, A.; Rasing, T.; Tsirlina, G., Controlled Growth of Metallic Inverse Opals by Electrodeposition. *Phys. Chem. Chem. Phys.* (2010), **12**, 15414-15422.
27. Cottrell, F. G., *Z. Phys. Chem.* (1903), **42**, 385.
28. Grujicic, D.; Pesic, B., Electrodeposition of Copper: the Nucleation Mechanisms. *Electrochim. Acta* (2002), **47**, 2901-2912.
29. Ramirez-Garcia, S.; Alegret, S.; Cespedes, F.; Forster, R. J., Carbon composite electrodes: surface and electrochemical properties. *Analyst* (2002), **127**, 1512-1519.
30. Chung, Y.-W.; Leu, I.-C.; Lee, J.-H.; Yen, J.-H.; Hon, M.-H., Fabrication of Various Nickel Nanostructures by Manipulating the One-Step Electrodeposition Process. *J. Electrochem. Soc.* (2007), **154**, E77-E83.
31. Kim, J.; Kim, H. S.; Choi, J. H.; Jeon, H.; Yoon, Y.; Liu, J.; Park, J.-G.; Braun, P. V., Epitaxial Growth of Three-Dimensionally Mesoporous Single-Crystalline Cu₂O via Templated Electrodeposition. *Chem. Mater.* (2014), **26**, 7051-7058.
32. Wong, S.; Kitaev, V.; Ozin, G. A., Colloidal Crystal Films: Advances in Universality and Perfection. *J. Am. Chem. Soc.* (2003), **125**, 15589-15598.
33. Hatton, B.; Mishchenko, L.; Davis, S.; Sandhage, K. H.; Aizenberg, J., Assembly of Large-area, Highly Ordered, Crack-free Inverse Opal Films. *Proc. Natl. Acad. Sci. U. S. A.* (2010), **107**, 10354-10359.
34. Whittingham, M. S., The Role of Ternary Phases in Cathode Reactions. *J. Electrochem. Soc.* (1976), **123**, 315-320.
35. West, K.; Zachau-Christiansen, B.; Jacobsen, T.; Skaarup, S., Vanadium Oxide Xerogels as Electrodes for Lithium Batteries. *Electrochim. Acta* (1993), **38**, 1215-1220.
36. Cheah, S. K.; Perre, E.; Rooth, M.; Fondell, M.; Hårsta, A.; Nyholm, L.; Boman, M.; Gustafsson, T.; Lu, J.; Simon, P.; Edström, K., Self-Supported Three-Dimensional Nanoelectrodes for Microbattery Applications. *Nano Lett.* (2009), **9**, 3230-3233.
37. Long, J. W.; Dunn, B.; Rolison, D. R.; White, H. S., Three-Dimensional Battery Architectures. *Chem. Rev.* (2004), **104**, 4463-4492.

38. Wang, Z.; Fierke, M. A.; Stein, A., Porous Carbon/Tin (IV) Oxide Monoliths as Anodes for Lithium-Ion Batteries. *J. Electrochem. Soc.* (2008), **155**, A658-A663.
39. Ergang, N. S.; Lytle, J. C.; Yan, H.; Stein, A., Effect of a Macropore Structure on Cycling Rates of LiCoO₂. *J. Electrochem. Soc.* (2005), **152**, A1989-A1995.
40. Baddour-Hadjean, R.; Golabkan, V.; Pereira-Ramos, J. P.; Mantoux, A.; Lincot, D., A Raman Study of the Lithium Insertion Process in Vanadium Pentoxide Thin Films Deposited by Atomic Layer Deposition. *J. Raman Spectrosc.* (2002), **33**, 631-638.
41. Baddour-Hadjean, R.; Pereira-Ramos, J. P.; Navone, C.; Smirnov, M., Raman Microspectrometry Study of Electrochemical Lithium Intercalation into Sputtered Crystalline V₂O₅ Thin Films. *Chem. Mater.* (2008), **20**, 1916-1923.
42. Baddour-Hadjean, R.; Navone, C.; Pereira-Ramos, J. P., In situ Raman Microspectrometry Investigation of Electrochemical Lithium Intercalation into Sputtered Crystalline V₂O₅ Thin Films. *Electrochim. Acta* (2009), **54**, 6674-6679.
43. Baddour-Hadjean, R.; Pereira-Ramos, J. P., New structural approach of lithium intercalation using Raman spectroscopy. *J. Power Sources* (2007), **174**, 1188-1192.
44. Baddour-Hadjean, R.; Marzouk, A.; Pereira-Ramos, J. P., Structural Modifications of Li_xV₂O₅ in a Composite Cathode (0 ≤ x < 2) Investigated by Raman Microspectrometry. *J. Raman Spectrosc.* (2012), **43**, 153-160.
45. O'Dwyer, C.; Gannon, G.; McNulty, D.; Buckley, D. N.; Thompson, D., Accommodating Curvature in a Highly Ordered Functionalized Metal Oxide Nanofiber: Synthesis, Characterization, and Multiscale Modeling of Layered Nanosheets. *Chem. Mater.* (2012), **24**, 3981-3992.
46. Gannon, G.; O'Dwyer, C.; Larsson, J. A.; Thompson, D., Interdigitating Organic Bilayers Direct the Short Interlayer Spacing in Hybrid Organic-Inorganic Layered Vanadium Oxide Nanostructures. *J. Phys. Chem. B* (2011), **115**, 14518-14525.
47. O'Dwyer, C.; Lavayen, V.; Tanner, D. A.; Newcomb, S. B.; Benavente, E.; González, G.; Torres, C. M. S., Reduced Surfactant Uptake in Three Dimensional Assemblies of VOx Nanotubes Improves Reversible Li⁺ Intercalation and Charge Capacity. *Adv. Funct. Mater.* (2009), **19**, 1736-1745.

Chapter 8

Conclusions

8.1 Introduction

This chapter briefly outlines the significant conclusions from each of the four results chapters. Recommendations for continued investigation are also presented.

8.2 Ordered 2D Colloidal Photonic Crystals on Gold Substrates by Surfactant-assisted Fast-rate Dip Coating

Advances in template fabrication onto metallic, conductive substrates at higher fabrication rates, without a reduction in ordering is particularly useful for sensing and/or electrochemical applications that require a current collecting support. Difficulties arise however for the assembly of polymer spheres on metallic surfaces hydrophobic in air. In **Chapter 4**, this problem was addressed by the addition of an anionic surfactant to a solution of 700 nm poly(methyl methacrylate) PMMA spheres prior to assembly. When the anionic surfactant sodium dodecyl sulphate (SDS) was added to a 5 wt% aqueous solution of 700 nm PMMA spheres at a concentration above the critical micelle concentration of SDS, an ordered monolayer of spheres formed on the gold coated substrate when withdrawn from the solution at a rate of 1 mm min^{-1} . Assembly at these concentrations at the slower rate of withdrawal of 1 mm hr^{-1} was less effective typically producing a disordered assembly. At sphere and SDS concentrations reduced by $\sim 50\%$ however, 2D structures with a further improved order, compared with the fast rate 2D monolayer, were obtained at the slower rate of withdrawal. The improved quality of the 2D structures formed using the SDS addition was investigated using an angle resolved spectroscopy measurement system. The angle resolved 2D diffraction from the sample surface was compared with the diffraction recorded from a disordered array and a clear improvement in diffractive behaviour for the SDS assisted sample is shown.

8.3 Methods of Affecting and Directing Opal Growth by Dip Coating

In **Chapter 5**, glass substrates were prepared by two different cleaning methods, one with piranha solution resulting in a water contact angle of $\sim 30^\circ$, and the other with O_2 plasma resulting in a highly hydrophilic surface with a contact angle of $\sim 0^\circ$. Colloidal self-assembly of 700 nm PMMA spheres by noise-assisted dip coating produced 3D colloidal crystals with high degrees of order. Through angle resolved transmission measurements the internal long range order of the structures was investigated and the superior quality of photonic crystal formation on the O_2 Plasma cleaned glass surface was demonstrated by monitoring a more defined optical transmission resonance for the (111) plane.

Next, the application of heat was demonstrated as another route towards improving the order and thickness of opal deposits formed at a faster rate of dip coating. The application of heat to an aqueous solution of PS spheres improved sphere assembly on ITO-coated glass and gold-coated silicon substrates. The increased particle flux towards the liquid meniscus at the higher evaporation rate compensated for the faster withdrawal from solution, improving the 2D optical reflectivity and thickness for PS spheres compared with deposition at room temperature. However, the addition of heat for the deposition of PMMA spheres was less successful. The lower net repulsion between PMMA spheres compared with PS spheres led to an insufficient time for the PMMA spheres to reach the thermodynamically favoured FCC ordering. High temperatures resulted in a greater number of irregularities in array growth and further investigation is needed to quantify the needed increase in temperature to produce an evaporation rate able to accommodate a particular increase in withdrawal rate for a particular colloid.

In the last part of chapter 5, the dip coating of e-beam patterned substrates with polymer pillar arrays non-commensurate with the normally favoured (111) fcc arrangement

of PS spheres, allowed the formation of an adsorbate unit cell a factor of $\sqrt{2}$ smaller than the substrate unit cell in both directions and rotated by 45° with respect to the substrate fcc (100) unit cell. The ability to predetermine sphere arrangement and symmetry is highly desirable for the fabrication of specific templates for the synthesis of functional devices, for example, for sensing or waveguide applications. Using polymer e-beam resists similar to the sphere composition, patterns can influence and enforce order in the dip-coated 2D colloidal crystal to form quasi-binary colloids that cannot be formed by co-deposition using 2 or more sphere sizes. The use of PMMA as the patterning media could allow better control over defect introduction in monolayer coatings for the formation of 2D PhCs with a highly specific optical sensitivity, and subsequent growth allows 3D colloidal photonic crystals with photonic band gaps defined by the single sphere 3D colloidal assembly on the alternative reduced dimension 2D assembly caused by patterning.

8.4 2D and 3D Vanadium Oxide Inverse Opals and Hollow Sphere Arrays

In **Chapter 6**, the formation of multilayer PS opal templates using electrophoretic deposition was described. The colloidal crystal thickness was varied and controlled with deposition time and voltage. For longer electrophoresis times, thickness fluctuations across the template increased as the PS sphere solution settled over time. Vanadium oxide (V_2O_5) inverted opals (IOs) were then synthesised by infiltrating these templates with vanadium oxytriisopropoxide diluted with IPA, in the ratio 100:1 IPA:OV(OCH(CH₃)₂)₃. Nitrogen gas at over-pressure was developed to improve template infiltration and slow down hydrolysis to improve uniformity in crystallisation. Samples were heated at 300 °C for 12 h, a lower temperature than typically used so as to maintain the shape dimensions of the IO network.

The crystallinity and phase of the subsequent IO material was comprehensively examined using Raman scattering to illustrate the sensitivity of the material composition to

IO structural morphology. Drop casting the 100:1 precursor solution with the applied nitrogen on the monolayer PMMA sphere templates described in chapter 1 produced basin-like V_2O_5 structures with visible 2D diffraction. It was also determined that repeated dip coating of the PMMA monolayer templates in the IPA diluted precursor led to the formation of 2D V_2O_5 hollow sphere arrays, due to an over-filling and rapid hydrolysis of the precursor solution. Also discussed in this chapter was the formation of amorphous IO materials using UV Ozone exposure for sphere removal, which allowed a crystalline 2D inverse opal structure with amorphous V_2O_5 . These structures were also shown to remain stable after crystallization at 300 °C for 12 hours with no noticeable structural deformation. Controlling 2D and 3D inverse opal and related structures, without solvent etching that may dissolve or disrupt the template order, is a viable route for the formation of amorphous material IOs, provided polymeric templates capable of decomposition under UV-ozone exposure are used. The ability to form IO materials on metallic surfaces using amenable synthetic procedures applicable to a range of surfaces (flexible, plastic, temperature sensitive etc.) to other methods like ALD or CVD is potentially important for the incorporation of IO designs into functional devices.

8.5 Electrodeposited Vanadium Oxide Inverse Opal Lithium Ion Battery Cathodes

In the final results chapter, **Chapter 7**, PS templates formed by electrophoretic deposition were infiltrated by electrodeposition to form thicker V_2O_5 IO samples than obtained by precursor drop casting. The electrochemical performance of these IO structures was then compared to the drop cast IO material, the as-deposited material electrodeposited onto the current collector directly with no PS template, heated as was the electrodeposited IO to 300 °C for 24 h. According to galvanostatic cycling the mole fraction of intercalated lithium increase from the 2nd to 10th cycle for both the electrodeposited IO structure and the

electrodeposited as-deposited material. A maximum capacity loss of ~ 33% from the 2nd to 100th cycle is found for the electrodeposited IO. The specific capacity however, is still comparable to commercial cathode materials and the coulometric efficiency during cycling (without the addition of binder or conductive additives) his still amounts to significant capacity retention over 100 cycles for a constant current of 30 μ A. Of the IO materials the specific capacity appears highest for the drop cast material, but this could be partially due to mass loading and further investigation at masses closer to those of the electrodeposited materials is needed. All three materials exhibited high stability during high rate capability tests with specific capacity values returning to values obtained before cycling at the higher charge rates. Excluding the first discharge capacity, all delivered specific capacities (>150 mAh g^{-1}) above those measured for the bulk V_2O_5 powder, and with minimal capacity fading. The as deposited material in particular presented higher specific capacity values, however the as-deposited material did appear to present a greater instability over a short cycle range than other materials.

Using Raman and XRD at various depths of discharge, the structural deformation of the orthorhombic V_2O_5 layered structure during discharging in a battery cell was demonstrated by a shift in the (001) diffraction reflection to lower angles indicative of an increase in interlayer spacing with increasing lithium insertion, and also by a quenching of the B_{1g} phonon mode for orthorhombic V_2O_5 at 145 cm^{-1} related to order within the layers for the material. At discharge potential of $\sim 3.142\text{ V}$ under voltammetric polarization, and corroborated by XRD and Raman scattering, the dominant phase appears to be that of the ϵ -phase V_2O_5 which relates well with the galvanostatic discharge profile. The reduced dimensions of the V_2O_5 material in the IO structure prevents solid state diffusion limitations and is electrically interconnected so that ambipolar conductivity is maintained throughout cycling. Second, high mole fraction lithiation to irreversible phases is prevented even at deep

discharge. Crystalline order is retained at this phase, but after 10 cycles the material appears to reach a primarily amorphous state.

8.6 Summary of Conclusions

- Ordered 2D monolayer colloidal crystals of PMMA spheres can form on gold surfaces at a faster rate of dip coating by the addition of the surfactant SDS above CMC.
- A more hydrophilic surface promotes long range order in opal deposits dip coated at slow rates with noise agitation.
- An increase in temperature increases thickness and order for PS spheres at faster withdrawal rates but forms only disordered photonic glass for PMMA spheres dip coated at the same rate.
- Dip coating of PS spheres is highly sensitive to substrate conditions and patterned substrates can influence packing and symmetry.
- Well-ordered crystalline V_2O_5 IOs can be formed by drop casting IPA diluted vanadium oxytriisopropoxide under nitrogen gas over-pressure to force impregnation of the template and slow down hydrolysis.
- Overfilling of monolayer substrates by dip coating and removal of the spheres can create hollow sphere arrays that visibly diffract light.
- Underfilling of monolayer substrates by drop casting under nitrogen can create an array of V_2O_5 basins that behave as 2D diffraction gratings.
- UV ozone can be used for the removal of a monolayer of polymer sphere infilled with precursor to form amorphous IO that can later be crystallized under temperature with no structural variation.
- V_2O_5 IOs can be formed by electrodeposition on a number of metallic and transparent conductive substrates.

- Both electrodeposited and drop cast V_2O_5 IO structures show better electrochemical response to cycle reversible lithiation than bulk V_2O_5 .
- Electrodeposited IOs show good capacity retention over 100 cycles but the crystalline V_2O_5 still suffers a high degree of structural deformation on increasing lithium content.
- The IO structure prevents irreversible phase formation and promotes electronic and ionic diffusion without binders or conductive additives at deep discharge and maintains good coulometric efficiency at slow and fast discharge-charge rates.

8.7 Future Work

8.7.1 Sphere Deposition on Patterned Substrates

A higher sensitivity resist was shown in chapter 5 to form higher resolution pillars at lower dose patterns. In order to improve the uniformity of the substrate patterns used dose characteristics need to be tuned to suit the higher sensitivity and scanning direction and exposure mode should be explored as a method of improving the pillar resolution. In this work positive resist was used, however, negative resist might be better suited for the formation of these types of pillar patterns. With negative resist it is the area exposed that remains after developing, meaning exposure areas would be much smaller than for positive resist, and the pattern much simpler. Patterning in this case was performed on a system outside of a cleanroom environment, and with the tendency of negative resists to be UV sensitive, use of them would require better facilities and extra sample preparation and care. However this would no doubt lead to better structures and subsequently a more uniform coating of spheres. As was suggested at the end of chapter 5, topographical and chemical patterning techniques^{1, 2} could be combined by modifying the pillar and/or sphere surfaces with material selective self-assembled monolayers (SAMs). The use of different sphere types

could also be used which could allow one sphere type to then be selectively removed or altered to create the desired structure. Electrophoretic deposition, as used in chapter 6 and 7 for the assembly of PS spheres on conductive substrates, could also be investigated using patterned substrates. It would be of interest also, to determine and analyse the photonic band gap by modelling in order to gain some insight into the optical signature for an artificial opal with unit cell a factor of $\sqrt{2}$ smaller than an fcc (100) substrate unit cell in both directions.

8.7.2 Binary Colloidal Crystals by One-step EPD

In chapter 6 and 7, multilayer PS templates with the fcc (111) plane grown parallel to the substrate surface were formed on conductive substrates using electrophoretic deposition. In these instances a single sphere size was used in order to promote ordered assembly. As discussed in the review chapter binary colloidal crystals,³⁻⁵ formed using spheres of two sizes hold significant untapped potential, both optically and as structural templates for complex IO fabrication. However, many current growth methods for the self-assembly of binary colloids are limited by lengthy time requirements, poor control over larger dimensions and/or sedimentation of the larger particles before growth is completed. Future development of a fast single step process for the controllable formation of binary colloidal crystals is therefore a necessity if these structures are to reach their full potential.

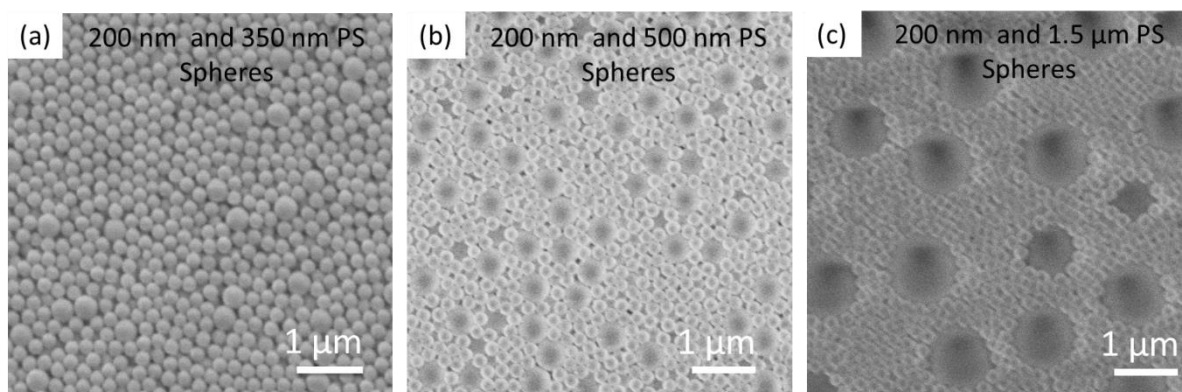


Fig. 8.1 SEM images of binary colloidal crystals fabricated using EPD at 3 V using a 1:1 solution of 200 nm PS spheres and (a) 350 nm (b) 500 nm or (c) 1.5 μm PS spheres.

As described in the review (chapter 2), the assembly of smaller spheres by EPD on to a layer of larger spheres deposited by relatively slow evaporative assembly is possible and this cycle can be repeated for successive layers.⁵ Not yet reported to the best of my knowledge is the use of EPD for one step binary colloidal crystal growth. Preliminary investigation into the use of a single solution, containing spheres of two different diameters in a 1:1 concentration ratio and the application of an electric field for the assembly of ordered binary crystals is optimistic, see Fig. 8.1. While the structures are primarily disordered, variations in size ratio have shown some improvement, and as discussed in the chapter 2, the arrangement of binary crystals is determined by two factors - the size ratio and the number ratio (the concentrations of the two sphere types). By experimenting with these factors, ordered binary colloidal crystals may be possible using one-step EPD, but electrophoretic mobility needs to be controlled for spheres with large diameter differences to avoid size separation prior to deposition and ordering.

The growth of multilayer heterostructures⁶ may also be possible by successive EPD using solutions of different sphere sizes as is shown in Fig. 8.2 (b) and (c). Incremental increases in the voltage and deposition time would likely be needed to continuously overcome the electrostatic screening by previously assembled spheres and allow the growth

of thicker sequential deposits. A combination between dip coating and EPD may be a viable route to rational control of binary, ternary or more complex colloidal crystal assemblies.

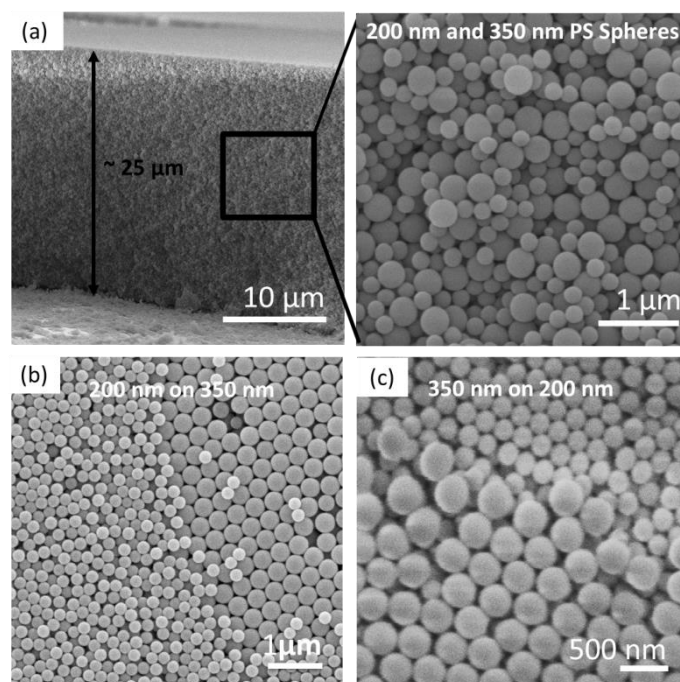


Fig. 8.2 SEM image of (a) a cross section of a colloidal binary crystal assembled from a mixture of 200 and 350 nm PS spheres illustrating that while disordered, the assembly of the two different spheres reaches through the whole structure (b) a 200 nm PS spheres assembled by EPD on a 350 nm PS template and (c) 350 nm PS spheres deposited by EPD on a 200 nm PS sphere template.

8.7.3 V_2O_5 IO Formation and Optical/Electrochemical Characterisation

V_2O_5 IOs were synthesised in chapter 6 by the drop casting of IPA diluted precursor in the ratio of 100:1. Two different opal templates were used for infilling. However, as mentioned in chapter 7, the mass of the resultant IO structure was less than that of the electrodeposited material. Future efforts could explore the use of different dilution ratios or different dilution solvents. A lower dilution factor would ensure a higher filling fraction and increase the mass of V_2O_5 formed. However, with less dilution the rate of hydrolysis in air increases. Rapid hydrolysis has a tendency to cause delamination of the template structure from the substrate surface, therefore a balance must be made. Delamination of the infilling template was

problematic throughout this thesis. Thick sphere depositions frequently became brittle and unstable and detached from the substrate. This was observed both during drop cast IO formation and with electrodeposition as well. Research into methods for improving sphere adhesion to substrate and each other after assembly, alternative to annealing methods, should be made. Perhaps the use of SAMs would be beneficial, or a slower heating/drying method which might allow for a less abrupt change in sphere size may prevent delamination after infilling and heating.

The electrodeposition of V_2O_5 IO materials would benefit from further investigation into correlating deposition time, voltage and electrolyte concentration with template thickness. This would prevent template overfilling but allow the full thickness of the template to be infilled. A dedicated body of work focused on pulsed electrodeposition, and potential step experiments that control the mechanism of nucleation and progressive material growth may offer finer control over the infilling depth. However, an in-situ method to predetermine the physical thickness of opal template prior to infilling may be useful to offset the timely SEM examination of each template prior to each deposition step.

As discussed in the chapter 2, IO materials are currently of interest primarily due to their photonic characteristics, the formation of a photonic band gap the ability to direct and control particular wavelengths of light though its design is of great utility and interest. It would be interesting therefore to probe the structure of the V_2O_5 IO materials optically, this would give greater insight into the long range order of the materials. It would allow better comparison between the two infilling routes described, particularly with respect to filling fraction and the preservation of template structural order.⁷

Raman and XRD investigations into the phase formation were carried out for material discharged to voltages correlated to the cyclic voltammetry data. While the mechanism of

structural changes during discharging-charging is clearer, further work on the charge rate capability as a function of the porous nature of the IO would be advantageous. When the walls of the IO are below the solid state diffusion limit of Li ion, theoretical there is no limit to the charge rate provided optimum electrolyte infiltration. The IO structure provide an ideal platform for fundamental investigation into the rate capability limits of real active material electrodes. The electrochemical performance of the drop cast IO should also be monitored for a larger number of cycles as was the electrodeposited IO in chapter 7, and at a comparable mass loading.

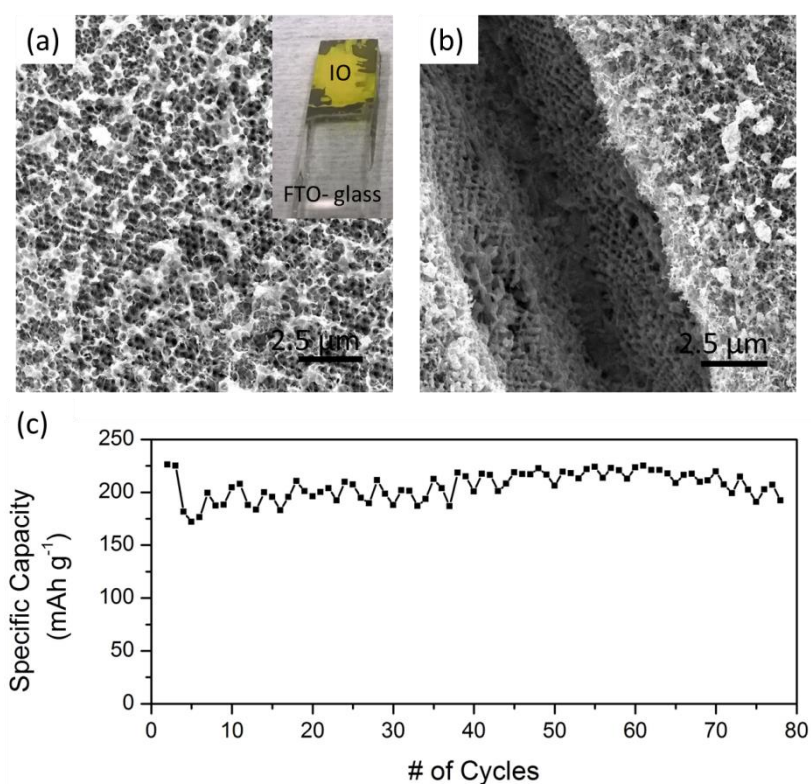


Fig. 8.3 (a) and (b) SEM images of IO structure formed on FTO-coated glass by electrodeposition at 2 V vs SCE for 15 minutes into a 350 nm PS template using an aqueous VOSO₄ solution and (c) the specific capacity (mAh g⁻¹) as a function of cycle number for the electrodeposited IO on FTO-coated glass, galvanostatically cycled at a current of 30 μA in a potential window of 4.0-1.2 V in a flooded cell arrangement with Li foil as the anode.

Electrochemical performance of V_2O_5 IOs on FTO-coated glass (Fig. 8.3(a) and (b)) in a flooded cell at a constant current of $30 \mu\text{A}$ has also shown promising cycling performance, as can be seen from the plot in Fig. 8.3 (c) of specific capacity across ~ 70 cycles. Therefore further investigation into the use of the flooded cell and IOs formed on this transparent substrate could allow in-situ optical characterisation to be more easily developed. The stainless steel substrates require optical reflectance spectroscopy and not transmission spectroscopy, which can prove more difficult from within a cell. The development of an *in-situ* IO characterisation technique could give increased information on the macro-structural degradation of the IO material throughout cycling (change in dielectric and index contrast, porosity change due to material swelling upon lithiation, and changes in the photonic band gap from order disintegration), which in turn could be related to *in-situ* Raman scattering^{8, 9} i.e. the phase changes and atomic structural degradation of the V_2O_5 material as a function of the depth of discharge or the state of charge.

8.8 References

1. Masuda, Y.; Itoh, T.; Koumoto, K., Self-Assembly Patterning of Silica Colloidal Crystals. *Langmuir* (2005), **21**, 4478-4481.
2. Masuda, Y.; Tomimoto, K.; Koumoto, K., Two-Dimensional Self-Assembly of Spherical Particles Using a Liquid Mold and Its Drying Process. *Langmuir* (2003), **19**, 5179-5183.
3. Dai, Z.; Li, Y.; Duan, G.; Jia, L.; Cai, W., Phase Diagram, Design of Monolayer Binary Colloidal Crystals, and Their Fabrication Based on Ethanol-Assisted Self-Assembly at the Air/Water Interface. *ACS Nano* (2012), **6**, 6706-6716.
4. Malekpourkoupaei, A.; Kostiuik, L. W.; Harrison, D. J., Fabrication of Binary Opal Lattices in Microfluidic Devices. *Chem. Mater.* (2013), **25**, 3808-3815.
5. Huang, X.; Zhou, J.; Fu, M.; Li, B.; Wang, Y.; Zhao, Q.; Yang, Z.; Xie, Q.; Li, L., Binary Colloidal Crystals with a Wide Range of Size Ratios via Template-Assisted Electric-Field-Induced Assembly. *Langmuir* (2007), **23**, 8695-8698.
6. Khunsin, W.; Romanov, S. G.; Torres, C. M. S.; Ye, J.; Zentel, R., Optical Transmission in Triple-film Hetero-opals. *J. Appl. Phys.* (2008), **104**, 013527.
7. Yu, X.; Lee, Y. J.; Furstenberg, R.; White, J. O.; Braun, P. V., Filling Fraction Dependent Properties of Inverse Opal Metallic Photonic Crystals. *Adv. Mater.* (2007), **19**, 1689-1692.
8. Baddour-Hadjean, R.; Navone, C.; Pereira-Ramos, J. P., In situ Raman Microspectrometry Investigation of Electrochemical Lithium Intercalation into Sputtered Crystalline V₂O₅ Thin Films. *Electrochim. Acta* (2009), **54**, 6674-6679.
9. Baddour-Hadjean, R.; Marzouk, A.; Pereira-Ramos, J. P., Structural Modifications of Li_xV₂O₅ in a Composite Cathode (0 ≤ x < 2) Investigated by Raman Microspectrometry. *Journal of Raman Spectroscopy* (2012), **43**, 153-160.